Millimeter-wave radar imaging systems : focusing antennas, passive compressive devicefor MIMO configurations and high resolution signal processing

Antoine Jouadé

To cite this version:

Antoine Jouadé. Millimeter-wave radar imaging systems : focusing antennas, passive compressive devicefor MIMO configurations and high resolution signal processing. Signal and Image processing. Université de Rennes, 2017. English. NNT : 2017REN1S154 . tel-01933731

HAL Id: tel-01933731
https://theses.hal.science/tel-01933731

Submitted on 24 Nov 2018

ANNÉE 2017

THÈSE / UNIVERSITÉ DE RENNES 1
sous le sceau de l'Université Bretagne Loire

pour le grade de

DOCTEUR DE L'UNIVERSITÉ DE RENNES 1

Mention : Traitement du signal et Télécommunications
Ecole doctorale MathSTIC
présentée par

Antoine JOUADÉ

préparée à l'unité de recherche UMR-CNRS 6164, IETR
Institut d'Electronique et Télécommunications de Rennes
UFR Informatique et Electronique

Millimeter-wave Radar Imaging Systems : Focusing Antennas, Passive Compressive Device for MIMO configurations and High Resolution Signal Processing

Soutenance prévue à Rennes
le 23 Novembre 2017
devant le jury composé de :

Marc LESTURGIE
Professeur, Centrale Supélec / rapporteur
Wolfgang MENZEL
Professeur, Université de Ulm / rapporteur
Hélène ORIOT
Maitre de recherche, établissement / examinateur
Atika MENHAJ
Professeur, Université de Valenciennes / examinateur
Olivier LAFOND
Maitre de Conférence HDR, Université de Rennes 1 / directeur de thèse
Laurent FERRO-FAMIL
Professeur, Université de Rennes 1 / Co-directeur de thèse
Mohamed HIMDI
Professeur, Université de Rennes 1 / Co-encadrant
Stéphane MÉRIC
Maitre de Conférence HDR, INSA / Co-encadrant

On Feb 14, 1990 Voyager 1 looked back at Earth from a distance of 3.7 billion miles and took a picture... The image is known as the "Pale Blue Dot." We succeeded in taking that picture, and, if you look at it, you see a dot. That's here. That's home. That's us. On it, everyone you ever heard of, every human being who ever lived, lived out their lives. The aggregate of all our joys and sufferings, thousands of confident religions, ideologies and economic doctrines, every hunter and forager, every hero and coward, every creator and destroyer of civilizations, every king and peasant, every young couple in love, every hopeful child, every mother and father, every inventor and explorer, every teacher of morals, every corrupt politician, every superstar, every supreme leader, every saint and sinner in the history of our species, lived there – on a mote of dust, suspended in a sunbeam.

The Earth is a very small stage in a vast cosmic arena. Think of the rivers of blood spilled by all those generals and emperors so that in glory and in triumph they could become the momentary masters of a fraction of a dot. Think of the endless cruelties visited by the inhabitants of one corner of the dot on scarcely distinguishable inhabitants of some other corner of the dot. How frequent their misunderstandings, how eager they are to kill one another, how fervent their hatreds. Our posturing, our imagined self-importance, the delusion that we have some privileged position in the universe, are challenged by this point of pale light. [...] To my mind, there is perhaps no better demonstration of the folly of human conceits than this distant image of our tiny world. To me, it underscores our responsibility to deal more kindly and compassionately with one another and to preserve and cherish that pale blue dot, the only home we've ever known.

Carl Sagan, speech at Cornell University, October 13, 1994

Contents

1 Introduction **1**
1.1 Context of study . . . 1
1.2 Thesis Organization . . . 2

2 RADAR systems **5**
2.1 Frequency spectrum . . . 6
2.2 Radar equation . . . 7
2.2.1 Antenna parameters . . . 9
2.2.2 Configuration . . . 10
2.3 Range focusing using frequency diversity . . . 11
2.4 State-of-art of Radar imaging systems . . . 15
2.4.1 Direct imaging . . . 16
2.4.2 Indirect imaging . . . 25
2.5 Summary . . . 29
Bibliography . . . 31

3 Real Aperture Radar (RAR) imaging systems: Direct imaging technique **35**
3.1 Introduction . . . 35
3.2 Fresnel lens antennas . . . 36
3.2.1 Theoretical efficiency . . . 38
3.2.1.1 Phase compensation efficiency . . . 39
3.2.1.2 Amplitude tapering efficiency . . . 40
3.2.2 Design and measurement of the feeder . . . 42
3.2.3 Fresnel lens theory . . . 44
3.2.4 Simulation . . . 48
3.2.5 Realization . . . 48
3.2.6 Radiation pattern measurements . . . 50
3.3 RAR measurements . . . 56
3.4 Summary . . . 56
Bibliography . . . 60

4 Radar imaging systems: indirect imaging technique 63
4.1 Introduction . . . 63
4.2 Virtual array principle . . . 66
4.3 SIMO configuration . . . 73
4.3.1 Description . . . 73
4.3.2 Simulations . . . 75
4.3.3 Measurements . . . 76
4.4 MIMO configuration . . . 80
4.4.1 Passive Compressive Device (PCD) . . . 80
4.4.1.1 Details of PCD and associated antennas . . . 81
4.4.1.2 Direct Port-to-Port measurement of the PCD using a Vector Network Analyzer . . . 85
4.4.1.3 Estimating transfer functions using Compact Antenna Test Range measurements . . . 87
4.4.2 MIMO-SAR configuration measurement . . . 94
4.4.3 Stacked-patch antenna array . . . 98
4.4.3.1 Design of the antenna element . . . 98
4.4.3.2 Passive prototypes . . . 99
4.4.3.3 Active prototype . . . 105
4.5 Summary . . . 107
Bibliography . . . 107

5 Spectral estimation methods 113
5.1 Near-field and wide-band environments . . . 115
5.1.1 Geometry configuration . . . 115
5.1.2 Near-field and wide-band configurations . . . 117
5.2 Compensation using focusing techniques . . . 123
5.3 Spectral analysis algorithms . . . 127
5.3.1 Signal Model . . . 127
5.3.2 Spectral Estimation Methods . . . 128
5.3.3 Near-field wide-band configuration . . . 129
5.4 Simulations . . . 133
5.5 Measurements . . . 135
5.6 Summary . . . 141
Bibliography . . . 141

Conclusion 145

Scientific production 149

A Emitted waveform I
A.1 Matched filter . . . I
A.2 Pulsed linear frequency modulated waveform: Chirp waveform . . . V
A.3 Increasing linear frequency modulated continuous waveform: L-FMCW VII
A.4 Stepped frequency continuous waveform: SFCW . . . XII

B Résumé étendu en français XV

List of Figures

2.1 A geometric representation using the polar coordinate (d, θ, ϕ) from the Cartesian coordinate (x, y, z). 10
2.2 (a) Point-like targets location, (b) received signal in the spatial domain after range focusing. 14
2.3 Received signal in the spatial domain after range focusing and (a) Hamming amplitude tapering and (b) Hanning amplitude tapering. . 14
2.4 Mechanically beam-scanning antenna solutions with in (a) the overall system is steered, in (b) only the feeder is steered and finally in (c) only the focusing aperture is steered. 17
2.5 (a) Active system developed by JPL [6] with measurement results [25] in (b) for different target scenario for through-jacket of a mock pipe bomb. 18
2.6 (a) Mechanically rotated reflect array with horn [26] with (b) an example of the image reconstruction. 19
2.7 Electronically beam-scanning antenna solutions. 20
2.8 (a) Structure of the phased array [27] with (b) the beam scanning capability. A measurement result is shown in (c). 22
2.9 Frequency beam-scanning antenna solution. 24
2.10 (a) The printed progressive wave antenna [31] with (b) and (c) the beam scanning capability. 24
2.11 (a) Sar configuration with (b) a 2D measured image and (c) a 3D measured image. [36] 27
2.12 SAR system mounted on a van at 300 GHz in (a) with in (b) the imaging result and in (c) the optical image. [37] 28
2.13 In (a) and (b) are shown the MIMO aperture configuration with in (c) the scene with the imaging result. [38] 29

3.1 (a) A multi-dielectric Fresnel Zone plate lens [7] with in (b) the corresponding focusing gain. (c) A grooved Fresnel Zone plate lens [8] with in (d) the corresponding focusing gain. (c) A perforated dielectric Fresnel lens [9] with in (d) the corresponding focusing gain. . . . 37

3.2 Sectional and top views of the flat Fresnel lens with F the focal distance, D the diameter of the lens, d the thickness of the lens. θ_i yields for a particular angle of incidence with the corresponding refracted angle θ_t. The variable Δ corresponds to the phase shift that occurs at the input of the lens due to the spherical wavefront. 38

3.3 Phase shift that occurs at 75 GHz along the circular aperture diameter due to the spherical wave front and the generated phase compensation using the five cases. 40

3.4 Phase compensation efficiency of the five cases versus the normalized frequency band. 40

3.5 Theoretical aperture efficiency over the amplitude weighting generated by a cos^n-like radiation pattern. 41

3.6 (a) Sketch of the elliptical horn antenna and (b) the manufactured elliptical horn with rectangular-to-circular transition producing an axially symmetric $\cos^n$-like radiation pattern 42

3.7 Simulated and measured radiation pattern of the feeder at 90 GHz . . 42

3.8 Measured (Co/Cross polarization) radiation pattern of the optimized feeder along the E ($\phi = 90°$) / H ($\phi = 0°$) / 45° ($\phi = 45°$) planes compared with the associated $\cos^n$-like radiation pattern at the extreme frequencies (a) 75 GHz and (b) 110 GHz. 43

3.9 Oblique wave propagation through N layers of dielectric slabs with $mathbfE$ and $mathbfH$ the electric and magnetic fields, respectively. 44

3.10 Comparison of the determined permittivity variation along the diameter of the 2 circular lens apertures. 46

3.11 Variation of the transmission coefficient along the diameter and versus the considered frequency range for the (a) *smooth* and (b) $smooth\left[2\pi\right]$ cases. (c) Variation of the transmission coefficient efficiency versus the considered frequency range for the two cases. 47

3.12 Simulated Electric field (at 90 GHz) at the output of (a), (c), (e) the *smooth* lens and (b), (d), (f) the $smooth[2\pi]$ lens with a diameter of 12 cm; (a), (b) show the variation of the permittivity over the lens surface, while (c), (d) show the normalized electric field distribution in amplitude (dB) over the lens surface and (e), (f) show the electric field distribution in phase (°) over the lens surface. 49

3.13 Initial thickness along the aperture diameter of each sub-lens before being pressed. 50

3.14 Manufactured sub-lenses before pressing them for the (a) $smooth\left[2\pi\right]$ and (b) *smooth* cases. 50

3.15 Manufactured sub-lenses for the (left side) $smooth\left[2\pi\right]$ and (right side) *smooth* cases after being pressed. 51

3.16 Measured radiation performance of the *smooth* lens. (a) radiation pattern along the E/H/45° planes at 90 GHz. (b) Side lobe level along the E/H/45° planes versus the frequency range. (c) Half-power beam-width along the E/H/45° planes versus the frequency range. (d) Normalized E-plane radiation pattern (Co-polarization) versus the frequency range. (e) Normalized H-plane radiation pattern (Co-polarization) versus the frequency range. (f) Normalized 45°-plane radiation pattern (Co-polarization) versus the frequency range. 51

3.17 Measured radiation performance of the *smooth*$\left[2\pi\right]$ lens. (a) radiation pattern along the E/H/45° planes at 90 GHz. (b) Side lobe level along the E/H/45° planes versus the frequency range. (c) Half-power beam-width along the E/H/45° planes versus the frequency range. (d) Normalized E-plane radiation pattern (Co-polarization) versus the frequency range. (e) Normalized H-plane radiation pattern (Co-polarization) versus the frequency range. (f) Normalized 45°-plane radiation pattern (Co-polarization) versus the frequency range. 52

3.18 Simulated directivity and measured gain versus the frequency range for the *smooth*[2π] and *smooth* cases. The results are compared with the theoretical directivity optained by a uniform amplitude and phase aperture of same physical dimension than the manufactured lenses. The results are also compared to a uniform phase aperture with amplitude weighting generated by a $\cos^n$-like feeder radiation pattern with n lying between 35 and 70. 53

3.19 Simulated aperture efficiency for the *smooth*[2π] and *smooth* cases versus the frequency. 53

3.20 Measured loss efficiency for the *smooth*[2π] and *smooth* cases versus the frequency. 54

3.21 Measured total efficiency for the *smooth*[2π] and *smooth* cases versus the frequency. 54

3.22 Schematic of the measurement setup. 57

3.23 Google map of the outdoor scene with (x), the location of the Direct radar imaging, (1), the building, (2), the old tractor, (3), the antenna support and (4) the bruches and tall grass 58

3.24 Measurement results with (a) the RAR image and (b) the RAR image superposed to the Google map picture of the scene. 59

4.1 The different indirect radar imaging configurations. 64

4.2 Scheme of the Near-field/Far-field transition 67

4.3 Simulated results using a linear array with $N_x = 10$ and $\Delta_x = 1\lambda$, with the dashed blue line corresponding to the element radiation pattern, the red line corresponding to the array factor and the black line the array radiation pattern with a digitally beam scanning (a) $\theta_0 = 0°$ (b) $\theta_0 = 30°$ and (c) $\theta_0 = 60°$. 69

4.4 Simulated results using a linear array with $N_x = 10$, with the dashed blue line corresponding to the element radiation pattern, the red line corresponding to the array factor and the black line the array radiation pattern with (a) $\Delta_x = 0.5\lambda$, (b) $\Delta_x = 1\lambda$ and (c) $\Delta_x = 2\lambda$. . . . 70
4.5 Simulated results using a square array with $N_x = N_y = 10$ and $\Delta_x = 1\lambda$ and $\Delta_y = 2\lambda$, with (a) the element radiation pattern, (b) the array factor and (c) the array radiation pattern. 71
4.6 MIMO configuration (Tx: transmitting antenna location and Rx: reiceiving antenna location) used to generate a (a) fully populated linear virtual array, (b) and (c) a fully populated virtual array. 72
4.7 Geometry of the radar imaging configuration. 73
4.8 Simulated result of (a) the back-projected signal of the first receiving antenna, (b), the final SAR image after back-projection, (c) the final SAR image when the 2D Hamming tapering function is applied and (d) the final SAR image when the 2D Hanning tapering function is applied. 76
4.9 Measurement setup. 77
4.10 Picture of the three scene configurations with (a) 50 bolts of 5mm diameter configured to spell IETR,(b) a screw clamp, and (c) a knife hidden inside a thick book. 78
4.11 SAR image results considering the scene with (a) bolts configured to spell IETR, (b) the screw clamp and (c) the knife hidden in a book. . 78
4.12 Cutting view drawing of the 1x4 passive device with associated transfer functions 82
4.13 Exploded view drawing of the passive device with 1) the lower part with 2) the input and 3) the output ports. In 4) the diffractive element at the center of the cavity and in 5/6) the upper parts to close the cavity. 82
4.14 Photography of (a) the output face of the realized passive compressive device, which works at millimeter-wave, and (b) the output face of the horn antenna module. 84
4.15 Details of the antenna module with (a) Exploded view drawing of the horn antenna module with 1) the lower part, 2) the input ports attached to the output ports of the passive compressive device and (3) the upper part. The measured radiation pattern of the first port along (b) the E-plane Co-polar and (c) H-plane Co-polar ($G(\theta, f)$). . 85
4.16 Absolute value in dB of the measured transfer functions by means of a VNA along the frequency band. 86
4.17 The auto/cross-correlation results, $\mathbf{r_{ij}}(\tau) = DFT^{-1}[h_i(f)h_j(f)^*]$, between the measured transfer functions (VNA measurements), with the time domain τ (ns) along the horizontal axis and the normalized amplitude (dB) along the vertical axis. It is normalized by the maximum peak of the auto-correlation fonctions. DFT^{-1} yields for the inverse discete Fourier transform. 86

4.18 Measured power efficiency of the passive device corresponding to the outgoing powers from the four ports versus the incoming power along the frequency. 87
4.19 Setup measurement using a Compact Antenna Test Range. 88
4.20 Sketch of the phase variation that occurs when the DUT is looking at (a) broadside and (b) at squint angle. 90
4.21 Measured data along (b) the frequency domain and azimuth axis and along (a) the azimuth axis at the first frequency $f + f_c = 50GHz$. . . 91
4.22 Measured data at $f + f_c = 50$ GHz in (a) amplitude and (b) phase. The black line corresponds to the measured data ($\mathbf{S}_r(\theta, f)$) and the dashed red line corresponds to the result of the data model using the estimated transfer function found from minimization ($\hat{\mathbf{S}}_r(\theta, f)$). . . . 92
4.23 The auto/cross-correlation results, $\mathbf{r_{ij}}(\tau) = DFT^{-1}[h_i(f)h_j(f)^*]$, between the measured transfer functions ($\mathbf{h}(f)$) and the estimated transfer functions ($\hat{\mathbf{h}}(f)$), with the time domain τ(ns) along the horizontal axis and the normalized amplitude (dB) along the vertical axis. It is normalized by the maximum peak of the auto-correlation fonctions. DFT^{-1} yields for the inverse discete Fourier transform. 93
4.24 Absolute value of the complex inner product results between the measured transfer functions ($\mathbf{h}(f)$) and the estimated transfer functions ($\hat{\mathbf{h}}(f)$), along the frequency. 93
4.25 Measurement setup. 94
4.26 Scene in the anechoic chamber composed of two corner reflectors. . . 96
4.27 Measurement imaging results, by using 4.30, of two isotropic targets (corner reflectors) captured by (a) a classic SIMO configuration with 1Tx (transmitting element) and 40 Rxs (receiving elements), (b) the passive compressive device with 10 Rxs elements where the Port-to-Port measurement is used to have the transfer function and (c) the passive compressive device with 10 Rxs elements where the plane-wave estimation is used to have the transfer function. 97
4.28 Schematic of the stacked patch antenna 98
4.29 Feeding network dimension of the array of eight elements. 100
4.30 Simulated S-parameter of one single element and an array of 8 elements.100
4.31 Simulated Co/Cross radiation pattern of the element along (a) the E-plane and (b) the H-plane. 101
4.32 Simulated Co/Cross radiation pattern of the passive array along (a) the E-plane and (b) the E-plane. 102
4.33 Single element with (a) the fabricated prototype and (b) the exploded view. 103
4.34 Passive array of 8 elements prototype 103
4.35 Simulated and measured S-parameter of (a) the single element and (b) the array of 8 elements. 104
4.36 (a) schematic drawing and (b) the manufactured Active array layout of 8 independant elements. 106

5.1 Geometry of the Radar imaging configuration. 115

5.2 Sketch of the propagation of the range resolution front for a point-like target in a (a) far-field narrow-band configuration, (b) far-field wide-band configuration,(c) near-field narrow-band configuration,(d) near-field wide-band configuration. The blue dots represent the extreme sides of the aperture represented by the dashed line. The arrow gives the angle of incidence of the wave. 117
5.3 Simulation results of the matrix **S** for a point-like target in a far-field narrow-band configuration after (a) the range focusing and (c) the range and the cross-range focusing (Fourier SAR image without compensations). (b) shows the phase variation along the aperture. . . 118
5.4 Simulation results of the raw data matrix **S** in the far-field wide-band configuration (a), (c), (e) without the wide-band compensation and (b), (d), (f) with the wide-band compensation. The results in (a) and (b) are shown after the range focusing and (e), (f) after the range and the cross-range focusing (Fourier SAR image). In (c) and (d) are shown the phase variation along the aperture after the range focusing. 120
5.5 Simulation results of the raw data matrix **S** in the near-field narrow-band configuration (a), (c), (e) without the near-field compensation and (b), (d), (f) with the near-field compensation. The results in (a) and (b) are shown after the range focusing and (e), (f) after the range and the cross-range focusing (Fourier SAR image). In (c) and (d) are shown the phase variation along the aperture after the range focusing. 121
5.6 Simulation results of the raw data matrix **S** in the near-field wide-band configuration after (a), (d), (g) the range focusing and after (c), (f),(i) the range and the cross-range focusing (Fourier SAR image). In (b), (e) and (h) are shown the phase variation along the aperture after the range focusing. In (a), (b), (c) no compensation occurs. In (d), (e), (f), only the wide-band compensation is applied and finally in (g), (h), (i), the near-field and the wide-band compensations are applied. 122
5.7 Imaging geometry of the synthetic aperture Radar with the received raw data focused over (a) a 2D Cartesian grid (b) a 2D polar grid. . . 123
5.8 Cutting views of the Imaging geometry showing the variation of (a) the range resolution along the plane considered (b) the azimuth angular resolution along the range of observation angles. 125
5.9 Simulation results of the raw data matrix **S** after applying the focusing technique in the near-field wide-band configuration. The raw data is projected over (a), (c), (e), (g) a Cartesian grid (see Fig. 5.7a) and over (b), (d), (f), (h) a polar grid (see Fig. 5.7b) after (a), (b) the range focusing, after (g), (h) The range and the cross-range focusing (Fourier SAR image). In (c) and (d) are shown the phase variation after the range focusing and (e), (f) shows the 2D spectrum of the reconstructed image. 126
5.10 (a) 1D (b) 2D Spatial smoothing applied on the irregular grid. 131
5.11 Flow chart of applying the spectral analysis algorithms in a near-field environment with wide-band signals. 132

5.12 Simulated results of 2D spectral estimation methods using (a), (b), (c), (d) a Cartesian grid and (e), (f), (g), (h) a polar grid with (a), (e) the beamforming method, (b), (f) spatial smoothed beamforming, (c), (g) the CAPON method and (d), (h) the MUSIC method. 132
5.13 Imaging configurations with the two closely spaced point scatterers located in the broadside angle area I and the squint angle area II. . . 133
5.14 1D spectral estimation methods applied along cross-range direction on the (a), (b), (c) broadside angle area I and (d), (e) (f) squint angle area II. (a), (d) show the beamforming method, while (b), (e) show the CAPON method and (c), (f) show the MUSIC pseudo-spectra method. 134
5.15 2D spectral estimation methods applied on the (a), (b), (c) broadside angle area I and (d), (e) (f) squint angle area II. (a), (d) show the beamforming method, while (b), (e) show the CAPON method and (c), (f) show the MUSIC pseudo-spectra method. 134
5.16 Measurement setup. 135
5.17 Picture of the three scene configurations with (a) 50 bolts of 5mm diameter configured to spell IETR,(b) a screw clamp, and (c) a knife hidden inside a thick book. 136
5.18 2D spectral estimation methods applied on the (a), (d), (g), (j) bolts configured to spell IETR; (b), (e), (h), (k) the screw clamp and (c), (f), (i), (j) the knife hidden in a book. (a), (b), (c) show the beamforming method and (d), (e), (f) show the beamforming method after spatial smoothing, while (g), (h), (i) show the CAPON method and (j), (k), (l) show the MUSIC methods. 137
5.19 2D spectral estimation methods applied on the imaging results (Cartesian grid) using the MIMO configuration with the passive compressive device considering (a), (e), (i), (m) one output, (b), (f), (j), (n) two outputs, (c), (g), (k), (o) three outputs and (d), (h), (l), (p) four outputs of the passive compressive device. (a), (b), (c), (d) show the beamforming method result and (e), (f), (g), (h) show the beamforming method result after spatial smoothing, while (i), (j), (k), (l) show the CAPON method result and (m), (n), (o), (p) show the MUSIC method result. 139
5.20 2D spectral estimation methods applied on the imaging results (Polar grid) using the MIMO configuration with the passive compressive device considering (a), (e), (i), (m) one output, (b), (f), (j), (n) two outputs, (c), (g), (k), (o) three outputs and (d), (h), (l), (p) four outputs of the passive compressive device. (a), (b), (c), (d) show the beamforming method result and (e), (f), (g), (h) show the beamforming method result after spatial smoothing, while (i), (j), (k), (l) show the CAPON method result and (m), (n), (o), (p) show the MUSIC method result. 140

A.1 Synoptic of a pulsed RADAR V
A.2 Chirp Waveform and the associated impulse response VIII

A.3 Synoptic FMCW RADAR IX
A.4 Instantaneous frequency X

B.1 (a) efficacité de compensation de phase, (b) efficacité d'illumination de la lentille, (c) variation de permittivités nécessaire des lentilles, (d) les lentilles réalisées et (e), (f) résultats de mesures du système antennaire. XVI
B.2 Résultats des mesures radar avec (a) le système radar utilisé et (b), l'image radar et (c) l'image radar superposée avec une image de la scène pris grâce à google map. XVII
B.3 Résultats de mesures pour trois différentes scènes. XVIII
B.4 Dispositif compressif passif. XIX
B.5 Flow chart of applying the spectral analysis algorithms in a near-field environment with wide-band signals. XX
B.6 Resultats des méthodes d'estimation spectrales (Beamforming, Beamofrming avec "spatial smoothing", CAPON et MUSIC) 2D appliqué sur une scène avec un couteau caché dans un livre.2D spectral estimation methods applied on the knife hidden in a book. XX

List of Tables

2.1 The main techniques 8
2.2 Classification of antenna parameters 9
2.3 Evaluation of the different direct techniques 23
2.4 Evaluation of the indirect techniques 30

3.1 Measured dielectric properties obtained from AIREX82 depending on the thickness ratio 50
3.2 Summarized radiation performances for two lenses 55

4.1 Summarized point spread function performances 96

5.1 Simulation parameters for the different configurations (FF: Far-field, NF: Near-field, NB: Narrow-band and WB: Wide-band). 119
5.2 Spectral estimation methods 129

Chapter 1

Introduction

1.1 Context of study

The majority of the regions of the electromagnetic spectrum can be used for imaging the unseen. The different operating frequencies provide various information about the area of interest that are interesting in many applications. The microwave operating frequencies enable to see at night, through clouds and some materials and thus provide a valuable supplement to other imaging techniques such as infrared or X-ray techniques.

The ability to distinguish small details of an object, also known as the spatial resolution, is directly linked to the frequency bandwidth used and the radiating aperture size of the device. At the visible frequencies, with a human eye having a pupil diameter of about 5 mm, the angular resolution is approximately equal to 0.0084°. Such result corresponds to a spatial resolution of about 1 cm at a distance of 70 meter from the eye. To achieve the same resolution at microwave frequencies, an aperture length of 250 m at a frequency of 10 GHz is required which makes it rather difficult to realize. In order to obtain high resolution images even at microwave frequencies, one of the greatest advance is the principle of synthetic aperture thanks to a radar system embedded on a moving platform (satellite, plane, drone, ...). It has widely been used for the earth observation. For near-range applications such as automotive, concealed object detection under clothes and plenty of other applications, a more compact system working with real-time acquisitions is required. This is where the Synthetic Aperture Radar (SAR) technique reaches its limit because it is required that the area of interest is motionless during the travel path of the moving platform.

To improve the resolution while keeping an acceptable size, increasing the frequency such as going at millimeter-wave is of great interest thanks to its reduced wavelength and wide frequency bands available. However, for real time acquisitions, it is needed to physically sample an aperture with a large number of antennas and associated chains (transmitter/receiver). Due to the small wavelength and then the small components size, the fabrication process complexity is increased as for the cost. Nowadays, main researches are concentrating their efforts to find solutions to reduce the number of chains while keeping an acceptable spatial resolution. Either the sampling pattern over the aperture is studied or it is developed advanced signal processing techniques or tools to improve the spatial resolution.

Among all the methods allowing to improve the Radar imaging capability, the goal of this study is to investigate various solutions and techniques while keeping and improving the more relevant ones.

1.2 Thesis Organization

The thesis is organized around four main chapters:

The chapter 2 outlines the basic of radar followed by a brief state-of-arts on radar imaging systems. Two main radar configurations will be presented. First, the Real Aperture Radar (RAR), also known as the direct imaging technique. The main solutions to scan the beam of antennas to produce a radar image will be given. Second, the Synthetic Aperture Radar, also known as indirect imaging technique. Different modes of SAR may be used. The modes are listed and compared to determine the relevant one that will be deeper studied. Finally, the theory of the radar principle is studied and applied on simulated data to determine the achievable range resolution using frequency diversity. This chapter permits to select among the different methods presented, the more relevant ones that will be further detailed or improved in the next chapters.

In the chapter 3 is further presented the Real Aperture Radar configuration, where the image is realized pixel by pixel using high directive antennas in which the main beam is scanned. A high directive Fresnel lens antenna is studied, simulated and measured. As compared to the literature in which the lens is sampled in multiple but limited zones, in this work, a smooth version is realized thanks to a new technological process. As compared to other methods, the smooth version of the Fresnel lens leads to an improvement of efficiency and a stable gain over a wide frequency band. Finally, the Fresnel lens antenna will be used in a RAR configuration using only one couple of transmitter (Tx) and receiver (Rx) chains to generate a radar image of an outdoor scene using a mechanically beam scanning capability. However, this solution reaches its limit when real-time radar imaging systems are necessary.

In the chapter 4 is presented the SAR theory with the associated focusing algorithm required to generate the SAR image. Thanks to a scanner system, measurements are performed at millimeter-wave to create high spatial resolution SAR images of small objects such as a knife. The scanner synthesizes a receiving array of independent elements. When a real receiving array is used, a high number of Rx chains is required which leads to a complex and costly solution. To reduce the number of chains, the next study focuses on the use of a Multiple-Input-Multiple-Output (MIMO) configuration where the main goal is to reduce the number of chains by means of the virtual array theory. To further reduce the number of chains, a passive compressive device is studied, realized and measured, which has the capability to compress multiple signals into one while making each signal decorrelated from each other in a passive manner. Each channel inside the device is related to its own transfer function in the frequency domain. Two methods to measure or to estimate the transfer functions with great accuracy are studied. Finally, the passive compressive device is used in a MIMO configuration showing the great capability of the passive compressive device to reduce the number of chains while maintaining unchanged the spatial resolution.

In the previous chapter, it is shown how it is possible to reduce the number of Tx and Rx chains while maintaining unchanged the spatial resolution by modifying the geometry of the transmitting and receiving antenna array. In the chapter 5, from a limited number of elements (antennas and associated chains), the received signals are digitally processed by means of spectral estimation methods to improve the spatial resolution. The method is dedicated to specific configurations and assumptions are made such as the narrow band and the far-field configuration. A solution able to use spectral estimation methods in a near-field and wide-band configuration is shown. The solution is applied on real data showing the improved spatial resolution in a near-field and wide-band configuration.
Finally, the last chapter concludes the study and points to several directions for future researches to improve the spatial resolution while keeping as low as possible the number of Tx/Rx chains available.

Chapter 2

RADAR systems

Radar systems are used to detect the electromagnetic waves that propagates within a certain domain of space and to measure the electromagnetic responses. Three different Radar systems may be used.

- **Passive radar** [1, 2]: The passive radar system detects the energy naturally emitted by the scene (naturally emitted black-body radiation). Because, the passive radar does not transmit any signals, it only requires receiving chains. However, one of the main drawback of a passive system, is that it is not possible to focus along the range axis which is a strong limitation for our goal.

- **Passive radar using signals of opportunity** [3–5]: Because in the electromagnetic spectrum, frequency bands are already allocated for various applications such as railway/maritime/aeronautical/spatial/military communications, wireless multimedia communications, radiolocalisation and satellite navigation systems, radio astronomy, earth exploration, weather satellite, active radar and imaging Synthetic Aperture Radar applications, the passive radar system using signals of opportunity detects the backscattered signals coming from the applications listed above. Such a radar has the capability of operation without any spectrum resource allocation and a potentially null probability of being intercepted. It only requires receiving chains to acquire the backscattered signals. However, it is spatially limited by the coverage of the transmitter.

- **Active radar** [6, 7]: An active radar transmits its own signal over a limited frequency band through a certain domain of space and measure the electromagnetic responses of obstacles, also called targets or scatterers. The system requires both transmitting and receiving chains.

A passive imaging system has the advantage to be simpler to implement because there is no need for a transmitter chain (use of free natural illumination). This kind of system is safe for humans because there is no illumination to human body. On the contrary, a passive system suffers from the problem of a small received power due to the thermal noise of the target. So the image contrast can be very low within a limited range of distance. If the application needs to extend the distance and increase the received power, an active system is desirable even if the global implementation is more costly and complex. It has to be underlined that using active sensors and knowing the emitted signal, we are able to compare the emitted and received signals, and set up an improvement of the signal-to-noise ratio thanks to the matched filter and therefore improve the ability to analyze and detect the scene and the targets.

2.1 Frequency spectrum

In the past decades, we have witnessed an impressive development to extend the capability of detection based on magnetic, acoustic, ultrasound, microwave, millimeter-wave, TeraHertz, infrared and x-ray sensors [8–11]. An overview of the different imaging technologies available will be briefly considered showing the most relevant techniques found in the literature.

- **Infrared technique** (3 THz - 300 THz) [12]: This technique is based on the detection of thermal radiations which is a function of the frequency and absolute temperature. In another word, the capability of detection of such a system depends on the temperature difference between the different objects to be detected and the human body. When used for Concealed Weapon Detections (CWD) operations, infrared imaging has some drawbacks. First of all, the short wavelength of infrared doesn't permit to penetrate thick clothes. Another drawback is that as soon as the temperature of the object is close to the body's one, the detection is impossible. This occurs when the object is kept under clothing for a long time.

- **X-ray technique** (300 PHz - 30 EHz) [13]: Medical screening is the main use of X-ray imaging thanks to its ability to penetrate body and clothes with high spatial resolution but certain studies have focused on concealed human detection inside a truck. The main drawback of this system is that X-ray radiation is ionizing and so, a dose is radiated toward human.

- **Micro/millimeter-wave technique** (3 GHz - 300 GHz) [14]: Millimeter waves are suitable for security surveillance and especially for the detection of objects concealed under people's clothing and baggage. In fact, thanks to the short wavelengths (from 30 GHz (10 mm wavelength) to 300 GHz (1 mm wavelength)) which have the ability to penetrate dielectric materials such as plastic or cloth and are strongly reflected by metallic materials, it is able to pass through obscurants such as fog, cloud, smoke and night. Unlike X-ray, millimeter waves are non-ionizing and can be used to detect both metallic and nonmetallic objects. They can achieve high spatial resolution by going in higher frequencies but material and atmosphere attenuation also increase so a trade-off has to be addressed. Depending on the applications, we are able to define an optimal frequency which allow to detect and image a weapon for instance at 10 meter from the system.

- **Terahertz technique** (300 GHz - 3THz) [15, 16]: THz is also interesting because it allows to classify different type of materials. In fact each material has a different absorption spectra in THz frequency range. THz can be used for security screening but its applications is limited to a very short range 3D imaging.

The different concealed weapon detection techniques are tabulated in the Table 2.1 showing their main advantages and issues but also the type of illumination, the possibility of penetration and also the distance of the imaging scene capability. MMW based technology has the widest range of possibility to make an imaging system. The system can be transportable and both metals and non-metals can be detected. Even though THz provides high resolution, it doesn't permit to illuminate a large scene because of the high atmospheric absorption and its medium penetration.

As explained before, infrared technique is not a suitable solution due to its low penetration which doesn't fit the requirement. Moreover, this kind of systems is not able to differentiate targets having the same temperature. X-ray imager due to its safety concerns (ionizing radiation) hinders its acceptance to illuminate human body but this is also because of its low range of detection and imaging. The choice of MMW system is the most suitable solution to fit the requirement thanks to its good penetration ability and high resolution but also the capability of size reduction, wide available bandwidth and industrial interference frequencies which are really much weaker than those at microwave bands. In this frequency range, the electromagnetic wave penetrates most of dielectrics and it exists some particular and advantageous atmospheric windows (no additional absorption) allowing to implement imaging systems for security and people protection.

For a near-range imaging system up to about 20 meters, the study will mainly focus on active systems working at millimeter-wave. As explained previously, the active system allows to detect targets farther while going through material such as detecting concealed objects under clothes. Furthermore, thanks to the small wavelength at millimeter-wave, it allows to manufacture active radar with an acceptable size.

2.2 Radar equation

Let consider an active radar having only one transmitting and one receiving chain with antennas in the front-end of the chains. A RF stimulus signal ($S_e(f)$) with output power P_e is transmitted with a frequency diversity over a frequency bandwidth B_f with $f \in [-B_f/2, B_f/2]$. Before being sent through the medium, the signal has been transposed around the carrier frequency f_c, with its counterpart in the spatial frequency domain (wavenumber domain) $k_c = 4\pi/\lambda_c = 4\pi f_c/c$ and the spatial frequency band $k \in [-2\pi B_f/c, 2\pi B_f/c]$. The speed of light is set out with c and λ_c corresponds to the wavelength at the carrier frequency f_c. We note that the expression of the wave number shows a factor of 2 as compared with common conventions. The transmitted signal will be delayed from the propagation from the transmitted antenna to a specific target and backscattered to the receiving antenna. It is because we are only interested in the one-way distance between the radar to

Table 2.1: The main techniques

Technologies	Illumination	Proximity	Penetration	Main advantages	Main issues
Infrared	Passive	Far	Low	Passive system and possible detection and imaging at far distance	Low penetration and no differentiation when temperature contrast is low
X-Ray	Active	Near	Very-high	Allow to detect inside the body	Safety concerns and low proximity
MMW	Active or Passive	Far	High	Resolution high enough to image concealed objects, good penetration, possible portable system	high-cost (non-availability of components in high-frequencies, important atmospheric absorption at specific frequency bands)
THz	Active	Near	Medium	High-spatial resolution and possible detection and separation of materials	high-absorption lost, stand-off detection unsuitable, high atmospheric absorption

Table 2.2: Classification of antenna parameters

Radiation properties	**Circuits properties**	**Mechanical properties**
Radiation pattern (Directivity, Beam width, Side lobe level) Radiation efficiency Gain Effective area Aperture efficiency Phase radiation pattern Polarization of EM wave Cross-Polarization	Impedance (matching) Frequency bandwidth	Type of antenna Shape Size Mass

the target, that the factor two in the wavenumber arises. It will be useful when we will derive the data model.

2.2.1 Antenna parameters

An antenna is a device which converts circuit currents into propagating electromagnetic waves and, by reciprocity, collects propagating electromagnetic waves and converts it into circuit currents. Several quantities may be defined in order to describe an antenna that are summarized in the Table 2.2.

In this section, a perfect antenna with an optimal efficiency and null cross-polarization level is considered. The maximum gain corresponds to the directivity and we are only concerned by the radiation pattern. When it is needed to display the radiation pattern of an antenna, it is more common to use a spherical reference. However, in the Section 2.2.2, the configuration that will be used is considered with respect to an orthogonal Cartesian reference. It is then required a Cartesian to spherical coordinate transformation. The transformation is shown in (2.1) using the Fig. 2.1.

For expressing the far-field quantities, a spherical reference coordinate (d, θ, ϕ) is considered with $\theta \in [-\pi, \pi]$ measuring the rotation from the $x - axis$ in the $xy - plane$ and with $\phi \in [0, \pi]$ measuring the tilting with respect to the $z - axis$. From a particular point $P_i(x_i, y_i, z_i)$, the transformation is given by (2.1).

$$\begin{aligned} x_i &= d_i \cos\theta_i \sin\phi_i \\ y_i &= d_i \sin\theta_i \sin\phi_i \\ z_i &= d_i \cos\phi_i \end{aligned} \tag{2.1}$$

In what follows, $G(k, \theta, \phi)$ corresponds to the variation of the gain along the spatial frequency domain within the two angular sectors θ and ϕ. Here, k is the wavenumber variable directly linked to the frequency. The expression corresponds to the ratio between the surface density of the radiated power and that radiated by an isotropic antenna with a radiation pattern uniformly distributed on a sphere.

The angles θ_i and ϕ_i correspond to the look angles from the center of the spherical coordinates.

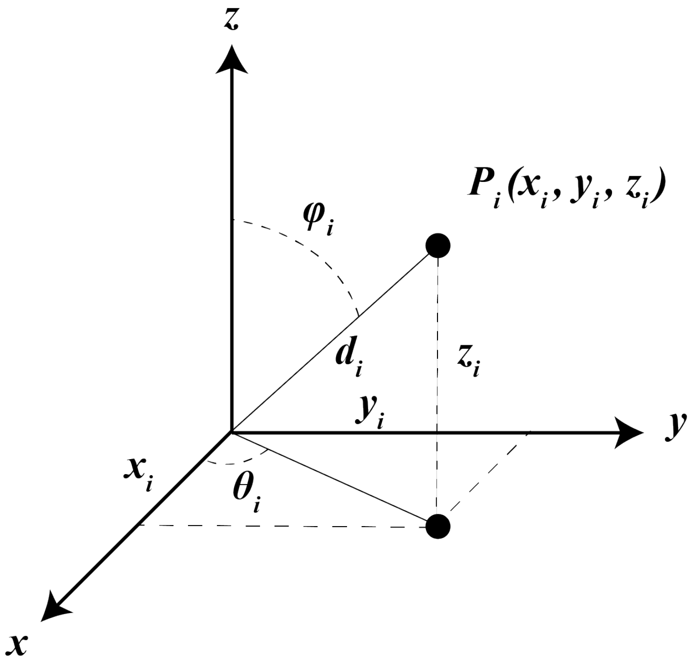

Figure 2.1: A geometric representation using the polar coordinate (d, θ, ϕ) from the Cartesian coordinate (x, y, z).

2.2.2 Configuration

In a 3-Dimensional spatial space, a transmitting antenna is located at a fixed position with a gain variation $G_t(k, \theta, \phi)$. The location of its phase center is (x_t, y_t, z_t). The phase center of the receiving antenna is (x_a, y_a, z_a) with a gain variation $G_a(k, \theta, \phi)$. It is considered N_s point scatterers which are identified by their Cartesian coordinates (x_i, y_i, z_i). The index i yields for the i^{th} point scatterer P_i with $\sigma_i(k, \theta_i, \phi_i)$ the Radar Cross-Section (RCS) of the i^{th} target over the frequency diversity. In this situation, it is considered that the RCS of the target is a constant through time and look angles and variations only occur over the frequency band B_f. The one-way distance (corresponding to the radial distance) for the wave propagating from the transmitting antenna to the point scatterer P_i and then reflected back upon the receiving antenna is given by [17]:

$$
\begin{aligned}
d_i &= \frac{1}{2}(dTx_i + dRx_i) \\
&= \sqrt{(x_t - x_i)^2 + (y_t - y_i)^2 + (z_t - z_i)^2}/2 \\
&+ \sqrt{(x_a - x_i)^2 + (y_a - y_i)^2 + (z_a - z_i)^2}/2
\end{aligned}
\tag{2.2}
$$

The received signals, at the receiving antenna level, are modeled as a sum of transmitted signals that are weighted and delayed [18]. The complex weighting $s_i(k, \theta_i, \phi_i)$ represents all the attenuations that occur during the round-trip propagation and the reflectivity (RCS) $\sigma_i(k, \theta_i, \phi_i)$ of the i^{th} point scatterer P_i. The RCS is a characteristic of the observed scatterer and can be expressed as a function of the reflection coefficient $\sigma_i(k,\theta_i,\phi_i) = \lim_{d_i\to\infty} 4\pi\, d_i^2 \frac{|E_s(d_i)|^2}{|E_0|^2}$ with E_0 that represents the incident field on the scatterer and $E_s(d_i)$ is the amplitude of the reflected field from the scatterer at a distance d_i away from it. The interaction of the electro-magnetic wave with a scatterer can be briefly described by four elementary mechanisms: reflection, refraction, diffraction and scattering [19, 20]. Considering that the look angles θ_i and ϕ_i are similar (mono-static configuration) for the transmitting and receiving antennas, the complex weighting can be modeled using the radar equation [21] in (2.3).

$$s_i(k,\theta_i,\phi_i) = P_e\, G_t(k,\theta_i,\phi_i)\, G_a(k,\theta_i,\phi_i)\, \frac{(2\pi)^2}{((k+k_c)/2)^2 (4\pi)^3\, d_i^4} \sigma_i(k,\theta_i,\phi_i) \tag{2.3}$$

The delays arise from the round-trip distances determined in (2.2). Furthermore, a Gaussian white noise $n(k) \sim \mathcal{N}_{\mathbb{C}}(0,\sigma^2)$ with zero mean and variance σ^2 is present. The received signals can then be modeled as:

$$S_r(k) = S_u(k) + n(k) = \sum_{i=1}^{N_s} s_i(k,\theta_i,\phi_i)\, S_e(k)\, e^{-j(k+k_c)\, d_i} + n(k) \tag{2.4}$$

with $S_u(k)$ corresponds to the useful signals. The Gaussian white noise $n(k)$ is a measurement noise with a noise power P_n, inherent to the use of electronic devices and random by nature. We measure the quality of the received signal through the ratio of powers associated with the useful component and the noise, called the Signal-to-Noise power Ratio (SNR). As the noise is considered as white on the effective band (B_f) of the receiver, it has a spectral density with uniform power on this domain equal to N_n in W/Hz. A sampling of this signal at a frequency $f_s = B_f$ gives uncorrelated sampled with a variance equal to $B_f\, N_n$. The signal to noise ratio is then derived as in (2.5).

$$\mathrm{SNR} = \frac{s_i(k,\theta_i,\phi_i)}{B_f\, N_n} \tag{2.5}$$

The radar system can be optimized to improve the SNR. Because we are considering a radar working at millimeter-wave, the delivered output power remains relatively low (from -10 to 10 dBm in general). The RCS and the distance between the target and the radar are fixed parameters by essence. Then, in order to improve the SNR, it is only possible to increase the gain (more efficient antenna or more directive radiation pattern), in the desired look angles at the transmitting and receiving levels. By doing so, this allows to improve the SNR of the systems but the field of view of the system will be reduced.

2.3 Range focusing using frequency diversity

From now, we have only received the backscattered signals but it is not possible to estimate the reflectivities and the distance d_i of the i^{th} backscattered signal. Thanks to the frequency diversity, it is possible to estimate the N_s targets range location with the help of a sufficient number of frequency components. Considering τ as the time variable, we therefore use a waveform $u(\tau)$ with the bandwidth B_f adapted to the analysis of the observed scene.

In order to enhance, distinguish and extract the desired signal knowing that the receiver has the knowledge of the transmitted signal, the optimal filter, also called the matched filter, is performed on the received raw data [17]. When the noise affecting the measurement does not present a particular structure, in other words, when it is white, the filtering solution leading to an optimal SNR is given by $g_r(k) = S_e^*(k)$ with $(\cdot)^*$ the complex conjugate operator. The function $g_r(k)$ is considered as the transfer function of the radar system. In the Appendix A.1 is shown the theoretical development to reach the optimal solution.

The impulse response in the time domain of the processing chain is then given by:

$$h(\tau) = \int_{-\infty}^{+\infty} s_e(t) s_e^*(t-\tau) dt \tag{2.6}$$

In Appendix A.2 is shown the theoretical development to reach the impulse response when a pulsed linear frequency modulated waveform (chirp) is used [22]. Using the Chirp waveform, it is required to sample the down-converted received signal at the frequency bandwidth used (B_f) with respect to the Shannon criterion. The expression of the radar impulse response for the pulsed linear frequency modulated waveforms is:

$$\begin{aligned} h_c(\tau) &= \tau_p \mathrm{tri}(\frac{\tau}{2\tau_p}) \,\mathrm{sinc}(B_f \,\mathrm{tri}(\frac{\tau}{2\tau_p})\tau) \\ &\approx \tau_p \,\mathrm{sinc}(B_f \tau) \end{aligned} \tag{2.7}$$

The approximation is valid if we consider $B_f \tau_p >> 1$ with τ_p the pulse duration. After range focusing, the Signal-to-Noise Ratio is given by $\mathrm{SNR}_f = T_p \, f_s \, \mathrm{SNR}$ with $f_s \geq B_f$ the sampling frequency.

In Appendix A.3 is shown the theoretical development to reach the impulse response when an increasing linear frequency modulated continuous waveform is used. As compared to the Chirp waveform, using the FMCW waveform, the received signal is directly demodulated by the transmitted signal. The sampling is not linked to the frequency bandwidth used but by the slope of the linear frequency transmitted with $f_s \geq N_f / T_p$. After range focusing, the Signal-to-Noise Ratio is given by $SNR_f = T_p \, f_s \, SNR$.

In Appendix A.4 is shown the theoretical development to reach the impulse response when a stepped frequency continuous waveform is used. After range focusing, the Signal-to-Noise Ratio is given by $SNR_f = N_f \, SNR$ with N_f the number of frequency bins.

$$\begin{aligned} h_{\mathrm{FMCW}}(\tau) \approx h_{\mathrm{SFCW}}(\tau) &= \frac{\sin(\pi B_f \tau)}{\sin(\pi \delta_f \tau)} \\ &\approx N_f \mathrm{sinc}(B_f \tau) \end{aligned} \tag{2.8}$$

The approximation is valid if we consider $B_f = \delta_f (N_f - 1) \approx \delta_f N_f$ with δ_f the step frequency. The range resolution that corresponds to the width of the main lobe at

-3 dB is:

$$\delta_r = \frac{c}{2B_f} \tag{2.9}$$

The received signal in the frequency domain after applying the range focusing technique by adapted filtering is expressed as:

$$S(k) = S_r(k)S_e^*(k) = H(k)\sum_{i=1}^{N_s} s_i(k,\theta_i,\phi_i)\, e^{-j(k+k_c)\,d_i} + n_f(k) \tag{2.10}$$

where $H(k)$ is the transfer function of the system in the wavenumber domain. The expression $n_f(k) = n(k)\,S_e^*(k)$ corresponds to the filtered white noise by means of the matched filtering technique.

The received signal in the spatial domain after an inverse Fourier Transform of (2.10) is expressed as:

$$s(d) = \sum_{i=1}^{N_s} s_i(d,\theta_i,\phi_i)\, h(d-d_i)\, e^{-jk_c\,d_i} + n(d) \tag{2.11}$$

where $h(d)$ is the impulse response in the spatial domain, with d, the radial distance or the range.

Considering a SFCW radar with a carrier frequency $f_c = 60$ GHz and a frequency bandwidth $B_f = 5$ GHz which provides a transmitted power of 0 dBm, this corresponds to a range resolution $\delta_r = 3$ cm. Both the transmitting and the receiving antennas are located at the origin of the Cartesian coordinate (i.e. $x_t = x_a = 0, y_t = y_a = 0, z_t = z_a = 0$). Both antennas have an isotropic radiation pattern $G_t = G_a = 0$ dBi. In this example, there is no noise that corrupts the received signals. In order to simulate targets, it is considered 5 point-like targets with uniform and time-invariant RCSs. For the simulation, it is considered that the weighting s_i is unitary and isotropic for $i = \{1, \cdots, 5\}$. The location of each target is: $P_1(x_1 = -0.5\text{ m}, y_1 = +4.75\text{ m}, z_1 = 0\text{ m})$, $P_2(x_2 = +0.5\text{ m}, y_2 = +4.75\text{ m}, z_2 = 0\text{ m})$, $P_3(x_3 = 0\text{ m}, y_3 = +5\text{ m}, z_3 = 0\text{ m})$, $P_4(x_4 = -0.5\text{ m}, y_4 = +5.25\text{ m}, z_4 = 0\text{ m})$, $P_5(x_5 = +0.5\text{ m}, y_5 = +5.25\text{ m}, z_5 = 0\text{ m})$ as shown in Fig. 2.2a for $z = 0$ m.

Because the distances of P_1 and P_2 to the radar are similar, both have the same range which is also the case for P_4 and P_5. In Fig. 2.2b, it is shown the simulated result of (2.11) after range focusing. Only three peaks are visible with the first peak corresponding to the reflected signals from P_1 and P_2, the second peak for P_3 and the last peak for P_4 and P_5. The highest Side Lobe Level (SLL) is -13.6 dB from the peak lobes due to the impulse response that corresponds to a sinc-function. But, farther from the main lobe, the lower become the SLL. In order to reduce the highest Side-Lobe Level, it is possible to apply an amplitude tapering function on (2.10) such as Hamming or Hanning [23]. It drastically reduces the highest side lobes level. Nevertheless, due to the amplitude tapering, the effective frequency bandwidth is also reduced inducing an increase of the range resolution. The amplitude tapering is a useful tool when the area of interest is in a near-range region. In fact, the strong coupling between the transmitting and reflecting antennas generates a strong peak at a distance corresponding to the distance between the antennas (or the strong

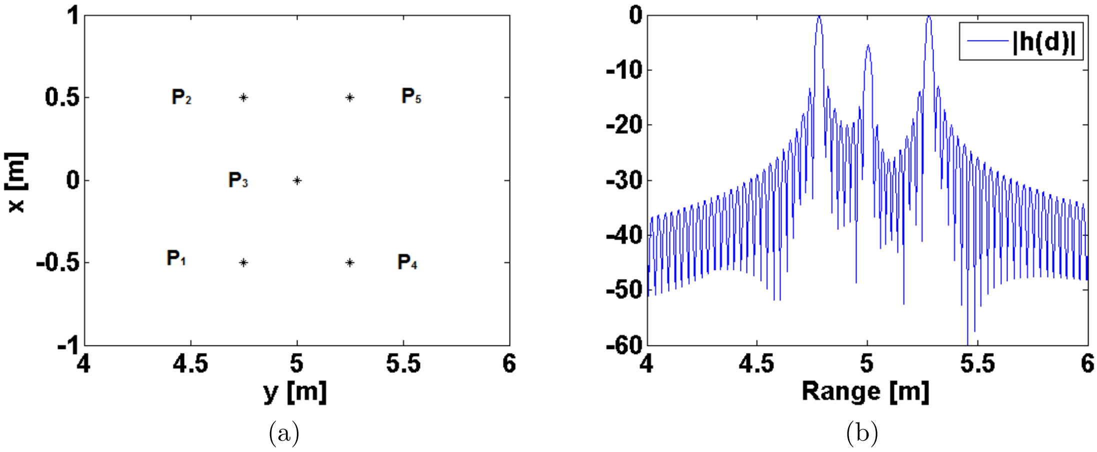

(a) (b)

Figure 2.2: (a) Point-like targets location, (b) received signal in the spatial domain after range focusing.

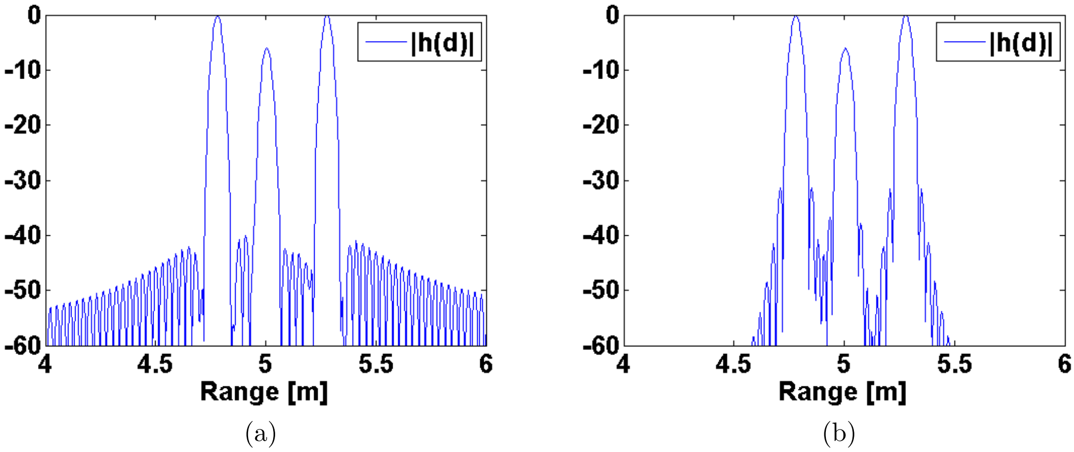

(a) (b)

Figure 2.3: Received signal in the spatial domain after range focusing and (a) Hamming amplitude tapering and (b) Hanning amplitude tapering.

reflection coefficient of the antenna if the measurement is performed using the same antenna in reflection mode (S_{11} measurements)). The side-lobes level of the strong peak may hide the weaker backscattered signals (signals of interest). Applying an amplitude tapering reduces the side lobes level of the strong peak due to the antenna coupling allowing to extract the weaker desired signals.

The amplitude coefficients of the hamming window is given by the following equation:

$$w(n) = 0.54 - 0.46\cos(2\pi\frac{n}{N}), 0 \leq n \leq N \tag{2.12}$$

with the window length $N_f = N + 1$. The amplitude coefficients of the hanning window is given by the following equation:

$$w(n) = 0.5(1 - \cos(2\pi\frac{n}{N}), 0 \leq n \leq N \tag{2.13}$$

with the window length $N_f = N + 1$. The windowed received signal after range focusing is given by:

$$s_w(d) = \frac{1}{2\pi} \int_{-\infty}^{+\infty} w(k)S(k)e^{jkd}\mathrm{d}k \tag{2.14}$$

In Fig. 2.3, it is shown the same simulated result as in Fig. 2.2b but it is applied a Hamming and a Hanning amplitude taper function on (2.10). The highest side lobe level is -40.6 dB from the main peak lobe but farther from the main lobes, the SLL is slowly reduced. Furthermore, the range resolution has been increased with $\delta_r = 4.5$ cm for the Hamming function. For the Hanning function, the highest side lobe level is -30.6 dB from the main peak lobe but farther from the main lobes, the SLL is rapidly reduced with a slope similar to the uniform amplitude taper. Furthermore, the range resolution has been increased with $\delta_r = 5.05$ cm.

2.4 State-of-art of Radar imaging systems

In the previous section, it has been shown the great capability of millimeter-wave for radar applications. It has been demonstrated through simulations that using only one pair of transmitting and receiving antennas, it is possible to estimate the location of targets only along the range direction (distance between targets and radar). Then, for targets having the same range from the radar perspective, it is not possible to resolve or separate the targets thanks to spectral diversity. In this section, two methods are shown to resolve and locate targets in range and cross-range directions in order to perform 2-Dimensional or 3-Dimensional Radar imaging, the Direct and Indirect imaging techniques.

- **Direct Imaging technique**: The technique uses **spatial filtering** or **beamforming** thanks to the radiation pattern of the antenna that is scanned over an area of interest. The half-power beam width gives the resolution of the system to discriminate targets along the cross-range direction. Then it is required a high-directive antenna to achieve great resolution. The scanning capability may be classified in three groups: Mechanically beam-scanning, Electronically beam-scanning and Frequency beam-scanning.

- **Indirect Imaging technique**: The technique uses **spatial diversity** or **digital beamforming** thanks to a group of independent antennas that acquires the signals and by means of signal processing. The beam is digitally scanned by coherently combining in amplitude and phase the signals received by the independent antennas.

A state of art of imaging systems using both direct and indirect imaging techniques mainly used in the literature are presented to show advantages and drawbacks of the techniques. It is a general "state of the art" in which, the details of the antennas, the algorithms are not provided because these aspects are assessed and addressed in the next chapters.

2.4.1 Direct imaging

Plenty of configurations exist in the literature for direct imaging. Nonetheless, only the main configurations are detailed and compared in this section.

The antenna design is of major interest for the direct imaging in order to have an optimal Signal-to-Noise Ratio in the desired frequency bandwidth. The different types of antenna subject to the kind of beam-scanning chosen may be evaluated following the different parameters stated in the Table 2.2. At millimeter wave, five major criteria have to be considered:

- **The overall efficiency**: The gain of the antenna as compared to the gain of a uniform amplitude and phase aperture of same dimensions as the antenna.
- **Easiness of realization**: At millimeter-wave, the complexity of manufacturing antennas may generate small irregularity during the manufacturing process that may impact the gain of the antenna.
- **Frequency bandwidth**: The intrinsic characteristics of the antenna should provide a stable overall efficiency over a wide frequency-bandwidth.
- **Beam-scanning capability**: The antenna should provide a stable overall efficiency over a wide range of scanning angles.
- **Real-time acquisition constraint**: the beam-scanning of the antenna must be performed as fast as possible in order to assume a stationary area of interest during the scanning process.

In the direct imaging study, only one couple of receiver and transmitter chains is considered attached either on the same antenna system or on two separated (but similar) antenna systems.
High gain antennas [24] are suitable solutions to achieve high spatial resolution. To generalize, there are two major ways of performing high-gain antennas. The first way is to use a large focusing aperture (reflectors, lenses, transmit/reflect-arrays) that focuses the beam of a lower gain antenna used as a primary source. The focusing aperture allows to compensate the spherical wavefront onto a plane-wave front in order to focus the electromagnetic field in a narrower angular region. The second way is the use of a Direct Radiation Arrays. The high-gain is obtained by combining a group of small radiating sources in such a way that their received or transmitted signals have an amplitude and phase relationship with each other that allow to generate a high gain beam. The radiating sources or radiating elements assume many forms and shapes such as dipoles, slots, waveguides, helix etc.

The simplest form of direct imaging employs a mechanically scanned antenna where the entire antenna can be turned and tilted to radiate an identical radiation pattern toward every point as shown in the Fig. 2.4a. A focusing aperture is used for compensation of a spherical wave-front at the input into a plane wave-front at the output to have a high directive antenna.

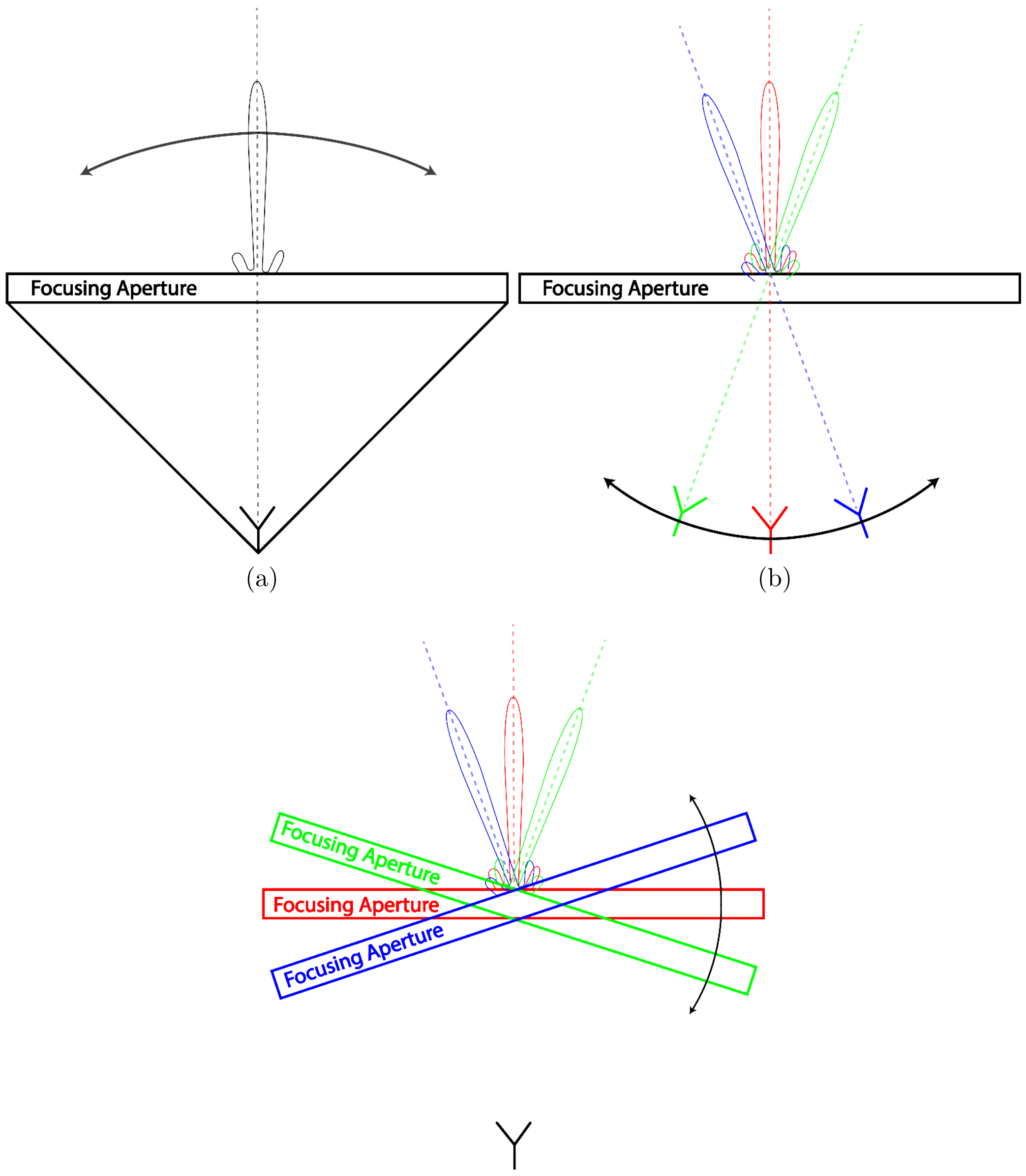

(a) (b)

(c)

Figure 2.4: Mechanically beam-scanning antenna solutions with in (a) the overall system is steered, in (b) only the feeder is steered and finally in (c) only the focusing aperture is steered.

It is a great candidate for direct imaging because its radiating properties (half-power beam width, gain, side lobe level) are not modified during the scanning process keeping stable results over the entire area of interest. Considering the millimeter-wave frequency band, small irregularity during the realization of the focusing aperture may impact the overall efficiency of the system. Using reflectors or lenses, the frequency bandwidth is mainly limited by the primary source. If a horn antenna is used, the overall system allow a wide frequency bandwidth. Using reflect-arrays or transmit-arrays, the element cells which composed the panels are usually band-limited which may impact the overall frequency bandwidth. In the case of a large focusing aperture that focuses the beam of a primary source, it is also possible to only turn and tilt the focusing aperture in order to scan the beam of the entire antenna as in Fig. 2.4c. In the same manner, it is possible to turn and tilt the primary source considering the center of the focusing aperture as the center of rotation (Fig. 2.4b). Nonetheless, the radiating properties are modified during the scanning process which implies stable results within a smaller region (limited scan angle) and a stable gain over a smaller frequency bandwidth. Furthermore, the main drawback of mechanically beam scanned antenna is the attainable scanning rates (time delay to scan an entire area of interest).

In [6, 25], the authors developed active sub-millimeter wave systems especially at 670 GHz with a wide bandwidth (B= 30GHz). This fast scanning long range 0.67 THz radar imaging system includes a 1 m diameter (2233 λ) ellipsoidal main reflector and a fast-rotating mirror for beam steering. This rotating mirror avoids to rotate the main reflector which is very heavy. At 25 m range, they obtain a 13 mm spatial resolution corresponding to a 0.03° antenna beam-width. The field of view (size of image) is 0.5 m x 0.5 m. The global system with quasi-optical antenna system and block diagram are represented in the Fig. 2.5a.

The Fig. 2.5b shows an image of the target scenario and back-surface image overlay for the through-jacket detection of a mock pipe bomb. The THz radar image is acquired in 5 seconds at a standoff range of 25 m. Different results are compared for four levels of signal attenuation to mimic the lower SNR that would result from faster scans. This kind of system gives very good resolution and quality of image for important standoff range application. But to obtain such results, the system includes a very large antenna (1 m) at Terahertz frequency then the system is neither compact nor low cost.

A beam scanning antenna is discussed in [26]. In this study, the authors have developed a reflect-array antenna. The emitted radiation by the target (passive imaging technique) is picked up by a horn after reflexion on the reflect-array which is composed of printed patches. To scan all the scene, the plane reflect array is rotated compared to the horn (Fig. 2.6a). The working frequency bandwidth is 32-37 GHz and the size of the reflect array is 220 mm x 220 mm allowing to get a 3° beam width for the radiation pattern. The Fig. 2.6b shows an example of reconstructed image of a human with a concealed weapon. The advantage of this system is to use only one simple receiver and a flat printed antenna (light weight) but the drawback is the time of image reconstruction due to the mechanical process.

Avoidance of any mechanical motion has become a key requirement in modern direct radar imaging systems. This has led to an increasing interest in electrically beam scanning antennas in which the antenna stays fixed in space and the main beam is scanned electronically.

A first solution is to use a single focusing aperture (parabolic, Fresnel lens, transmit/reflect array, etc.) with multiple primary sources. Each primary source location is determined to perform a beam at a particular beam direction as shown in Fig. 2.7a. The primary sources are fed sequentially using switch electronic components. Depending on the requirement, the multi-beams must overlap in order to guarantee a minimum gain at the End Of Coverage (EOC). This corresponds to the minimum

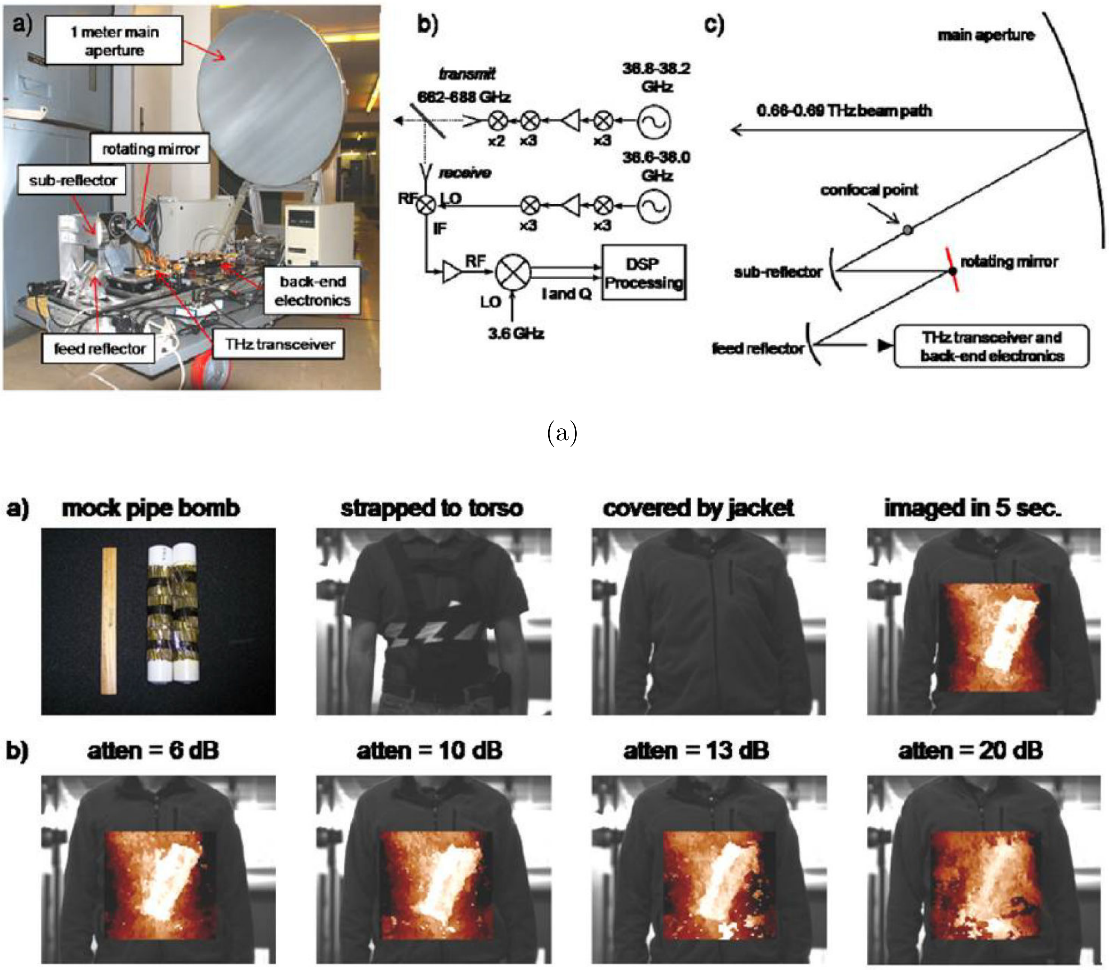

(a)

(b)

Figure 2.5: (a) Active system developed by JPL [6] with measurement results [25] in (b) for different target scenario for through-jacket of a mock pipe bomb.

gain achievable between the two closest beams. In such a case, it is not possible to smoothly scan the beam in all direction and only limited scanning angles are considered. Furthermore, because the focusing aperture is optimized for a primary source at broadside angle, the gain of the overall system is reduced when wide scanning angle are desired. Instead of having a focusing aperture which is located at a focal distance F from the phase center of each primary source, it is possible to use 2D or 3D integrated lenses where the primary sources are directly located at the surface of the lens which permits to drastically decrease the volume size of the overall antenna. The lens is then fed by the multiple radiating sources (primary sources) that are switched sequentially. Only one of the radiating source is supplied to generate a beam at a particular beam direction. Using integrated lenses, the gain during the scanning process remains sufficiently stable.

It is also possible to use a phased array as in Fig. 2.7b to focus the beam in a given direction by controlling the phase shifters directly connected to the radiating

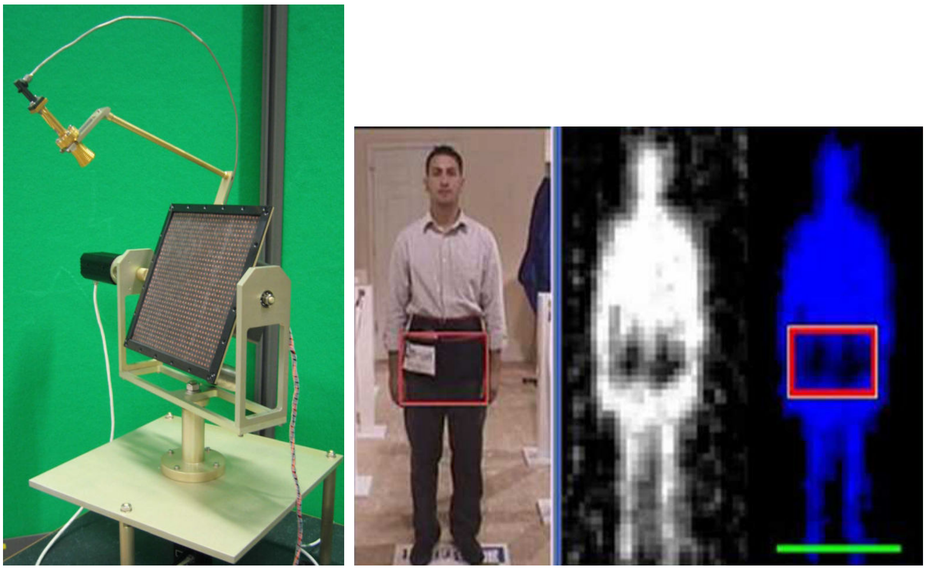
(a)
(b)

Figure 2.6: (a) Mechanically rotated reflect array with horn [26] with (b) an example of the image reconstruction.

elements. The circuitry, which controls the excitation of elements in an array, is called the beam forming network (BFN). The phase shifters are directly connected to the radiating sources and control their excitations. By providing a specific phase delay for each radiating source, the array will produce a beam in a given direction. The advantage of this solution is the speed of detection and imaging reconstruction (real time) thanks to the electronic system (without mechanical displacement) but, the drawback is mainly due to the commercial availability and loss of phase shifters at millimeter waves. Because, the gain during the scanning process varies according to the radiation pattern of the radiation source, an isotropic source is ideal to generate wide scanning properties.

A phased array for advanced automotive radars is proposed in [27] with a frequency bandwidth of 4 GHz around a carrier frequency of 79 GHz. The structure is shown in Fig. 2.8a. It is composed of 16 elements with beamforming capability as shown in Fig. 2.8b. The beam of the phased array can be scanned in 1°-steps. A measurement result shown in Fig. 2.8c is performed showing the great spatial resolution of the system with an angular resolution between 5.5° to 7°.

To avoid the use of phase shifters, it is possible to implement a beamforming network based on a Butler matrix [28] or Rotman lenses [29, 30]. These microwave designs are mainly manufactured with printed technology. The number of beams are defined by the number of inputs of these systems as shown in Fig. 2.7c (one input per one beam). So to have a narrow beam, it needs to design large butler matrix or Rotman lenses suffering from losses.

To avoid the use of active components such as switches or phase shifters to scan the beam of the antenna, it is possible to use progressive wave antenna as shown in Fig. 2.9. It is composed of a serial distribution of radiating elements. Thanks to the serial distribution, the electric phase between them changes with the frequency. Then, the beam direction progresses with frequency. The technique allows to scan

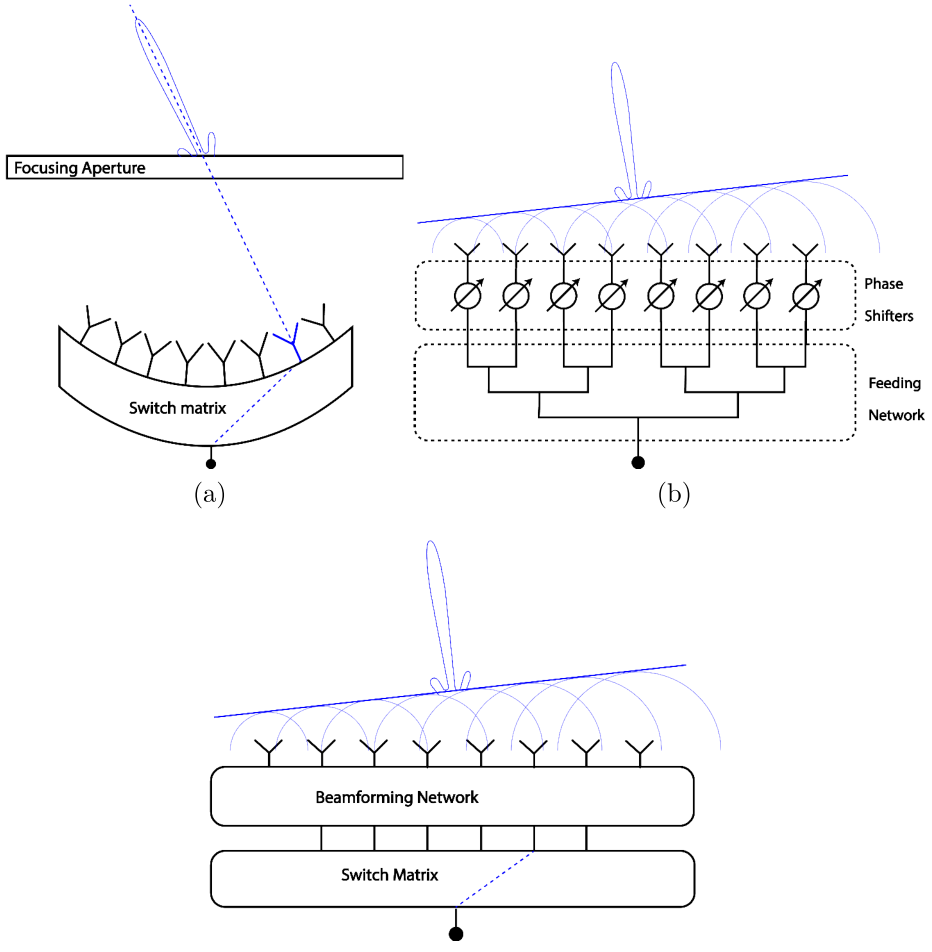

(a) (b) (c)

Figure 2.7: Electronically beam-scanning antenna solutions.

the beam without any electronic device. If it used fully metallic slotted waveguide antenna, the efficiency of the system is high.

A research group of Spain has worked on a frequency beam scanning antenna system for imaging application in Ku (18 GHz) band [31]. They developed a Ku frequency beam scanning antenna based on printed technologies and length lines to excite patches and create a progressive wave antenna. The design of this antenna is given in Fig. 2.10a. The radiation patterns versus frequency between 15 and 18 GHz are shown in Fig. 2.10b demonstrating the possibility to scan the beam with frequency. The objective of their system is to divide the total bandwidth in sub-bandwidths and for each one the beam is considered stable and illuminates a particular zone of the target as represented in Fig. 2.10c.

Because one particular target will be illuminated over a limited sub-bandwidth, the frequency scanning-based imaging systems comprise a trade-off between range and cross-range resolution. Moreover, they deal only with 1D frequency beam scanning antenna.

In Table 2.3, a summarized evaluation of the different direct techniques is performed showing the main advantages and drawbacks of each technique. It is decided

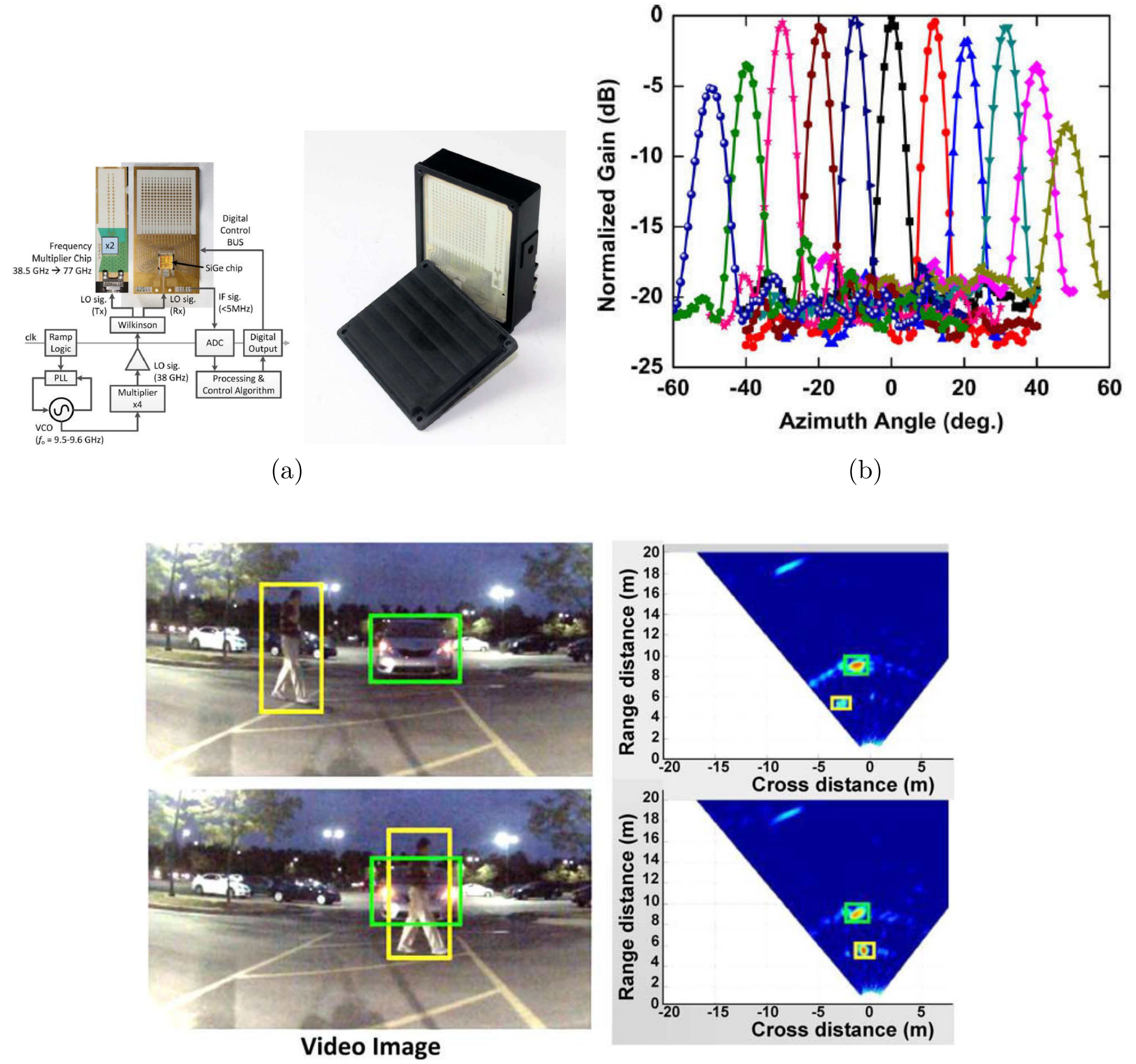

(a)

(b)

(c)

Figure 2.8: (a) Structure of the phased array [27] with (b) the beam scanning capability. A measurement result is shown in (c).

to investigate, in the Chapter 3, a mechanically beam-scanning antenna. More precisely, it is used Fresnel lens as a focusing aperture associated with a horn antenna as the primary source. A deep study for the obtention of a high efficiency Fresnel lens and its associated primary source is explained.

Table 2.3: Evaluation of the different direct techniques

Technologies	**Efficiency**	**Realization**	**Frequency bandwidth**	**Beam-scanning capability**	**Acquisition time**
Mechanically beam-scanning antenna (overal system rotation: Fig. 2.4a)	✓✓✓	✓✓	✓✓✓	✓✓✓	✓
Mechanically beam-scanning antenna (focusing aperture rotation Fig.2.4c)	✓✓✓	✓✓	✓✓	✓✓	✓
Switch based array antenna (Fig. 2.7a)	✓✓	✓✓	✓✓	✓	✓✓✓
Switch based primary source array (Fig. 2.7a)	✓✓	✓✓	✓✓✓	✓✓	✓✓✓
Phased array antenna (Fig. 2.7b)	✓✓	✓✓	✓✓	✓	✓✓✓
Beamforming network based array antenna (Fig. 2.7c)	✓✓	✓✓✓	✓	✓	✓✓✓
Frequency beam-scanning antenna (Fig. 2.9)	✓✓✓	✓✓✓	✓✓	✓	✓✓✓

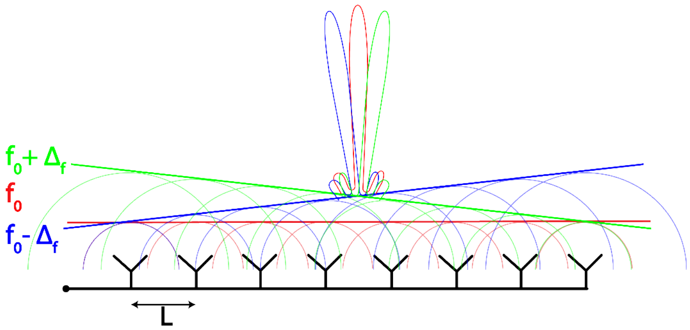

Figure 2.9: Frequency beam-scanning antenna solution.

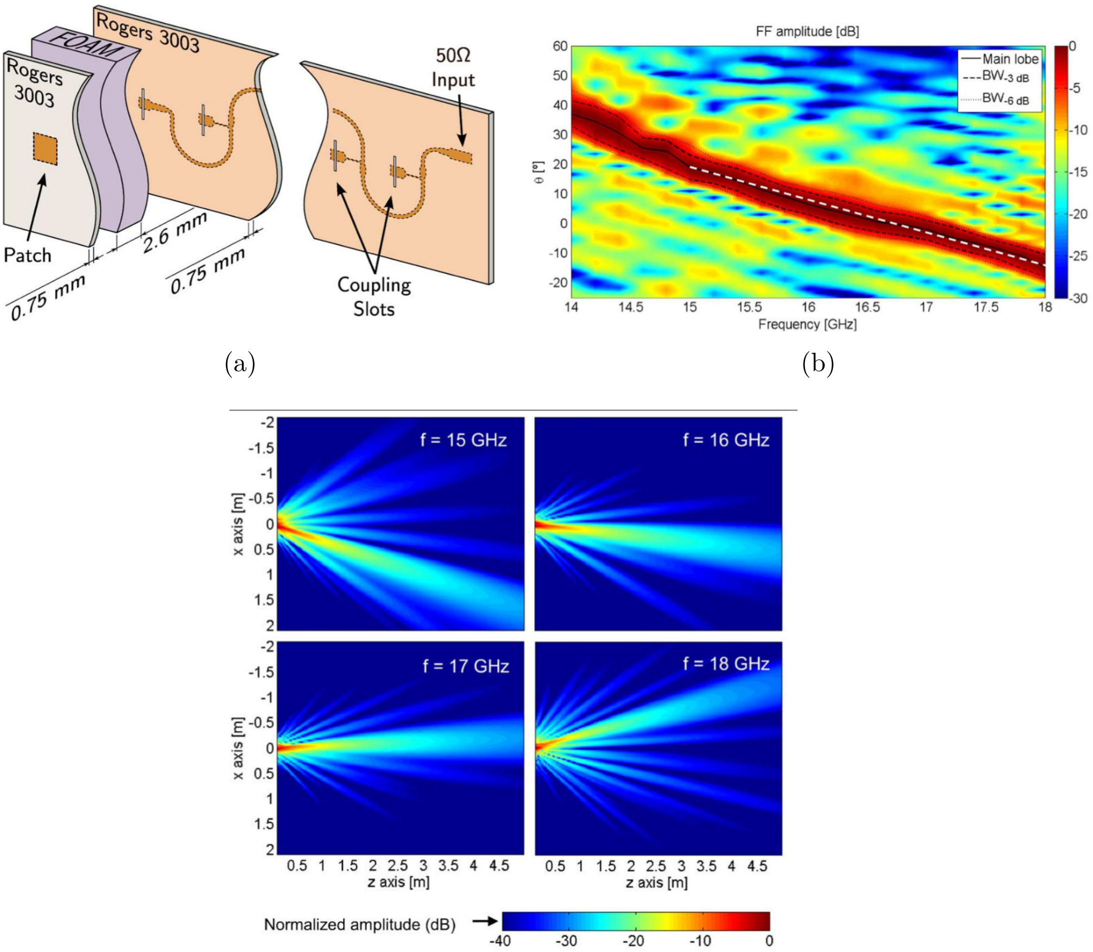

(a)

(b)

(c)

Figure 2.10: (a) The printed progressive wave antenna [31] with (b) and (c) the beam scanning capability.

2.4.2 Indirect imaging

Indirect imaging is a technique that allows to estimate the EM field backscattered within an area of interest by means of the coherent combination of multiple measurements at different locations. Thanks to this spatial diversity, it allows to synthesize a large aperture that provides a finer cross-range resolution than it is possible with conventional beam-scanning radars. However, it is required that the area of interest is motionless during the acquisitions. The spatial diversity combined with the frequency diversity allows to perform 2-Dimensional or 3-Dimensional complex image. The indirect technique may be divided into two different configurations. The first one is the **imaging Synthetic Aperture Radar** (SAR) technique. The pair of transmitting and receiving antennas are mounted on a moving platform and acquisitions are taken through time allowing to synthesize a large aperture (usually a linear [17] or a circular path [32]). The synthetic aperture length is directly linked to the platform path and the half-power beam width of the transmitting and receiving antennas. The moving platform may be a scanner, a car, a drone or a satellite for instance.

The synthesized linear aperture of a SAR can be based on different modes [17, 33, 34]:

- **Stripmap mode**: The antenna pointing direction is maintained unchanged along the (synthetic) array allowing to estimate the reflectivity within a large area of interest.
- **Spotlight mode**: The antenna pointing direction is changed (in the azimuth direction) along the (synthetic) array to point at a specific location. The area of interest is reduced but the synthetic aperture is thus enlarged increasing the cross-range resolution.
- **Scan-mode**: The antenna pointing direction is scanned (in the elevation direction) in order to increase the ground-range area of interest. It achieves similar cross-range resolution as the Stripmap mode but because of the scan process, fewer acquisitions are taken for one particular area of interest.

The modes aim to improve one of the characteristics of the resulting image, mainly its cross-range resolution or the scope of the imaged zone (a wider scanning angle). Nevertheless, each improvement of certain criteria lead to the declining quality of other parameters [35]. The use of a particular mode thus requires a set of compromises associated with certain objectives and applications. Because the imaging array radar is of interest at millimeter-wave ,the strip-map mode is the most appropriate mode to guarantee fine cross-range resolution over a wide area of interest. Further, it is the easiest mode to be used while using a scanner system.

Thanks to the spectral diversity in range and spatial diversity in cross-range, it permits to acquire the received signals to generate a raw data matrix where one element of the matrix corresponds to the received signal for one particular frequency within the frequency bandwidth at one particular location within the (synthetic) aperture.

In [36], 2D and 3D images are realized from a SAR configuration from 15 to 26.5 GHz using both the stripmap and the spotlight modes. The transmitting and receiving antennas are moved thanks to a Robot system as shown in Fig. 2.11a. The antennas are moved over the azimuth direction for a total distance of 0.6 m using a step size of 4 mm. The antennas are 10 dB standard horn antennas with half power beam width of about 58° along the E and H-plane. The configuration permits a ground range resolution of 13.6 mm and a cross-range resolution of 7.1 mm at 50 cm from the synthetic aperture. Both, 2D and 3D image examples are shown in the Fig. 2.11b and the Fig. 2.11c respectively.

In [37], a radar is mounted on a van for imaging urban scene. The radar has a bandwidth of 30 GHz at 300 GHz. The synthetic aperture length is 0.7 m corresponding to a range and azimuth resolutions of 5 mm at 5 m from the synthetic aperture. The radar system is shown in Fig. 2.12a. One result is shown in the Fig. 2.12b with its associated optic image in the Fig. 2.12c demonstrating the spatial resolution capability of working at millimeter wave.

Because SAR can only be implemented by moving one or more antennas over immobile targets, replacing synthetic aperture with real-aperture array is an essential step toward demanding imaging applications where both high-resolution and real-time operations are required. Hence, the latter is the **imaging Array Radar** or the **real-aperture Radar**. It is composed of one transmitting antenna attached to one transmitter chain and multiple receiving antennas located at different locations (Single Input Multiple Output (SIMO) configuration). Behind each receiving antenna is attached one receiver chain or only one receiving chain is used and the receiving antennas are sequentially switched through time. In the same manner, it is possible to use a Multiple Input Multiple Output (MIMO) configuration in which multiple transmitter and receiver chains are required.

The comparison between SAR, SIMO and MIMO array is summarized in Table 2.4. It is a non-exhaustive comparison that may be modified depending on the application. However, the SAR configuration does not have access to channel measurements for all transmit-receive combinations or pairs. In this sense, the MIMO configuration can take full advantages of the degrees of freedom and diversity from all transmit-receive combinations which allows the reduction of the number of chains as compared to the SIMO case. However, this is a more complex configuration because multiple signals are transmitted at the same time, hence it requires that the transmitted signals are orthogonal to be separated, which complicates the implementation of this configuration.

In [38] and Fig. 2.13, it is shown a MIMO configuration working from 72 to 80 GHz that achieves a sparse MIMO array of around 50 cm x 50 cm with a 4×4 clusters. This results in a total of 736 Tx antennas and 736 Rx antennas. Its counterpart design using a dense array results in 25 600 antennas. Therefore, the sparse array contains only 5.75% of that number of antennas. To avoid the complexity to transmit multiple signals that has to be orthogonal, the authors have chosen to switch sequentially each Tx antenna. Only a single transmitter illuminates the scene at any time instance, and the reflected wavefront is then sampled by all the receivers. Such configuration achieves a measurement time for a scan of 157 ms for 32 frequency step, making it a real-time capable system for imaging humans with a

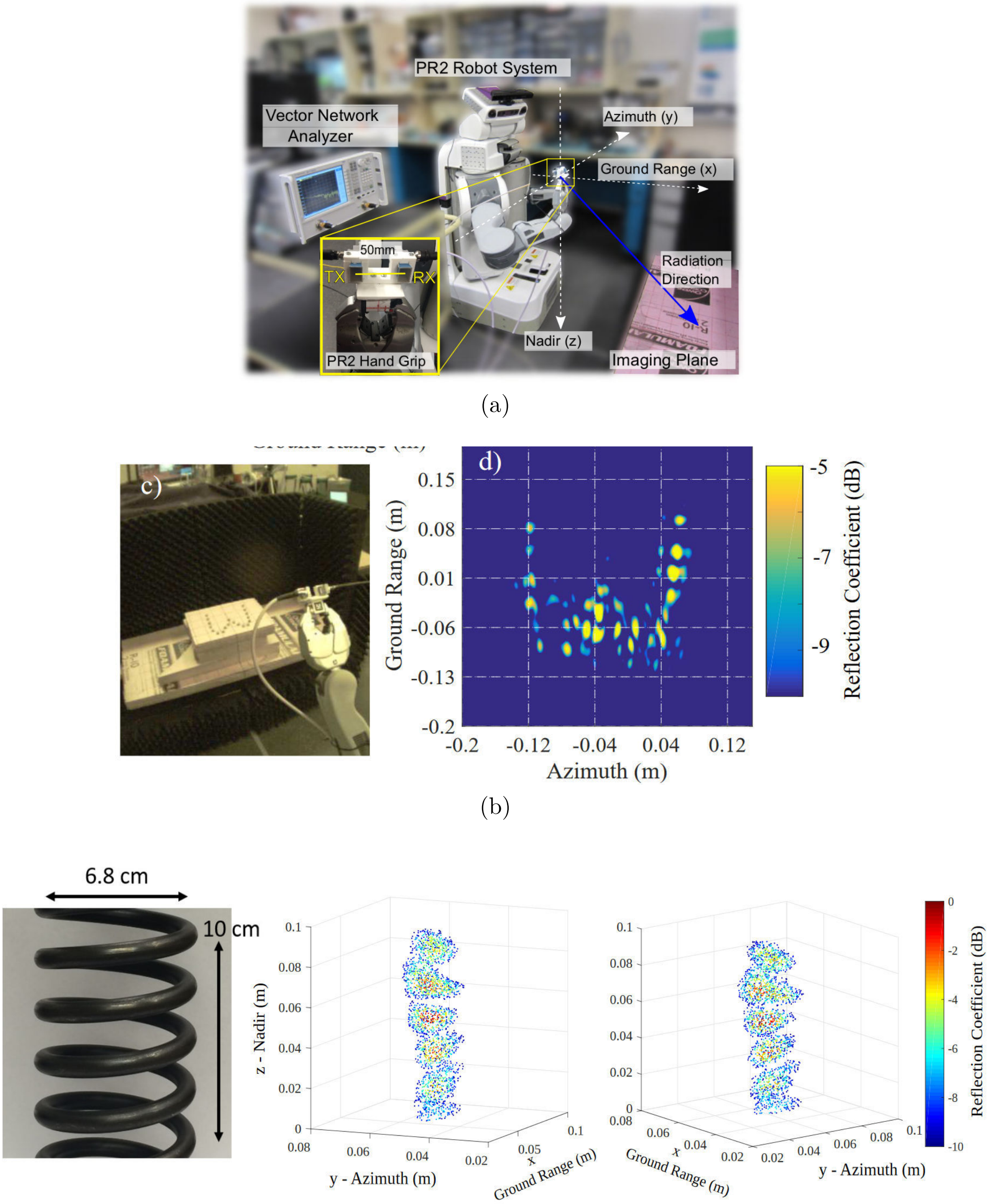

(a)

(b)

(c)

Figure 2.11: (a) Sar configuration with (b) a 2D measured image and (c) a 3D measured image. [36]

lateral resolution of approximately 2 mm as shown in Fig. 2.13c.

In order to create a complex image that corresponds to the reflectivity fields of the area of interest, it is required focusing algorithms to compensate the changing distance from one particular target and the radar. Several algorithms can be found in the time or frequency domains with exact compensations or based on approximations. The commonly used algorithms are [39–42]:

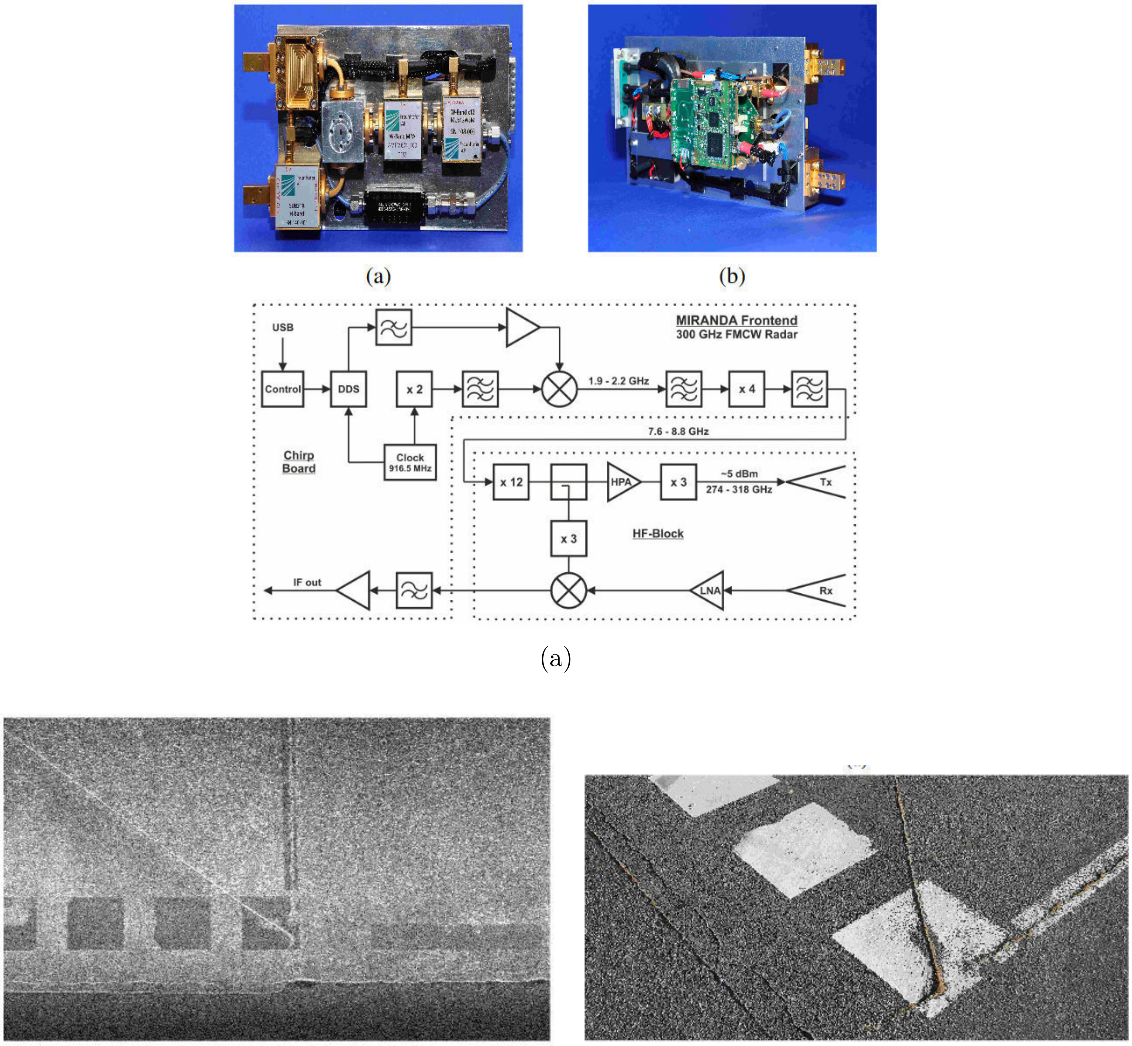

(a)

(b) (c)

Figure 2.12: SAR system mounted on a van at 300 GHz in (a) with in (b) the imaging result and in (c) the optical image. [37]

- **Back-projection**: It is an exact method in the time domain which takes into account the geometry of the problem and no approximations are used making this method robust. However this algorithm is slower than other methods which may be an issue for real-time application.

- **Range-doppler**: It is a fast algorithm that may be used in the case where the area of interest is located in the far-field region. If the changing distance, for one particular target, is greater than the range cell resolution (range migration), the final image will be defocused. However, it is possible to rectify the migration by means of the Range Cell migration compensation algorithm [43].

- **Range-migration (Omega-k)**: It is a quasi-exact method in the frequency domain based on the adapted filter and the Stolt interpolation [44] in the frequency domain. The Stolt interpolation allows to compensate the migration and to properly focus the received signals.

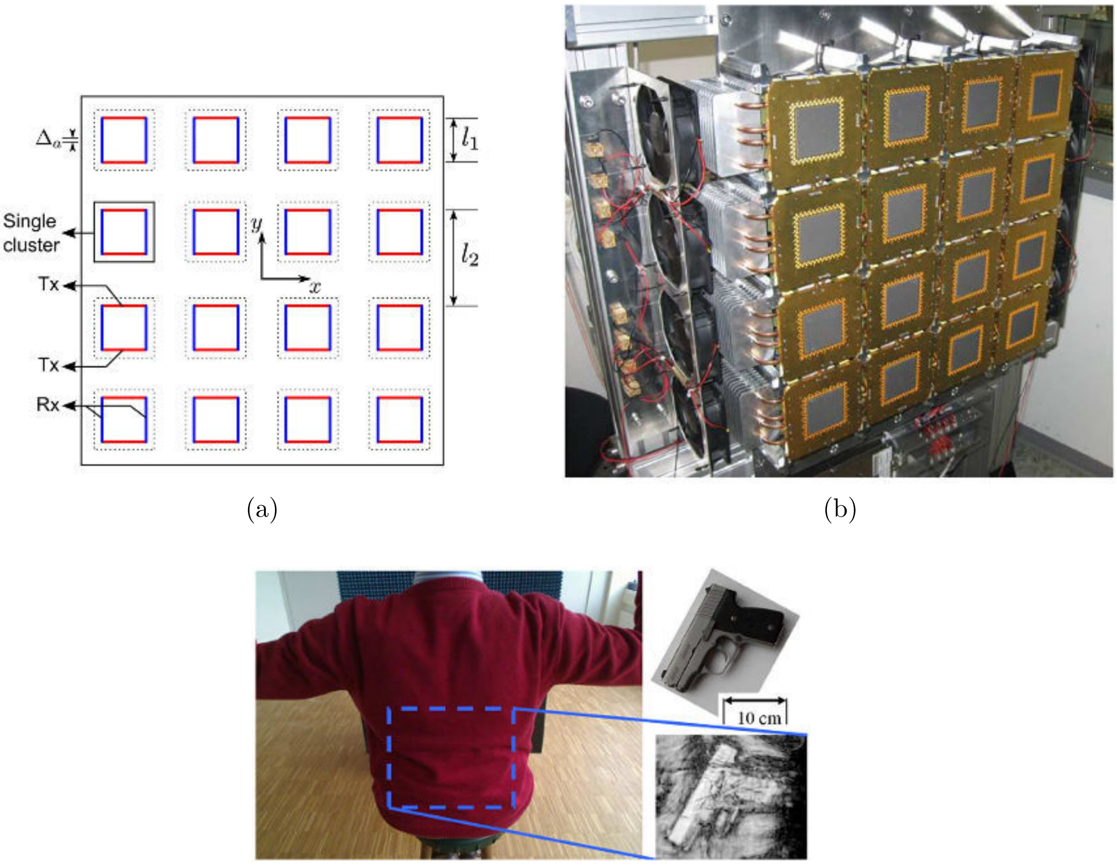

(a) (b)

(c)

Figure 2.13: In (a) and (b) are shown the MIMO aperture configuration with in (c) the scene with the imaging result. [38]

Because the back-projection algorithm represents an exact and generic solution of focusing, that is, it can be adapted to any configuration of acquisition without modifications, it is chosen and detailed in the Chapter 4 to generate complex images.

2.5 Summary

In this chapter, a first overview of radar imaging systems is explained. It is shown that to produce a radar image, diversities are required: a frequency diversity dedicated to discriminate targets in range and a spatial diversity dedicated to discriminate targets in azimuth and/or elevation. The frequency diversity is directly linked to the transmitted signals, which may be Chirp, SFCW or FMCW waveforms. The spatial diversity is performed either using direct imaging systems or indirect imaging systems. Direct imaging systems perform radar image thanks to the beam scanning process of one pair of Tx and Rx chains with the associated antennas while the indirect imaging systems, that include multiple Tx and Rx chains with the associated antennas, perform the radar image by post-processing thanks to the multiple received signals from the multiple chains. Working at millimeter-wave is of great interest because it allows to have a wide-frequency band available to achieve a great

Table 2.4: Evaluation of the indirect techniques

Technologies	**Advantages**	**Disadvantages**
SAR	Simpler design process, flexible to change the scanning scheme, no coupling effects between the acquisitions	Limited data acquisitions speed, suitable for stationary targets
SIMO radar	Fast data acquisitions, possible to image targets in motion, only one transmitted signal	High number Rx chains, high antennas coupling
MIMO radar	Fast data acquisitions, requires less Tx and Rx chains than the SAR and SIMO configurations, possible to image targets in motion	More challenge for array topology, more challenge for reducing the orthogonality between the multiple transmitted signals, high antennas coupling

range resolution. Both, the direct and the indirect imaging techniques are further investigated. Chapter 3 investigates a mechanically beam scanning system where a Fresnel lens antenna is used. It is explained how to manufacture such lens with high directivity over a wide frequency bandwidth while maintaining high efficiency. The antenna is used to produce a radar image in an outside environments. Chapter 4 investigates the indirect imaging techniques for multiple configurations that are SIMO or MIMO configurations. Simulations and measurements are performed. The large aperture required is synthesized thanks to a scanner system to produce a high-resolution radar image. In this chapter, solutions are provided to reduce the number of chains in an array radar for real-time applications by means of both the virtual array principle and a passive compressive device.

Bibliography

[1] NA Salmon, J Beale, J Parkinson, S Hayward, P Hall, R Macpherson, R Lewis, and A Harvey. Digital beam-forming for passive millimetre wave security imaging. In *Antennas and Propagation, 2007. EuCAP 2007. The Second European Conference on*, pages 1–11. IET, 2007.

[2] Yassine Aouial, Stephane Meric, Olivier Lafond, and Mohamed Himdi. A synthetic aperture interferometric radiometer test at x-band for potential improvements at w-band. In *Microwave Conference (EuMC), 2013 European*, pages 1851–1854. IEEE, 2013.

[3] Danny KP Tan, Hongbo Sun, Yilong Lu, Marc Lesturgie, and Hian Lim Chan. Passive radar using global system for mobile communication signal: theory, implementation and measurements. *IEE Proceedings-Radar, Sonar and Navigation*, 152(3):116–123, 2005.

[4] Michail Antoniou, Zhangfan Zeng, Liu Feifeng, and Mikhail Cherniakov. Experimental demonstration of passive bsar imaging using navigation satellites and a fixed receiver. *IEEE Geoscience and Remote Sensing Letters*, 9(3):477–481, 2012.

[5] Lukasz Maslikowski, Piotr Samczynski, Marcin Baczyk, Piotr Krysik, and Krzysztof Kulpa. Passive bistatic sar imaging—challenges and limitations. *IEEE Aerospace and Electronic Systems Magazine*, 29(7):23–29, 2014.

[6] Ken B Cooper, Robert J Dengler, Nuria Llombart, Ashit Talukder, Anand V Panangadan, Chris S Peay, Imran Mehdi, and Peter H Siegel. Fast high-resolution terahertz radar imaging at 25 meters. In *SPIE Defense, Security, and Sensing*, pages 76710Y–76710Y. International Society for Optics and Photonics, 2010.

[7] Christoper Adams, David Holbrook, and Robert Sengsten. A handheld active millimeter wave camera. In *Technologies for Homeland Security (HST), 2010 IEEE International Conference on*, pages 283–286. IEEE, 2010.

[8] Alan Agurto, Yong Li, Gui Yun Tian, Nick Bowring, and Stephen Lockwood. A review of concealed weapon detection and research in perspective. In *Networking, Sensing and Control, 2007 IEEE International Conference on*, pages 443–448. IEEE, 2007.

[9] Hua-Mei Chen, Seungsin Lee, Raghuveer M Rao, M-A Slamani, and Pramod K Varshney. Imaging for concealed weapon detection: a tutorial overview of development in imaging sensors and processing. *IEEE signal processing Magazine*, 22(2):52–61, 2005.

[10] Peter J Costianes. An overview of concealed weapons detection for homeland security. In *Applied Imagery and Pattern Recognition Workshop, 2005. Proceedings. 34th*, pages 5–pp. IEEE, 2005.

[11] Yuri Alvarez, Rene Camblor, Cebrian Garcia, Jaime Laviada, Carlos Vazquez, Samuel Ver-Hoeye, George Hotopan, Miguel Fernandez, Andreea Hadarig, Ana Arboleya, et al. Submillimeter-wave frequency scanning system for imaging applications. *IEEE Transactions on Antennas and Propagation*, 61(11):5689–5696, 2013.

[12] Siu-Yeung Cho and Nanda-Pwint Tin. Using infrared imaging technology for concealed weapons detection and visualization. In *TENCON 2010-2010 IEEE Region 10 Conference*, pages 228–233. IEEE, 2010.

[13] Dean Chapman, W Thomlinson, RE Johnston, D Washburn, E Pisano, N Gmür, Z Zhong, R Menk, F Arfelli, and D Sayers. Diffraction enhanced x-ray imaging. *Physics in medicine and biology*, 42(11):2015, 1997.

[14] M Moreno-Moreno, J Fierrez, and J Ortega-Garcia. Millimeter-and submillimeter-wave imaging technologies for biometric purposes. *Proceedings of XXIV Simposium Nacional de Union Cientifica Internacional de Radio, URSI 2009*, 2009.

[15] Ken B Cooper, Robert J Dengler, Nuria Llombart, Bertrand Thomas, Goutam Chattopadhyay, and Peter H Siegel. Thz imaging radar for standoff personnel screening. *IEEE Transactions on Terahertz Science and Technology*, 1(1):169–182, 2011.

[16] Michael C Kemp. Millimetre wave and terahertz technology for detection of concealed threats-a review. In *Infrared and Millimeter Waves, 2007 and the 2007 15th International Conference on Terahertz Electronics. IRMMW-THz. Joint 32nd International Conference on*, pages 647–648. IEEE, 2007.

[17] Mehrdad Soumekh. *Synthetic aperture radar signal processing*, volume 7. New York: Wiley, 1999.

[18] M Skolnik. Radar handbook, electronics electrical engineering, 2008.

[19] Akira Ishimaru. *Wave propagation and scattering in random media*, volume 2. Academic press New York, 1978.

[20] Leung Tsang, Jin Au Kong, Kung-Hau Ding, and Chi On Ao. *Scattering of electromagnetic waves, numerical simulations*, volume 25. John Wiley & Sons, 2004.

[21] John C Curlander and Robert N McDonough. *Synthetic aperture radar*. John Wiley & Sons New York, NY, USA, 1991.

[22] Laurent Ferro-Famil. Principes de l'imagerie radar à synthèse d'ouverture (rso). *Techniques de l'Ingenieur*, page Te6702, 2013.

[23] Fredric J Harris. On the use of windows for harmonic analysis with the discrete fourier transform. *Proceedings of the IEEE*, 66(1):51–83, 1978.

[24] Wolfgang Menzel, Dietmar Pilz, and Ralf Leberer. A 77-ghz fm/cw radar front-end with a low-profile low-loss printed antenna. *IEEE Transactions on Microwave Theory and Techniques*, 47(12):2237–2241, 1999.

[25] K. B. Cooper, R. J. Dengler, N. Llombart, B. Thomas, G. Chattopadhyay, and P. H. Siegel. Thz imaging radar for standoff personnel screening. *IEEE Transactions on Terahertz Science and Technology*, 1(1):169–182, Sept 2011.

[26] Juri Zuccarelli. *Passive millimeter wave imaging camera viky as technology transfer of planck-lfi*. PhD thesis, Università degli studi di Ferrara, 2009.

[27] B. H. Ku, P. Schmalenberg, O. Inac, O. D. Gurbuz, J. S. Lee, K. Shiozaki, and G. M. Rebeiz. A 77-81-ghz 16-element phased-array receiver with $pmhbox50^{circ}$ beam scanning for advanced automotive radars. *IEEE Transactions on Microwave Theory and Techniques*, 62(11):2823–2832, Nov 2014.

[28] B. Cetinoneri, Y. A. Atesal, and G. M. Rebeiz. An $8, times,$ 8 butler matrix in 0.13-$muhboxm$ cmos for 5-6-ghz multibeam applications. *IEEE Transactions on Microwave Theory and Techniques*, 59(2):295–301, Feb 2011.

[29] Leonard T Hall, Hedley J Hansen, and Derek Abbott. Rotman lens for mm-wavelengths. In *SPIE's International Symposium on Smart Materials, Nano-, and Micro-Smart Systems*, pages 215–221. International Society for Optics and Photonics, 2002.

[30] Jaeheung Kim and Frank Barnes. Scaling and focusing of the rotman lens. In *Antennas and Propagation Society International Symposium, 2001. IEEE*, volume 2, pages 773–776. IEEE, 2001.

[31] Carlos Vazquez, Cebrian Garcia, Yuri Alvarez, Samuel Ver-Hoeye, and Fernando Las-Heras. Near field characterization of an imaging system based on a frequency scanning antenna array. *IEEE Transactions on Antennas and Propagation*, 61(5):2874–2879, 2013.

[32] Stephan Palm, Hélène M Oriot, and Hubert M Cantalloube. Radargrammetric dem extraction over urban area using circular sar imagery. *IEEE Transactions on Geoscience and Remote Sensing*, 50(11):4720–4725, 2012.

[33] Ian G Cumming and Frank H Wong. Digital processing of synthetic aperture radar data. *Artech house*, 1(2):3, 2005.

[34] Jean-Baptiste Poisson, Hélène M Oriot, and Florence Tupin. Ground moving target trajectory reconstruction in single-channel circular sar. *IEEE Transactions on Geoscience and Remote Sensing*, 53(4):1976–1984, 2015.

[35] Didier Massonnet and Jean-Claude Souyris. *Imaging with synthetic aperture radar*. CRC Press, 2008.

[36] Claire M Watts, Patrick Lancaster, Andreas Pedross-Engel, Joshua R Smith, and Matthew S Reynolds. 2d and 3d millimeter-wave synthetic aperture radar imaging on a pr2 platform. In *Intelligent Robots and Systems (IROS), 2016 IEEE/RSJ International Conference on*, pages 4304–4310. IEEE, 2016.

[37] S Palm, R Sommer, A Hommes, N Pohl, and U Stilla. Mobile mapping by fmcw synthetic aperture radar operating at 300 ghz. *International Archives of the Photogrammetry, Remote Sensing & Spatial Information Sciences*, 41, 2016.

[38] S. S. Ahmed, A. Schiessl, and L. P. Schmidt. A novel fully electronic active real-time imager based on a planar multistatic sparse array. *IEEE Transactions on Microwave Theory and Techniques*, 59(12):3567–3576, Dec 2011.

[39] Lars MH Ulander, Hans Hellsten, and Gunnar Stenstrom. Synthetic-aperture radar processing using fast factorized back-projection. *IEEE Transactions on Aerospace and electronic systems*, 39(3):760–776, 2003.

[40] Ciro Cafforio, Claudio Prati, and Fabio Rocca. Sar data focusing using seismic migration techniques. *IEEE transactions on aerospace and electronic systems*, 27(2):194–207, 1991.

[41] AS Milman. Sar imaging by ω—κ migration. *International Journal of Remote Sensing*, 14(10):1965–1979, 1993.

[42] Hans Hellsten and Lars-Erik Andersson. An inverse method for the processing of synthetic aperture radar data. *Inverse problems*, 3(1):111, 1987.

[43] Yang Li, Tao Zeng, Teng Long, and Zheng Wang. Range migration compensation and doppler ambiguity resolution by keystone transform. In *Radar, 2006. CIE'06. International Conference on*, pages 1–4. IEEE, 2006.

[44] F Rocca, C Prati, and A Monti Guarnieri. New algorithms for processing of sar data. *Eur. Space Center Contract Rep., Ispra, Italy, ESRIN Contract*, 1(7998/88), 1989.

Chapter 3

Real Aperture Radar (RAR) imaging systems: Direct imaging technique

3.1 Introduction

In this chapter, the capability of Real Aperture Radar imaging systems is investigated. Because it only requires one pair of transmitter and receiver chains associated with a passive or an active antenna, it makes this solution the easiest to implement among the other methods detailed in the previous chapter. To have a great spatial resolution, the half-power beam-width of the antenna must be as narrow as possible. This narrow beam width allows for a more precise targeting. Because the study focuses upon millimeter-wave, it is critical to manufacture a large aperture antenna with low losses. A key indicator of how properly the signal is transmitted through the medium is called the overall antenna efficiency η. This is a comparison between the achieved gain of the antenna and a loss-free aperture with uniform amplitude and phase of same dimension as the considered radiating aperture antenna. This indicator combines all the losses that occur from the input to the output of the antennas.

$$\eta = \eta_{lo}\,\eta_s \tag{3.1}$$

with:
η : overall antenna efficiency
η_{lo} : loss efficiency
η_s : surface efficiency

This is a general equation, however, when a focusing aperture is used, such as a reflector [1], with a primary source, it is possible to further detail the equation as follows:

$$\eta = \eta_m\,\eta_l\,\eta_a\,\eta_{sp}\,\eta_{ph}\,\eta_p \tag{3.2}$$

with:
η : overall antenna efficiency
η_m : mismatch losses

η_l : feed, line and radiating element ohmic losses
η_a : taper (apodisation) efficiency
η_{sp} : spill-over efficiency
η_{ph} : illumination phase errors or phase compensation errors
η_p : polarization loss due to the presence of energy in cross-polarization

For real Aperture Radar, it is required to manufacture an antenna with an aperture efficiency as high as possible to have a narrow beam-width with a maximized gain. In this chapter, a high-directive antenna is developed to be used in a Real Aperture Radar (RAR) configuration. The study focuses on Fresnel lens antenna as the focusing aperture to achieve high-directivity over a wide frequency bandwidth with a high efficiency as compared to other designs found in the literature. For our concern, only the taper, spill-over and phase compensation errors efficiency are taken into account in the following sections.

3.2 Fresnel lens antennas

At millimeter-wave, the complexity of manufacturing shaped reflectors becomes higher and a small irregularity during the manufacturing process may impact the gain of the antenna [2, 3]. Taking this factor into account, the antenna community is now focusing on other antenna designs not only to moderate the manufacturing complexity but also by keeping acceptable efficiency over a wide frequency bandwidth. Fresnel lenses permit to focus the signal by using the phase shifting property of the antenna surface, rather than its shape. The spherical wavefront that arrives at the surface of the lens is then compensated to be uniform at the output of the lens. The compensation permits to have a uniform phase over the entire surface of the lens that permits to have a larger aperture which creates a high directive beam.

We will focus the study on Fresnel lenses at millimeter wave from 75 to 110 GHz. It will be shown that this antenna may reach high aperture efficiency with low side-lobe level, if simple rules are applied during the design process. To keep the complexity acceptable it is possible to use phase transformer steps that will compensate the phase only when the phase shift reaches a limit, such as the half-phase, the quarter-phase and Q-phase transformer that compensate the phase every time the phase shift reach 180°, 90° and $360/Q°$ respectively [4–6]. The variable Q corresponds to the number of compensations that is performed during a phase shift of 360°. It is clear that since the compensation is not perfectly performed, the antenna will have a limited efficiency. The spherical phase front can be compensated using different material permittivity [7] (see Figs. 3.1a & 3.1b) or the phase correcting zones can be achieved by implementing a grooved dielectric Fresnel Zone plate lens [8] (see Figs. 3.1c & 3.1d). Among plenty of solutions, the dielectric properties can be varied in a controlled way by appropriately changing the composition or structure of the material. One interesting solution is to make multiple holes locally that are placed at different distance from each other in order to vary the overall permittivity [9, 10] (see Figs. 3.1e & 3.1f). It seems to be a better candidate, however, the diameter of the holes can not be smaller due to manufacturing issues. The solution will show its limit when the frequency becomes too high.

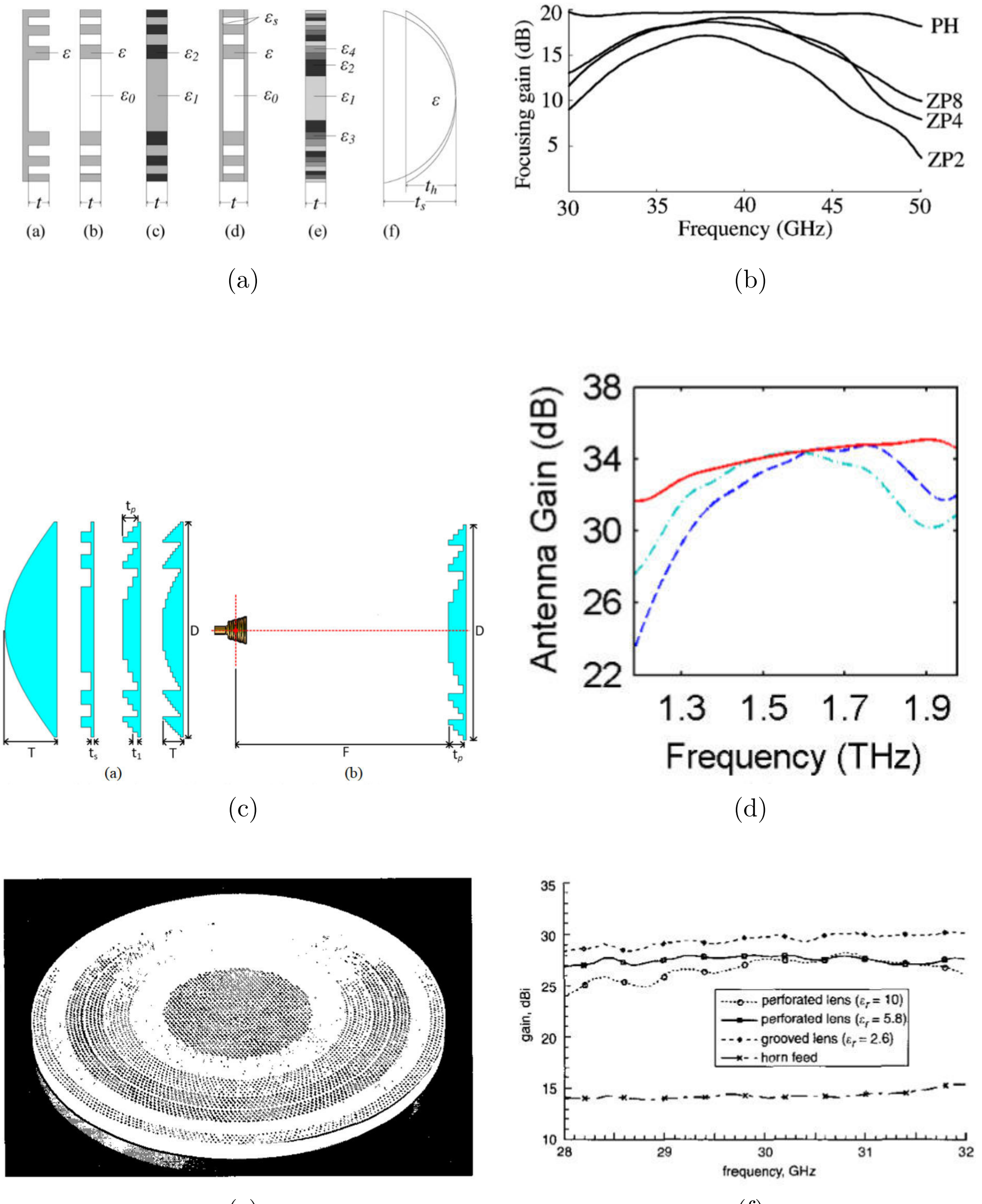

(a) (b)

(c) (d)

(e) (f)

Figure 3.1: (a) A multi-dielectric Fresnel Zone plate lens [7] with in (b) the corresponding focusing gain. (c) A grooved Fresnel Zone plate lens [8] with in (d) the corresponding focusing gain. (c) A perforated dielectric Fresnel lens [9] with in (d) the corresponding focusing gain.

The study mainly focuses on increasing the efficiency of Fresnel lens antennas while keeping low side lobe levels. In Section 3.2.1, is firstly presented the parameters that drastically affect the behavior and the efficiency of Fresnel lens antenna, starting by an evaluation of the efficiency depending on the amplitude and the phase of the field within a finite radiating aperture. It allows to further investigate solutions to maintain high-efficiency and wide frequency bandwidth. In Section 3.2.3 the study is followed by the theory of Fresnel lens in order to determine the permittivities that are needed to compensate the phase shift. In Section 3.2.4, simulations is performed to demonstrate that the efficiency is impacted by another parameter that generates multiple unwanted reflections that has not been taken into account in theory. A technological process that allow to vary smoothly the permittivity of a material even at high frequency with good accuracy is presented in Section 3.2.5. Finally in Section 3.2.6, measurements are shown and compared to the theory and the simulations showing the viability of the concept.

3.2.1 Theoretical efficiency

To have high directive antennas, one solution is to use a Fresnel lens to produce a uniform (phase) field distribution at the output of the lens by compensating the phase shift that occurs toward the lens due to the incoming spherical phase front. The aperture is usually divided into sub-zones of similar thicknesses, but different permittivities, which allow compensation of the phase shift. The number of the sub-zones is usually limited to avoid high manufacturing complexity. However, as will be shown later, it drastically impacts the focusing quality of the lens.

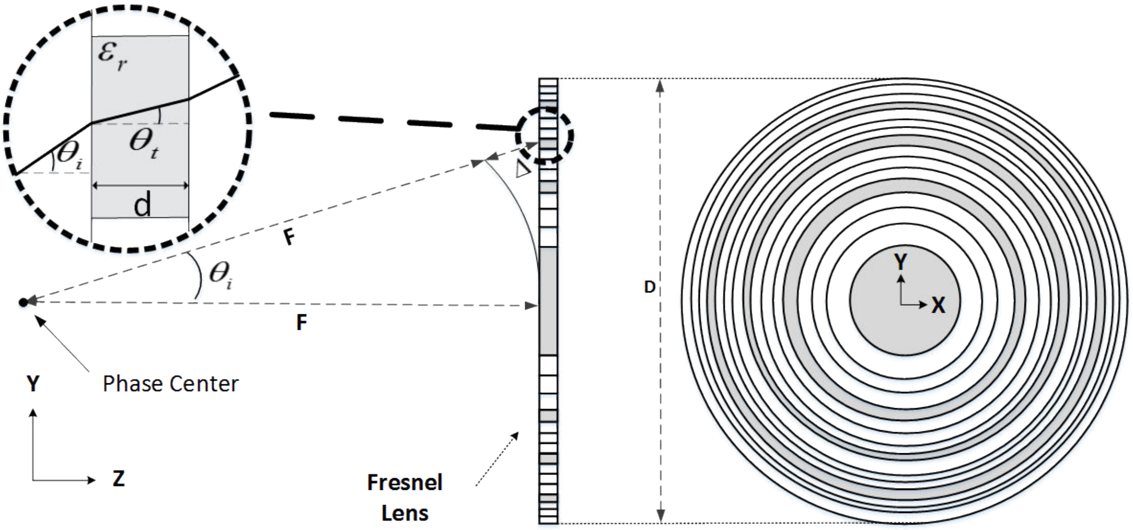

Figure 3.2: Sectional and top views of the flat Fresnel lens with F the focal distance, D the diameter of the lens, d the thickness of the lens. θ_i yields for a particular angle of incidence with the corresponding refracted angle θ_t. The variable Δ corresponds to the phase shift that occurs at the input of the lens due to the spherical wavefront.

The amplitude tapering (3.2) of the finite aperture due to the feeder radiation pattern is another important parameter that must be considered to improve efficiency [11]. Without going into any details of the lens design shown in Fig. 3.2, the results presented here for analysis are for a focal distance (F) of 170 mm and a lens diameter (D) of 120 mm corresponding to a half-intercept angle with the edge of the lens of $\theta_0 = 20°$. The lens diameter has been kept fixed to compare the results obtained by a previous work at the same frequency band (75-90 GHz) [6].

3.2.1.1 Phase compensation efficiency

In [12, 13], the efficiency of a finite radiating aperture is shown, representing phase aberration (η_{ph} efficiency loss due to non-uniform phase illumination of the aperture plane) is given by:

$$\eta_{ph} = \frac{\left| \int_{0}^{2\pi} \int_{0}^{\theta_0} G(\theta,\phi) \tan(\frac{\theta}{2}) d\theta d\phi \right|^2}{\left[\int_{0}^{2\pi} \int_{0}^{\theta_0} |G(\theta,\phi)| \tan(\frac{\theta}{2}) d\theta d\phi \right]^2} \tag{3.3}$$

where $G(\phi,\theta) = A(\theta,\phi)\exp(j\Phi(\theta,\phi))$ is the complex co-polar radiation pattern of the feeder which will be approximated by an axially symmetric pattern (not dependent on ϕ, any longer), $A(\theta,\phi)$ is the amplitude which is considered to be uniform in this part, and Φ is the phase along the aperture.

Five different cases, which can be divided into two configurations, are considered here. One type of configuration accomplishes a stepwise phase correction, such as the half-wave Fresnel zone plate lens (FZPL), which accomplishes a half-wave stepwise phase correction ($Q = 2[2\pi]$), quarter-wave FZPL ($Q = 4[2\pi]$) or eighth-wave FZPL ($Q = 8[2\pi]$). The second type of configuration corresponds to a smooth phase correction with two different cases: the first one is a smooth phase correction (*smooth*) and the second one is also a smooth phase correction, but is combined with a full-wave stepwise phase correction ($smooth[2\pi]$); in other words, the smooth phase correction is wrapped using a modulo 2π.

For a given working frequency at $f = 75$ GHz (Fig. 3.3), the black line corresponds to the phase of the spherical phase front that arrives onto the finite aperture. The phase shift determined is then corrected using the five different cases. As presented above, only the "smooth" phase correction case is not wrapped which implies that such a configuration has no frequency dependency and hence allows for a wider frequency band. From the results shown in Fig. 3.3 and using (3.3), the phase compensation efficiency of the different configurations can be determined, as shown in Fig. 3.4. The results presented hold good for a fixed focal distance and lens diameter. It can be seen that depending on the number of stepwise phase corrections, the phase compensation efficiency varies from about 40% to 95% for the half-wave and eighth-wave FZPLs, and 100% for the smooth cases.

Further, the unlimited frequency bandwidth of the smooth case will no longer be valid, when phase compensation wrapping is applied, which drastically decreases the available frequency bandwidth ($f/f_0 = 0.83$ at 75 GHz and $f/f_0 = 1.22$ at 110 GHz using f_0= 90 GHz).

Only the last two configurations are considered, because only they allow for achieving the maximum phase compensation efficiency, unlike the other methods. However, considering the processes used for manufacturing the lenses, it appears that manufacturing a smooth lens is difficult. But, the technological process used in this study, which will be explained in Section 3.2.5, allows for creating such a lens. The ongoing study allows for a comparison of the *smooth* case with the $smooth[2\pi]$

case, which is used as a reference.

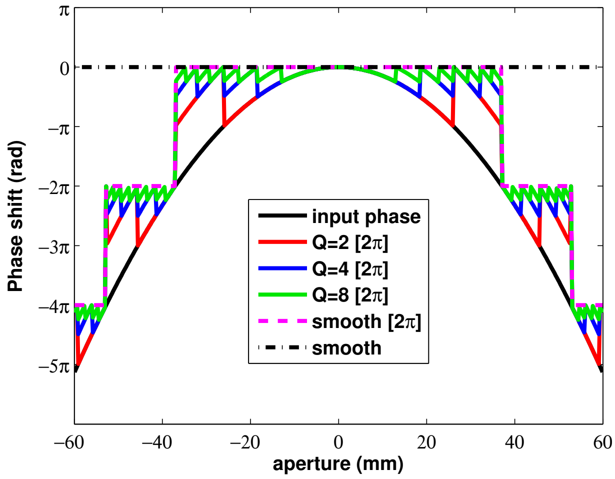

Figure 3.3: Phase shift that occurs at 75 GHz along the circular aperture diameter due to the spherical wave front and the generated phase compensation using the five cases.

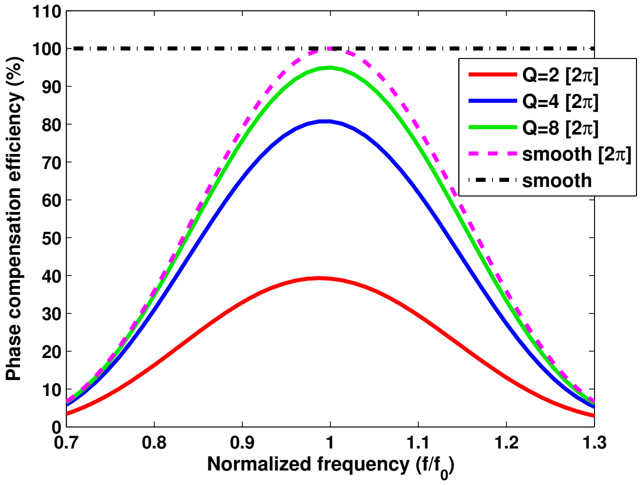

Figure 3.4: Phase compensation efficiency of the five cases versus the normalized frequency band.

3.2.1.2 Amplitude tapering efficiency

At millimeter wave, because it is hard to manufacture a feeder that uniformly illuminates the lens surface [14], amplitude tapering must be considered to obtain high efficiency. As for the phase compensation efficiency, a finite circular aperture is considered in this study. The goal is to find the optimum solution that helps in attaining the highest aperture efficiency in the considered frequency bandwidth. Two main factors are investigated: the taper efficiency and the spill-over efficiency. Where horn antennas are used, the radiation pattern of the feeder usually follows a $\cos^n$-like function. However, at millimeter wave, it becomes complex to manufacture a specific type of horn, such as the corrugated horn that maintains low side lobe level. And, that is why classic horn has been chosen for the design of the feeder. Hence, the feeder radiation pattern, approximated by an axially symmetric radiation pattern is given by the following equation:

$$G(\theta, n) = \begin{cases} (2n+1)\cdot\cos^n(\theta), & \text{for } 0 \leq \theta \leq \frac{\pi}{2} \\ 0, & \text{for } \theta > \frac{\pi}{2}. \end{cases} \tag{3.4}$$

From [11–13], it is shown that taper efficiency η_a (corresponding to the loss due to non-uniform amplitude illumination of the aperture plane) and spillover efficiency η_{sp} (corresponding to the ratio of the power intercepted by the aperture to the total power) are given by (3.5) and (3.6) respectively.

$$\eta_a = \frac{1}{\pi\tan^2(\frac{\theta_0}{2})} \cdot \frac{\left[\int_0^{2\pi}\int_0^{\theta_0} |G(\theta,\phi)|^{1/2}\tan(\frac{\theta}{2})d\theta d\phi\right]^2}{\int_0^{2\pi}\int_0^{\theta_0} |G(\theta,\phi)|\sin(\theta)d\theta d\phi} \tag{3.5}$$

$$\eta_{sp} = \frac{\int_0^{2\pi}\int_0^{\theta_0} G(\theta,\phi)\sin(\theta)d\theta d\phi}{\int_0^{2\pi}\int_0^{\pi} G(\theta,\phi)\sin(\theta)d\theta d\phi} \tag{3.6}$$

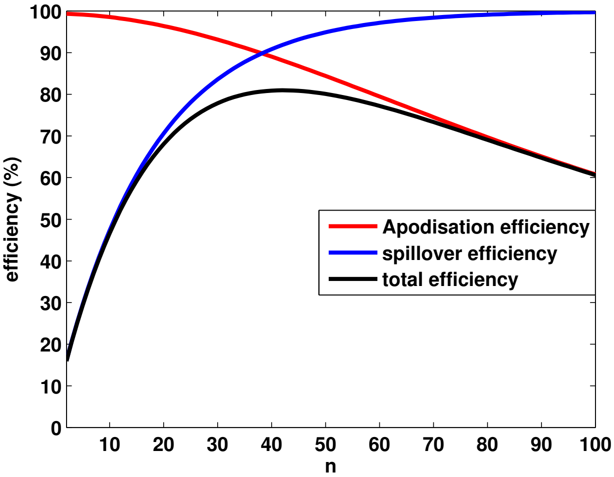

Figure 3.5: Theoretical aperture efficiency over the amplitude weighting generated by a cos^n-like radiation pattern.

It is evident that a directive feeder (high value of n (see Fig. 3.4)) will generate high spill-over efficiency but low taper efficiency. Considering the physical dimensions of the lens and the focal distance, it is desirable to find the n that maximizes the product of the two efficiencies ($\eta_T = \eta_a \cdot \eta_{sp}$). Figure 3.5 shows the evolution of the two efficiencies depending on n. From this figure, it can be seen that the optimum value is $n = 40$ corresponding to efficiency $\eta_T = 0.81$. However, the directivity of a horn antenna increases with the frequency. It corresponds to the increase in the value of n with respect to the frequency. Hence the idea is to optimize a horn antenna which has a radiation pattern that matches as far as possible the $\cos^n$-like pattern of the model maintaining a stable radiation pattern along the considered frequency band.

3.2.2 Design and measurement of the feeder

An elliptical aperture horn antenna has been optimized to match the $\cos^n$-like pattern of the model.

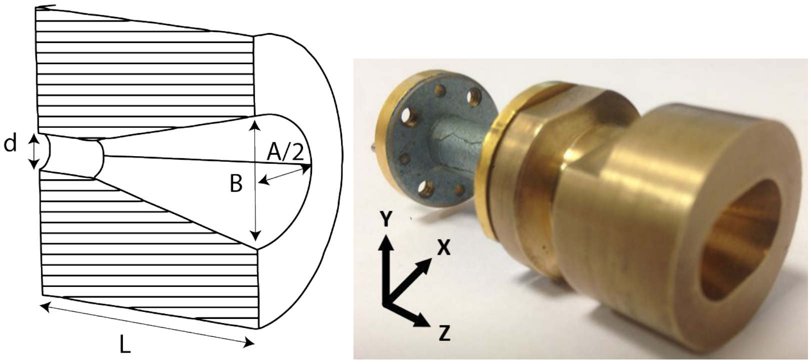

(a) (b)

Figure 3.6: (a) Sketch of the elliptical horn antenna and (b) the manufactured elliptical horn with rectangular-to-circular transition producing an axially symmetric $\cos^n$-like radiation pattern

According to the information provided by Fig. 3.5, the value of n should be between 22 and 78 to maintain an amplitude taper efficiency that is higher than 70%.

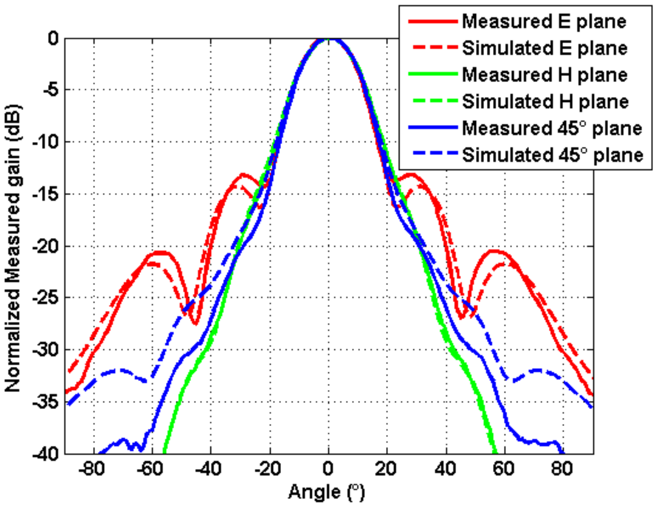

Figure 3.7: Simulated and measured radiation pattern of the feeder at 90 GHz

The optimized horn working from 75 to 110 GHz has aperture dimensions of

A=14 and B=10 mm for the major and minor axes, respectively. The length of the horn is L=15 mm and the horn's minor axis is oriented along the E-plane. The horn is fed by a rectangular to circular waveguide transition as shown in Fig. 3.6 with d=2.82 mm. In Fig. 3.7 is shown a comparison between the simulated and measured radiation pattern of the feeder at 90 GHz. The simulations have been performed using CST-Microwave Studio [15] and the simulation results are in good agreement with the measurement results.

Figures. 3.8a and 3.8b show the measured radiation patterns at, respectively, 75 GHz and 110 GHz with the matched $\cos^n$-like radiation pattern with $n = 35$ (75 GHz) and $n = 70$ (110 GHz).

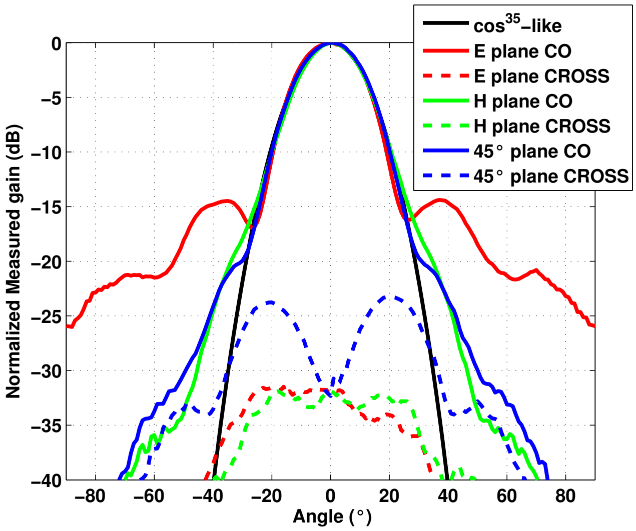

(a)

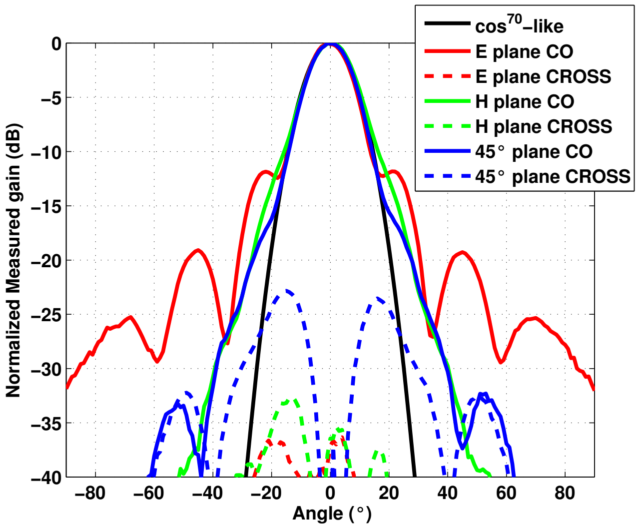

(b)

Figure 3.8: Measured (Co/Cross polarization) radiation pattern of the optimized feeder along the E ($\phi = 90°$) / H ($\phi = 0°$) / 45° ($\phi = 45°$) planes compared with the associated $\cos^n$-like radiation pattern at the extreme frequencies (a) 75 GHz and (b) 110 GHz.

From theses figures, it can be seen that the shapes of the radiation patterns are stable for the three planes as compared to the $\cos^n$-like radiation pattern until ±25° at 75 GHz and ±20° at 110 GHz. This implies that the theoretically determined taper efficiency is valid. However, as regards the spill-over efficiency, it has been slightly overestimated because of the side lobe levels, which are much higher than those of the cos^n-like model, reaching, in the worst case, -12 dB for the E-plane at 110 GHz. The measured gain over the frequency band varies from 18.2 to 22.8 dBi. The S_{11}-parameter is lower than -20 dB, over the frequency range. The measured cross-polarization level remains lower than -23 dB, over the frequency range.

3.2.3 Fresnel lens theory

From Fig. 3.2, and according to the wave propagation theory at oblique-wave incidence, it follows that a wave arriving upon a medium of dielectric constant ϵ_r, at incidence angle θ_i, will be transmitted through the medium of thickness d with transmitting angle θ_t. The wave will travel for a distance of $d/\cos\theta_t$ within the lens before emerging from the lens. The optimum permittivity allows for canceling out the phase shift, generated by the incoming spherical phase front. Because of this compensation, a uniform phase distribution at the output of the lens will be produced.

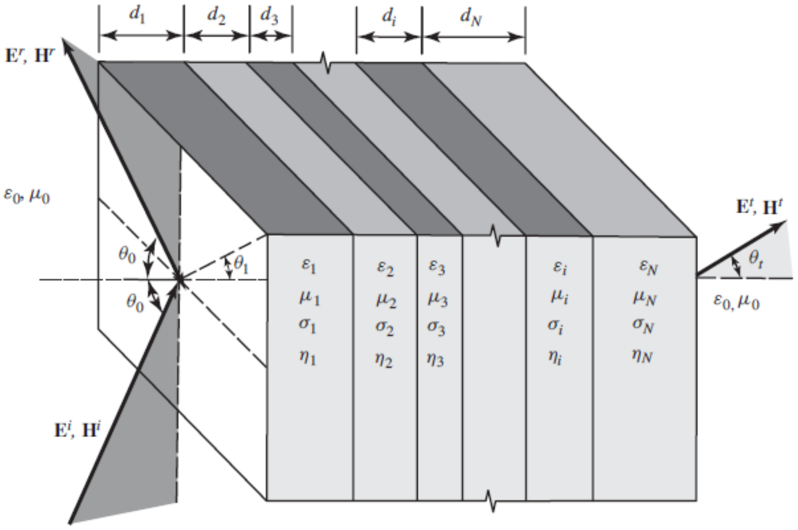

Figure 3.9: Oblique wave propagation through N layers of dielectric slabs with $mathbfE$ and $mathbfH$ the electric and magnetic fields, respectively.

According to [16] and using Fig. 3.9, and considering the traveling path of the incoming spherical wave from the phase center of the feeder until the output surface of the lens, the complex transmission coefficient is given by the following recursive equation:

$$T = \frac{1}{A_0}$$

with

$$A_j = \frac{e^{\psi_j}}{2}\Big[A_{j+1}(1+Y_{j+1}) + B_{j+1}(1-Y_{j+1})\Big] \tag{3.7}$$

and

$$Y_{j+1} = \frac{\cos\theta_{j+1}}{\cos\theta_j}\sqrt{\frac{\epsilon_{j+1}(1-j\tan\delta_{j+1})}{\epsilon_j(1-j\tan\delta_j)}}$$

where $A_{N+1} = 1$, $B_{N+1} = 0$, $\psi_j = \gamma_j d_j / \cos\theta_j$, and $\gamma_j = \sqrt{j\omega\mu_j(\sigma_j + j\omega\epsilon_j)}$. θ_j yields for the angle of refraction.
It is a generic equation that allows for the calculation of the complex transmission coefficient at oblique incidence of N dielectric layers. In this study the number of layers is $N = 1$. Furthermore, the index j corresponds to the j^{th} layer, considered with $j = 0$ for the area between the phase center and the input of the lens, $j = 1$ for the area within the lens, and $j = 2$ for the area at the output of the lens. Rearrangement of the equations and modification of the variables used to our notation ($\theta_i = \theta_0$, $\theta_t = \theta_1$, $F = d_0$ and $d = d_1$), yields, the following:

$$T(\theta_i, \epsilon_r; f_0) = e^{-(\psi_1+\psi_0)} \cdot \frac{\dfrac{4}{(1+Y_2)(1+Y_1)}}{1 - \left[e^{-\psi_1}\dfrac{1-Y_1}{1+Y_1}\right]^2} \tag{3.8}$$

where

$$\psi_0 = j\beta_0\frac{F}{\cos\theta_i}, \;\; \psi_1 = j\beta_0\sqrt{\epsilon_r}\frac{d}{\cos\theta_t} \tag{3.9}$$

and

$$\frac{4}{(1+Y_2)(1+Y_1)} = \frac{4\cos\theta_i\cos\theta_t\sqrt{\epsilon_r(1-j\tan\delta)}}{\left[\cos\theta_i + \cos\theta_t\sqrt{\epsilon_r(1-j\tan\delta)}\right]^2} \tag{3.10}$$

$$\frac{1-Y_1}{1+Y_1} = -\frac{1-Y_2}{1+Y_2} = -\frac{\cos\theta_i - \cos\theta_t\sqrt{\epsilon_r(1-j\tan\delta)}}{\cos\theta_i + \cos\theta_t\sqrt{\epsilon_r(1-j\tan\delta)}} \tag{3.11}$$

with $\beta_0 = \frac{2\pi f_0}{c}$ and c the free space speed of light.

Finally, using (3.8), a reference has to be taken to have a uniform aperture phase at the output of the lens. By taking the normal incidence as a reference ($\theta_i = 0$) and a fixed permittivity (ϵ_{ref}), the phase that will be generated at the output of the lens after compensating for all the phase shifts is given by $\arg(T(0, \epsilon_{ref}))$. Hence the desired permittivities along the lens are assessed by minimizing the objective function under a constraint such as the following:

$$\begin{aligned} &\underset{\epsilon_r}{\text{minimize}} && \arg\Big(T(\theta_i, \epsilon_r; f_0)\Big) - \arg\Big(T(0, \epsilon_{ref}; f_0)\Big) \\ &\text{subject to} && \epsilon_{r_{min}} \le \epsilon_r \le \epsilon_{r_{max}} \end{aligned} \tag{3.12}$$

The technological process which will be explained later allows for performing any permittivity in a fixed range between $\epsilon_{r_{min}}$ and $\epsilon_{r_{max}}$. However, depending on the solution that is used to realize the lens, the constraint can be modified. Where a wrapped phase correction is planned by using modulo 2π the following minimizing problem has to be applied:

$$\begin{aligned} &\underset{\epsilon_r}{\text{minimize}} && \Big(\arg\Big(T(\theta_i, \epsilon_r; f_0)\Big) - \arg\Big(T(0, \epsilon_{ref}; f_0)\Big)\Big)\ [2\pi] \\ &\text{subject to} && \epsilon_{r_{min}} \leq \epsilon_r \leq \epsilon_{r_{max}} \end{aligned} \tag{3.13}$$

In both cases, the material is considered lossy ($\tan\delta > 0$). The loss tangent can be related to permittivity in terms of the measurements performed and summarized in Tab. 3.1. Depending on the constraints, it may so happen that the minimizing problem does not converge to zero. This problem can be overcome by increasing the thickness d of the lens. From Fig. 3.10, it can be seen that the calculated permittivities, which are of interest, are the smooth phase correction (*smooth*) and the wrapped smooth phase correction (*smooth*[2π]) for thicknesses of 20 mm and 10 mm, respectively. Using Fig. 3.2, it can be shown that the phase at the output of the lens for one particular incidence angle is equal to the phase at the output of the lens at normal incidence, as given in (3.14).

$$\frac{2\pi f_0}{c} \cdot \Big(F + \sqrt{\epsilon_{ref}}d\Big) = \frac{2\pi f_0}{c} \cdot \Big((F + \Delta) + \sqrt{\epsilon_r}d/\cos\theta_t\Big) \tag{3.14}$$

The first term $(\frac{2\pi f_0}{c})$, on both sides of the $=$ symbol in (3.14), cancels out, implying that there is no frequency dependency in the *smooth* case. This, however, is not valid for the *smooth*[2π] case because the modulo is applied for one particular frequency.

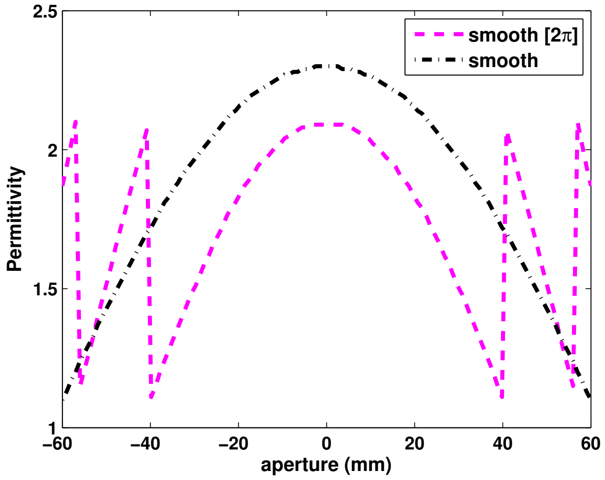

Figure 3.10: Comparison of the determined permittivity variation along the diameter of the 2 circular lens apertures.

Depending on the permittivity and the thickness of the lens used, the transmission coefficient may fluctuate along the frequency band. If high permittivity material is used at a high angle of incidence, the efficiency may drastically decrease.

In Figs. 3.11a & 3.11b is shown the magnitude of the transmission coefficient along the lens diameter within the desired frequency range. This permits calculation of the transmission coefficient efficiency along the frequency, using (3.15), as shown in Fig. 3.11c. As the transmission coefficient may be significantly affected by high permittivity, the maximum permittivity ($\epsilon_{r_{max}}$) has been fixed to 2.3, to maintain high transmission coefficient efficiency of about 96%in both cases. The variations seen in the oscillation along the frequency (see Fig. 3.11c) are due to the difference between the thicknesses of the two lenses.

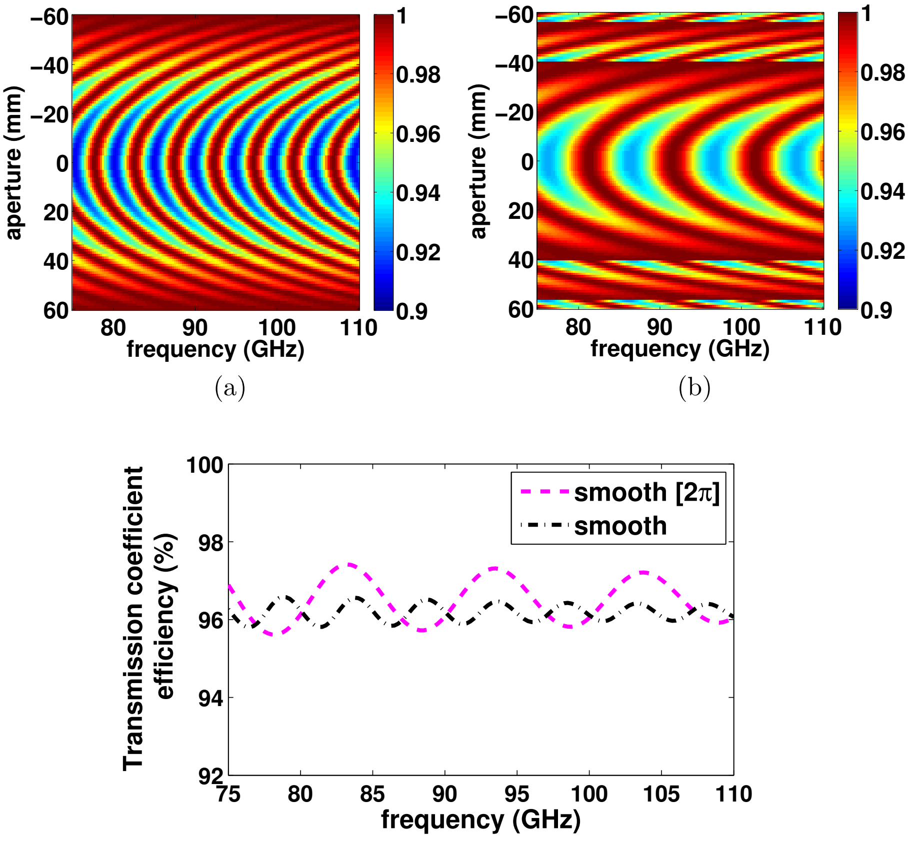

(a) (b)

(c)

Figure 3.11: Variation of the transmission coefficient along the diameter and versus the considered frequency range for the (a) *smooth* and (b) *smooth*$\left[2\pi\right]$ cases. (c) Variation of the transmission coefficient efficiency versus the considered frequency range for the two cases.

$$\eta_{|T|} = \frac{\int\limits_0^{2\pi}\int\limits_0^{\theta_0} |T(\theta, f; \epsilon_r)|^2 \sin(\theta) d\theta d\phi}{\int\limits_0^{2\pi}\int\limits_0^{\theta_0} |T_0(\theta, \phi)|^2 \sin(\theta) d\theta d\phi} \tag{3.15}$$

where $T_0(\theta, \phi)$ corresponds to a uniform aperture ($|T| = 1$).

3.2.4 Simulation

To ensure that the lens can be simulated by using electromagnetic software (CST-MW) [15], it is desirable to sample the lens aperture (the permittivity variation) in small zones. Hence, the aperture is sampled in multiple rings of 1 mm width. From Fig. 3.4, it can be seen that the *smooth* and the *smooth*$[2\pi]$ cases reach 100% phase compensation efficiency at the working frequency of $f_0 = 90$ GHz. This is theoretically correct, because at the output of the lens the phase is uniform. However, in practice, because of the wrapped phase correction that has been performed to limit the thickness of the lens, the permittivity along the lens does not progressively vary, when the modulo is applied. Hence, strong variations in permittivity occurs starting from 1.1 to 2.2, as shown in Fig. 3.10. This generates unwanted multiple reflections that cannot be compensated, resulting in deterioration of antenna's efficiency. This phenomenon is illustrated in Fig. 3.12 at 90 GHz, showing the *smooth* case on the left and the *smooth*$[2\pi]$ case on the right.

The two lenses are illuminated by the same feeder as the one used in the investigation covered by 3.2.2. From a comparison of the electric fields at the outputs of the two cases, it is seen that the effective aperture is evidently smaller in the *smooth*$[2\pi]$ case than the one in the *smooth* case, and this impacts the efficiency. To avoid unnecessary repetition, in the measurement part of Section 3.2.6, only the simulated directivity will be compared with the measurement gain for the two lenses.

3.2.5 Realization

AirexR82 foam composite material, with initial low dielectric constant, very close to 1.1, is used. This composite material is full of air bubbles surrounded by a material with an intrinsic relative permittivity. The lenses are manufactured by following the procedure given in [17]. The technological process allows for controlling the dielectric constant in a controlled manner by appropriately changing the structure of the foam. In fact, it allows extraction of air bubbles from the composite by pressing it at a controlled temperature thanks to a hydraulic heat press machine. The thickness ratio is $\xi = \frac{d_i}{d_f}$, d_i being the initial thickness and d_f the final thickness after pressing. This process enables smooth control of the dielectric constant in a permittivity range that allows creation of inhomogeneous structures. Multiple measurements on the same foam with different thickness ratios for a fixed d_f, allows for generation of a relationship between the thickness ratio and the achieved permittivity. The measurements have been performed with different pressed foam samples and they have been characterized thanks a quasi-optic measurement setup based on a Free space technique (see [17]).

Table 3.1 shows the measured dielectric properties of the AirexR82 foam with a final thickness of 2.5 mm.

In this study, the maximum permittivity needed is 2.3 corresponding to a pressing ratio of 11, which means that initial thickness of $20 \times 11 = 220$ mm is needed for the *smooth* case. Unfortunately, the thickness of the foam used for this study is limited to 30 mm; hence, it has been decided to realize 8 identical sub-lenses, each of an initial thickness of 27.5 mm at the center of the lens and a final thickness of 2.5 mm,

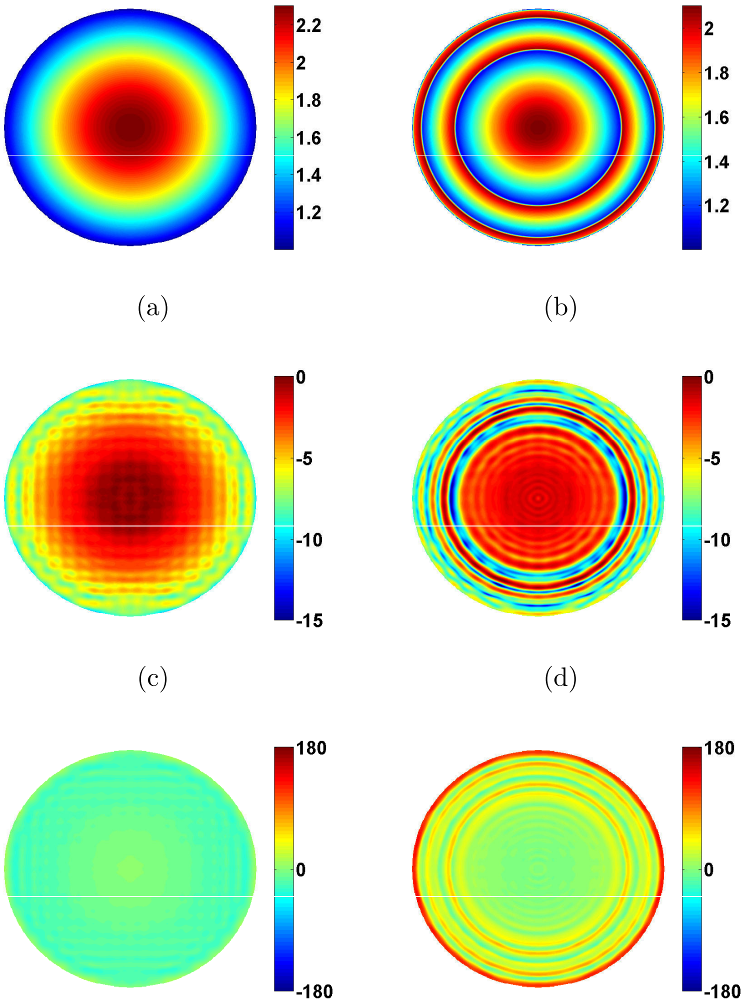

(a) (b)

(c) (d)

(e) (f)

Figure 3.12: Simulated Electric field (at 90 GHz) at the output of (a), (c), (e) the *smooth* lens and (b), (d), (f) the *smooth*[2π] lens with a diameter of 12 cm; (a), (b) show the variation of the permittivity over the lens surface, while (c), (d) show the normalized electric field distribution in amplitude (dB) over the lens surface and (e), (f) show the electric field distribution in phase (°) over the lens surface.

and then stack them to form a unique lens of 20 mm thickness. The same procedure is followed for the *smooth*[2π] case, but only 4 identical sub-lenses, each of a final thickness of 2.5 mm, are used to produce a unique lens of 10 mm thickness. Figure 3.13 shows the cross-section of a sub-lens, with initial thickness, prior to pressing.

Fig. 3.14b shows a *smooth* lens composed of 8 sub-lenses. The metallic rings that surround the sub-lenses enable the lenses retain their original diameters, when they are pressed. These sub-lenses are pressed simultaneously. On the other side, Fig. 3.14a shows a *smooth*[2π] lens composed of 4 sub-lenses. These lenses are pressed three times, first by using the metallic cylinders for pressing the centers of the sub-lenses, and then the metallic rings for pressing the surrounding area and finally the remaining area. The lenses after pressing are shown in Fig. 3.15.

Table 3.1: Measured dielectric properties obtained from AIREX82 depending on the thickness ratio

$\xi = \mathrm{d_i/d_f}$	Permittivity	Loss Tangent
1	1.12	0.007
3	1.35	0.008
5	1.58	0.012
7	1.8	0.014
9	2.05	0.015
11	2.3	0.016

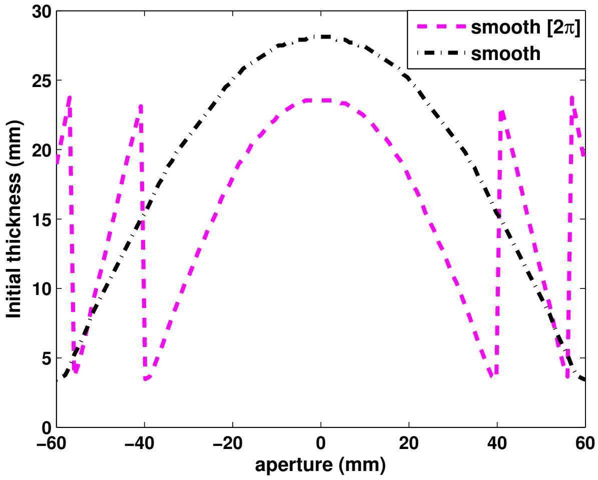

Figure 3.13: Initial thickness along the aperture diameter of each sub-lens before being pressed.


(a)

(b)

Figure 3.14: Manufactured sub-lenses before pressing them for the (a) *smooth*$\left[2\pi\right]$ and (b) *smooth* cases.

3.2.6 Radiation pattern measurements

To prove that the foam material can retain its final thickness through time by using the technological process, the measurement has been carried out three months after realizing the lenses. However, to avoid any air gap between the sub-lenses, they are slightly compressed by two panels made of Rohacell foam (permittivity close to

Figure 3.15: Manufactured sub-lenses for the (left side) *smooth*$\left[2\pi\right]$ and (right side) *smooth* cases after being pressed.

1.04). The panels are attached to four pillars which are fixed to the measurement setup, to get the desired focal distance between the horn and the lens. The measurements have been performed at the Institute of Electronics and Telecommunications of Rennes (IETR) using a Compact Antenna Test Range (CATR) [18] which allows measurement of high gain antennas with great accuracy. The measurements of the realized *smooth* and *smooth*[2π] lenses are compared below.

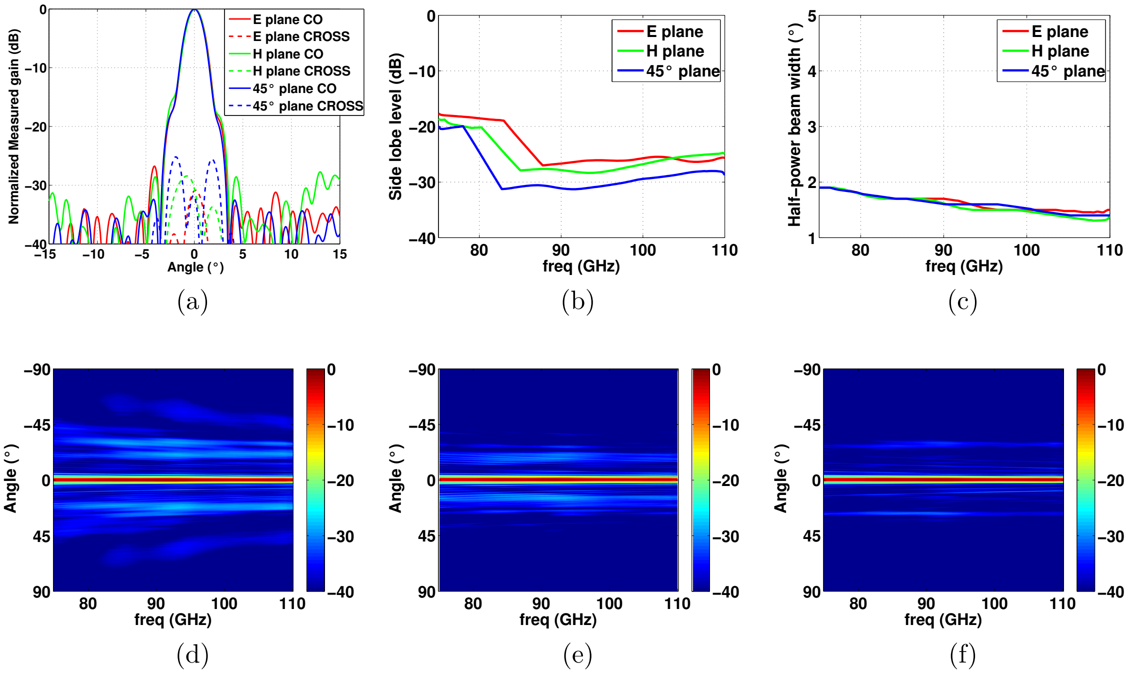

(a) (b) (c)

(d) (e) (f)

Figure 3.16: Measured radiation performance of the *smooth* lens. (a) radiation pattern along the E/H/45° planes at 90 GHz. (b) Side lobe level along the E/H/45° planes versus the frequency range. (c) Half-power beam-width along the E/H/45° planes versus the frequency range. (d) Normalized E-plane radiation pattern (Co-polarization) versus the frequency range. (e) Normalized H-plane radiation pattern (Co-polarization) versus the frequency range. (f) Normalized 45°-plane radiation pattern (Co-polarization) versus the frequency range.

Figure 3.16 depicts the measured antenna characteristics of the *smooth* lens. Figure 3.16a shows the normalized radiation patterns (Co and Cross-polarization) at 90 GHz in E/H and 45° planes, and Figure 3.16b the evolution of the side lobe level (SLL) along the frequency. It can be seen that SLL remains stable, reaching less than -25 dB over a wide frequency bandwidth of 20 GHz. At the beginning of the frequency band, between 75 and 90 GHz, an increase of SLL can be seen, which could be due to the spillover effect that decreases with frequency as depicted in

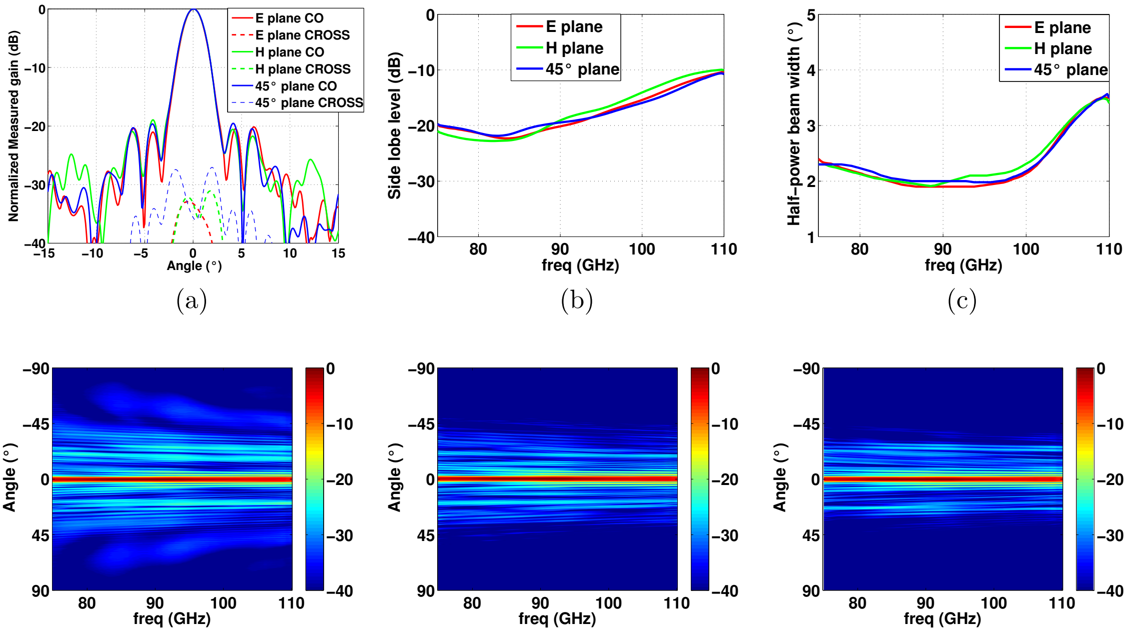

(a) (b) (c)

(d) (e) (f)

Figure 3.17: Measured radiation performance of the *smooth*$[2\pi]$ lens. (a) radiation pattern along the E/H/45° planes at 90 GHz. (b) Side lobe level along the E/H/45° planes versus the frequency range. (c) Half-power beam-width along the E/H/45° planes versus the frequency range. (d) Normalized E-plane radiation pattern (Co-polarization) versus the frequency range. (e) Normalized H-plane radiation pattern (Co-polarization) versus the frequency range. (f) Normalized 45°-plane radiation pattern (Co-polarization) versus the frequency range.

Fig. 3.5. The Half-Power Beam Width (HPBW) evolution over the frequency band, shown in Fig. 3.16c, in the three planes going from 1.9° to 1.5°, demonstrates a stable amplitude tapering over the surface of the lens, thanks to the axially symmetric radiation pattern of the optimized feeder (see Fig. 3.8). Figures 3.16d, 3.16e & 3.16f show the evolution, over the frequency band, of the normalized (at the highest gain) Co-polarization radiation patterns in E, H and 45°-planes, respectively. This shows the stability of the radiation pattern over a wide-frequency band, thanks to the no frequency-dependency of the *smooth* lens, as shown in Fig. 3.4.

Figure 3.17 shows the measured antenna characteristics of the *smooth*$[2\pi]$ lens. The shape of the normalized radiation patterns (Co and Cross-polarization) in the three-planes at 90 GHz are shown in Fig. 3.17a. The SLL evolution of the *smooth*$[2\pi]$ lens, over the frequency band shown in Fig. 3.17b, is almost equivalent to that of the *smooth* case at the beginning of the frequency band-width. However, in the case of *smooth*$[2\pi]$ lens, from 90 to 110 GHz, the SLL rises until it reaches -10 dB, because of using a frequency-dependency lens. Going farther from the working frequency (90 GHz) reduces the effective aperture (see Fig. 3.17c), which in turn increases the HPBW. In the *smooth*$[2\pi]$ case, the HPBW remains stable at about 2° over 10 GHz and then rises, reaching 3.5°. Figures 3.17d, 3.17e & 3.17f show the evolution over the frequency band of the normalized (at the highest gain) Co-polarization radiation patterns, of the *smooth*$[2\pi]$ lens, in the E, H and 45°-planes, respectively.

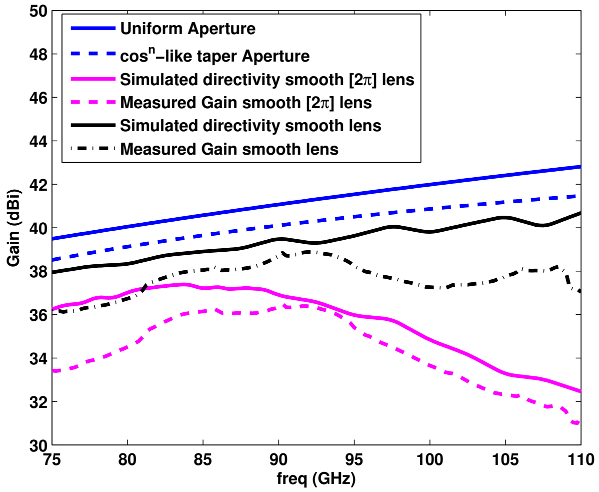

Figure 3.18: Simulated directivity and measured gain versus the frequency range for the *smooth*[2π] and *smooth* cases. The results are compared with the theoretical directivity optained by a uniform amplitude and phase aperture of same physical dimension than the manufactured lenses. The results are also compared to a uniform phase aperture with amplitude weighting generated by a $\cos^n$-like feeder radiation pattern with n lying between 35 and 70.

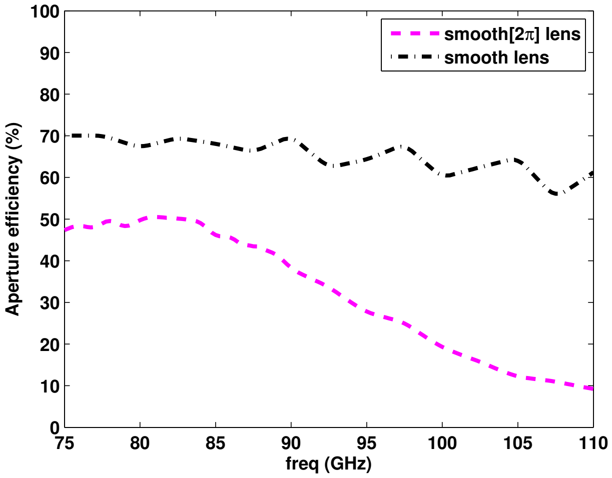

Figure 3.19: Simulated aperture efficiency for the *smooth*[2π] and *smooth* cases versus the frequency.

The simulated directivity and the measured gain of the two lenses are shown in Fig. 3.18 and compared with the directivity of a uniform amplitude and phase aperture (blue line in Fig. 3.18) of the same diameter size as that of the lens. They are also compared with a uniform phase aperture illuminated by the $\cos^n$-like radiation pattern (dashed blue line in Fig. 3.18) used previously for n varying from $n = 35$ to 70 over the frequency band. As expected, the simulated directivity and measured gain of the *smooth*[2π] lens are much lower than those of the *smooth* lense, because of the internal reflections that occur inside the *smooth*[2π] lens (see Fig. 3.12). More clearly, the capability of the *smooth* lens to maintain the gain over a wide frequency bandwidth is more than that of the *smooth*[2π] lens, as already stated in Section

3.2.1.1. For the *smooth* lens, the maximum measured gain corresponds to 38.9 dBi at 92 GHz with a radiation frequency bandwidth of 29.25 GHz with no significant decrease in gain (-2 dB), whereas for the *smooth*[2π] lens, the maximum measured gain corresponds to 36.5 dBi at 90 GHz with a radiation frequency bandwidth of 17 GHz with no significant decrease in gain (-2 dB).

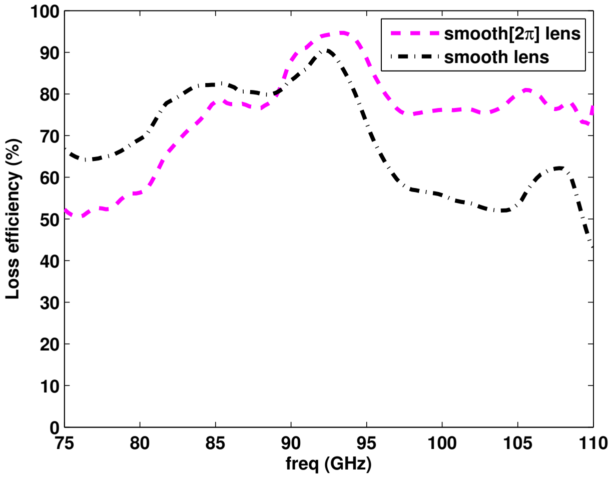

Figure 3.20: Measured loss efficiency for the *smooth*[2π] and *smooth* cases versus the frequency.

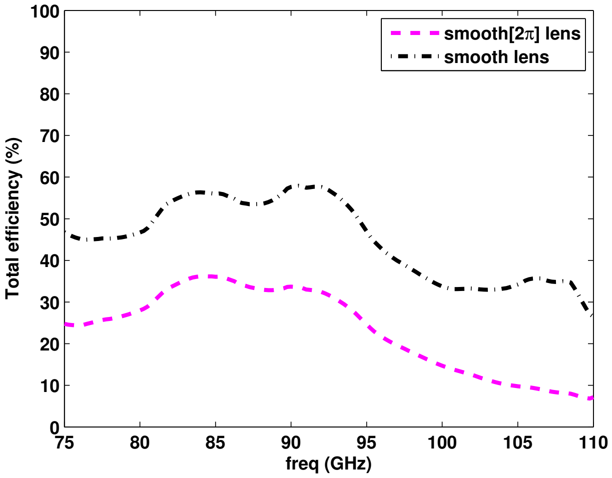

Figure 3.21: Measured total efficiency for the *smooth*[2π] and *smooth* cases versus the frequency.

Figure 3.19 shows the simulated aperture efficiency of *smooth* and *smooth*[2π] lenses, through a comparison between uniform aperture directivity (blue line) and simulated directivity of each lens. The simulated aperture efficiency reaches 70% for the *smooth* lens and 51% for the *smooth*[2π] lens. The measured loss efficiency comparing the measured gain with the simulated directivity of each lens is presented in Fig. 3.20. In showing acceptable performance of the two cases, the comparison takes into account the manufacturing defects and the intrinsic loss inside the material. The total efficiency (measured aperture efficiency) through a comparison between the uniform aperture directivity and the measured gain of each lens is shown in Fig. 3.21. The measured aperture efficiency of the *smooth* lens reaches 59% with a measured aperture efficiency higher than 50% over 14 GHz frequency bandwidth from 81 to 95 GHz. In comparison, the measured aperture efficiency of the *smooth*[2π] lens only reaches 37%.

A comparison of the achieved directivity of the $\cos^n$-like tapering aperture (blue, dashed line in Fig. 3.18) with the simulated directivity of the *smooth* lens, shows that the overall efficiency may improve by either better optimizing the horn antennas for reducing the SLL or by using other type of feeder that can be practically manufactured. This is because the foam that has been used had limited thickness, and hence the lens had to be divided into sub-lenses. And, when the sub-lenses are stacked one over the other, small air gaps are created between them, which may slightly affect their performance. Using a thicker material may help to overcome this problem and thus increase the overall performance of the antenna. The radiation performances of the two lenses are summarized in Table 3.2.

Table 3.2: Summarized radiation performances for two lenses

Performance	**smooth lens**	**smooth[2π] lens**
Maximum measured gain	38.9 dBi	36.5 dBi
-2dB Radiation frequency bandwidth	29.25 GHz (32.5 %)	17 GHz (18.9 %)
Maximum Cross-polarization level	-25 dB	-25 dB
HPBW (90 GHz)	1.7°	2.1°
SLL (90 GHz)	-26 dB	-19 dB
Maximum measured loss efficiency	90%	95%
Maximum simulated aperture efficiency	70%	51%
Maximum measured aperture efficiency	59%	37%

3.3 RAR measurements

In this Section, the manufactured *smooth* lens is used to perform a Real Aperture Radar measurement. The automotive radar frequency band from 76 to 82 GHz is chosen corresponding to a gain of approximatively 36-38 dBi over the considered frequency band. The frequency bandwidth allows to achieve a range resolution δ_r of 2.5 cm with cross-range angular resolution (half-power beam width of the antenna) between 1.7 to 1.9° with Side lobes level of about -20 dB. The measurement is performed using a Stepped Frequency Continuous Waveform (SFCW) with 1001 frequency points. The Fresnel lens will be mechanically beam-scanned by rotating the overall system by 1° step over the 360 °. The measurement provides information about the area of interest for each step angle to produce a 2D radar image. The RF measurement system uses a classical architecture with a VNA and external extenders. The transmitting and receiving chains are attached to the same antenna and separated using coupler devices to perform a S_{11} measurement. The received signals taken at one particular angular direction is then projected over a 2D image taking into account the measured radiation pattern of the antenna (H-plane) over the considered frequency bandwidth (Fig. 3.16e) and the corresponding angular direction. The measurement setup is shown in Fig. 3.22. By means of a multiplicator, -3 dB couplers and harmonic mixers, the setup allows to measure in reflection mode using the same antenna in transmission and reception. The circulator that is required is achieved by means of two -3 dB couplers. When rotating the system, the phase center of the antenna performs a circle with radius 0.3 m around $x = y = 0$ m. The area of interest is decomposed into four different parts as shown in Fig. 3.23, with on the top left part of the image a building, on the top right part of the image is an old tractor. On the bottom right is a fully metallic antenna support. Finally on the bottom left part of the image, close to the building are brushes and tall grass. In Fig. 3.24a and 3.24b are shown the RAR image results and the RAR image results superposed to the Google map picture of the scene. The received data, by using VNA, corresponds to the backscattered signals along the range for each angle step that has been measured. Then, the signals are projected over a Cartesian grid (from a range/theta grid to a x/y grid) to produce the reconstructed image. Because the H-plane radiation pattern of the Fresnel lens is known, the signals are spatially filtered when projected to the Cartesian grid.

3.4 Summary

In this chapter, it has been shown a new process to manufacture Fresnel lenses while maintaining high directivity over a large frequency bandwidth and with high efficiency. Very good radiation patterns are demonstrated with a maximum gain of 38.9 dBi. Such lens has been used in a direct imaging system to produce a radar image of an outdoor environment. However, to produce the radar image, it has been required to mechanically rotate the overall system by 1° step over the 360 °. This mechanically beam scanning cannot be used in a real-time acquisition. In the next chapter, Indirect imaging technique is explained to produce high-resolution images with the capability of real-time acquisitions. As, a high number of Tx and Rx

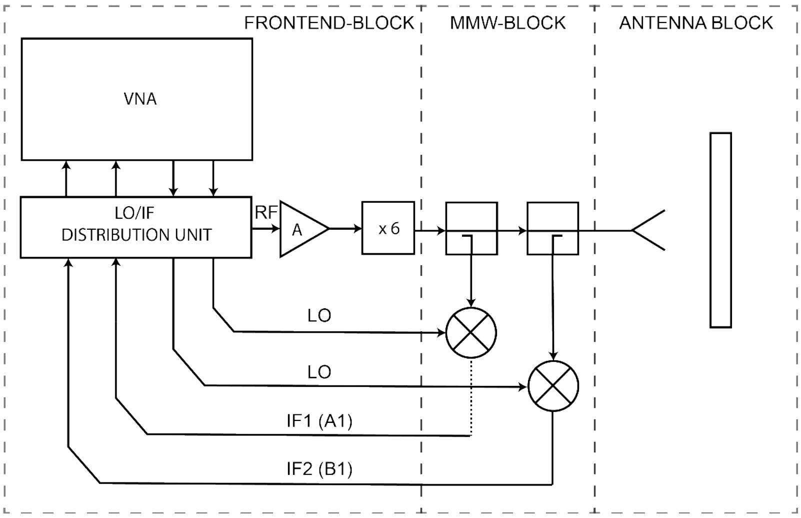

Figure 3.22: Schematic of the measurement setup.

chains is required, in the next chapter are explained solutions to reduce the number of chains while maintaining the resolution.

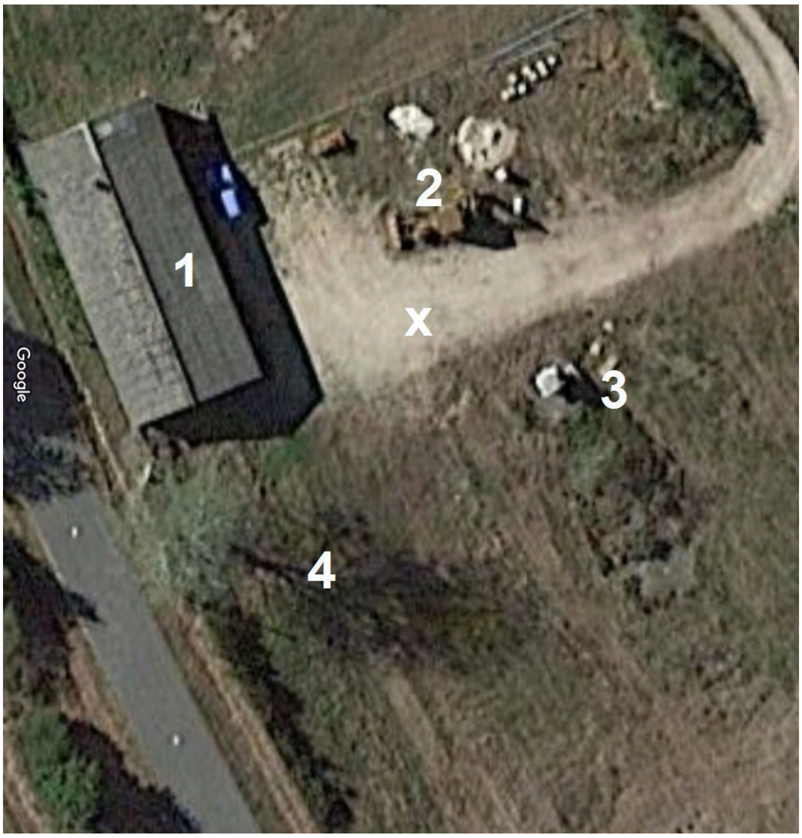

Figure 3.23: Google map of the outdoor scene with (x), the location of the Direct radar imaging, (1), the building, (2), the old tractor, (3), the antenna support and (4) the bruches and tall grass

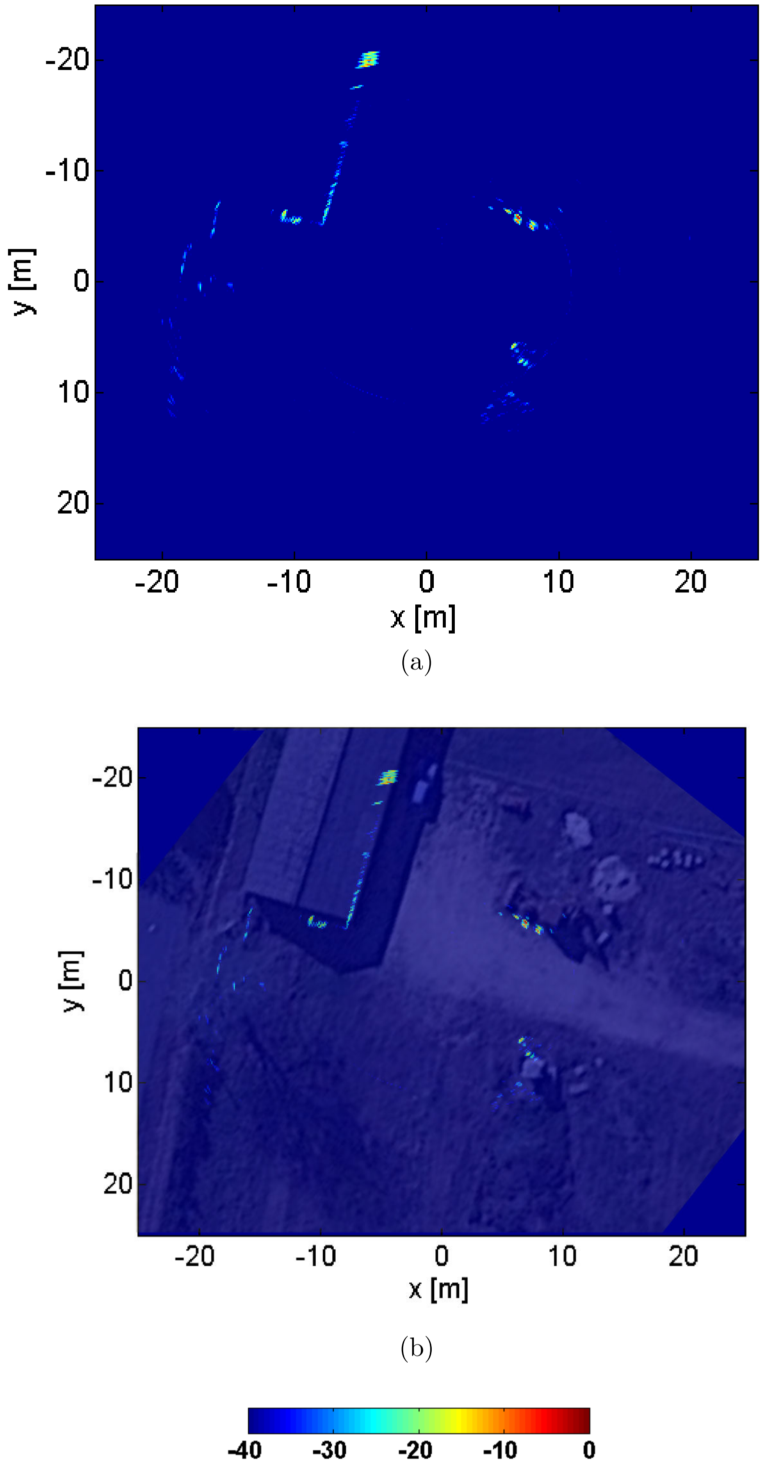

(a)

(b)

Figure 3.24: Measurement results with (a) the RAR image and (b) the RAR image superposed to the Google map picture of the scene.

Bibliography

[1] Wolfgang Menzel, Dietmar Pilz, and Maysoun Al-Tikriti. Millimeter-wave folded reflector antennas with high gain, low loss, and low profile. *IEEE Antennas and Propagation magazine*, 44(3):24–29, 2002.

[2] H. Zucker. Gain of antennas with random surface deviations. *Bell System Technical Journal*, 47(8):1637–1651, 1968.

[3] A. D. Olver. Tolerances on millimetre wave reflector antennas. In *Reflector Antennas for the 90's, IEE Colloquium on*, pages 4–1. IET, 1992.

[4] Donald N. Black and James C. Wiltse. Millimeter-wave characteristics of phase-correcting Fresnel zone plates. *IEEE Transactions on Microwave Theory and Techniques*, 35(12):1122–1129, 1987.

[5] Hristo D. Hristov and Mathieu HAJ Herben. Millimeter-wave Fresnel-zone plate lens and antenna. *IEEE Transactions on Microwave Theory and Techniques*, 43(12):2779–2785, 1995.

[6] Antoine Jouade, Jonathan Bor, Mohamed Himdi, and Olivier Lafond. Millimeter-wave fresnel zone plate lens with new technological process. *International Journal of Microwave and Wireless Technologies*, pages 1–6, 008 2016.

[7] Hristo D. Hristov and José Miguel Rodriguez. Design Equation for Multidielectric Fresnel Zone Plate Lens. *IEEE Microwave and Wireless Components Letters*, 22(11):574–576, November 2012.

[8] J. M. Rodríguez, H. D. Hristov, and W. Grote. Fresnel zone plate and ordinary lens antennas: Comparative study at microwave and terahertz frequencies. In *2011 41st European Microwave Conference*, pages 894–897, Oct 2011.

[9] A. Petosa and A. Ittipiboon. Design and performance of a perforated dielectric fresnel lens. *Antennas and Propagation IEE Proceedings - Microwaves*, 150(5):309–314, October 2003.

[10] Shiyu Zhang. Design and fabrication of 3d-printed planar Fresnel zone plate lens. 2016.

[11] R. Collin. Aperture efficiency for paraboloidal reflectors. *IEEE Transactions on Antennas and Propagation*, 32(9):997–1000, Sep 1984.

[12] P. S. Kildal. Factorization of the feed efficiency of paraboloids and cassegrain antennas. *IEEE Transactions on Antennas and Propagation*, 33(8):903–908, Aug 1985.

[13] J. Ruze. Antenna tolerance theory #8212;A review. *Proceedings of the IEEE*, 54(4):633–640, April 1966.

[14] Andrea Neto, Nuria Llombart, Giampiero Gerini, Magnus D. Bonnedal, and Peter de Maagt. EBG Enhanced Feeds for the Improvement of the Aperture Efficiency of Reflector Antennas. *IEEE Transactions on Antennas and Propagation*, 55(8):2185–2193, August 2007.

[15] CST Microwave Studio. Computer simulation technology. *GmbH, Darmstadt, Germany*, 2009.

[16] Constantine A. Balanis. *Advanced engineering electromagnetics*, pages 234–236. John Wiley & Sons, Hoboken, N.J, 2nd ed edition, 2012.

[17] J. Bor, O. Lafond, H. Merlet, P. Le Bars, and M. Himdi. Technological process to control the foam dielectric constant application to microwave components and antennas. *IEEE Transactions on Components, Packaging and Manufacturing Technology*, 4(5):938–942, May 2014.

[18] Laurent Le Coq, Benjamin Fuchs, Thomas Kozan, Sara Burgos, and Per O. Iversen. IETR millimeter-wave Compact Antenna Test Range implementation and validation. In *2015 9th European Conference on Antennas and Propagation (EuCAP)*, pages 1–5. IEEE, 2015.

Chapter 4

Radar imaging systems: indirect imaging technique

4.1 Introduction

As introduced in Section 2.4.2, Indirect imaging techniques permit to estimate the EM field backscaterred within an area of interest by means of the coherent combination H_{ij} of multiple measurements at different locations (spatially independent conbination). The radar imaging system configuration can be divided into five configurations as shown in Fig. 4.1:

- **Single-Input-Single-Output (SISO) configuration**: Only one pair of transmitting and receiving antennas is used. The configuration is mainly used for range detection or for Real-Aperture-Radar imaging [1] where the spatial filtering is used thanks to the high-directivity radiation pattern of both the transmitting and receiving antennas. It permits to image an area of interest using the scanning process detailed in the Chapter 3.

- **Synthetic Aperture Radar (SAR) configuration**: The pair of transmitting and receiving antennas are mounted on a mobile plateform [2, 3] in order to produce a large synthetic aperture.

- **Single-Input-Multiple-Outputs (SIMO) configuration**: Only one transmitting antenna is used in this configuration [4] and the backscattered received signals is acquired by a (synthetic) array of receiving antennas.

- **Multiple-Inputs-Single-Output (MISO) configuration**: Multiple transmitting antennas are used in this configuration and the backscattered received signals are acquired by only one receiving antenna.

- **Multiple-Inputs-Multiple-Outputs (MIMO) configuration**: Multiple transmitting antennas and multiple receiving antennas are used [5] in this configuration in order to improve the diversity that is required to have a finer spatial resolution.

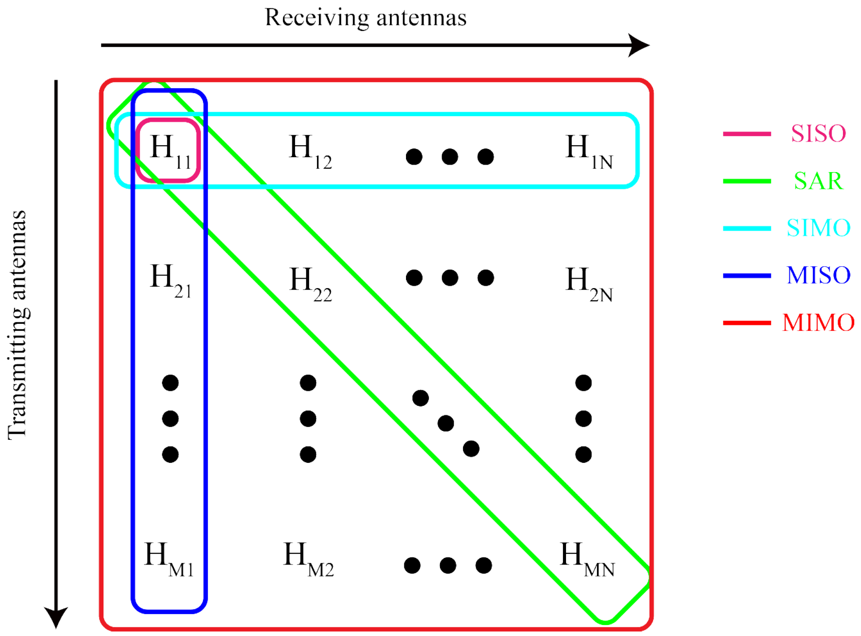

Figure 4.1: The different indirect radar imaging configurations.

The only differences among the configurations are the different angular diversities that are performed. In the SAR configuration, both the transmitting and receiving antennas have the same look angle as respect to a specific target within the area of interest. For the SIMO case, the look angle is invariant for the transmitting antenna while the receiving antennas have different look angles as regards to a specific target location. For the MISO case, the look angle is invariant for the receiving antenna while the transmitting antennas have different look angles as regards to a specific target location. In the MIMO case, the spatial diversity is optimal because the receiving antennas acquired more than the diversity that is performed by combining the SAR, the MISO and the SIMO configuration. The same spatial resolution as the SAR configuration is achieved but with a better Signal-to-Noise ratio thanks to the higher number of transmitting and receiving antennas combination. Such combination is called the virtual array. By combining all the combination, it is possible to generate a virtual array which is larger than the physical array dimension. By fixing the same spatial resolution (same physical or virtual aperture), the use of M transmitting antennas in an array allows to decrease by a factor of M-1 the number of receiving chains as compared to the SIMO case if the location of the transmitting antennas is properly chosen as regards to the location of the receiving antennas in order to avoid redundancy which is interesting when a wide aperture needs to be sampled.

However, in the case where multiple transmitting antennas are used, the transmitting signals must be decorrelated from each other to be properly processed. This is why in practice, the MISO case is not used because it has the same efficiency as the SIMO case while it is required that the transmitting waveforms are fully decorrelated. The decorrelation between the transmitted waveform signals may be performed in various ways [6, 7] with the main ones listed as follow:

- **Time domain** [8, 9]: The transmitted signal from one transmitting antenna shares the time domain with the other transmitting antennas in order to avoid any overlap. Either one transmitting chain is used and the signal is sent to one of the transmitting antennas by means of switch devices (MIMO configuration) or because of the motion of the transmitting antenna in the SAR configuration, there is no correlation between the signals because each transmitting signal is sent within a specific time slot and over a specific spatial location. This is called the Time division multiplexing.

- **Frequency domain** [10]: The signals transmitted by the transmitting antennas are fully decorrelated from each other over the frequency bandwidth either by generating different waveforms (orthogonal independently transmitted waveform) or the frequency bandwidth is divided into smaller sub-bandwidth and allocated to the different transmitting signals. This constitutes the so-called Frequency Diverse Array (FDA).

- **Polarization domain** [11]: It is also possible to use the polarization in order to decorrelate only two transmitting signals.

- **Coding domain** [12]: It is also possible to employ an active phase encoding technique (CDMA) in order to make each signals orthogonal from the others.

The diversity chosen aims to improve one of the characteristics of the auto/cross-correlation function. The auto-correlation corresponds to the ambiguity function [13] of the radar system. It permits to determine the characteristic of the matched filtering function as regards to the kind of waveforms.

Nevertheless, each improvement, of certain criteria lead to the declining quality of other parameters. Using the time domain diversity, it is clear that the acquisitions are not taken at the same time which may impact the result for an area of interest in motion.

Considering the frequency domain technique, the frequency bandwidth is divided in sub-bandwidth, the global range resolution is naturally degraded. However, it is possible to improve the range resolution by exploiting the OFDM signals as in [14, 15]. The polarization domain does not improve the spatial resolution but it provides more information about the area of interest. As compared to the other techniques, the coding domain diversity is of interest because, the transmitting signals are sent through the same area of interest, at the same time and over the same frequency bandwidth. However, it requires complex architectures to ensure the transmitting signals to be decorrelated. Furthermore, depending on the number of frequency bins taken, the number of transmitted signals is limited to ensure great decorrelation between the transmitting signals. Hence, bounds on the achievable decorrelation constrain quasi-orthogonal waveform design and performance.
Given M aperiodic complex sequences of length N_f, the maximum peak auto-correlation (R_{aa}) sidelobe ratio and peak cross-correlation (R_{ab}) response ratio are related via the inequality [16]:

$$\max\left(\mathbf{R}_{aa}, \mathbf{R}_{ab}\right) \geq \frac{(M-1)}{2N_f M - M - 1} \tag{4.1}$$

A MIMO configuration is of great interest because it has the capability to generate a large virtual array from reduced number of transmitting and receiving chains. However, even with a reduced number of transmitting and receiving chains, it is still complex and expensive to realize. In order to fully exploit the MIMO configuration in a straightforward manner, a new way has recently emerged that is the passive compressive device [17–20]. It takes advantage of frequency-diversity inside a cavity, where the fields interfere destructively or constructively to create multiple modes that vary along frequencies. It is a device that allows thanks to its physical properties and its shape to compress the transmitting or receiving signals arriving at each port thanks to the spectral diversity. In the Section 4.3 is presented the theory, simulations and measurements of a Single-Input-Multiple Output configurations where one fixed transmitting antenna is used. In Section 4.4 a study of a Multiple-Input-Multiple-Output configuration is performed where it is presented a passive compressive device working at millimeter wave. The transmitting antennas will be fed by the passive compressive device where only one transmitting chain is used. At the receiving antenna level, an array of stacked patch antennas that are sequentially fed using switch devices is studied.

4.2 Virtual array principle

Considering only point-like targets as backscatterers, the performance of a specific virtual array configuration is usually evaluated in the case where the backscattered EM waves are considered as plane-wave. It means that the targets that backscatter the transmitted EM wave are relatively far from the receiving array to consider that the spherical wave-front is a plane-wave. This is known as the far-field approximation. Using a target located at broadside, a rule of thumb is that the phase variation of the spherical wave from the center of the array to the border of the array does not exceed $\pi/8$ corresponding to a distance variation of $\Delta_\Phi = \lambda/16$. Considering an array of length L, the transition between the near-field and the far-field regions r_0 is determined using the Fig. 4.2 and stated in 4.2.

$$\begin{gathered} r_1 = \sqrt{r_0^2 + (L/2)^2} = r_0 + \lambda/16 \\ \rightarrow r_0 = \frac{2L^2}{\lambda} - \lambda/32 \approx \frac{2L^2}{\lambda} \text{ for } L >> \lambda \end{gathered} \tag{4.2}$$

When a MIMO configuration is used with M transmitting antennas and N receiving antennas, a total of MN channels is processed creating a virtual array of up to $(M \times N)$ receiving elements [21]. The configuration of the virtual array is dependent upon the relative spacing of the transmitting and receiving antenna locations and is defined as the spatial convolution between the transmitting antennas locations and the receiving antennas locations. The performance of a virtual array configuration is evaluated by comparing the half-power beam-width (HPBW), and the side lobes level (SLL) of the array radiation pattern with the achievable HPBW

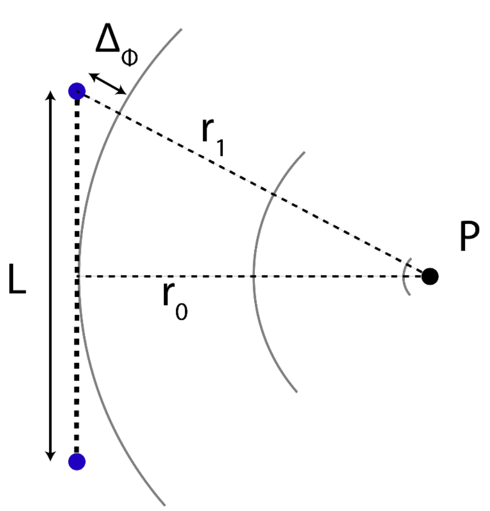

Figure 4.2: Scheme of the Near-field/Far-field transition

and SLL of a uniform amplitude and phase radiating aperture of same dimensions as the virtual array.

The radiation pattern of the array $G(\theta, \phi, \lambda)$ is defined as the product of the element radiation pattern $f(\theta, \phi, \lambda)$ and the array factor $g(\theta, \phi, \lambda)$. The element radiation pattern is given by the intrinsic characteristic of the element antenna used over the (θ,ϕ) direction at a specific wavelength λ. The array factor represents the contribution of all isotropic sources located at the location of the elements inside the array that receive signals from all (θ, ϕ) observation points located in the far-field region (the plane-wave assumption). In a 3-dimensionnal space, the vector $\vec{k}$ defines the observation point direction (Direction-Of-Arrival (DOA)) of the plane-wave toward the array. The vector $\vec{k}$ can be divided into 3 components in which the directions fit the cartesian coordinates system such as:

$$\begin{aligned} \vec{k} &= (\vec{k}_x, \vec{k}_y, \vec{k}_z) = k_x\,\vec{x} + k_y\,\vec{y} + k_z\,\vec{z} \\ &= \frac{2\pi}{\lambda}(\cos\phi\,\sin\theta\,\vec{x} + \sin\phi\,\sin\theta\,\vec{y} + \cos\theta\,\vec{z}) \end{aligned} \tag{4.3}$$

with $k = \frac{2\pi}{\lambda}$ the spatial frequency or the wavenumber directly related to the wavelength λ.
The vector r_n defines the location of the n^{th} element antenna from the center of the Cartesian coordinate by:

$$\vec{r_n} = r_x(n)\,\vec{x} + r_y(n)\,\vec{y} + r_z(n)\,\vec{z} \tag{4.4}$$

Furthermore, it is introduced the excitation of each element that corresponds to the amplitude and phase that is added by digital processing in order to digitally focus the beam in a given direction and to have the capability of using amplitude tapering functions in order to reduce the SLL. The n^{th} excitation I_n is given by:

$$I_n = A_n\,e^{i\alpha_n} \tag{4.5}$$

with A_n is the amplitude and α_n the phase digitally added to the n^{th} element. Using (4.3), (4.4) and (4.5) the array factor is given by:

$$\begin{aligned} g(\theta, \phi, \lambda) &= \sum_{n=1}^{N_a} I_n \, e^{-j \, \vec{k} \vec{r_n}} \\ &= \sum_{n=1}^{N_a} I_n \, e^{-j \, \frac{2\pi}{\lambda}(\cos\phi \, \sin\theta \, r_x(n) + \sin\phi \, \sin\theta \, r_y(n) + \cos\theta \, r_z(n))} \end{aligned} \tag{4.6}$$

with N_a the number of element antenna used in the array. One specific linear combination with coefficients adjusted using the excitation lead to a certain array factor pattern. This is called the digital beamforming. The radiation pattern of the array $G(\theta, \phi, \lambda) = f(\theta, \phi, \lambda) \, g(\theta, \phi, \lambda)$ is used to determine the directivity of the array which corresponds to the ratio between the radiating intensity in a given direction and the radiation intensity averaged over all directions.

The directivity $D(\theta, \phi, \lambda)$ is given by:

$$D(\theta, \phi, \lambda) = 4\pi \frac{|\, G(\theta, \phi, \lambda) \,|^2}{\displaystyle\int_0^{2\pi} \int_0^{\pi} |\, G(\theta, \phi, \lambda) \,|^2 \, \sin\theta \, \mathrm{d}\phi \, \mathrm{d}\theta} \tag{4.7}$$

In the case of a $N_x \times N_y$ planar equally spaced array with N_x the number of elements along the x direction with element spacing Δ_x and N_y the number of elements along the y direction with element spacing Δ_y and with uniform excitation $I_n = 1$ for $n = 1, \cdots, N_x \cdot N_y$.
The array factor is given by:

$$g(\theta, \phi, \lambda) = \frac{\sin(\frac{N_x}{2} \frac{2\pi}{\lambda} \Delta_x \sin\theta \cos\phi)}{\sin(\frac{\frac{2\pi}{\lambda} \Delta_x \sin\theta \cos\phi}{2})} \cdot \frac{\sin(\frac{N_y}{2} \frac{2\pi}{\lambda} \Delta_y \sin\theta \sin\phi)}{\sin(\frac{\frac{2\pi}{\lambda} \Delta_y \sin\theta \sin\phi}{2})} \tag{4.8}$$

Considering only a linear array along the x-axis, with equidistant spacing Δ_x, the location of the n^{th} element is $(n-1)\,\Delta_x$. For the linear array case, only the first component θ is considered with $\phi = 0$. The ϕ-direction is only dependant on the element radiation pattern. The linear array factor is:

$$g(\theta, \lambda) = \sum_{n=1}^{N_x} I_n \, e^{-j \, \frac{2\pi}{\lambda} \sin\theta \, (n-1) \, \Delta_x} \tag{4.9}$$

Considering a uniform amplitude and uniform phase excitation $I_n = 1$, the phase difference between each element is given by $\frac{2\pi}{\lambda} \Delta_x \sin\theta$.
It yields:

$$g(\theta, \lambda) = \frac{\sin(\frac{N_x}{2} \frac{2\pi}{\lambda} \Delta_x \sin\theta)}{\sin(\frac{\frac{2\pi}{\lambda} \Delta_x \sin\theta}{2})} \tag{4.10}$$

It is seen that the array factor has a maximum for $\theta = 0$. However, the array factor also has maximum for other directions when $\theta = \pm \arcsin(m \, \frac{\lambda}{\Delta_x})$ for $m = 1, \cdots, \infty$. In order to avoid any ambiguity area (grating lobes) and to have only one beam within an angular region of interest $(\pm\theta_M)$, the element spacing Δ_x should not exceed a certain distance. In the case where $\Delta_x < \lambda/2$, no grating lobes

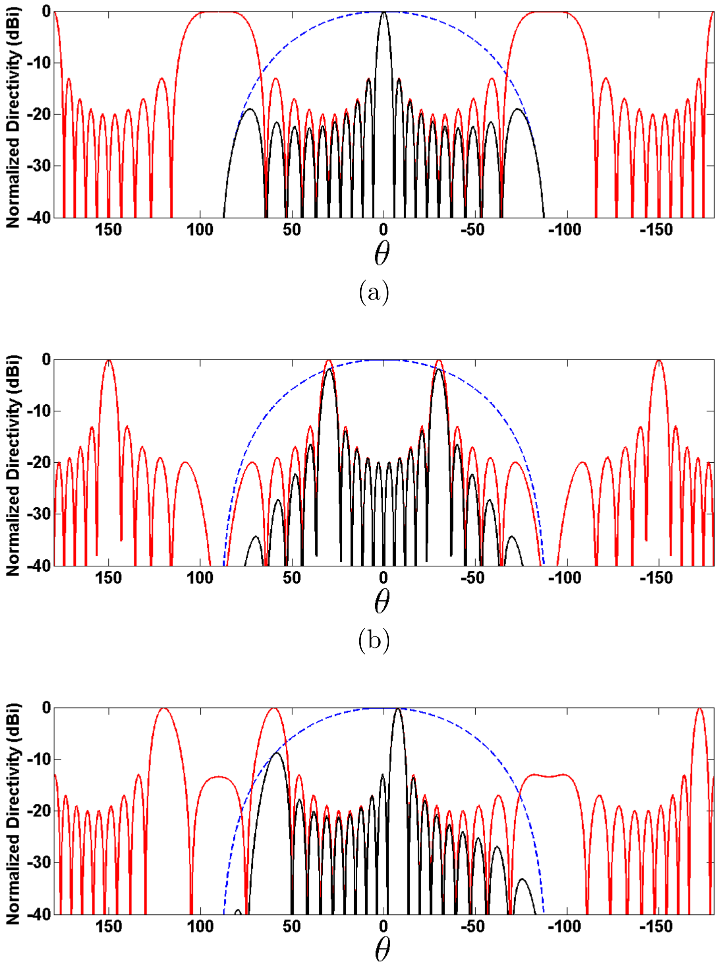

(a)

(b)

(c)

Figure 4.3: Simulated results using a linear array with $N_x = 10$ and $\Delta_x = 1\lambda$, with the dashed blue line corresponding to the element radiation pattern, the red line corresponding to the array factor and the black line the array radiation pattern with a digitally beam scanning (a) $\theta_0 = 0°$ (b) $\theta_0 = 30°$ and (c) $\theta_0 = 60°$.

exist in the visible observation angle region ($\theta \in [-90°, 90°]$).

Because the digital beamforming is a linear combination of all the elements, at some angles, full-constructive interferences (main lobe and grating lobes), constructive interferences (side lobes) and destructive interferences (nulls in the radiation pattern) occur as shown in Fig. 4.4 with an element spacing $\Delta_x = 0.5\lambda$ in Fig. 4.4a, $\Delta_x = 1\lambda$ in Fig. 4.4b and $\Delta_x = 2\lambda$ in Fig. 4.4c.

With the increasing of the element spacing, the HPBW of the main lobes is reduced however the gain is not increased because the power is shared between the main lobe and the grating lobes for the same number of elements.
Thanks to the knowledge of the geometry of the array, it is possible to use the excitation in 4.5 in order to modify the full-constructive interferences in a desired angle. In Fig. 4.3 is shown the digital beamforming variation for $\Delta_x = 1\lambda$ where the beam is digitally scanned at an angle $\theta_0 = 0°$ in Fig. 4.3a, at an angle $\theta_0 = 30°$ in Fig. 4.3b and at an angle $\theta_0 = 60°$ in Fig. 4.3c.

On the array radiation pattern (black line), it can clearly be seen the effects of

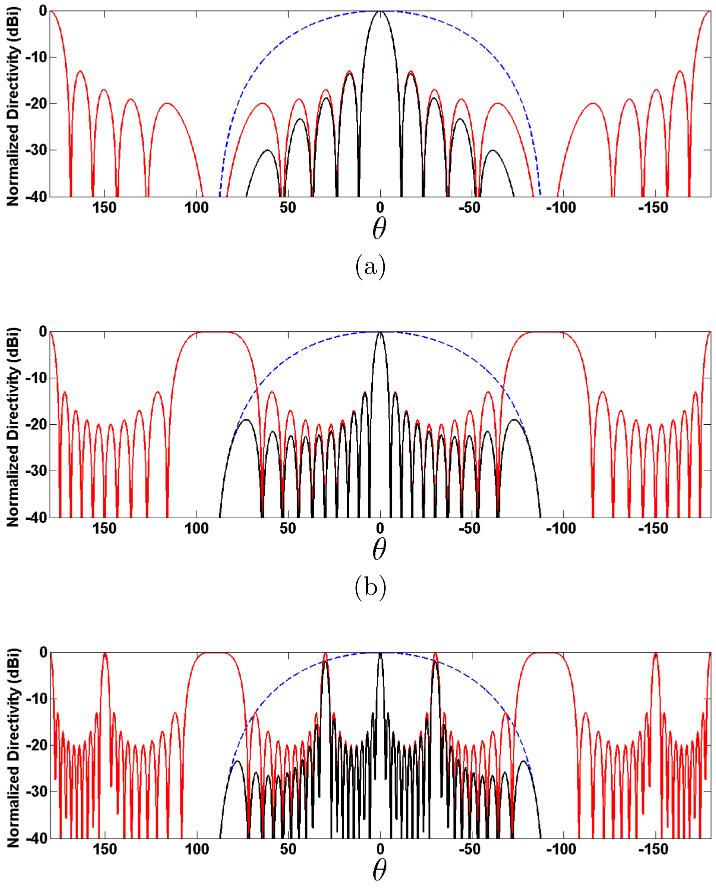

(a)

(b)

(c)

Figure 4.4: Simulated results using a linear array with $N_x = 10$, with the dashed blue line corresponding to the element radiation pattern, the red line corresponding to the array factor and the black line the array radiation pattern with (a) $\Delta_x = 0.5\lambda$, (b) $\Delta_x = 1\lambda$ and (c) $\Delta_x = 2\lambda$.

the grating lobes which implies that the angular region is reduced in order to avoid any grating lobes. Then it is required a more directive element radiation pattern that focuses the main lobe within the desired angular region while removing the grating lobes.

For a scanning angle θ_0, the location of the grating lobes θ_G is given by

$$\sin\theta_G = \sin\theta_0 - p\frac{\lambda}{\Delta_x} \text{ with } p = \pm 1, \pm 2 \cdots \tag{4.11}$$

In the similar manner, it is shown in the $(u = \sin\theta\,\cos\phi, v = \sin\theta\,\sin\phi)$ representation in Fig. 4.5 a rectangular array with $N_x = N_y = 10$ for $\Delta_x = 1\lambda$ and $\Delta_y = 2\lambda$.

For a given linear aperture L, it is possible to reduce the number of elements by increasing the element spacing Δ_x. The resolution of the radar system is maintained while the number of elements is reduced. However, due to the grating lobes effect, the angular region is then reduced.

In order to reduce the number of antennas while maintaining a wide angular region, some studies attempt to modify the location of each element to create a non-uniform array. Many solutions exist such as the Minimum redundancy array, nested array,

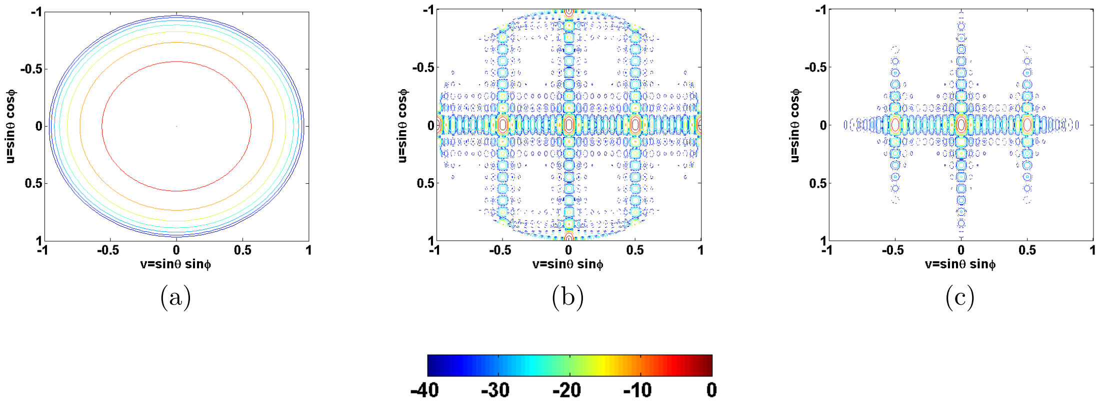

(a) (b) (c)

Figure 4.5: Simulated results using a square array with $N_x = N_y = 10$ and $\Delta_x = 1\lambda$ and $\Delta_y = 2\lambda$, with (a) the element radiation pattern, (b) the array factor and (c) the array radiation pattern.

Co-array or Co-prime array [22–26]. Even if the grating lobes effects are reduced, all the solutions suffers from high SLL due to the array that is not fully-populated. Furthermore, they attempt to create destructive interferences while maintaining the main lobe.

This is mainly why, the MIMO configuration is a great candidate because it allows to create a more populated array from reduced number of transmitting and receiving elements.

The location of the elements of the virtual array is defined as the spatial convolution between the transmitting and receiving antennas location such as:

$$V_a(x,y) = \sum_{m=0}^{M-1}\sum_{n=0}^{N-1} \delta(x-(x_m-x_n), y-(y_m-y_n)) \tag{4.12}$$

with M transmitting antennas and N receiving antennas with (x_m, y_m) the location of the m^{th} transmitting antenna and (x_n, y_n) the location of the n^{th} receiving antenna. $\delta(0,0)$ is the 2D dirac function located at (x=0,y=0).

As an exemple, Fig. 4.6a exhibits a fully-populated virtual linear array with $N_x = 6$ generated by using either 2 transmitting antennas and 3 receiving antennas or using 3 transmitting antennas and 2 receiving antennas, while maintaining the same performances.

In Fig. 4.6b and 4.6c are shown fully-populated virtual arrays with $N_x = N_y = 6$ corresponding to 36 elements generated by a MIMO configuration with either 6 transmitting antennas and 6 receiving antennas or using 4 transmitting antennas associated with 9 receiving antennas. Instead of having one transmitting antenna with 36 receiving antennas, thanks to the MIMO configuration, it is required only 4 transmitting and 9 receiving antennas.

It has been explained the virtual array principle that is going to be used in the following sections. Firstly, the Section 4.3 deals with the SIMO configuration based on an uniform linear array. To have optimal results in the near-field range region, the Section 4.4 only consider the fully populated virtual array for a MIMO configuration.

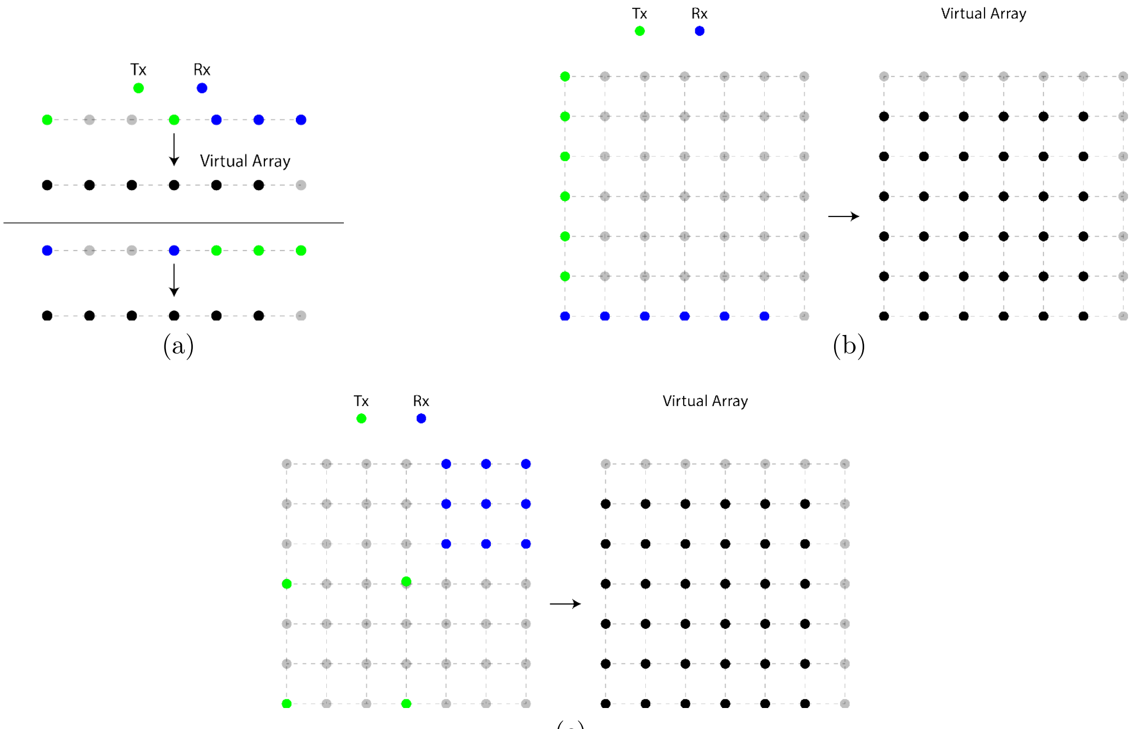

(a) (b) (c)

Figure 4.6: MIMO configuration (Tx: transmitting antenna location and Rx: reiceiving antenna location) used to generate a (a) fully populated linear virtual array, (b) and (c) a fully populated virtual array.

4.3 SIMO configuration

4.3.1 Description

Considering the case where a transmitting antenna is located at a fixed position in a 3-Dimensional spatial space in a Cartesian coordinate system as shown in Fig. 4.7. The location of its phase center is (x_t, y_t, z_t). A receiving (synthetic) array is located over an aperture of length L and aligned with the x-axis. The location of each phase center is (x_a, y_a, z_a) with $x_a \in [-L/2, L/2]$. The radiation pattern of each element is considered as isotropic. We consider N_s point scatterers located in the near-field region which are identified by their Cartesian coordinates (x_i, y_i, z_i). The index i yields for the i^{th} point scatterer P_i. Because the targets are located in the near-field region, the received signals are processed using focusing techniques.

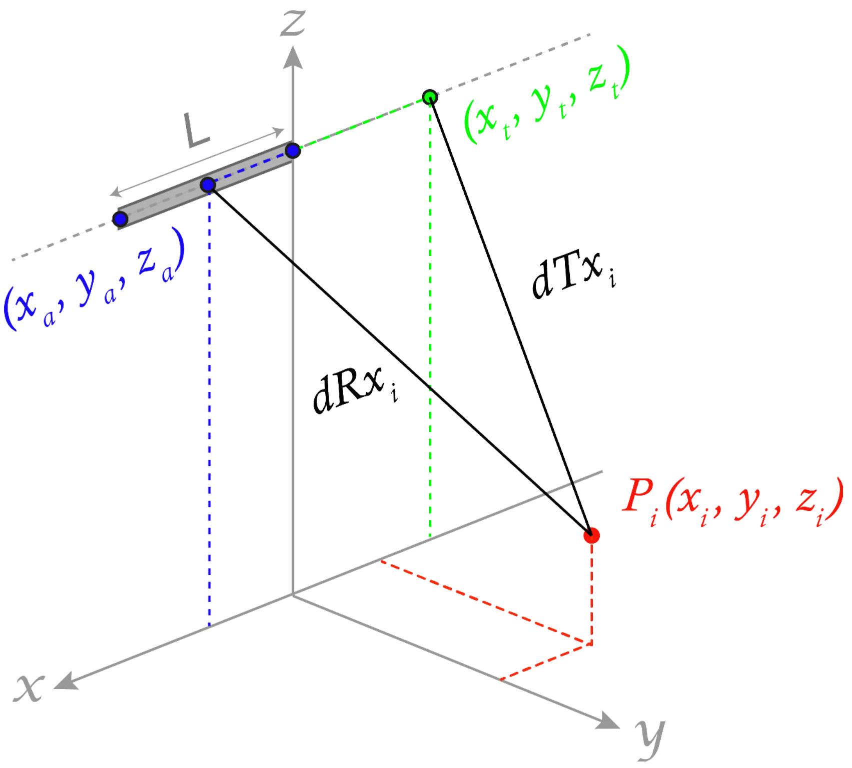

Figure 4.7: Geometry of the radar imaging configuration.

The distance for the wave propagating from the radar to the i^{th} point scatterer is given by:

$$\begin{aligned} d_i(x_a) &= (dTx_i + dRx_i)/2 \\ &= (\sqrt{(x_t - x_i)^2 + (y_t - y_i)^2 + (z_t - z_i)^2} \\ &+ \sqrt{(x_a - x_i)^2 + (y_a - y_i)^2 + (z_a - z_i)^2})/2 \end{aligned} \tag{4.13}$$

A transmitted baseband signal $u(d)$ (see Section 2.3) in the spatial domain with its counterpart in the wavenumber domain $U(k)$ is used, with a frequency diversity over a frequency bandwidth B_f. The signal has been transposed around the carrier frequency f_c before being sent through the medium and $k_c = 4\pi f_c/c$

is the round-trip carrier frequency wavenumber with frequency band wavenumber $k \in [-2\pi B_f/c, 2\pi B_f/c]$.

As the receiving antenna only moves along the x-axis, the received signals along the aperture $S_r(x_a, k)$ in (4.14) are modeled as a sum of transmitted signals that are weighted and delayed. The complex weighting s_i represents all the attenuations that occur during the round-trip propagation and the reflectivity of the i^{th} point-like target. In distributed environments, it is seen as the equivalent of the coherent reflectivity density of the superposition of different contributions of scatterers that are statistically independent. It can also be noticed that the reflectivity may vary along the aperture and over the time. The delays arise from the round-trip distance determined in (4.13). Furthermore, it is added a Gaussian white noise $n(x_a, k) \sim \mathcal{N}_{\mathbb{C}}(0, \sigma^2)$ with zero mean and variance σ^2.

$$S_r(x_a, k) = \sum_{i=1}^{N_s} s_i \, U(k) \, e^{-j(k+k_c)\, d_i(x_a)} + n(x_a, k) \tag{4.14}$$

The received signal after applying the range focusing technique along the aperture $S(x_a, k)$ by adapted filtering [27] is expressed as:

$$\begin{aligned} S(x_a, k) &= S_r(x_a, k) \, U^*(k) \\ &= \sum_{i=1}^{N_s} s_i \, H(k) \, e^{-j(k+k_c)\, d_i(x_a)} + n_f(x_a, k) \end{aligned} \tag{4.15}$$

where $H(k)$, the Fourier Transform of $h(d) = u(d) * u^*(-d)$, is called the range ambiguity function in the wavenumber domain. This function defines the properties of the focused signal. It is characterized by its range resolution (δ_r) that is inversely proportional to the frequency band such as $\delta_r = \frac{c}{2B_f}$. The operators $(\cdot)^*$, $(\cdot)^t$ and $(\cdot)^H$ yield for the conjugate, the transpose and the conjugate transpose operator, respectively. $n_f(x_a, k)$ is the filtered noise by means of the matched filter. In the case where the transmitted signal has a flat spectrum in a frequency band B_f, the range ambiguity function in the spatial domain corresponds to a sinc function.

The received signals in the spatial domain $s(x_a, d)$ after an inverse Fourier transform along the wavenumber domain is expressed as:

$$s(x_a, d) = \sum_{i=1}^{N_s} s_i \, h(d - d_i(x_a)) \, e^{-j\varphi_x(x_a)} + n_f(x_a, d) \tag{4.16}$$

with $\varphi_x(x_a) = k_c d_i(x_a)$ corresponds to the phase variation along the aperture.

The back-projection algorithm is used to generate the focused SAR image from the available received signal in (4.16). The focusing technique is applied when the area of interest is located in the near-field region.

The back-projection algorithm is used to generate the focused SAR image $f(x, y, z = C)$ with C a constant. The projection is performed over a 2D-plane at one particular height from the aperture of receiving antennas. For one particular range cell, it takes the received signal from a given position along the aperture x_a in (4.16), and back-projects it over a spherical arc corresponding to all the possible contributing image pixels. Once the back-projection is performed on the remainder received signals from the other ranges and the others positions along the aperture, then accumulated, the focused SAR image is obtained. One particular pixel p_i of the focused SAR image spanning the Cartesian grid is constructed by:

$$\hat{f}(x_i, y_i, z_i) = \int_{x_a=-L/2}^{L/2} s(x_a, d_i(x_a))e^{jk_c d_i(x_a)}\mathrm{d}x_a \tag{4.17}$$

When the received signals are acquired and sampled, the variable d becomes a discrete vector. Then, it is required to oversample the received data before applying an interpolation (a linear interpolation is sufficient). Finally, it is projected over the SAR image.

4.3.2 Simulations

Considering a radar having a carrier frequency $f_c = 60$ GHz with a frequency bandwidth $B_f = 5$ GHz which provides an emitted power of 0 dBm. This corresponds to a range resolution $\delta_r = 3$ cm. The transmitting antenna is located at the origin of the cartesian coordinate (i.e. $x_t = 0, y_t = 0, z_t = 0$). A receiving (synthetic) array is located over an aperture of length L and aligned with the x-axis. The location of each phase center is (x_a, y_a, z_a) with $x_a \in [-L/2, L/2]$. The aperture is sampled in 100 elements with an element spacing corresponding to half a wavelength ($\lambda/2 = 2.4$ mm) and $L = 237.6$ mm. Both antennas have an isotropic radiation pattern $G_t = G_a = 0$ dBi. In this exemple, there is no noise that corrupts the received signals. In order to simulate targets, it is considered 5 point-like targets with uniform and time-invariant RCSs. For the simulation, it is considered that the weighting s_i is unitary for $i = \{1, \cdots, 5\}$. The location of each target is: $P_1(x_1 = -0.5m, y_1 = +4.75m, z_1 = 0m)$, $P_2(x_2 = +0.5m, y_2 = +4.75m, z_2 = 0m)$, $P_3(x_3 = 0m, y_3 = +5m, z_3 = 0m)$, $P_4(x_4 = -0.5m, y_4 = +5.25m, z_4 = 0m)$, $P_5(x_5 = +0.5m, y_5 = +5.25m, z_5 = 0m)$ as shown in Fig. 2.2a for $z = 0$ m.

In Fig. 4.8a is shown the received signal from the first receiving antenna ((i.e. $x_a = -L/2, y_a = 0, z_a = 0$)) that is back-projected over the SAR image.

In Fig. 4.8b is shown the result after applying the back-projection where the signals coming from each receiving antenna have been back-projected over the SAR image. The five point-like targets are properly discriminated. Nonetheless, the SLL are high then in order to reduce the SLL, amplitude tapering function are applied using a 2D hamming function in Fig. 4.8c and the 2D hanning function in Fig. 4.8d. The SLL are reduced but the spatial resolution has been enlarged.

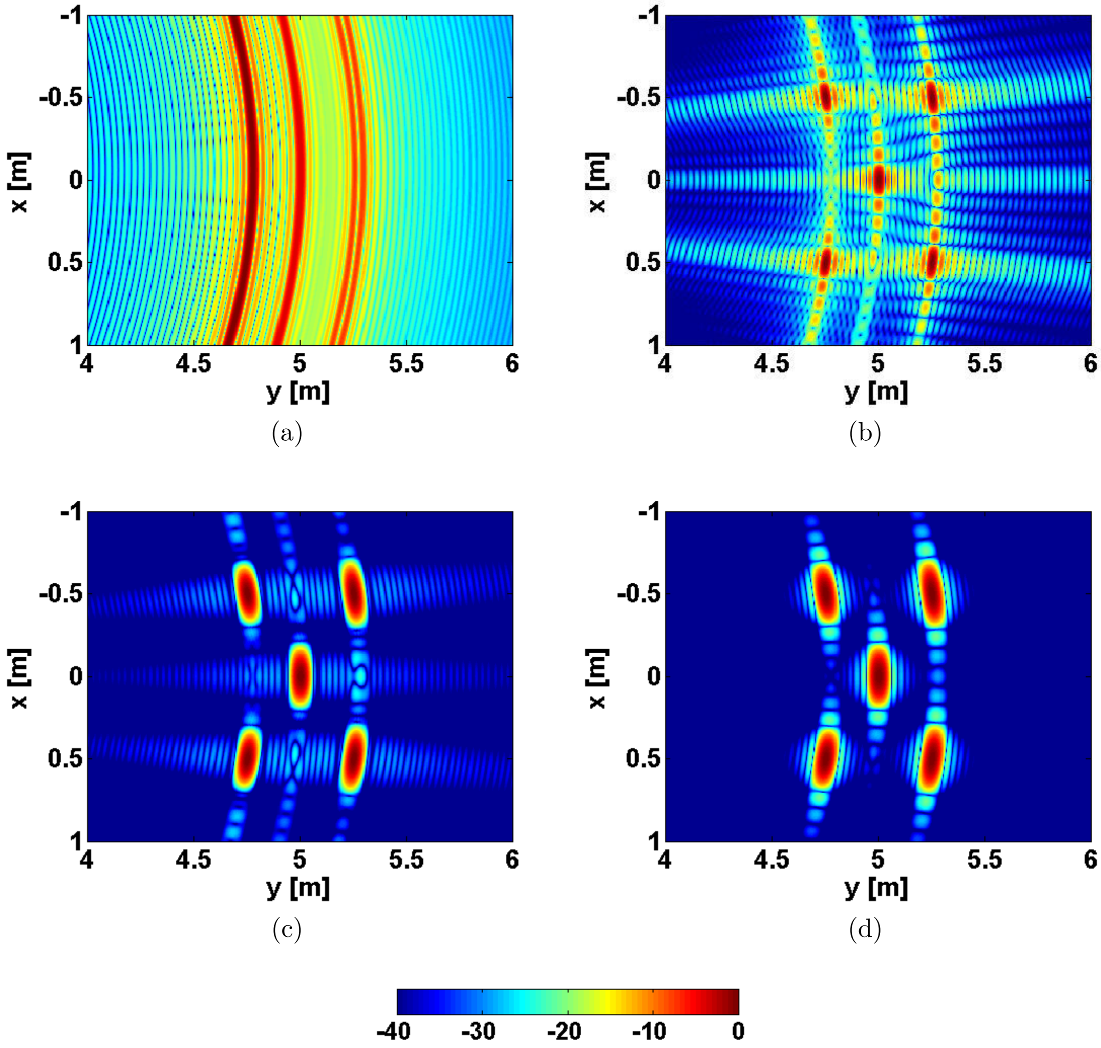

(a) (b)

(c) (d)

Figure 4.8: Simulated result of (a) the back-projected signal of the first receiving antenna, (b), the final SAR image after back-projection, (c) the final SAR image when the 2D Hamming tapering function is applied and (d) the final SAR image when the 2D Hanning tapering function is applied.

4.3.3 Measurements

The measurements are performed in the IETR facility DIADEM (DIagnostic, Analysis and Dosimetry of EM fields). This facility dedicated to ElectroMagnetic imaging is based on a $600 \times 600 \times 600$ mm^3 xyz scanner located in an anechoic chamber. The RF measurement system uses a classical architecture with a VNA (Vector Network Analyzer) and external VDI (Virginia Diodes, Inc) Tx and Rx frequency extenders. A specific measurement set up is developed to have a configuration similar to the simulation's one (Fig. 4.9). In this configuration, the emission part is fixed to illuminate the scene to be imaged with an incident elevation angle of 30°. A horn with a 20 dBi of gain is used as the transmitting antenna. The 300-elements reception array is synthetized moving the RF reception module to 2 mm spaced discrete positions thanks to the scanner. A waveguide antenna with approximatively 5 dBi of gain is used as the receiving antenna. The objects, to be imaged, are settled

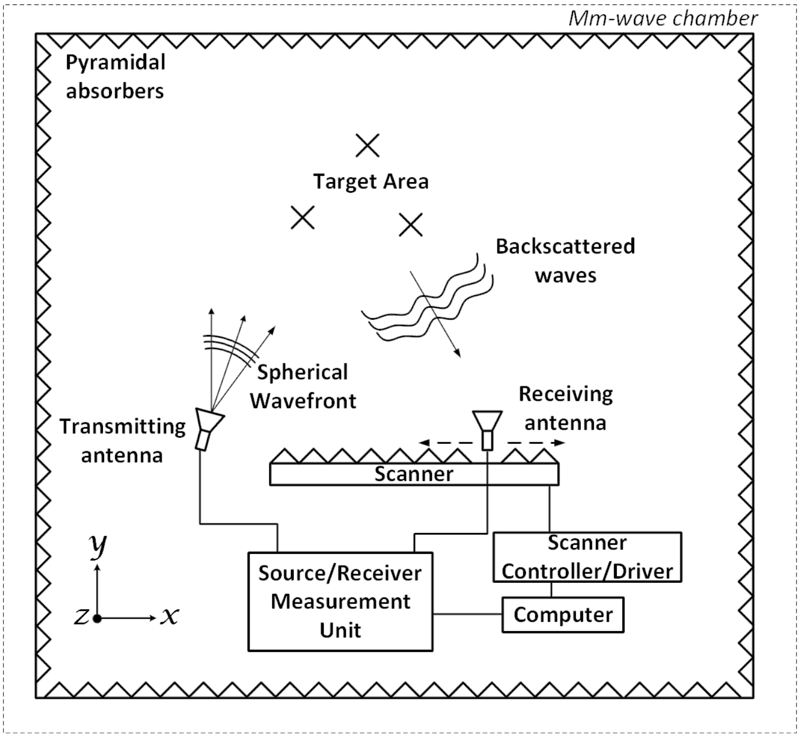

Figure 4.9: Measurement setup.

at 1 m distance on a 1.5 m height foam support. Thanks to this support whose relative electrical permittivity is close to one, the sources of undesired diffraction are minimized and mainly limited to the backscattering of the anechoic chamber. A 20 GHz bandwidth signal with a 50 GHz central frequency is used for all the tests. To speed up the acquisition of the 1001 frequency points obtained for each reception position, an IF Filter of 100 kHz is applied. It has to be noticed that even if the IF filter is broadband, the dynamic range provided by the VDI modules is high enough for the purposes of these tests. In such a configuration, a maximal range resolution of 7.5 mm can be obtained, with an azimuth angular resolution of 0.57° corresponding to a 1 cm cross-range resolution at 1 m range distance. Moreover, the 7.5 m ambiguous distance, longer than the anechoic chamber length, enables to compensate the chamber backscattering in an efficient way. Considering the 30° elevation orientation of the emission part, the ground range resolution is limited to 8.7 mm.

Three complex examples of targets that have been imaged are reported in Fig. 4.10: a canonical point scatterers scene made of dozen of 5mm diameter bolts positioned with a 10 mm spacing to write the word ‘IETR’; a realistic scene with a screw clamp; a realistic scene with a 1 mm blade stainless steel knife hidden inside a book. A SAR image is realized from the backscattered signals of the three scenes applying the back-projection algorithm as shown in Fig. 4.11.

Close observation reveals that the millimeter-wave frequencies are approriate for small objets imaging application such as concealed object under clothes for instance. However, to come closer to optical image, it would be preferable to work at higher frequencies. In fact, thanks to the smaller wavelength, the diffuse reflection becomes

(a) (b) (c)

Figure 4.10: Picture of the three scene configurations with (a) 50 bolts of 5mm diameter configured to spell IETR,(b) a screw clamp, and (c) a knife hidden inside a thick book.

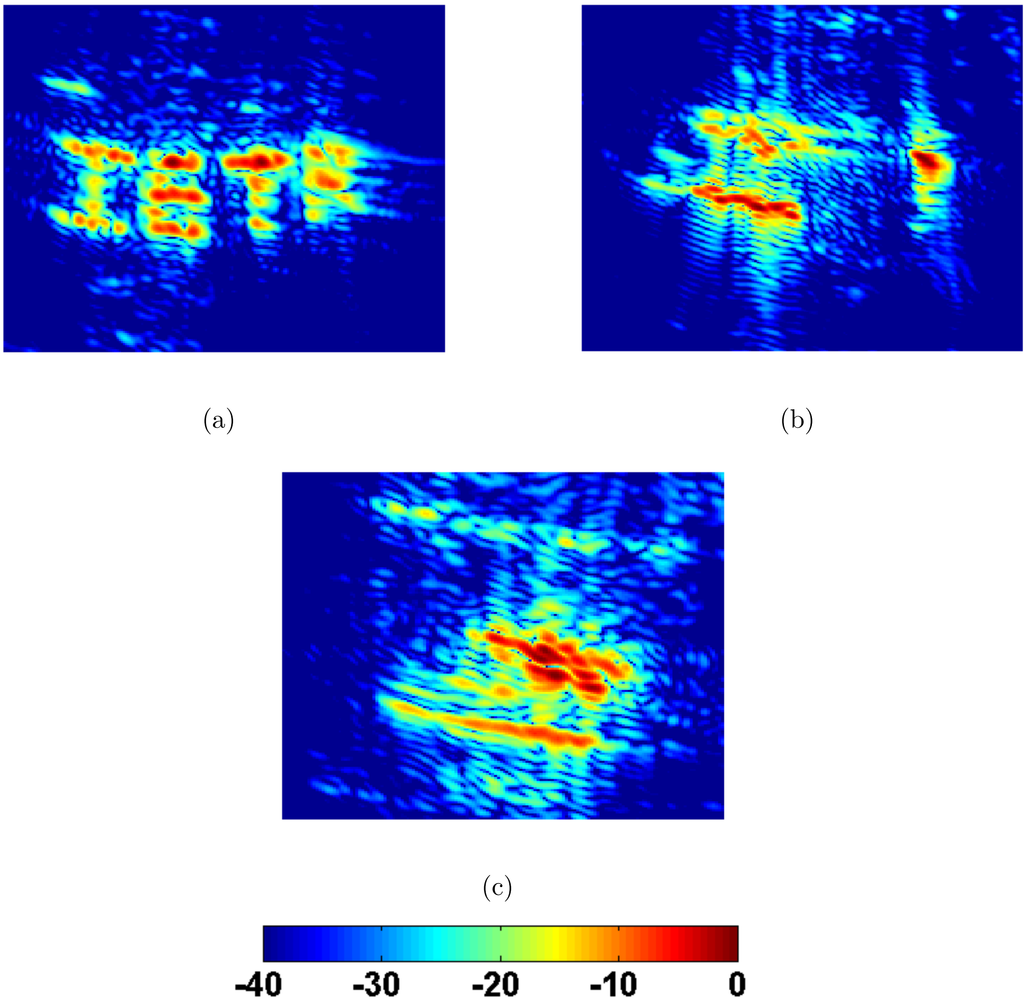

(a) (b)

(c)

Figure 4.11: SAR image results considering the scene with (a) bolts configured to spell IETR, (b) the screw clamp and (c) the knife hidden in a book.

higher as compared to specular reflection (like a mirror). The frequency band available at those frequencies is sufficient (higher than 4 GHz), however, to obtain high resolution images, it requires a large number of receiving antennas and associated modules which lead to a costly and complex technology. To reduce the complexity and the cost, a MIMO configuration using passive compressive device is investigated in the next section thanks to the virtual array principle.

4.4 MIMO configuration

A MIMO configuration is used to improve the spatial resolution while maintaining low the number of elements. To further reduce the number of element, a passive compressive device is used to even more reduce the number of elements.

4.4.1 Passive Compressive Device (PCD)

A new way, which has recently emerged, is the PCD. It takes advantage of the frequency-diversity inside a cavity, where the electromagnetic (EM) fields interfere destructively or constructively to create multiple modes, which vary with frequency. Two slightly different configurations can be dissociated. First, the modes are used to excite independent sources (slots, holes...) to produce distinct mode patterns as a function of frequency [28–32]. The distinct modes patterns generate spatial diversity required to reconstruct the image. However, a complete characterization of the aperture field distribution is necessary by using near-field scanning measurements [33]. In such a case, both the radiating elements and the cavity are used to reconstruct the image. The second configuration is to have multiple input ports and multiple output ports on the cavity's surface. Each port may be a coaxial connector or a waveguide port, that allows for a direct measurement of the complex transfer function along the frequency from one input to one output port by using a VNA. Finally, the ports are connected to antennas where their properties (locations, types, directivities, polarizations...) may be modified as desired without changing the overall system configuration [17–20]. The latter configuration is the one used in our study thanks to its capability to be used in various radar imaging configurations. Hence, it is a $N \times M$ passive device that allows for the compression, at the RF level, of N signals into M signals or M signals into N signals either for the reduction of the number of Tx chains in a MISO or MIMO configurations or for the reduction of the number of Rx chains in a SIMO or MIMO configurations. Furthermore, multiple PCDs may be used simultaneously. The correlations between the compressed signals are mainly dependent on the size and the shape of the device. Nonetheless, if used in transmission, the main drawback of using a PCD is that the limited transmitted power is shared among the output ports, implying a reduction of the range of detection. However, amplifiers may be used to counter the attenuations. Further, the transmitted powers delivered at the input ports are, in fact, shared among the output ports but also shared with the input ports. The power received by the input ports have to be considered as losses. Such a PCD has, by essence, low efficiency. But, these drawbacks have to be compared with the capability of the device to reduce the number of Tx and Rx chains, which maintains a great interest, particularly at millimeter-wave because it permits to have a cavity size at an acceptable level with a great compression thanks to the small wavelength at these frequencies.

The $N \times M$ compressive device with N inputs and M outputs can be used among numerous of radar configurations. Few of them are listed below:

- MIMO radar either in transmission or reception or both in the same time [34]. It can perform a uniform or a non-uniform array depending on the location of each port.

- Synthetic Aperture Radar (SAR) [35] or Multi-beam SAR configuration [36, 37] if the antennas at each output port are looking at different angles.
- Moving Target Identification (MTI) in a SAR configuration [38, 39] if the output ports are regularly placed in the along-track direction (Multi-channel SAR MTI by using either Displaced Phase centre Antenna (DPCA), Along track interferometry (ATI) or Space time adaptive processing (STAP)).
- Interferometry SAR (In-SAR) [40, 41] for tomography purpose if the output ports are placed along the elevation direction.
- Polarimetry SAR (Pol-SAR) [42] if the output port polarizations are alternatively changed.

In Section 4.4.1.1 are detailed the PCD and the associated antennas. In Section 4.4.1.2 is shown in two manners, how it is possible to measure the transfer functions by using classic Port-to-Port measurements thanks to a VNA or by estimating the transfer functions from measurements performed in a Compact Antenna Test Range (CATR) where the plane-wave assumption is considered. To validate the two methods, the PCD is used in a MIMO configuration in Section 4.4.2 to analyze the point spread function resolution from measurements and compared to a Single-Input-Multiple-Output (SIMO) configuration with a synthetic aperture length of the same size as the virtual array length generated by the MIMO configuration.

4.4.1.1 Details of PCD and associated antennas

From [43], if a cavity is excited by a sufficiently high number of frequency bins over a wide frequency bandwidth and if the cavity is big enough in terms of wavelength, it exhibits spatial and spectral statistical behaviours very close to the random theory thanks to the large number of modes that are present inside the cavity. For an asymmetric cavity, the fluctuation of the combination of all the modes (i.e. mode diversity) along the frequency increases as the number of modes increases (larger cavity dimension). By minimizing the number of outputs, the different scattering paths length inside the cavity increases, which in turn, leads to an increased mode diversity. If the transfer functions are known, the PCD permits to modulate, by different series of orthogonal waveform, the signal at each output, so that these signals can be separated in post-processing. Then, the transfer functions, which corresponds to each channel, satisfy the orthogonality requirement.

To maintain the power at an acceptable level, at the outputs of the device, we choose to use a 1×4 PCD with output ports that perform a uniform linear array (see Figs. 4.12 & 4.13).

In a 3-Dimensional spatial space, a transmitting antenna is located at a fixed position. The location of its phase center, aligned with the x-axis, is (x_t, y_t, z_t). The PCD is used as the receiving part with $M = 4$ linearly spaced receiving antennas. The phase centers are aligned with the x-axis and with an element spacing of Δ_x. Their locations are (x_a, y_a, z_a) with $\{x_a(m) = -\Delta_x \cdot (M-1)/2 + (m-1) \cdot \Delta_x\}_{m=1}^{M}$. It is considered N_s point scatterers identified by their Cartesian coordinates (x_i, y_i, z_i).

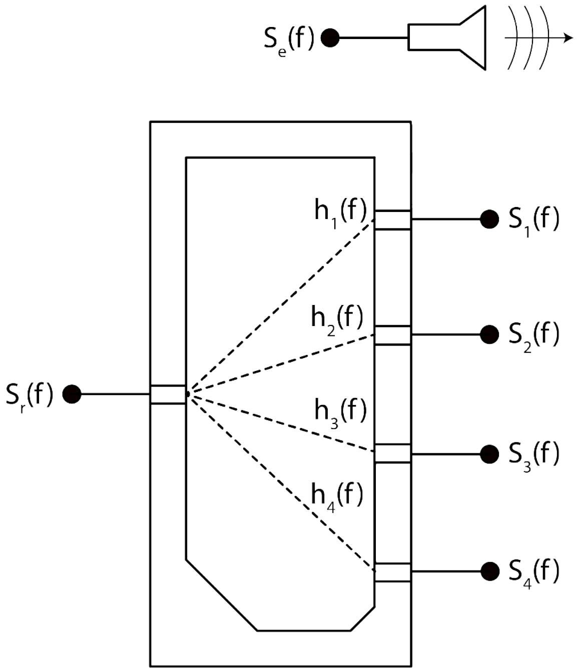

Figure 4.12: Cutting view drawing of the 1x4 passive device with associated transfer functions

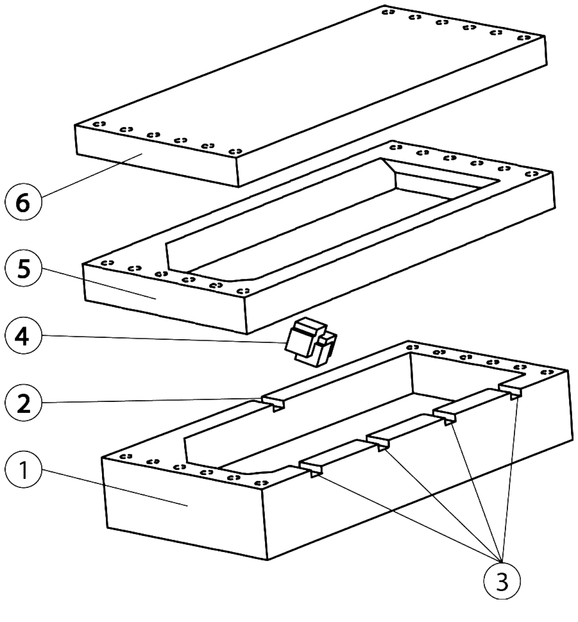

Figure 4.13: Exploded view drawing of the passive device with 1) the lower part with 2) the input and 3) the output ports. In 4) the diffractive element at the center of the cavity and in 5/6) the upper parts to close the cavity.

The index i yields for the i^{th} point scatterer P_i. The equivalent distance for the wave that propagates from the m^{th} receiving antenna of the PCD to the point scatterer P_i is given by:

$$\begin{aligned} d_i(m) &= (dTx_i + dRx_i(m))/2 \\ &= (\sqrt{(x_t - x_i)^2 + (y_t - y_i)^2 + (z_t - z_i)^2} \\ &+ \sqrt{(x_a(m) - x_i)^2 + (y_a - y_i)^2 + (z_a - z_i)^2})/2 \end{aligned} \tag{4.18}$$

A RF stimulus signal ($S_e(f)$) is transmitted with a frequency diversity over a frequency bandwidth B_f. Prior to being sent through the medium, the signal has been transposed around the carrier frequency f_c. The backscattered received signals, at the output of the PCD, are modeled as a sum of transmitted signals that are weighted and delayed. The complex weighting s_i represents all the attenuations that occur during the round-trip propagation and the reflectivity of the i^{th} point scatterer P_i. The delays arise from the round-trip distances determined in (4.18). Once the signals have been received by the receiving antennas (output ports), they are transmitted inside the PCD (i.e. the cavity) to be received by the input port. The propagation inside the PCD from the m^{th} output port to the input port corresponds to a multiplication, in the frequency domain, between the receiving signals $S_m(f)$ and the m^{th} transfer function $\dot{h}_m(f)$.
We consider $\dot{h}_m(f)$ as the transfer function along the entire frequency spectrum. Furthermore, $n(f) \sim \mathcal{N}_{\mathbb{C}}(0, \sigma^2)$ being a Gaussian white noise with zero mean and variance σ^2. The received signals at the input port of the PCD can be modeled as:

$$\begin{aligned} S_r(f) &= \sum_{m=1}^{M} \dot{h}_m(f) \cdot S_m(f) + n(f) \\ &= \sum_{m=1}^{M} \dot{h}_m(f) \cdot \sum_{i=1}^{N_s} s_i \, S_e(f) \, e^{-j4\pi(f+f_c)\, d_i(m)/c} + n(f) \end{aligned} \tag{4.19}$$

with c being the speed of light. A transmitted signal $S_e(f)$ is considered with a flat spectrum over a limited frequency bandwidth B_f. This corresponds to a rectangular function with a unitary amplitude over the frequency bandwidth B_f and zero elsewhere. By using $h_m(f)$ as the transfer function along the limited frequency bandwidth, yield the following:

$$h_m(f) = S_e(f)\dot{h}_m(f) = \frac{1}{B_f}\, \mathrm{rect}(\frac{f-f_c}{B_f})\, \dot{h}_m(f) \tag{4.20}$$

By adding (4.20) into (4.19), this gives:

$$S_r(f) = \sum_{m=1}^{M} h_m(f) \cdot \sum_{i=1}^{N_s} s_i \, e^{-j4\pi(f+f_c)\, d_i(m)/c} + n(f) \tag{4.21}$$

In the presence of additive stochastic noise, the matched filter is the optimal filter for maximizing the signal-to-noise ratio [27]. Then, on the received signal, are applied 4 different matched filters to extract the received signals that have been acquired by the four output ports. If the transfer functions $h_m(f)$ are known, the received signals that come from the m^{th} output port are extracted by matched filtering as shown in (4.22).

$$\begin{aligned} S_m(f) &= S_r(f)\, h_m^*(f) \\ &= h_m(f)\, h_m^*(f) \cdot \sum_{i=1}^{N_s} s_i \, e^{-j4\pi(f+f_c)\, d_i(m)/c} \\ &+ \sum_{\substack{l \neq m \\ l=1}}^{M} h_l(f)\, h_m^*(f) \cdot \sum_{i=1}^{N_s} s_i \, e^{-j4\pi(f+f_c)\, d_i(l)/c} \\ &+ n_{fi}(f) \end{aligned} \tag{4.22}$$

The first term is the useful received signal and the second term is the cross-correlation with the other ports, $n_{fi}(f) = n(f)\, h_m^*(f)$ being the filtered white noise by means of the matched filtering. In the perfectly orthogonal case where the transfer functions are uncorrelated, the second term vanishes.

The key factor is to manufacture a PCD whose transfer functions are relatively well decorrelated with each others to be discriminated. The optimized PCD has an overall dimension of 115 mm length by 55 mm width by 35 mm height ($23\lambda \cdot 11\lambda \cdot 7\lambda$ at 60 GHz) where $\lambda = c/(f + f_c)$ is the wavelength. It is made of aluminium with the walls thickness of 7.5 mm. The cavity is excited by a standard V-band waveguide (WR-15) for an operating frequency bandwidth from 50 to 66 GHz. From Fig. 4.13, some of the vertical and horizontal corners are bended in such a way to avoid any symmetry inside the cavity. Further, a diffractive element is located at the center of the cavity. It is composed of three $0.75 \times 0.75 \times 0.75$ mm^3 cubes that are overlapped and slithly displaced from each other along the three dimensions. The element provides sharpe edges that allows the incoming wave to be diffracted. It is used to decrease the level of the reflection coefficient at the input port because the wave is diffracted in all the directions. Furthermore, it is used to improve the spectral statistical behaviours of the cavity allowing a better decorrelation between the transfer functions. One of the corner of the diffractive element is welded at the bottom of the cavity.

There are four output waveguide ports placed to have a uniform linear array with an element spacing of 25 mm (5 λ at 60 GHz). A non-linear array may be preferable to decrease the correlation between each port. Nevertheless, the linear array has been chosen to be used in a MIMO configuration, for creating a fully populated virtual array. The output ports have the same vertical polarization as the input port polarization. The element spacing and the cavity dimensions have been chosen to be able to connect at each output a round flange waveguide of diameter 19 mm. It is used to measure the transfer function of each channel. The realized PCD is shown in Fig. 4.14a. The 13 screws are used to attach the different parts and to minimize the presence of air gaps.

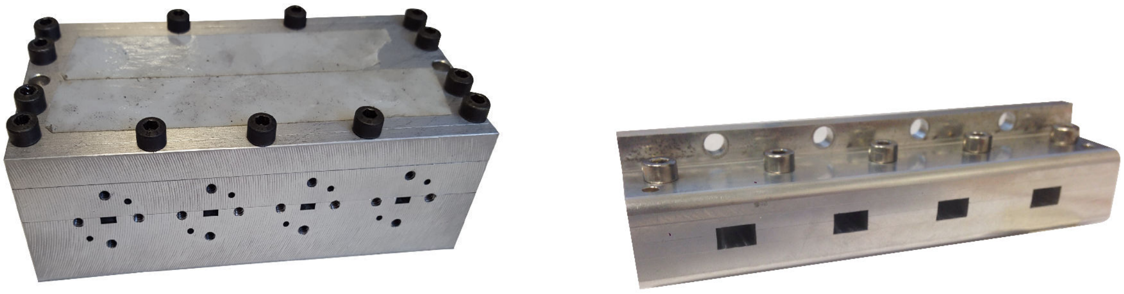
(a)

(b)

Figure 4.14: Photography of (a) the output face of the realized passive compressive device, which works at millimeter-wave, and (b) the output face of the horn antenna module.

A horn antenna module (see Figs. 4.14b & 4.15), made of aluminium, is attached at the output of the PCD to focus slightly the beams in a limited angular sector. Four similar horn antennas are used with a 8×5 mm^2 aperture size and with a horn length of 10 mm. The reflection coefficient of each port is lower than -15 dB and the coupling between the ports is lower than -55 dB over the frequency range. In Figs. 4.15b & 4.15c are shown the measured radiation patterns of the first horn fixed to the first port of the PCD along the E-plane and H-plane, respectively. The gain of the antenna varies from 11 to 15 dBi in the frequency range (50 to 66 GHz). Along the E-plane, the Half-Power Beam Width (HPBW) varies from 60° to 50° over the frequency range. Along the H-plane ($G(\theta, f)$), the HPBW varies from 48° to 38° over the frequency range. The sidelobe level (SLL) is lower than -40 dB for the H-plane and lower than -25 dB for the E-plane.

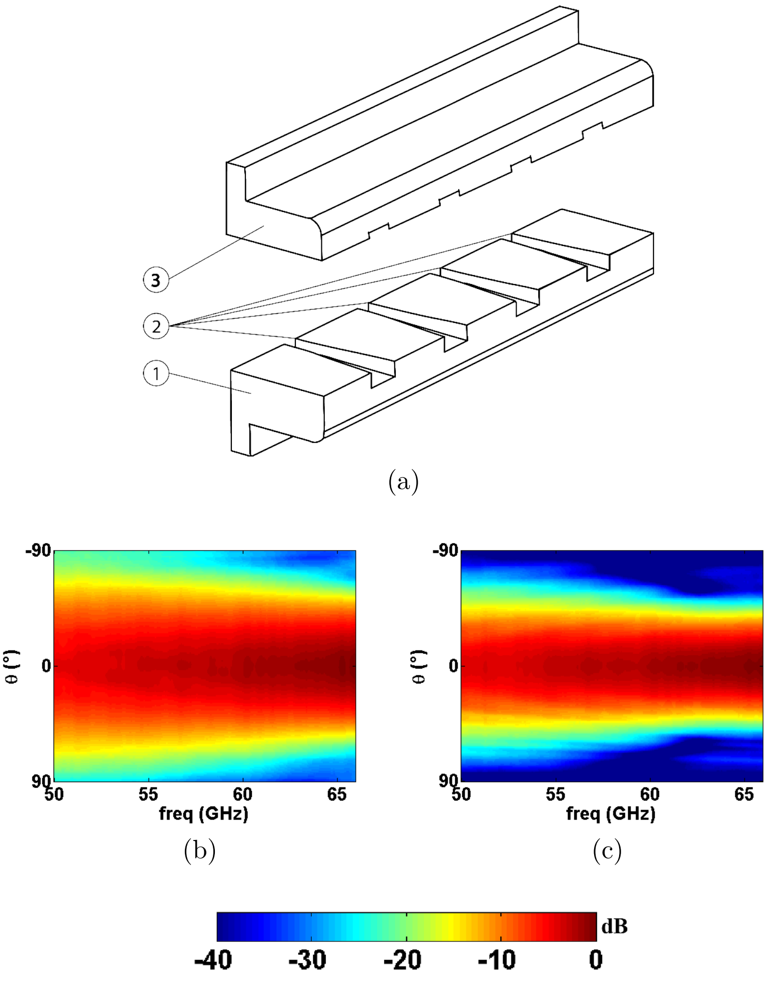

(a)

(b)

(c)

Figure 4.15: Details of the antenna module with (a) Exploded view drawing of the horn antenna module with 1) the lower part, 2) the input ports attached to the output ports of the passive compressive device and (3) the upper part. The measured radiation pattern of the first port along (b) the E-plane Co-polar and (c) H-plane Co-polar ($G(\theta, f)$).

4.4.1.2 Direct Port-to-Port measurement of the PCD using a Vector Network Analyzer

The knowledge of the transfer functions is needed to decorrelate the received signals. For a low number of ports, it is possible to individually measure each transfer function using a 2-ports Vector Network Analyzer (VNA). A full-port calibration is performed. The first port of the VNA is connected to the input port of the device. The latter port of the VNA is connected to the m^{th} output port of the device and loaded waveguides are attached to the other ports. Measuring the complex transmission coefficient gives the transfer function of the m^{th} port. Because, it is required a wide frequency bandwidth to give a full compression capability to the passive compressive device, the transfer functions are measured from 50 to 65.998 GHz with a frequency step of 80 MHz corresponding to 2001 frequency bins. The measured magnitude of the transfer functions along the frequency band are shown in Fig. 4.16. The spectral statistical behaviours of the transfer functions seem to be very close to a random process.

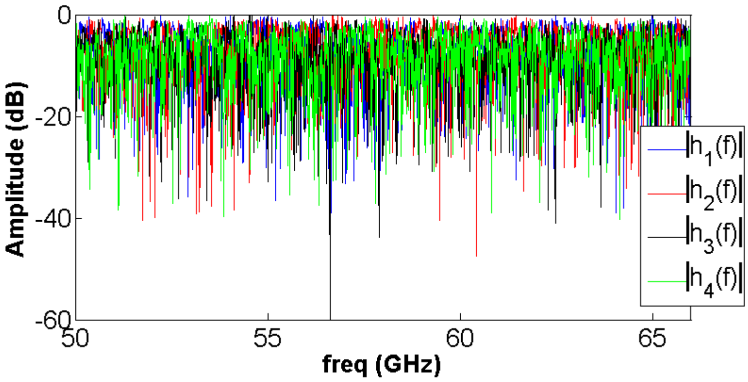

Figure 4.16: Absolute value in dB of the measured transfer functions by means of a VNA along the frequency band.

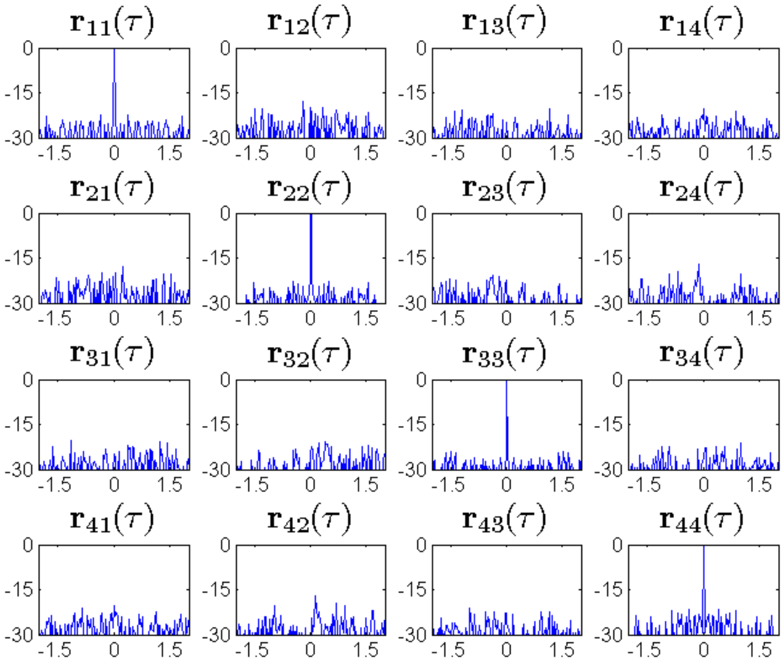

Figure 4.17: The auto/cross-correlation results, $\mathbf{r_{ij}}(\tau) = DFT^{-1}[h_i(f)h_j(f)^*]$, between the measured transfer functions (VNA measurements), with the time domain τ (ns) along the horizontal axis and the normalized amplitude (dB) along the vertical axis. It is normalized by the maximum peak of the auto-correlation fonctions. DFT^{-1} yields for the inverse discete Fourier transform.

In Fig. 4.17, are shown, along the diagonal, the autocorrelation of each measured transfer function ($\mathbf{r_{ij}}(\tau)$ for $i = j$), and above and below the diagonal, are shown the mutual cross-correlation between each port. Over the cross-correlation results, the highest measured peak reaches -15.5 dB as compared to the measured autocorrelation functions. The peak side lobe ratio (PSLR) [44] of the autocorrelation levels is lower than -20 dB from the main lobe peaks and with an integrated side lobe ratio (ISLR) [44] lower than -14.7 dB. To be improved, it would be required to enlarge the cavity size, however, it seems to be a good compromise between the cavity size and the cross-correlation results. The power efficiency η of the PCD is shown in Fig. 4.18. The power efficiency ($\eta(f) = 10\log_{10}(\sum_{m=1}^{4}|h_m(f)|^2)$), has a mean value of -5.17 dB, also named as the average radiation efficiency and is controlled by the reflection coefficient at the input port and the losses that occur inside the cavity because of the multiple reflections on aluminium walls.

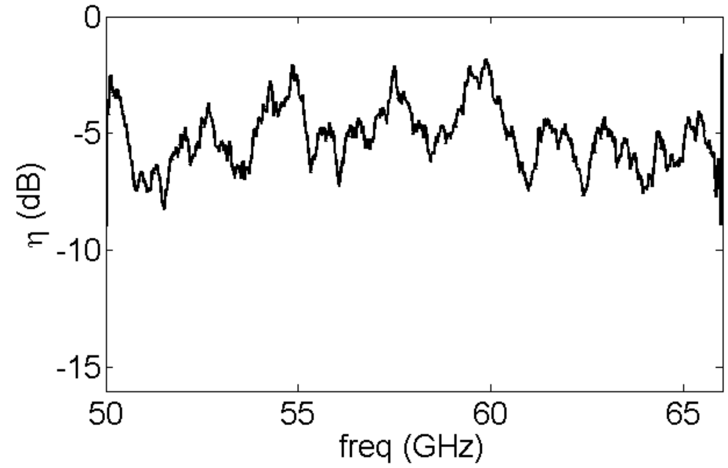

Figure 4.18: Measured power efficiency of the passive device corresponding to the outgoing powers from the four ports versus the incoming power along the frequency.

However, if the inter-element distance between the ports is lower than the diameter of the waveguide flange (19 mm in the case of the WR-15), measurements of the transfer functions are no longer possible. Furthermore, the loads used are not perfect which leads to a portion of the signals that arrive at the loads to be reflected back inside the cavity. Such behavior may cause errors when measuring the transfer functions. In addition, when a high number of ports are needed, it can become complex to measure individually each transfer function.
One solution is to perform a near-field scanning measurements to retrieve the transfer functions. However the probe and the scanning system used may interact with the PCD, leading to measurement errors. The next Section, presents a procedure that allows for the estimation of the transfer functions of a ($N \times M$) PCD. The procedure is tested on the fabricated (1×4) PCD.

4.4.1.3 Estimating transfer functions using Compact Antenna Test Range measurements

The measurements are performed in the Compact Antenna Test Range (CATR) IETR facility [45]. The RF measurement system uses a classic architecture with a

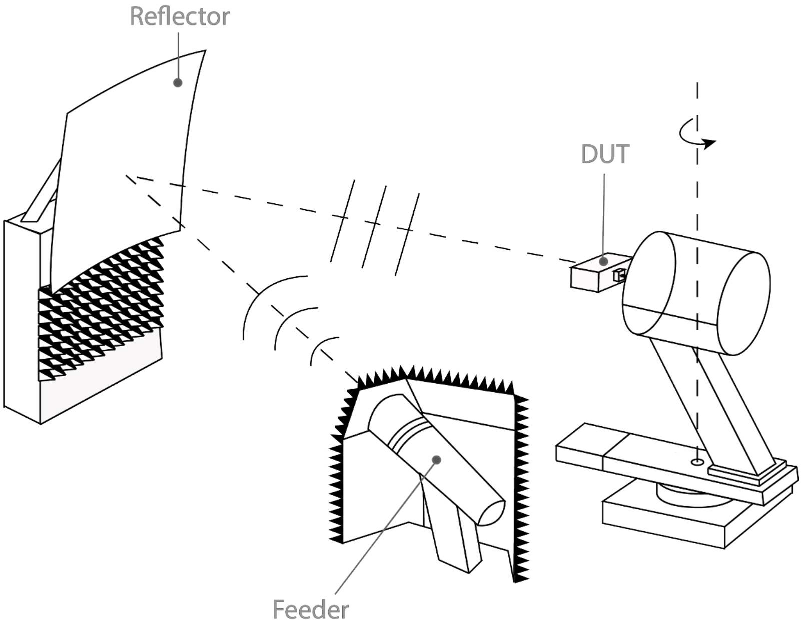

Figure 4.19: Setup measurement using a Compact Antenna Test Range.

VNA and external VDI Tx and Rx frequency extenders. It is dedicated to measure high gain antennas at a short distance thanks to the capability of a reflector to create a quiet zone at a fixed range of diameter 600 mm with a depth cylinder of 600 mm. Inside the quiet zone, the amplitude of the electric field is considered as uniform and the plane-wave assumption can be used. Figure 4.19 shows the measurement setup.

An optimized horn antenna (feeder) illuminates the reflector. The reflector is used to reflect a spherical wavefront into a plane wavefront within the quiet zone. Inside the quiet zone is placed the Device Under Test (DUT), attached to a receiver, which can be rotated along the azimuth direction. The received signal at the input port of the PCD is a linear combination between the received signals at each output port and the associated transfer functions. When rotating the PCD, the transfer functions are not modified, and only the phase variations along the output ports vary in a known way. Hence, the rotation along the azimuth direction gives the diversity needed to extract the transfer functions of the PCD.
Because the location of each output port is a known parameter, the phase shift between each port, based on the frequency and the angle of incidence of the plane wave, is given for the creation of a steering vector matrix according to the plane-wave assumption.

The round-trip carrier wavenumber is described as $k_c = 4\pi f_c/c$ whereas the baseband wavenumber domain is covered by the signal spectrum such as $k = 4\pi f/c$. By adding the azimutal diversity θ in (4.21), with $N_s = 1$, it yields:

$$S_r(\theta, k) = \sum_{m=1}^{M} h_m(k) \cdot s_1 \, G(\theta, k) \, e^{-j\varphi_m(\theta,k)} + n(\theta, k) \tag{4.23}$$

with $G(\theta, k)$ being the Co-polar H-plane radiation pattern of each antenna and $\varphi_m(\theta, k) = (k + k_c)\, d_1(\theta, m)$ that corresponds to the phase variation at the m^{th}

output port along the spatial frequency and azimutal diversities. The coefficient s_1 is the complex weighting coefficient, which represents the attenuations that occur during the round-trip propagation from the unique wave that arrives on the DUT, and $d_1(\theta, m)$ is the round-trip distance between the transmitting antenna and the m^{th} port of the PCD when it is rotated at an angle θ from broadside. Thanks to the plane-wave assumption that occurs in the quiet zone, the phase variation can be approximated according to the first order taylor expansion. By taking as a phase reference the first port of the PCD, it yields:

$$\begin{aligned}\Psi_m(\theta, k) &= \varphi_m(\theta, k) - \varphi_0(\theta, k) \\ &= (k + k_c)\,(d_1(\theta, m) - d_1(\theta, 0)) \\ &\approx -(k + k_c) m \Delta_x \sin(\theta)\end{aligned} \tag{4.24}$$

with Δ_x the inter-element distance between the ports.

A data model that estimates the receiving signal is explained. A finite range of azimuth angles is used with $\theta \in [\theta_{min}, \theta_{max}]$ for N_θ scanning angles. The phase, generated by the plane-wave that arrives at an angle θ from broadside between two ports, is $\Psi = -(k + k_c)\Delta_x \sin\theta$. The steering vector, which contains the phase shifts, is defined as $\mathbf{a}(\Psi) = [1, e^{j\Psi}, ..., e^{jM\Psi}]$. It yields the steering vector matrix by considering all the phase shifts at each port for all scanning angles such as $\mathbf{A} = [\mathbf{a}(\Psi_1), ..., \mathbf{a}(\Psi_{N_\theta})]^T$. The receiving signal at the input port of the PCD can be estimated as shown in (4.25).

$$\hat{\mathbf{S}}_r(\theta, k) = \mathbf{A}\,\hat{\mathbf{h}}(k) \tag{4.25}$$

with $\hat{\mathbf{h}}(k) = [\hat{h}_1(k), ..., \hat{h}_M(k)]^T = [\alpha_1(k) + j\beta_1(k), ..., \alpha_M(k) + j\beta_M(k)]^T$ being the estimated transfer functions vector at the wavenumber $k + k_c$ with α_i and β_i respectively, the real part and the imaginary part of the i^{th} transfer function, which has to be found. This procedure is valid if the DUT is located at the center of rotation of the receiving part, which is not the case in this study. The effect of rotating around the center of rotation has to be added in (4.25) to compensate for the phase variation when the receiving part is rotating (see Fig. 4.20). The phase shift is defined as $\delta(\theta, \phi, k) = \exp\left(j(k + k_c)(L - y(\theta)\right)$ with $y(\theta) = \sqrt{(\Delta_x/2)^2 + L^2} \cdot \cos(\phi + \theta)$. It yields:

$$\hat{\mathbf{S}}_r(\theta, k) = \mathbf{A}\,\hat{\mathbf{h}}(k) + \delta(\theta, \phi, k) \tag{4.26}$$

The estimation of the transfer functions, for a given spatial frequency $k + k_c$, is assessed by minimizing the residual error between the measured data $\mathbf{S}_r(\theta, k)$ and the data model $\hat{\mathbf{S}}_r(\theta, k)$ subject to the fact that the estimated transfer function vector $\hat{\mathbf{h}}(k)$ is a unit vector such as the following [46]:

$$\begin{aligned}&\underset{\hat{h}(k)}{\text{minimize}} && |\hat{\mathbf{S}}_r(\theta, k) - \frac{1}{G(\theta, k)}\mathbf{S}_r(\theta, k)|^2 \\ &\text{subject to} && ||\hat{\mathbf{h}}(k)|| = 1\end{aligned} \tag{4.27}$$

The DUT is measured for $\theta \in [-90°, 90°]$ with $N_\theta = 181$ scanning angles and $f + f_c = ((k + k_c)\,c)/(4\pi) \in [50 \text{ GHz}, 66 \text{ GHz}]$ with $N_f = 2001$. The corresponding

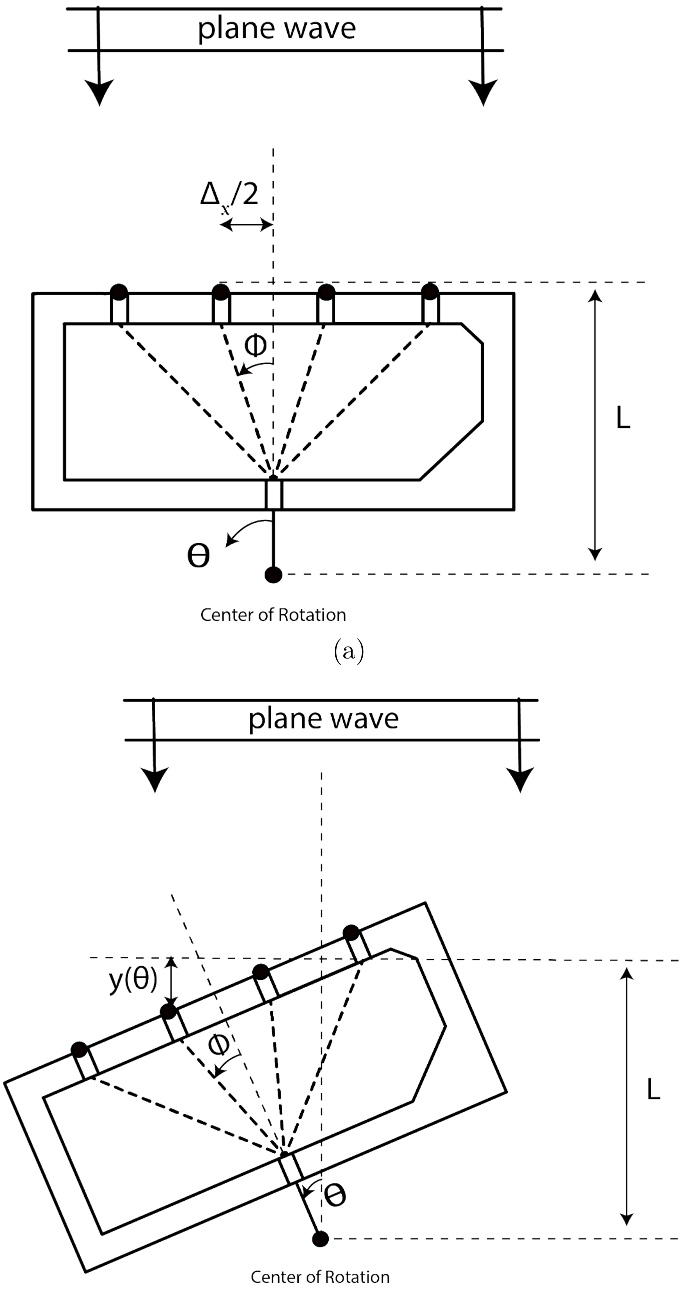

(a)

(b)

Figure 4.20: Sketch of the phase variation that occurs when the DUT is looking at (a) broadside and (b) at squint angle.

measured data $\mathbf{S}_r(\theta, f)$ is shown in Fig. 4.21. Because the element spacing is 2.5 cm, which corresponds to 5λ at $f + f_c = 60$ GHz, it can be seen the grating lobes effects spatially filtered by the radiation pattern of each element.

Because there is no need to use the full range of observation angles to retrieve the transfer function, the minimization is performed for a limited range of observation angles $\theta \in [-30°, 30°]$. Because, isotropic radiating sources are used in the data model, the radiation pattern effects, in the measured data, are compensated prior to applying the minimization to estimate the transfer functions at each frequency

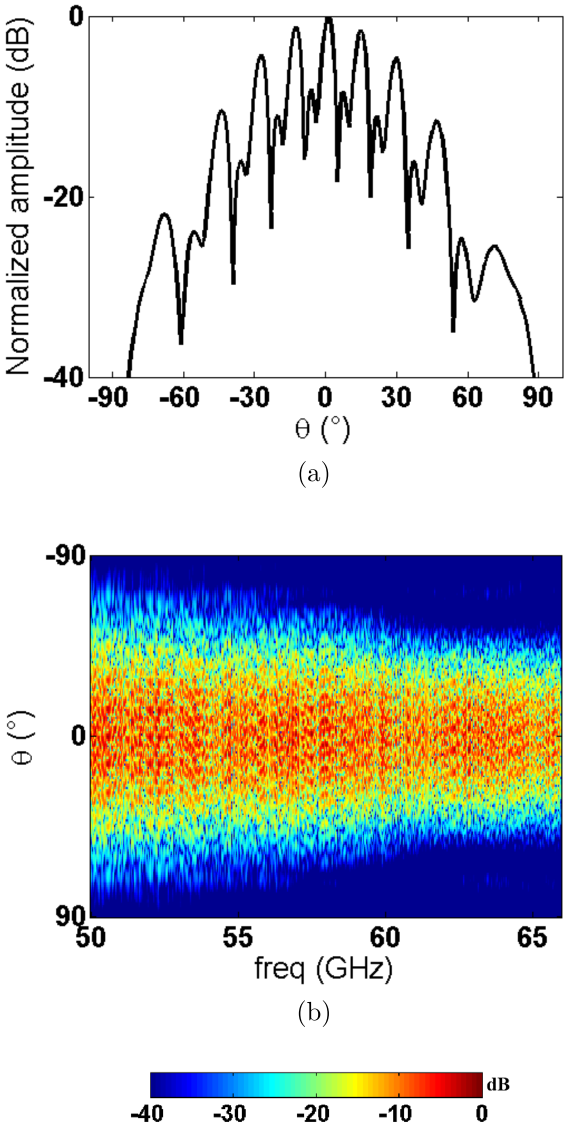

(a)

(b)

Figure 4.21: Measured data along (b) the frequency domain and azimuth axis and along (a) the azimuth axis at the first frequency $f + f_c = 50GHz$.

(see (4.27)). Figures 4.22a & 4.22b compare, at 50 GHz, the measured data and the data model results by using the estimated transfer function from the minimization in amplitude and phase respectively. It can be seen that the data model matches the measured received data, which implies that the estimated transfer functions are valid. From Fig. 4.23, it is shown the correlation between the measured transfer functions thanks to the port-to-port measurement from the VNA ($\mathbf{h}(f)$) and the estimated transfer functions from the plane-wave estimation method ($\hat{\mathbf{h}}(f)$). Over the correlation results, the PSLR of the correlation functions for each port (along the diagonal) is lower than -17.5 dB and with an ISLR lower than -14.1 dB. Over the cross-correlation results (above and below the diagonal), the highest peak reaches -15 dB. From Fig. 4.24, it is shown the absolute value of the complex inner product between the measured transfer vector ($\mathbf{h}(f)$) and the estimated transfer functions vector ($\hat{\mathbf{h}}(f)$). An inner product between two unit normal vectors equal to one is obtained if the two complex vectors are equals. The mean result along the frequency is 0.96.

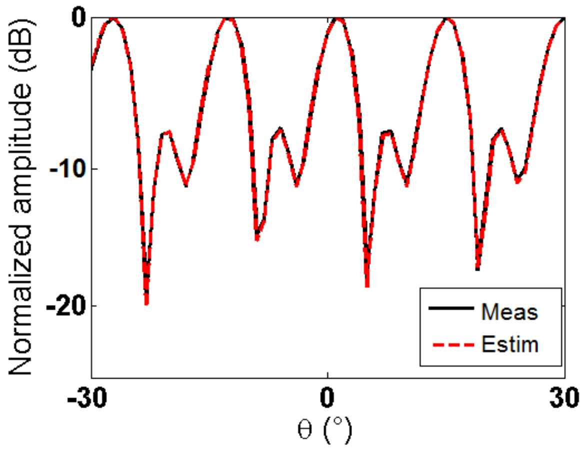

(a)

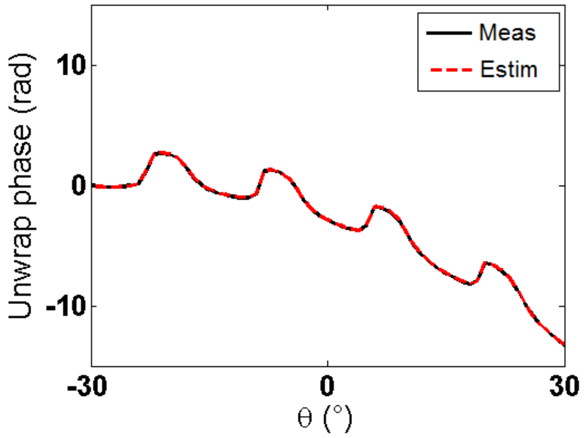

(b)

Figure 4.22: Measured data at $f + f_c = 50$ GHz in (a) amplitude and (b) phase. The black line corresponds to the measured data ($\mathbf{S}_r(\theta, f)$) and the dashed red line corresponds to the result of the data model using the estimated transfer function found from minimization ($\hat{\mathbf{S}}_r(\theta, f)$).

It is possible to estimate the transfer functions of a PCD where the ports are arranged in a uniform linear array according to the plane-wave estimation method. In a non-uniform or sparse linear array, the method can also be applied. To reduce the number of acquisitions, it is possible to estimate the transfer function from sparse acquisitions when the spatial k-space is undersampled by means of least squares minimization methods [47]. If the outputs of the PCD are located over a 2-Dimensionnal array, it is required to rotate along the azimuth and the elevation directions to extract the transfer functions in the same manner as in the 1-Dimensional case.

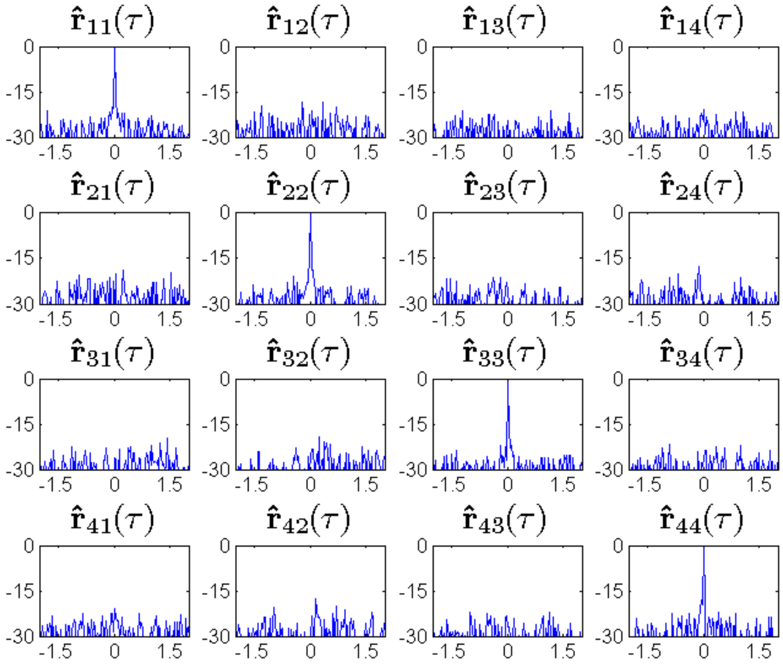

Figure 4.23: The auto/cross-correlation results, $\mathbf{r_{ij}}(\tau) = DFT^{-1}[h_i(f)h_j(f)^*]$, between the measured transfer functions ($\mathbf{h}(f)$) and the estimated transfer functions ($\hat{\mathbf{h}}(f)$), with the time domain τ(ns) along the horizontal axis and the normalized amplitude (dB) along the vertical axis. It is normalized by the maximum peak of the auto-correlation fonctions. DFT^{-1} yields for the inverse discete Fourier transform.

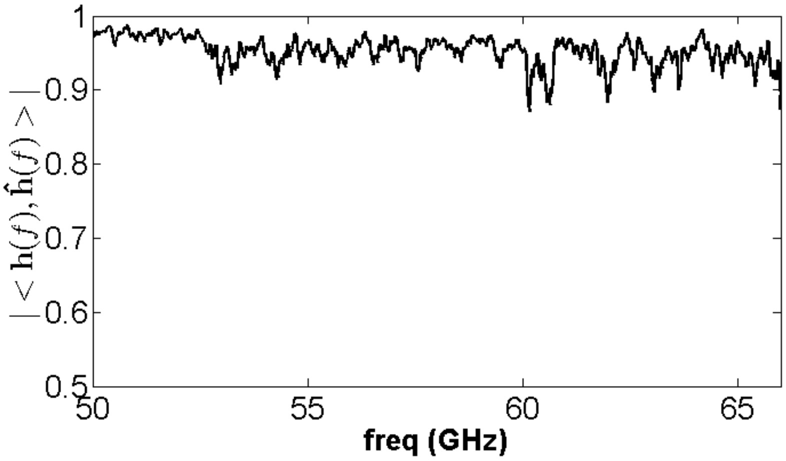

Figure 4.24: Absolute value of the complex inner product results between the measured transfer functions ($\mathbf{h}(f)$) and the estimated transfer functions ($\hat{\mathbf{h}}(f)$), along the frequency.

4.4.2 MIMO-SAR configuration measurement

To validate the accuracy of the transfer function retrievable technique, measurements of the system point spread function is performed in a MIMO configuration. The configuration is shown in Fig. 4.25. The measurements are performed thanks to the IETR facility DIADEM (DIagnostic, Analysis and Dosimetry of EM fields) already presented in the previous sections.

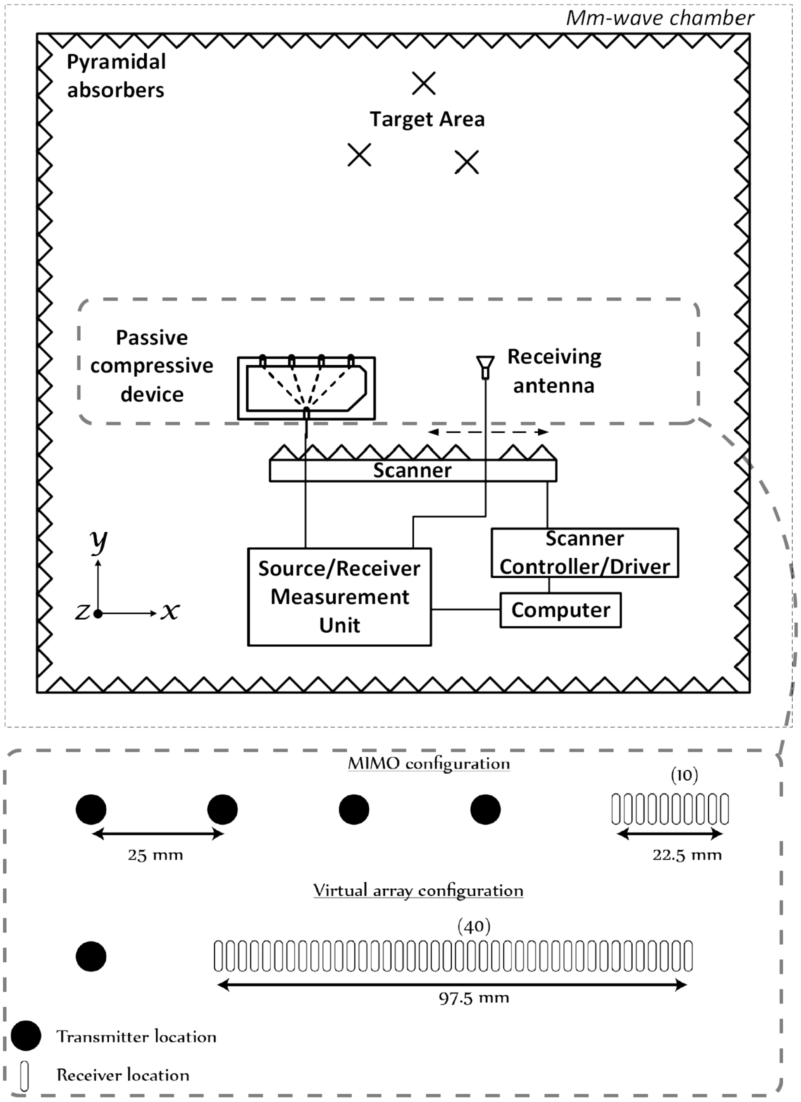

Figure 4.25: Measurement setup.

The four output ports of the PCD are used as the four transmitting antennas with element spacing Δ_x equal to 25 mm. Considering $\delta_x = 2.5$ mm as the element spacing of the receiving synthetic array, the receiving synthetic aperture is located over an aperture of length $\Delta_x - \delta_x$ and aligned with the x-axis. The location of each phase center is (x_a, y_a, z_a) with $x_a \in [-\Delta_x/2, \Delta_x/2 - \delta_x]$. According to the same notation as in (4.21), the receiving signals along the continuous receiving aperture is expressed as:

$$S_r(x_a,k) = \sum_{m=1}^{M} h_m(k) \cdot \sum_{i=1}^{N_s} s_i \, e^{-j(k+k_c)\, d_i(m,x_a)} + n(x_a,k) \tag{4.28}$$

with

$$\begin{aligned} d_i(m,x_a) &= dTx_i(m) + dRx_i(x_a) \\ &= \sqrt{(x_t(m)-x_i)^2 + (y_t-y_i)^2 + (z_t-z_i)^2} \\ &+ \sqrt{(x_a-x_i)^2 + (y_a-y_i)^2 + (z_a-z_i)^2} \end{aligned} \tag{4.29}$$

with $\{x_t(m) = -\Delta_x \cdot (M-1)/2 + (m-1) \cdot \delta_x - x_0\}_{m=1}^{M}$ and $x_0 = 20$ cm being a constant that corresponds to the distance between the center of the receiving aperture and the center of the PCD.

In the same manner as in (4.22), it is applied the four matched filters to extract the received signals from the four output ports. The expression $S_m(x_a,k)$ is the received signal, which comes from the m^{th} output port on the receiving array x_a, after matched filtering. $Y_m(x_a,d)$ is the received signal in the spatial domain d after applying an inverse Fourier transform along the wavenumber domain k.

Finally, the back-projection algorithm is used to generate the focused SAR image $f(x,y,z=C_0)$ with $C_0 = 0.3$ m a constant height. One particular pixel p_l with Cartesian coordinate (x_l,y_l,z_l) of the focused SAR image is constructed by:

$$f(x_l,y_l,z_l) = \sum_{m=1}^{M} \int_{x_a=-\Delta_x/2}^{\Delta_x/2} Y_m(x_a, d_l(m,x_a)) e^{jk_c d_l(m,x_a)} \mathrm{d}x_a \tag{4.30}$$

with $d_l(m,x_a)$ being the round-trip distance between the m^{th} port of the PCD, the l^{th} pixel location and the receiving aperture x_a. The 25-mm length receiving array is synthetized by moving the RF reception module to $\delta_x = 2.5$ mm spaced discrete positions thanks to the scanner, which corresponds to an array of 10 elements. The MIMO configuration generates a larger virtual array with fewer elements. In terms of achievable cross-range resolution, it is comparable to one fixed transmitting element with 40 receiving elements with element spacing equal to 2.5 mm. A 16 GHz bandwidth signal (B_f) with a 58 GHz carrier frequency (f_c) is used. To speed up the acquisition of the 2001 frequency points obtained for each reception position, an IF filter of 100 kHz was applied.

Figure 4.26 shows two metallic trihedral corners with an edge length of 50 mm settled at about 1.4 m distance from the imaging system, on a foam support. From Fig. 4.27a, it is shown the imaging result of the virtual array. The virtual array is synthetize by means of the scanner as already shown in the Fig. 4.25. The two target's positions can be retrieved. Such result is used as a reference to be compared with the imaging results where the PCD is used with a smaller receiving array.

From Fig. 4.27b, it can be seen the imaging result of the MIMO configuration associated with the PCD in which the transfer functions are measured thanks to the Port-to-Port measurements detailed in the Section 4.4.1.2. From Fig. 4.27c, it is shown the imaging result of the MIMO configuration associated with the PCD in which the transfer functions are estimated thanks to the plane-wave estimation measurements detailed in the Section 4.4.1.3. In the Table 4.1 are summarized

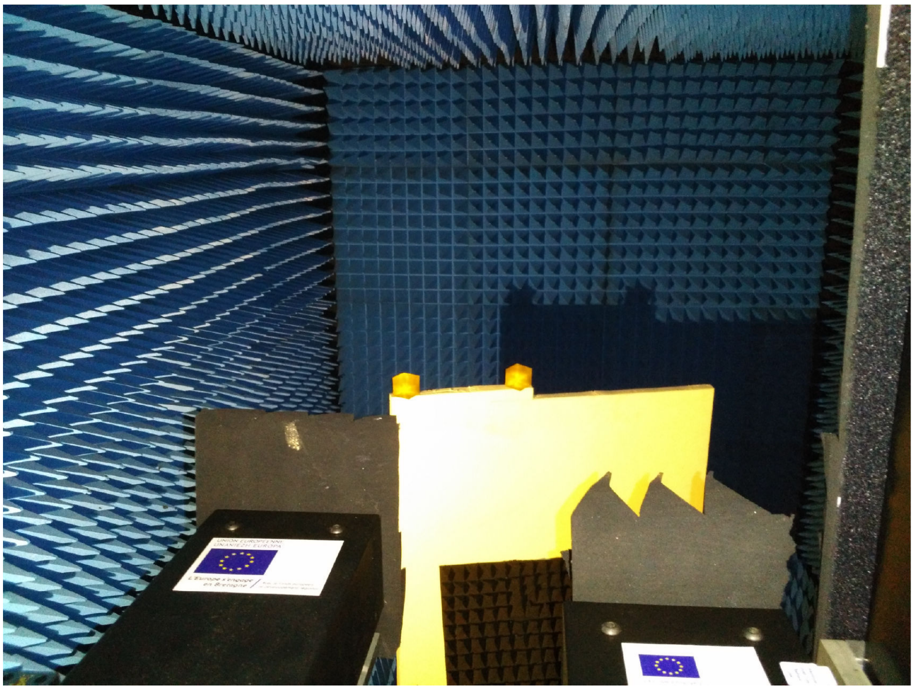

Figure 4.26: Scene in the anechoic chamber composed of two corner reflectors.

and compared the point spread function performances in terms of the range and cross-range resolutions and side lobe levels. Where the transfer function has been estimated from the plane-wave estimation method, the range/cross-range resolution is closer to the performance of the reference (the virtual array) than that where the transfer functions are measured from the Port-to-Port measurement method. To be more realistic, in the next section is studied an array of antenna to substitute the scanner.

Table 4.1: Summarized point spread function performances

Performance	**Virtual array**	**Port-to-Port measurement**	**plane-wave estimation method**
Range resolution (mm)	10.4	11.8	10.6
Cross-Range resolution (mm)	61.7	62	61.7
Side-lobe level (dB)	-13.58	-10.63	-12.5

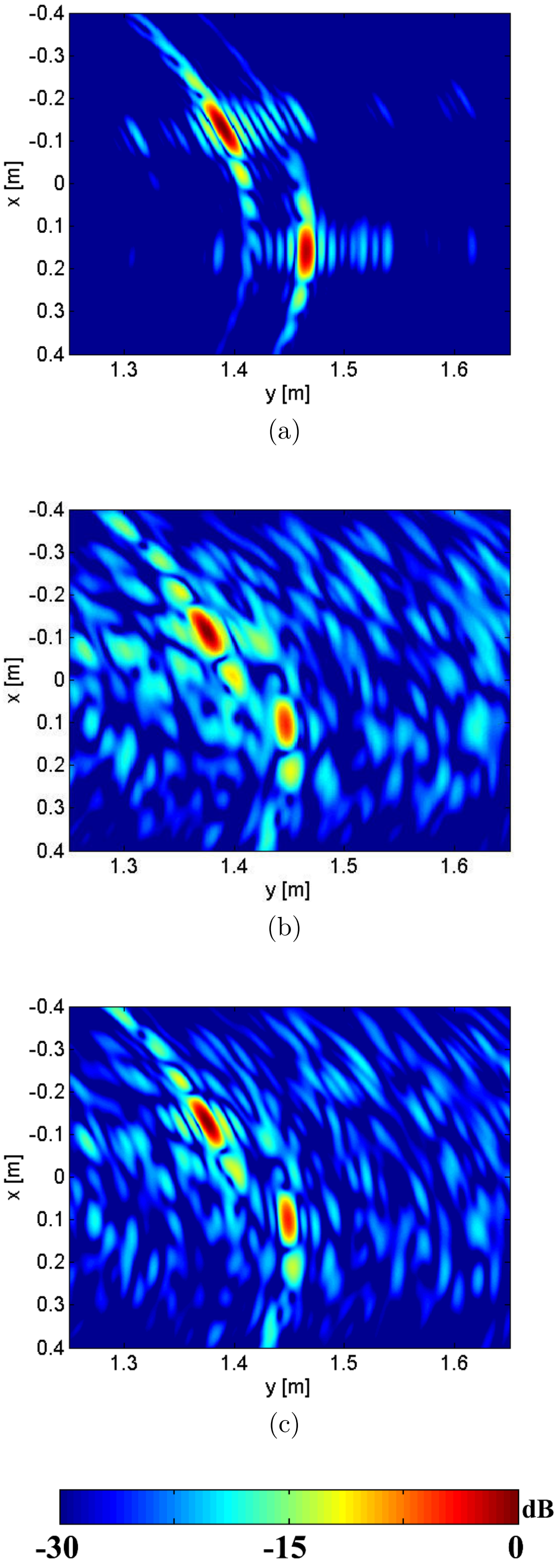

(a)

(b)

(c)

Figure 4.27: Measurement imaging results, by using 4.30, of two isotropic targets (corner reflectors) captured by (a) a classic SIMO configuration with 1Tx (transmitting element) and 40 Rxs (receiving elements), (b) the passive compressive device with 10 Rxs elements where the Port-to-Port measurement is used to have the transfer function and (c) the passive compressive device with 10 Rxs elements where the plane-wave estimation is used to have the transfer function.

4.4.3 Stacked-patch antenna array

It has been shown the capability of a MIMO configuration to drastically reduce the number of required chains in the radar imaging systems by means of both the virtual array theory and the passive compressive device. For the last results presented in the previous section, the receiving array is synthetized through the use of a scanner. To be more realistic, the scanner needs to be replaced by a real antenna array. So this part concerns the design of a printed antenna array with switching capability thanks to switch components. The 16 GHz frequency bandwidth required by the passive compressive device from 50 to 66 GHz imposes the use of a wide-band antenna element. The inter-element distance is fixed to 2.5 mm which drastically reduce the choice of wide-band antennas. It has been decided to use a stacked-patch antenna since the wide-band capability of the element is mainly due to the large spacing between the two patches that are aligned along the electromagnetic wave propagation axis. Such element permits to have a low inter-element distance of about $\lambda/2$ which permits to generate a fully-populated virtual array. At the receiving antenna level, the selection of one stacked-patch element among the others is performed by means of switch components.

4.4.3.1 Design of the antenna element

The stacked patch element is realized as shown in Fig. 4.28. It is a multi-layer based printed antenna having the following caracteristics (ϵ_r: permittivity of the substrate, h: thickness of the substrate, th: the metallic thickness):

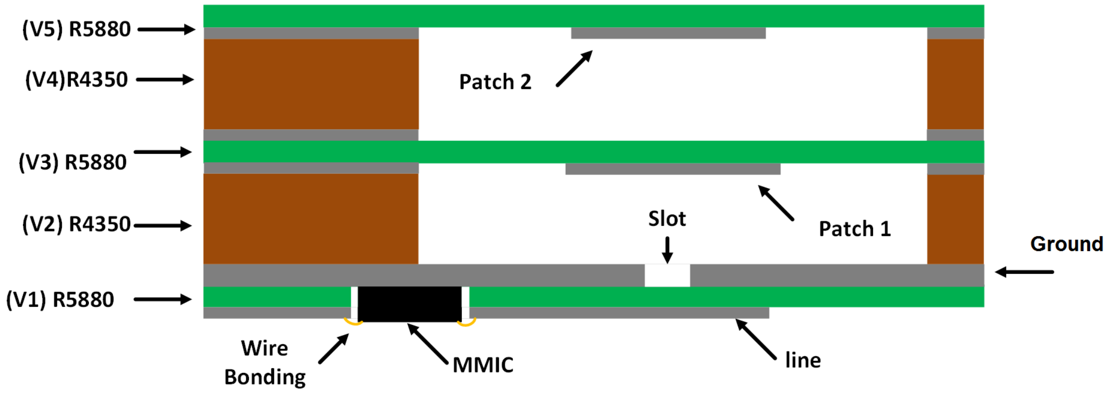

Figure 4.28: Schematic of the stacked patch antenna

- **V1** (Duroid R5880 ϵ_r = 2.2, h = 127 um, th = 17.5 um): The bottom face: the active MMIC components are placed and connected by a feeding line. The top face: An increase in the nominal ground from 17.5 um to 100 um has been applied where the slot are used to feed the patches. This increase is required to facilitate the MMIC bonding and for DC bias dissipation.
- **V2** (Duroid R4350 ϵ_r = 4.3, h = 280 um, th = 17.5 um): The substrate is used with a big cavity around the patch in order to have a sufficiently high height between the ground (top face of V1) and the patch 1 (bottom face of

V3). On both faces where the cavity is not present, it is fully metallized to be glued to V1 and V3.

- **V3** (Duroid R5880 $\epsilon_r = 2.2$, $h = 254$ um, $th = 17.5$ um): It has been used a thicker substrate as compared to V1 to have a rigid surface to avoid a distortion at the cavity location. It is added the first patch at the bottom face and a fully metallized surface at the top face where the cavity is not present to be glued with V2 and V4.

- **V4** (Duroid R4350 $\epsilon_r = 4.3$, $h = 280$ um, $th = 17.5$ um): The substrate is used with a big cavity around the patch in order to have a sufficiently high height between the patch 1 (bottom face of V3) and the patch 2 (bottom face of V5). On both faces where the cavity is not present, it is fully metallized to be glued to V3 and V5.

- **V5** (Duroid R5880 $\epsilon_r = 2.2$, $h = 254$ um, $th = 17.5$ um): It has been used a thicker substrate as compared to V1 to have a rigid surface to avoid a distortion at the cavity location. It is added the second patch at the bottom face and a fully metallized surface at the bottom face where the cavity is not present to be glued with V4.

- **Glue** ($\epsilon_r = 3.52$, $h = 90$ um): The pre-preg is used to glue the multilayer configuration. The thickness of $280um$ of V2 and V4 is made from an initial thickness of 100 um plus a 90 um of prepreg in both sides corresponding to a final thickness of 280 um.

Thanks to the optimization performed using CST microwave software, the side length of the Patch 1 located at V3 is 1.765 mm and the side length of the Patch 2 located at V5 is 1.280 mm. The length and the width of the slot are 1.275 mm and 0.4 mm, respectively. Because the beam of the passive compressive device outputs are slightly focused along the E-plane thanks to the horn antenna module, in the same manner, one element of the receiving array is composed of two patches aligned along the E-plane and the elements of the array are oriented along the H-plane.

Firstly, a passive antenna array has been designed without active MMIC (switch and amplifier) to validate the multilayer technology and the bandwidth capability.

4.4.3.2 Passive prototypes

In Fig. 4.29 is shown the dimensions of the feeding network design of the passive array of 8 elements (each one composed of two patches along the E-plane) with: $w1 = w5 = 0.380$ mm, $w2 = 0.900$ mm, $l2 = 1.580$ mm, $w3 = w4 = 0.800$ mm, $l3 = l4 = 1.1$ mm, $w6 = 0.240$ mm, $w7 = 0.700$ mm and $l7 = 1.400$ mm.

In Fig. 4.30 is shown the magnitude of the simulated S_{11}-parameter along the frequency for the single element and the array of 8 elements. Thanks to the optimization, a 15-GHz frequency bandwidth is achieved for both designs corresponding to a bandwidth of 26% centered at the carrier frequency 57.5 GHz.

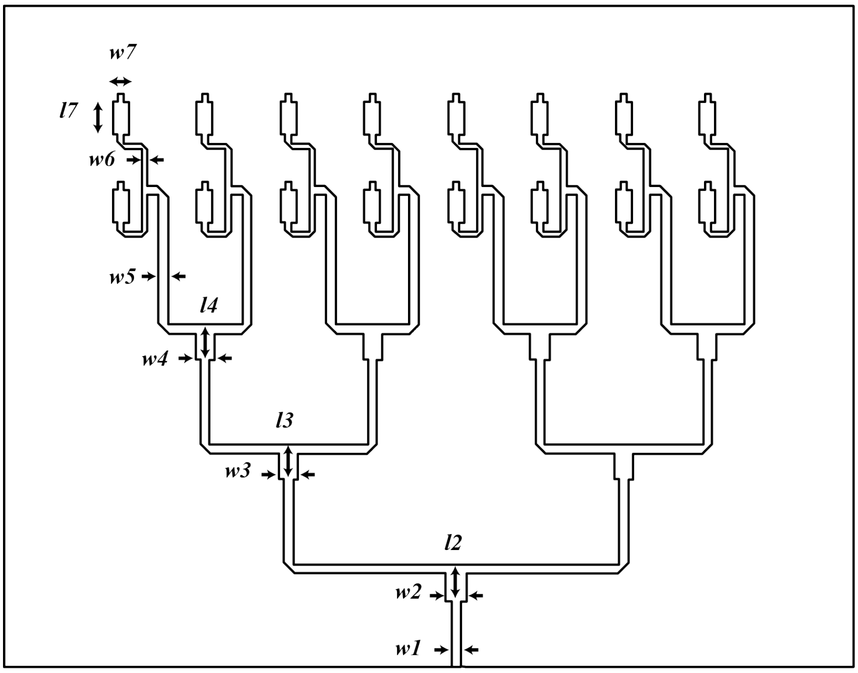

Figure 4.29: Feeding network dimension of the array of eight elements.

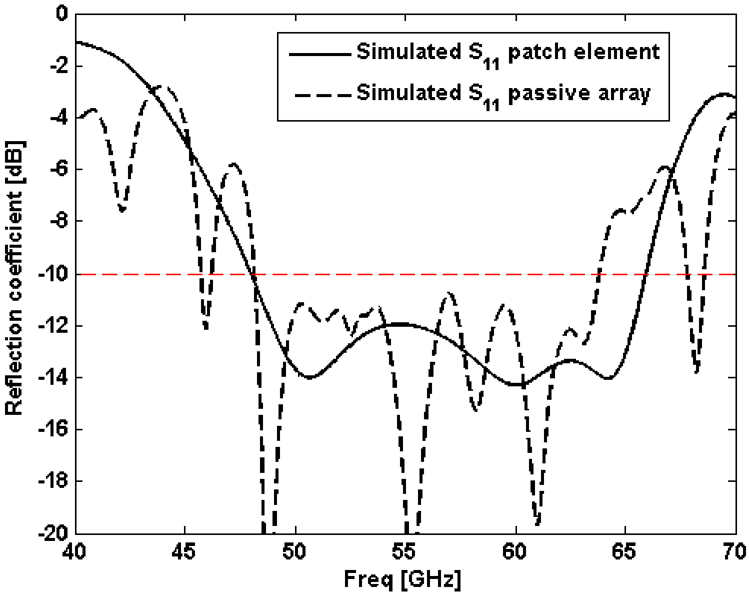

Figure 4.30: Simulated S-parameter of one single element and an array of 8 elements.

The simulated Co/Cross radiation pattern of a single element along the E and H-planes are shown in Fig. 4.31. The radiation patterns are shown for frequencies of 50/55/60 and 65 GHz. The SLL are lower than -10 dB with a directivity of approximately 10 dBi along the frequency band and a cross-polarisation level of 26 dB below the main beam. The HPBW along the H-plane is 80° and 40° along the E-plane.

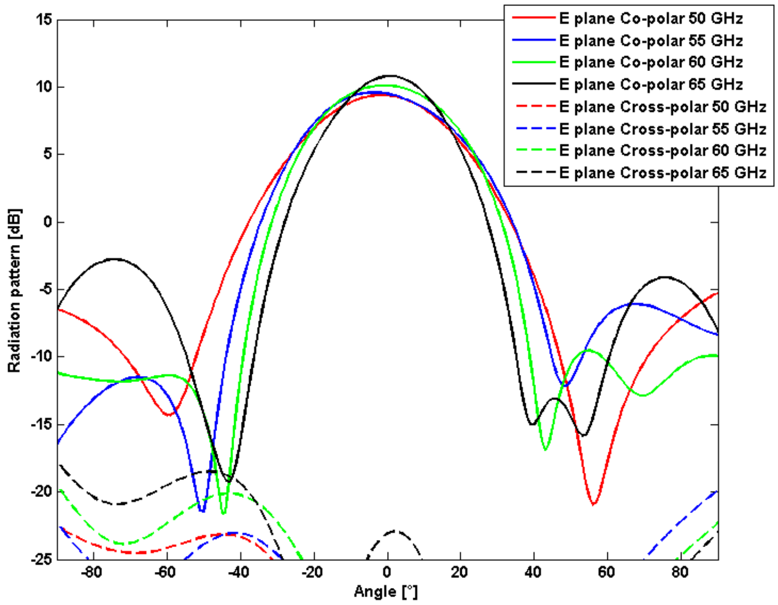

(a)

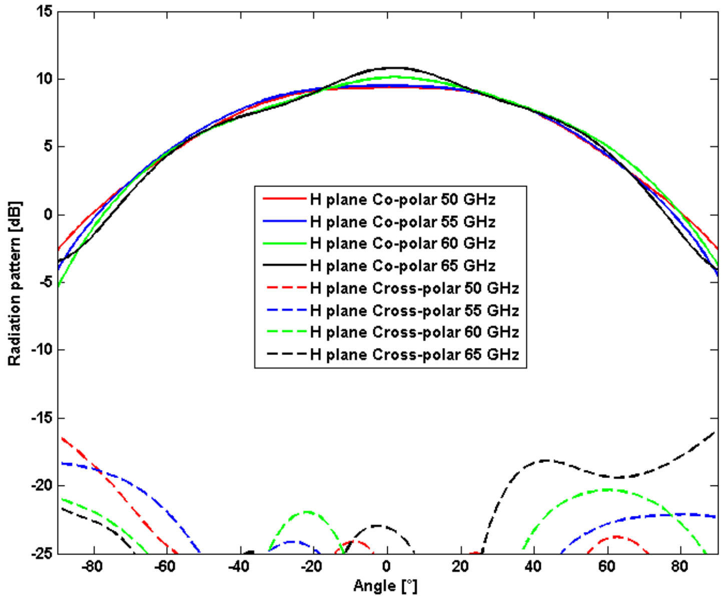

(b)

Figure 4.31: Simulated Co/Cross radiation pattern of the element along (a) the E-plane and (b) the H-plane.

In the same manner, in Fig. 4.32 is shown the simulated Co/Cross radiation pattern of the array of 8 elements along the E and H-planes. The SLL are lower than -12 dB with a directivity of approximately 16 dBi and with a cross-polarization level of 26 dB below the main beam. The HPBW along the H-plane is 9° and 40° along the E-plane.

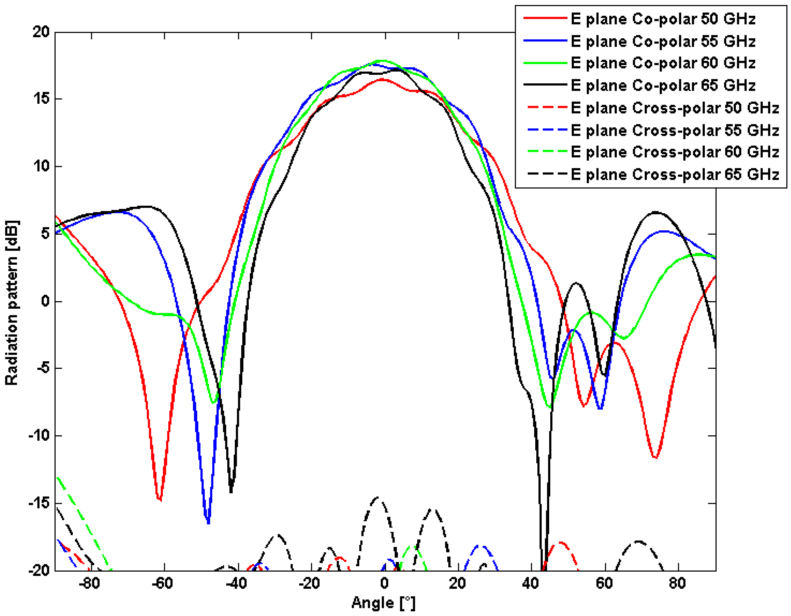

(a)

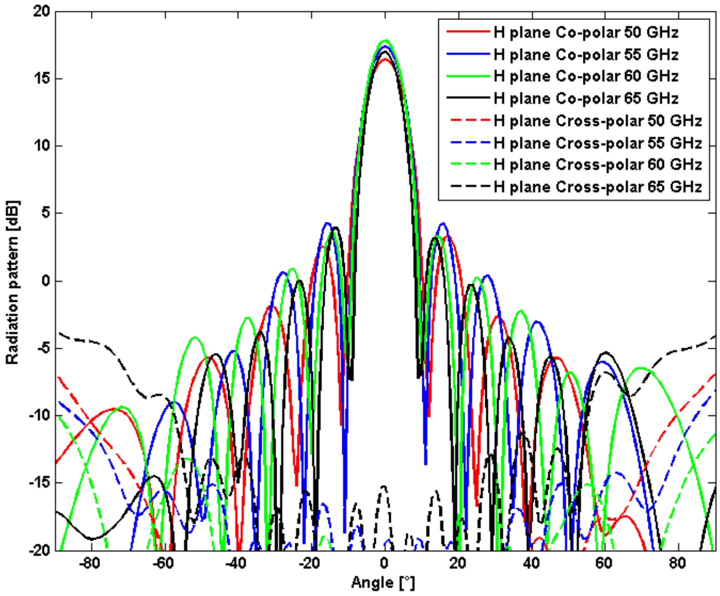

(b)

Figure 4.32: Simulated Co/Cross radiation pattern of the passive array along (a) the E-plane and (b) the E-plane.

In Fig. 4.33a & Fig. 4.33b are shown the fabricated patch antenna corresponding to a single element of the array and an exploded view of the different layers, respectively. In Fig. 4.34 is shown the fabricated passive array of 8 elements.

Finally, it is compared the simulated reflection coefficient and the measured reflection coefficient for the element and the array in Fig. 4.35a and Fig. 4.35b, respectively. The measured reflection coefficient result of the element permits to

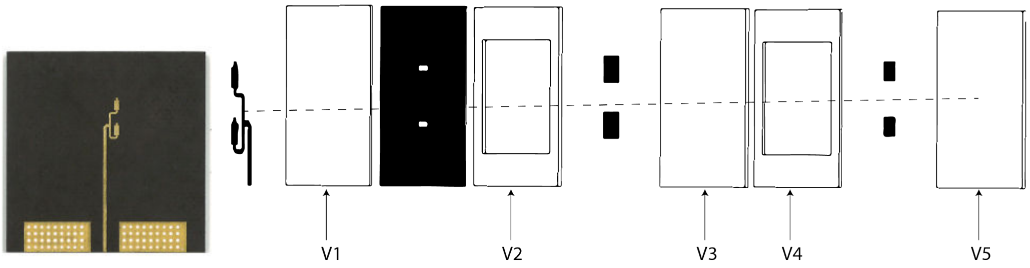

(a) (b)

Figure 4.33: Single element with (a) the fabricated prototype and (b) the exploded view.

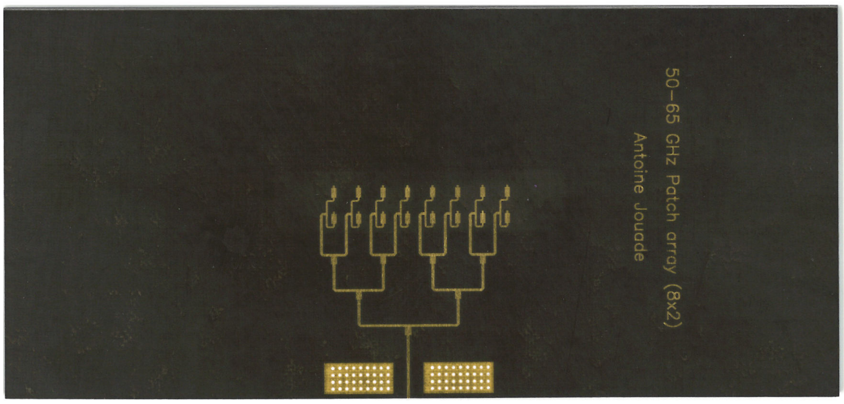

Figure 4.34: Passive array of 8 elements prototype

validate the multilayer technology and the bandwidth capability of the antenna to be used in the active prototype. At around 56 GHz, a small peak at -8.5 dB occurs for the array of elements, however, this also permits to validate the principle. The radiation patterns of the two passive prototypes have not been measured yet.

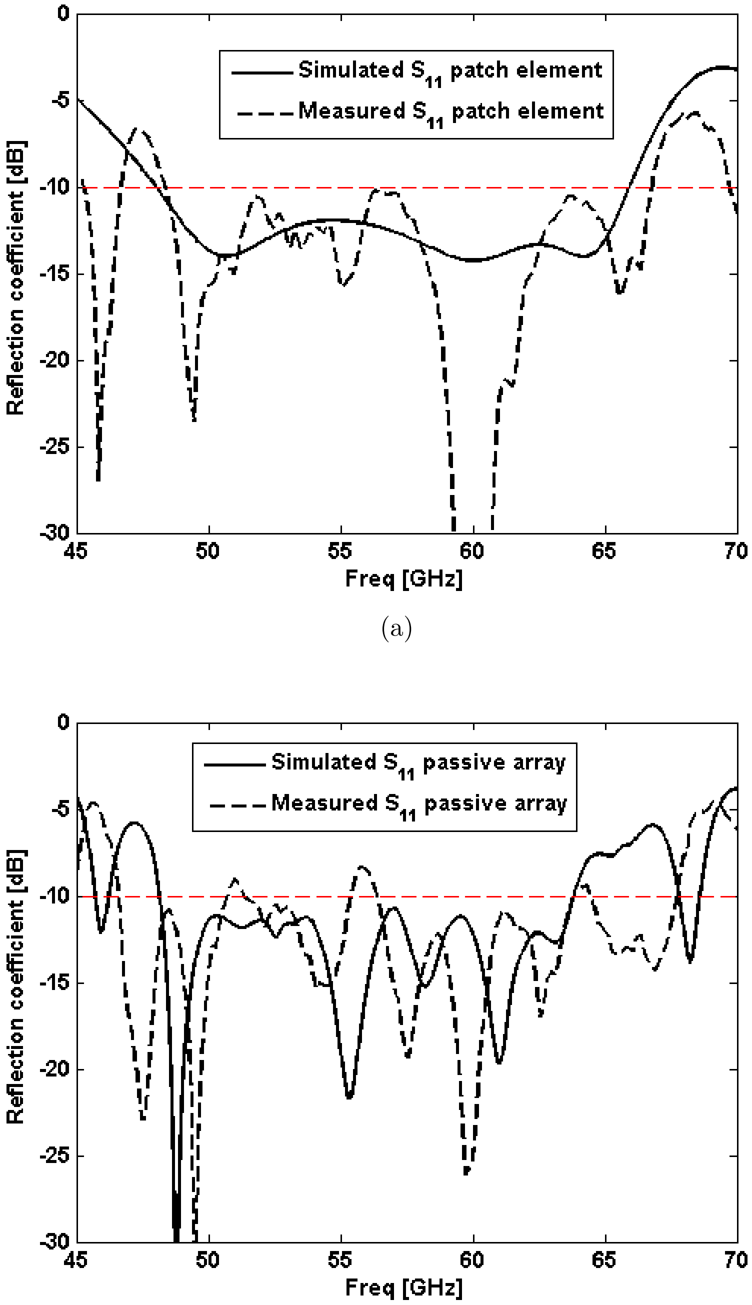

(a)

(b)

Figure 4.35: Simulated and measured S-parameter of (a) the single element and (b) the array of 8 elements.

4.4.3.3 Active prototype

The final objective of this section was to implement a radar with the passive compressive device as transmitting antenna part and an active switchable array as receiving antenna part and based on the precedent multilayer technology. This technology has been validated through the measurement of passive antenna element and array. The implementation of this active array using MMIC amplifiers and swithes is represented on Fig. 4.36a illustrating the principles of operation.

Further, the layout of the active prototype has been manufactured as shown in Fig. 4.36b. In the part A is added low noise amplifiers (Ref: UMC CHA2159) that have a gain above 18 dB between 50 to 66 GHz. The amplifiers are used to compensate the losses due to the switch components and all wire boundings used.Moreover the LNA allows to obtain an acceptable signal to noise ratio.

In the part B is added SPDT (Single pole, double throw) switch components (Ref: SPDT Hittite HMC-SDD112) working from 50 to 86 GHz with insertion loss from 1 to 3 dB and isolation of about 25 dB. the switch components are added in such a way to be able to receive the signal from one element among the others. Finally in part C are the BIAS pads used to control both the amplifiers and the switch components and the resistors required to properly feed the amplifiers.

Unfortunately, due to lack of time, the implementation of active MMIC on the layout has not been not yet but we hope it could be done in the next weeks.When this active prototype will be manufactured, it will be used in a MIMO configuration with thae passive compressive device to have a fully populated virtual array to image a scene in almost real time.

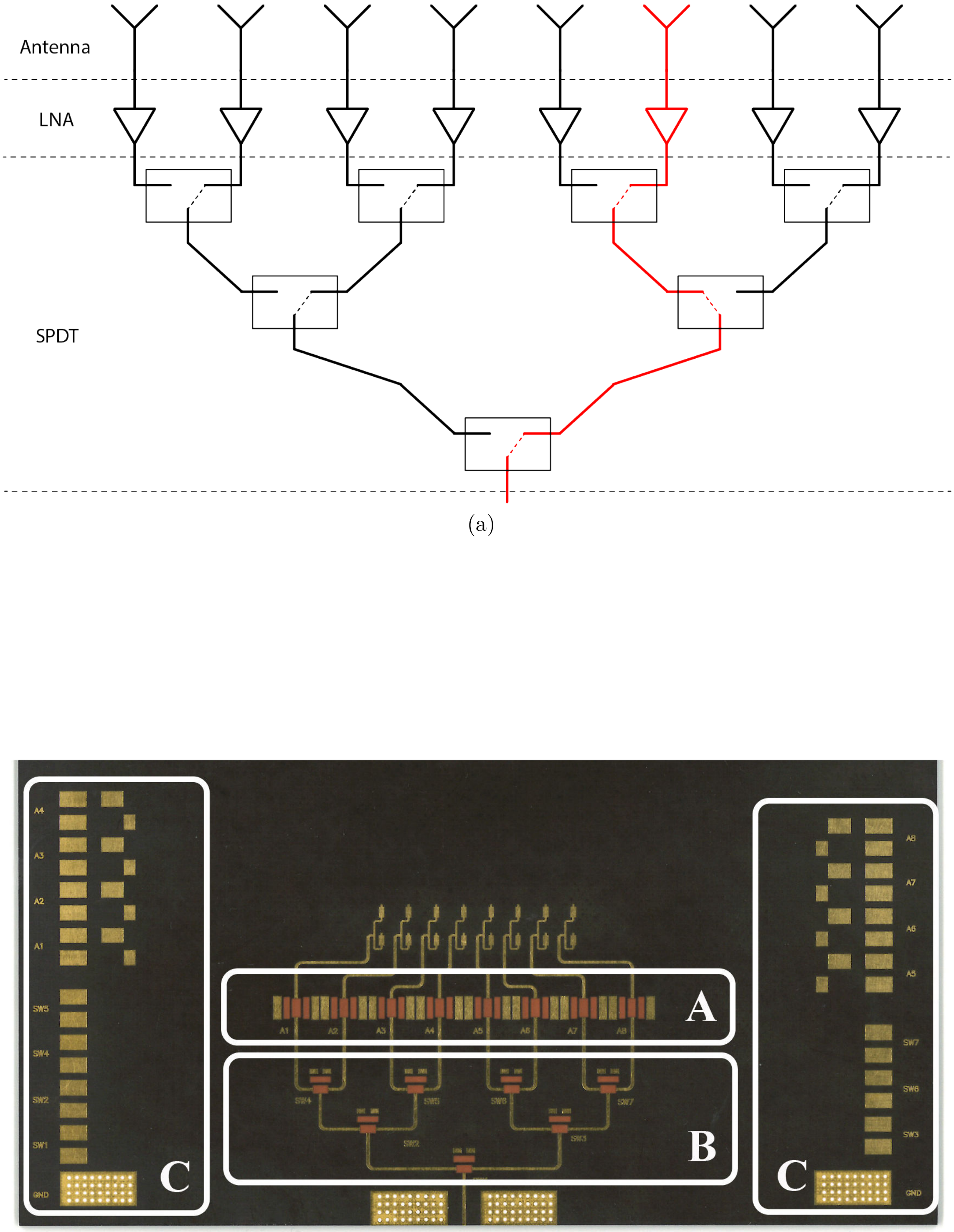

(a)

(b)

Figure 4.36: (a) schematic drawing and (b) the manufactured Active array layout of 8 independant elements.

4.5 Summary

Close observation reveals that the millimeter-wave frequencies are approriate for small objets imaging application such as concealed object under clothes for instance. The frequency band available at those frequencies is sufficient (higher than 4 GHz), however, to obtain high resolution images, it requires a large number of receiving antennas and associated chains which lead to a costly and complex technology. To reduce the complexity and the cost, a MIMO configuration using passive compressive device has been investigated thanks to the virtual array principle. The passive compressive device has been used with a synthetic receiving array using a scanner. To avoid the use of a moving plateform, a switch-based patch array has been studied with a wide frequency bandwidth.

Bibliography

[1] Ken B Cooper, Robert J Dengler, Nuria Llombart, Ashit Talukder, Anand V Panangadan, Chris S Peay, Imran Mehdi, and Peter H Siegel. Fast high-resolution terahertz radar imaging at 25 meters. In *SPIE Defense, Security, and Sensing*, pages 76710Y–76710Y. International Society for Optics and Photonics, 2010.

[2] S Palm, R Sommer, A Hommes, N Pohl, and U Stilla. Mobile mapping by fmcw synthetic aperture radar operating at 300 ghz. *International Archives of the Photogrammetry, Remote Sensing & Spatial Information Sciences*, 41, 2016.

[3] Temesgen Gebrie Yitayew, Laurent Ferro-Famil, Torbjørn Eltoft, and Stefano Tebaldini. Tomographic imaging of fjord ice using a very high resolution ground-based sar system. *IEEE Transactions on Geoscience and Remote Sensing*, 55(2):698–714, 2017.

[4] M. Younis, C. Fischer, and W. Wiesbeck. Digital beamforming in sar systems. *IEEE Transactions on Geoscience and Remote Sensing*, 41(7):1735–1739, July 2003.

[5] Chin Yuan Chong, Frédéric Pascal, Jean-Philippe Ovarlez, and Marc Lesturgie. Mimo radar detection in non-gaussian and heterogeneous clutter. *IEEE Journal of selected topics in signal processing*, 4(1):115–126, 2010.

[6] P. F. Sammartino, C. J. Baker, and H. D. Griffiths. Frequency diverse mimo techniques for radar. *IEEE Transactions on Aerospace and Electronic Systems*, 49(1):201–222, Jan 2013.

[7] Hongbo Sun, Frederic Brigui, and Marc Lesturgie. Analysis and comparison of mimo radar waveforms. In *Radar Conference (Radar), 2014 International*, pages 1–6. IEEE, 2014.

[8] G. L. Charvat, L. C. Kempel, E. J. Rothwell, C. M. Coleman, and E. L. Mokole. An ultrawideband (uwb) switched-antenna-array radar imaging system. In

2010 IEEE International Symposium on Phased Array Systems and Technology, pages 543–550, Oct 2010.

[9] Zhu Zhenbo, Tang Ziyue, and Jiang Xingzhou. Research on bistatic sar imaging. In *Geoscience and Remote Sensing Symposium, 2006. IGARSS 2006. IEEE International Conference on*, pages 1224–1227. IEEE, 2006.

[10] P. Antonik, M. C. Wicks, H. D. Griffiths, and C. J. Baker. Frequency diverse array radars. In *2006 IEEE Conference on Radar*, pages 3 pp.–, April 2006.

[11] H. Raza, A. Hussain, J. Yang, and P. S. Kildal. Wideband compact 4-port dual polarized self-grounded bowtie antenna. *IEEE Transactions on Antennas and Propagation*, 62(9):4468–4473, Sept 2014.

[12] Caicai Gao, Kah Chan Teh, and Aifei Liu. Frequency coding waveform with segment lfm. In *Synthetic Aperture Radar (APSAR), 2015 IEEE 5th Asia-Pacific Conference on*, pages 507–510. IEEE, 2015.

[13] Nadav Levanon and Eli Mozeson. *Radar signals*. John Wiley & Sons, 2004.

[14] François Septier, Yves Delignon, Atika Menhaj-Rivenq, and Christelle Garnier. Monte carlo methods for channel, phase noise, and frequency offset estimation with unknown noise variances in ofdm systems. *IEEE Transactions on Signal Processing*, 56(8):3613–3626, 2008.

[15] Vishal Riché, Stéphane Méric, Jean-Yves Baudais, and Eric Pottier. Investigations on ofdm signal for range ambiguity suppression in sar configuration. *IEEE Transactions on Geoscience and Remote Sensing*, 52(7):4194–4197, 2014.

[16] L. Welch. Lower bounds on the maximum cross correlation of signals (corresp.). *IEEE Transactions on Information Theory*, 20(3):397–399, May 1974.

[17] D. Carsenat and C. Decroze. Uwb antennas beamforming using passive time-reversal device. *IEEE Antennas and Wireless Propagation Letters*, 11:779–782, 2012.

[18] T. Fromenteze, C. Decroze, and D. Carsenat. Waveform coding for passive multiplexing: Application to microwave imaging. *IEEE Transactions on Antennas and Propagation*, 63(2):593–600, Feb 2015.

[19] Thomas Fromenteze, David Carsenat, and Cyril Decroze. A precorrection method for passive uwb time-reversal beamformer. *IEEE Antennas and Wireless Propagation Letters*, 12:836–840, 2013.

[20] Romain Négrier, Michèle Lalande, Joël Andrieu, Badr Mohamed Shalaby, Vincent Couderc, Thomas Fromenteze, Cyril Decroze, and David Carsenat. High-prf uwb optoelectronic radar system: a clean-type algorithm to overcome depth limitation. *IEEE Transactions on Antennas and Propagation*, 64(3):1080–1088, 2016.

[21] I. Bekkerman and J. Tabrikian. Target detection and localization using mimo radars and sonars. *IEEE Transactions on Signal Processing*, 54(10):3873–3883, Oct 2006.

[22] Chun-Lin Liu and PP Vaidyanathan. Super nested arrays: Linear sparse arrays with reduced mutual coupling part i: Fundamentals. *IEEE Transactions on Signal Processing*, 64(15):3997–4012, 2016.

[23] Chenglong Zhu, Wen-Qin Wang, Hui Chen, and Hing Cheung So. Impaired sensor diagnosis, beamforming, and doa estimation with difference co-array processing. *IEEE Sensors Journal*, 15(7):3773–3780, 2015.

[24] Elie BouDaher, Fauzia Ahmad, and Moeness G Amin. Sparsity-based direction finding of coherent and uncorrelated targets using active nonuniform arrays. *IEEE Signal Processing Letters*, 22(10):1628–1632, 2015.

[25] Jian Li and Petre Stoica. Mimo radar with colocated antennas. *IEEE Signal Processing Magazine*, 24(5):106–114, 2007.

[26] Si Qin, Yimin D Zhang, and Moeness G Amin. Generalized coprime array configurations for direction-of-arrival estimation. *IEEE Transactions on Signal Processing*, 63(6):1377–1390, 2015.

[27] Mehrdad Soumekh. *Synthetic aperture radar signal processing*, volume 7. New York: Wiley, 1999.

[28] JN Gollub, O Yurduseven, KP Trofatter, D Arnitz, MF Imani, T Sleasman, M Boyarsky, A Rose, A Pedross-Engel, H Odabasi, et al. Large metasurface aperture for millimeter wave computational imaging at the human-scale. *Scientific Reports*, 7, 2017.

[29] Timothy Sleasman, Michael Boyarsky, Mohammadreza F Imani, Jonah N Gollub, and David R Smith. Design considerations for a dynamic metamaterial aperture for computational imaging at microwave frequencies. *JOSA B*, 33(6):1098–1111, 2016.

[30] G. Montaldo, D. Palacio, M. Tanter, and M. Fink. Building three-dimensional images using a time-reversal chaotic cavity. *IEEE Transactions on Ultrasonics, Ferroelectrics, and Frequency Control*, 52(9):1489–1497, Sept 2005.

[31] O. Yurduseven, V. R. Gowda, J. N. Gollub, and D. R. Smith. Printed aperiodic cavity for computational and microwave imaging. *IEEE Microwave and Wireless Components Letters*, 26(5):367–369, May 2016.

[32] M. Fink. Time reversal of ultrasonic fields. i. Basic principles. *IEEE Transactions on Ultrasonics, Ferroelectrics, and Frequency Control*, 39(5):555–566, Sept 1992.

[33] O. Yurduseven, J. N. Gollub, K. P. Trofatter, D. L. Marks, A. Rose, and D. R. Smith. Software calibration of a frequency-diverse, multistatic, computational imaging system. *IEEE Access*, 4:2488–2497, 2016.

[34] C. L. Liu and P. P. Vaidyanathan. Super nested arrays: Linear sparse arrays with reduced mutual coupling;part i: Fundamentals. *IEEE Transactions on Signal Processing*, 64(15):3997–4012, Aug 2016.

[35] D. Tarchi, F. Oliveri, and P. F. Sammartino. Mimo radar and ground-based sar imaging systems: Equivalent approaches for remote sensing. *IEEE Transactions on Geoscience and Remote Sensing*, 51(1):425–435, Jan 2013.

[36] G. Krieger, N. Gebert, and A. Moreira. Multidimensional waveform encoding: A new digital beamforming technique for synthetic aperture radar remote sensing. *IEEE Transactions on Geoscience and Remote Sensing*, 46(1):31–46, Jan 2008.

[37] Andreas Pedross-Engel, Claire M Watts, David R Smith, and Matthew S Reynolds. Enhanced resolution stripmap mode using dynamic metasurface antennas. *IEEE Transactions on Geoscience and Remote Sensing*, 2017.

[38] Abigael Taylor, Hélène M Oriot, Laurent Savy, Franck Daout, and Philippe Forster. Moving targets detection capacities improvement in multichannel sar framework. *IEEE Transactions on Geoscience and Remote Sensing*, 2017.

[39] D. Cerutti-Maori, I. Sikaneta, J. Klare, and C. H. Gierull. Mimo sar processing for multichannel high-resolution wide-swath radars. *IEEE Transactions on Geoscience and Remote Sensing*, 52(8):5034–5055, Aug 2014.

[40] Paolo Berardino, Gianfranco Fornaro, Riccardo Lanari, and Eugenio Sansosti. A new algorithm for surface deformation monitoring based on small baseline differential sar interferograms. *IEEE Transactions on Geoscience and Remote Sensing*, 40(11):2375–2383, 2002.

[41] Maxim Neumann, Laurent Ferro-Famil, and Andreas Reigber. Multibaseline polarimetric sar interferometry coherence optimization. *IEEE Geoscience and Remote Sensing Letters*, 5(1):93–97, 2008.

[42] Laurent Ferro-Famil, Eric Pottier, and Jong-Sen Lee. Unsupervised classification of multifrequency and fully polarimetric sar images based on the h/a/alpha-wishart classifier. *IEEE Transactions on Geoscience and Remote Sensing*, 39(11):2332–2342, 2001.

[43] Jean-Baptiste Gros, Olivier Legrand, Fabrice Mortessagne, Elodie Richalot, and Kamardine Selemani. Universal behaviour of a wave chaos based electromagnetic reverberation chamber. *Wave Motion*, 51(4):664–672, 2014.

[44] Xin Lu and Hong Sun. Parameter assessment for SAR image quality evaluation system. In *2007 1st Asian and Pacific Conference on Synthetic Aperture Radar*, pages 58–60, Nov 2007.

[45] Laurent Le Coq, Benjamin Fuchs, Thomas Kozan, Sara Burgos, and Per O. Iversen. IETR millimeter-wave Compact Antenna Test Range implementation and validation. In *2015 9th European Conference on Antennas and Propagation (EuCAP)*, pages 1–5. IEEE, 2015.

[46] Donald W Marquardt. An algorithm for least-squares estimation of nonlinear parameters. *Journal of the society for Industrial and Applied Mathematics*, 11(2):431–441, 1963.

[47] E. J. Candes, J. Romberg, and T. Tao. Robust uncertainty principles: exact signal reconstruction from highly incomplete frequency information. *IEEE Transactions on Information Theory*, 52(2):489–509, Feb 2006.

Chapter 5

Spectral estimation methods

Synthetic Aperture Radar (SAR) combines 1-D or 2-D spatial diversity with spectral diversity to produce 2-D or 3-D maps of the electromagnetic reflectivity of environments. Exact focusing methods in time or frequency domain such as the Back-Projection [1, 2] or the Range migration ($\omega - k$) inversion [3–5] algorithms may be used to transform the coherent acquired raw data into images. The achieved spatial resolution is inherently limited by the processed frequency band and by the synthetic aperture dimensions. To overcome this limitation, imaging techniques based on spectral estimation methods are used to improve spatial resolution, that is a key factor for target detection and recognition. Spectral estimation methods consider the problem of determining the spectral content of a finite noisy set of measurements, by means of either parametric or nonparametric techniques [6, 7]. The spectral estimation methods considered here are covariance matrix-based algorithms, which have been originally adapted to array processing, according to a data model based on several assumptions, corresponding to the plane-wave (far-field region) and the narrow-frequency bandwidth configurations [8, 9]. In fact, the data model considers that the region of interest is located relatively far from the radar system so that the spherical wave-front arriving upon the synthetic aperture is considered as a plane wave. It also assumes that the transmitted signals have a narrow frequency bandwidth. In such cases, the signal history of a point-scatterer is considered as a 2D-sinusoid where the phase variation is considered as a linear function of the scatterer's position.

However, when the model is compromised, compensations are required to give full capability to spectral estimation methods. In the literature, specific spectral estimation methods are modified to consider the wide-band or near-field configurations as in [10–14]. Firstly, for a wide-band far-field configuration, the distance variation between one target and the full aperture may exceed the range resolution of the system. The target response is going to spread over multiple range cells leading to a reduction of the capability of spectral estimation methods. Because the spectral estimation methods considered use the covariance matrix from one particular range of the SAR data, the selected vector provides only a portion of the phase history of the target response. This therefore reduces the capability of spectral estimation methods to discriminate closely spaced targets. The wide-band compensation algorithm in [15, 16] has the ability to cancel out the range cell migrations that occur by means of a spatial re-sampling of the SAR data. Then the spectral estimation methods are applied on the compensated SAR data.

Secondly, for a narrow-band near-field configuration, the wave phase-front cannot longer be considered as a plane phase-front without producing severe errors and distortions, since phase history is no longer a linear function. Near-field compensation algorithms [17–19] locally compensate for the spherical phase-front over the aperture. The estimation problem consists in solving a set of two non-linear functions: the range and the Direction of Arrival (DoA). The compensation is done using the exact geometry of the problem. Once the compensation is performed, spectral estimation methods are applied on the resulting SAR data.

However, where the SAR data acquired in a wide-band and near-field configuration, the spherical wave-front curvature generates non-linear range cell migrations, whose imperfect compensation, using the plane wave assumption, generates residual range shifts whose magnitude might be comparable to the range resolution, and whose distribution over the aperture highly depends on the location of a scatterer and on the acquisition geometry. This variability prevents a generic correction procedure. Similarly, near-field phase patterns cannot be written under a convenient and generic formalism, i.e. the phase distribution over the aperture not only depends on a target azimuth, but on its range position too.

To avoid this, a solution is to perform spectral estimation methods from SAR images focused using an exact technique as in [20–23]. The near-field and wide-band compensations that were previously needed are no longer necessary. Then spectral estimation methods are directly applied on the resulting compensated complex SAR image.

Most of the SAR configurations encountered in the litterature [24] are data processed at zero doppler, i.e all the scatterers are seen by the radar over a symmetric angular domain with a similar range of the observation angles and focused SAR image are then well represented over a Cartesian (range-azimuth) grid.

However, in a fan-beam configuration [25], where the dimension of the synthetic aperture is smaller than the area that is imaged, multiple targets may be measured over different ranges of observation angles, i.e each scatterer is seen over a non-symmetric angular domain, where the median value depends on the acquisition geometry. As a result, such an information is much better represented using polar coordinates, rather than a Cartesian coordinates. This effect can be well observed on focused images where sidelobe target responses spread along a quasi-circular trajectory.

This property whose validity is based on the fact that the synthetic aperture is lower than the scene is used in this paper to significantly improve high-resolution focusing results thanks to spectral estimation methods.

First, the SAR geometry configuration and theory to build SAR raw data are presented in the Section 5.1.1. In the section 5.1.2, is demonstrated, by simulation, the undesired effects of four configurations (Far-field and narrow-band/ Far-field and wide-band/ near-field and narrow-band/ near-field and wide-band) on a particular point-like target located at a squint angle from broadside. The authors exhibit the undesired effects before and after applying the near-field, wide-band or both compensation methods from the literature on the four configurations. It reveals that in the near-field wide-band configuration, working directly on the raw data is not suitable to give full capability to spectral estimation methods. Then in Section 5.2, a SAR focusing technique (the back-projection algorithm), to reconstruct a focusing SAR image and to be able to use spectral estimation methods even for squint angle configuration, is applied. The projection over a Cartesian and a Polar grid is shown and spectral estimation methods are applied and compared for the two projections. The remainder of this chapter is organized as follows: Section 5.3 presents the data model, some spectral estimation methods and a flow chart of the proposed processing algorithm. Finally, these spectral estimation methods are applied on simulated data in Section 5.4 and on measured SAR data at millimeter wave with a wide frequency band width and a large aperture in Section 5.5.

5.1 Near-field and wide-band environments

5.1.1 Geometry configuration

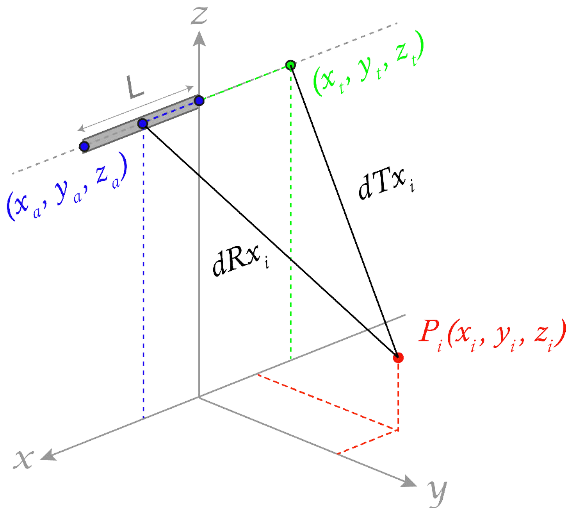

Figure 5.1: Geometry of the Radar imaging configuration.

Considering the case where a transmitting antenna is located at a fixed position in a 3-Dimensional spatial space in a Cartesian coordinate system (see Fig. 5.1). The location of its phase center is (x_t, y_t, z_t). A receiving synthetic array is located over an aperture of length L and aligned with the x-axis. The location of each phase center is (x_a, y_a, z_a) with $x_a \in [-L/2, L/2]$. The radiation pattern of each element is considered as isotropic. N_s point scatterers are considered and identified by their Cartesian coordinates (x_i, y_i, z_i). The index i yields for the i^{th} point scatterer P_i.

The equivalent distance from the radar to the i^{th} point scatterer is given by:

$$\begin{aligned} d_i(x_a) &= (dTx_i + dRx_i)/2 \\ &= (\sqrt{(x_t - x_i)^2 + (y_t - y_i)^2 + (z_t - z_i)^2} \\ &+ \sqrt{(x_a - x_i)^2 + (y_a - y_i)^2 + (z_a - z_i)^2})/2 \end{aligned} \tag{5.1}$$

A transmitted baseband signal $u(\tau)$ in the time domain with its counterpart in the frequency domain $U(f)$ is used, with a frequency diversity over a frequency bandwidth B_f. The signal has been transposed around the carrier frequency f_c before being sent through the medium. The received signals along the aperture $S_r(x_a, f)$ in (5.2) are modeled as a sum of transmitted signals, which are weighted and delayed. The complex weighting s_i represents all the attenuations that occur during the round-trip propagation and the reflectivity of the i^{th} point-like target. The delays arise from the round-trip distance determined in (5.1).

$$S_r(x_a, f) = \sum_{i=1}^{N_s} s_i \, U(f) \, e^{-j4\pi(f+f_c)\, d_i(x_a)/c} + n(x_a, f) \tag{5.2}$$

with c being the speed of light and $n(x_a, f) \sim \mathcal{N}_{\mathbb{C}}(0, \sigma^2)$ being a Gaussian white noise with zero mean and variance σ^2. The focused received signals ($S(x_a, f)$) by adapted filtering [1] along the aperture is expressed as:

$$\begin{aligned} S(x_a, f) &= S_r(x_a, f) \, U^*(f) \\ &= \sum_{i=1}^{N_s} s_i \, H(f) \, e^{-j4\pi(f+f_c)\, d_i(x_a)/c} + n_f(x_a, f) \end{aligned} \tag{5.3}$$

where $H(f)$ being the resulting transfer function which defines the properties of the focused signal and $n_f(x_a, f)$ the filtered white noise by adapted filtering. $(\cdot)^*$, $(\cdot)^t$ and $(\cdot)^H$ yield for the conjugate, the transpose and the conjugate transpose operator, respectively.
Its counterpart in the wavenumber domain is expressed as:

$$S(x_a, k) = \sum_{i=1}^{N_s} s_i \, H(k) \, e^{-j(k+k_c)\, d_i(x_a)} + n_f(x_a, k) \tag{5.4}$$

The round-trip carrier wavenumber is described as $k_c = 4\pi f_c/c$, whereas the baseband wavenumber domain is covered by the signal spectrum such as $k = 4\pi f/c$

The range focused received signals in the spatial domain $s(x_a, d)$ after an inverse Fourier transform along the wavenumber domain is expressed as:

$$s(x_a, d) = \sum_{i=1}^{N_s} s_i \, h(d - d_i(x_a)) \, e^{-j\varphi_x(x_a)} + n_f(x_a, d) \tag{5.5}$$

$h(d)$ is the range ambiguity function in the spatial domain. Where the transmitted signal has a flat spectrum over the frequency band B_f and zero elsewhere, the range ambiguity function corresponds to a sinc function characterized by its range resolution (δ_r) that is inversely proportional to the frequency band used such as $\delta_r = \frac{c}{2B_f}$. $\varphi_x(x_a) = k_c d_i(x_a)$ corresponds to the phase variation along the aperture.

5.1.2 Near-field and wide-band configurations

The range focused received signals $s(x_a, d)$ have exact phase history information about the area of interest. Nonetheless, approximations may be used in various cases.
A particular target is considered to be in a far-field region if it is located far enough from the radar so that the backscattered spherical wave arriving upon the aperture can be considered as a plane wave. It is highly dependent on the range between the target and the aperture length. A simple rule of thumbs is that a backscattered spherical wave from a broadside target is considered as a plane-wave if $d_i(x_a) > (2L^2)/(\lambda_c)$. It corresponds to a phase variation along the aperture lower than $\pi/8$ with λ_c, the wavelength at the carrier frequency.

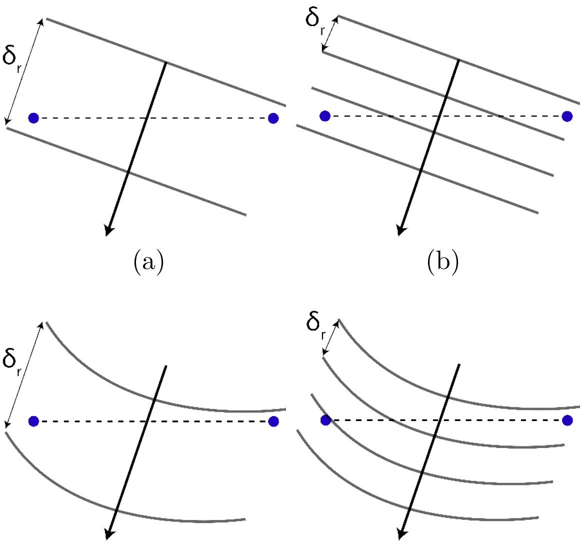

(a) (b)

(c) (d)

Figure 5.2: Sketch of the propagation of the range resolution front for a point-like target in a (a) far-field narrow-band configuration, (b) far-field wide-band configuration,(c) near-field narrow-band configuration,(d) near-field wide-band configuration. The blue dots represent the extreme sides of the aperture represented by the dashed line. The arrow gives the angle of incidence of the wave.

Four different configurations are studied and simulated with the corresponding simulated parameters of each configuration detailed in the Tab. 5.1. In the case of a far-field and narrow-band configuration (see Fig. 5.2a), the range and cross-range focusing are linked to a Fourier transform thanks to the linear phase variations that occurs.

Figure 5.3 shows a simulated raw data matrix for a far-field narrow-band configuration. It has been simulated using only one point-like target located at an angle $\theta_i = 20°$ from broadside with θ defining the cross-range look-angle. The intensity of each image is normalized, expressed in decibels, to peak at 0 dB and clipped at -40 dB. It has to be noticed that the final images are centered on the 2D point-spread function of the point-like target.

Figure 5.3a shows the raw data after range focusing (5.5) . It permits to show that no range migration occurs. The spatial frequency domain $k_x = [(k_c + k)\sin\theta]/2$

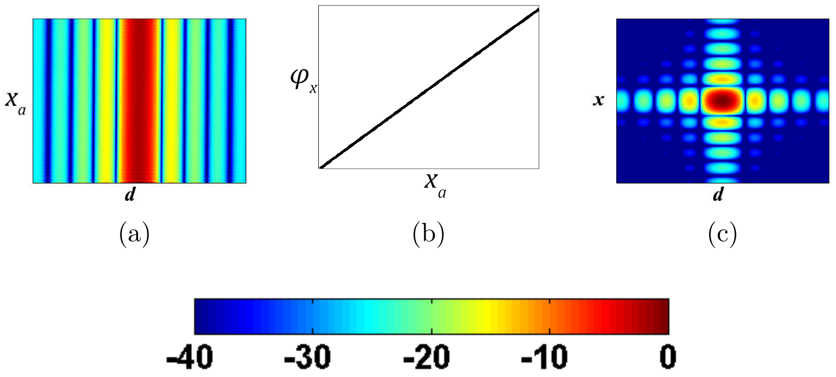

Figure 5.3: Simulation results of the matrix **S** for a point-like target in a far-field narrow-band configuration after (a) the range focusing and (c) the range and the cross-range focusing (Fourier SAR image without compensations). (b) shows the phase variation along the aperture.

corresponds to the projection of the wavenumber $(k_c + k)$ on the aperture plane. It is also referred as the slow-time frequency. Because the point-like target is located relatively far from the aperture ($d_i(x_a) >> L$), the phase variation along the aperture is considered as linear (see Fig. 5.3b). By taking as a reference the center of the synthetic array ($x_a = 0$) and by means of the first order Taylor expansion, the phase variation can be approximated by

$$\varphi_x(x_a) = k_c d_i(x_a) \approx k_c \left(d_i(0) - x_a \sin\theta_i/2\right) \tag{5.6}$$

Figure 5.3c shows the raw data matrix after range and cross-range focusing using a 2-D Discrete Fourier Transform (DFT). The point-like target response is then properly focused. Using (5.6) in (5.5), and omitting the noise, it yields:

$$s(x_a, d) = \sum_{i=1}^{N_s} \alpha_{c_i}\, h(d - d_i(x_a))\, e^{-jk_c x_a \sin\theta_i/2} \tag{5.7}$$

with $\alpha_{c_i} = s_i\, e^{-jk_c d_i(0)}$.

For a given angular sector that is illuminated (i.e. $|\theta_i| \leq \theta_M$), a Radar is considered in a narrow-band condition if the variation of the range Radar ambiguity function ($h(d - d_i(x_a))$) along the receiving aperture is lower than the range resolution (δ_r), avoiding any range cell migration. In other word, the phase shift generated by the back-scattered plane wave from a point-like target located at an angle θ_M from broadside must be lower than δ_r. It yields the following criterion: $B_f < c/(2L\sin\theta_M)$. In the narrow-band case, $k + k_c \approx k_c$, that allows for removing the frequency dependency in (5.4).

Contrarily, in a wide-band configuration (see Fig. 5.2b), the exponential term depends on both the wavenumber frequency $k + k_c$ and the receiving antenna location x_a. Using the wide-band compensation algorithm in [15, 16], the wavenumber frequency dependency can be eliminated using spatial re-sampling, such as:

$$x_a = \frac{k_c - 2\pi B_f/c}{k + k_c}\tilde{x}_a \tag{5.8}$$

Table 5.1: Simulation parameters for the different configurations (FF: Far-field, NF: Near-field, NB: Narrow-band and WB: Wide-band).

Parameter [unit]	**FF/NB**	**NF/NB**	**FF/WB**	**NF/WB**
$f_c/\ B_f$ [GHz]	50/0.5	50/0.5	50/20	50/20
L [m]	0.2	0.2	0.2	0.6
$d(x_a=0)$ [m]	50	1.5	50	1.5
Farfield criterion: $2l^2/\lambda_c$ [m]	13.3	13.3	13.3	120
Narrowband criterion: $c/(2L\sin\theta_M)$ [GHz]	2.2	2.2	2.2	0.73
Non-linear range migration condition: $(L-4\delta_r^2)/(8\delta_r)$ [m] if $\delta_r < L/2$	$\delta_r > L/2$	$\delta_r > L/2$	0.66	6

Substituting the expression of $\tilde{x}_a$ into (5.4) and according to the approximation in (5.6), it gives:

$$\tilde{S}(\tilde{x}_a,k) = \sum_{i=1}^{N_s} \alpha_{c_i}\, H(k) e^{-jkd_i(0)}\, e^{j\,(k_c-2\pi B_f/c)\tilde{x}_a\ \sin\theta_i/2} \tag{5.9}$$

This removes the frequency dependency of the signal and by means of interpolation, it permits to rearrange the raw data in such a way that one particular target response is seen in the same range cell along the aperture.

Figure 5.4 corresponds to the far-field wide-band configuration. In this particular configuration, range migrations occur (see Fig. 5.4a). Hence, the point-like target response is shared among multiple range cells. The selection of one particular range row, where the target is present, gives partial information about the target response. The target response is not properly focused as shown in Fig. 5.4e. Red dashed lines are added in Fig. 5.4c to show the location where a range migration occurs. It can also be used for the others configurations.

After applying the wide-band compensation using (5.9), the range migration is removed (see Fig. 5.4b) that allows for properly focusing the point-like target response (see Fig. 5.4f).

As regards the near-field narrow-band configuration (see Fig. 5.2c), the linear phase variation approximation in (5.6) is not valid anymore. In Figs. 5.5a & 5.5b, no range migration occurs but the non-linear phase shift generated by the spherical wave-front shown in Fig. 5.5c does not allow to properly focus the point-like target response (see Fig. 5.5e). Removing the spherical component, by only keeping the linear phase shift variation from the plane wave assumption, is desired. But the near-field compensation have to be determined for each SAR measurement cell. In fact, each target location has its own wave-front that is dependent on the pair of a range and a cross-range location. At one particular location $\hat{P}_i$ $(\hat{x}_i, \hat{y}_i, \hat{z}_i)$, the distance variation along the aperture $\hat{d}_i(x_a)$ is determined using (5.1). The phase

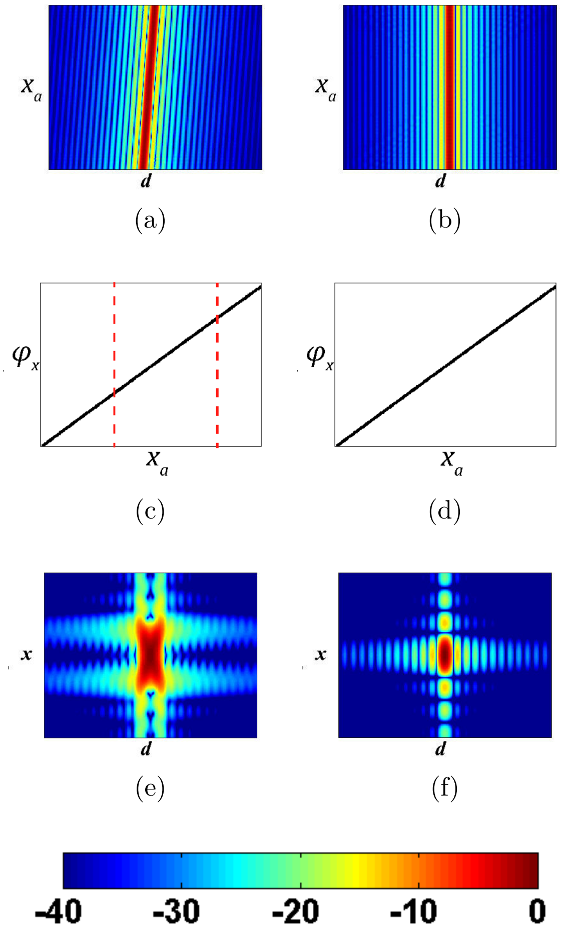

(a) (b)

(c) (d)

(e) (f)

Figure 5.4: Simulation results of the raw data matrix **S** in the far-field wide-band configuration (a), (c), (e) without the wide-band compensation and (b), (d), (f) with the wide-band compensation. The results in (a) and (b) are shown after the range focusing and (e), (f) after the range and the cross-range focusing (Fourier SAR image). In (c) and (d) are shown the phase variation along the aperture after the range focusing.

shift generated by the distance variation is then removed from the received raw data in (5.5) and replaced by a linear phase variation from the plane-wave assumption determined by the angular location of $\hat{P}_i$ from broadside (i.e. $\hat{\theta}_i$).

$$\hat{s}(x_a, d) = s(x_a, d)\, e^{jk_c \hat{d}_i(x_a)}\, e^{-jk_c x_a \sin\hat{\theta}_i/2} \tag{5.10}$$

Figure 5.5d shows the linear phase variation after near-field compensation. After being focused in range and cross-range, the point-like target is properly focused (see Fig. 5.5f).

Finally, the Figs. 5.2d & 5.6 correspond to the near-field wide-band case. The range migration in Fig. 5.6a is a combination of the linear range migration due to the wide-band signal used and a non-linear range migration due to the near-field location of the target. According to Fig. 5.6c, it is apparent that the target response is not properly focused. In Figs. 5.6c & 5.6f & 5.6i are shown the point-like target responses without compensations, with the wide-band compensation and with wide-band and near-field compensations, respectively. Exploiting the two previous

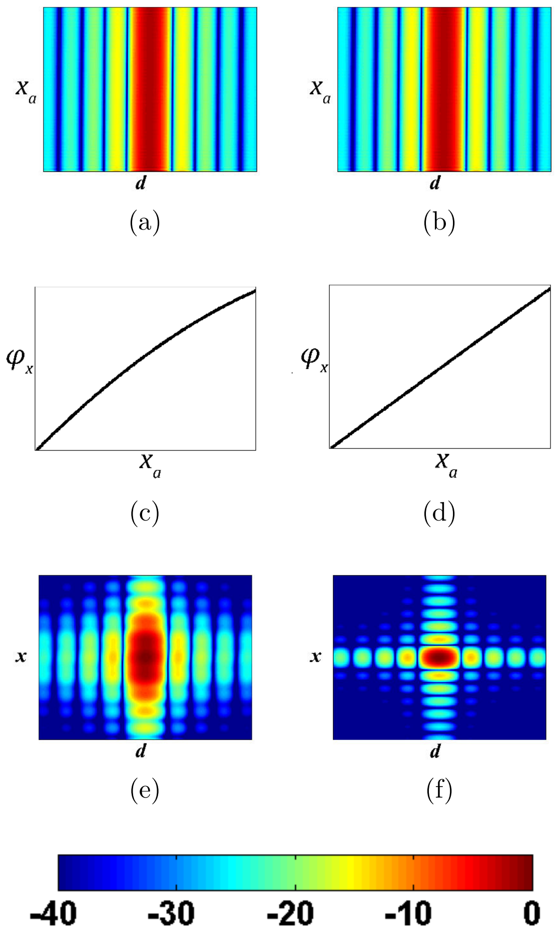

(a) (b)

(c) (d)

(e) (f)

Figure 5.5: Simulation results of the raw data matrix **S** in the near-field narrow-band configuration (a), (c), (e) without the near-field compensation and (b), (d), (f) with the near-field compensation. The results in (a) and (b) are shown after the range focusing and (e), (f) after the range and the cross-range focusing (Fourier SAR image). In (c) and (d) are shown the phase variation along the aperture after the range focusing.

algorithms together does not properly focus the point-like target due to the non-linear range migration generated by targets in a near-field environment. The non-linear range migration from a broadside target in near-field occurs if $d_i(x_a) < (L^2 - 4\delta_r^2)/(8\delta_r)$.

In the following section, focusing SAR techniques such as the back-projection algorithm are used to consider the exact geometry of the problem and to combine coherently the received signals to properly focus the point-like targets.

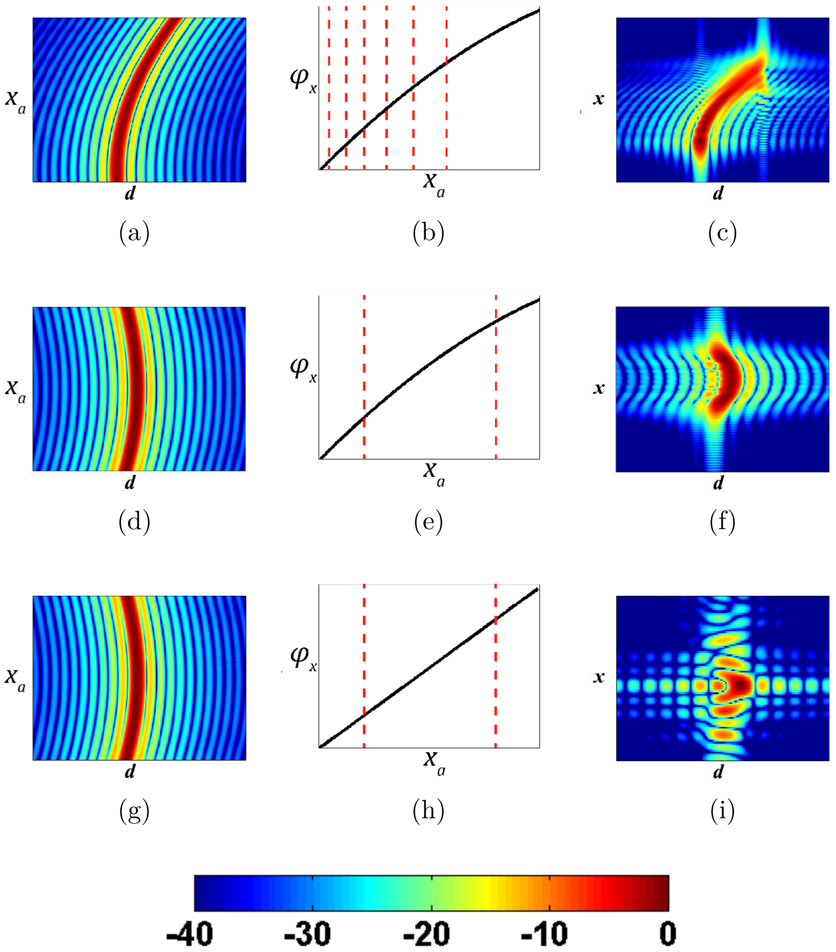

(a) (b) (c)

(d) (e) (f)

(g) (h) (i)

Figure 5.6: Simulation results of the raw data matrix **S** in the near-field wide-band configuration after (a), (d), (g) the range focusing and after (c), (f),(i) the range and the cross-range focusing (Fourier SAR image). In (b), (e) and (h) are shown the phase variation along the aperture after the range focusing. In (a), (b), (c) no compensation occurs. In (d), (e), (f), only the wide-band compensation is applied and finally in (g), (h), (i), the near-field and the wide-band compensations are applied.

5.2 Compensation using focusing techniques

To compensate for the near-field and wide-band behaviors on the raw-data, a focusing technique is employed to project the received signals over a 2D Cartesian grid to have an estimate of the complex 2D reflectivity field. The 2D plane, which is regularly sampled, usually follows a Cartesian grid having the origin located at the center of the synthetic receiving array. Each pixel corresponds to a 2D spatial area of size δ_y and δ_x with δ_y and δ_x perpendicular and parallel to the array aperture respectively. The i^{th} pixel p_i has a spatial coordinate $(x_i = \alpha\,\delta_x, y_i = \beta\,\delta_y)$ with α and β real numbers. The regular grid is shown in Fig.5.7a.

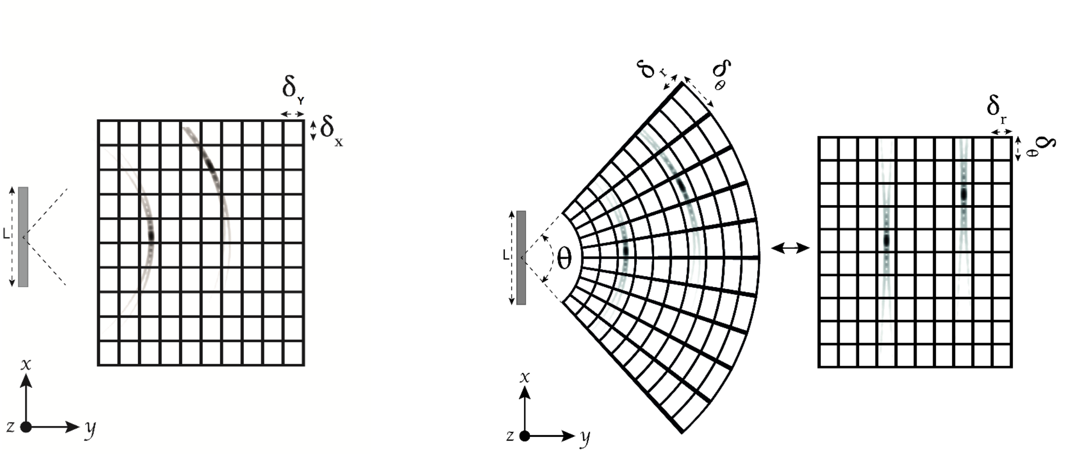

(a) (b)

Figure 5.7: Imaging geometry of the synthetic aperture Radar with the received raw data focused over (a) a 2D Cartesian grid (b) a 2D polar grid.

The back-projection algorithm is used for generation of the focused SAR image $f(x, y; z = z_0)$ with z_0 a constant. In what follows, the projection is performed over a 2D-plane at one particular height from the synthetic aperture. For one particular range cell, it takes the received signal from a given position along the aperture x_a in (5.5), and back-projects it over a spherical arc corresponding to all the possible contributing image pixels. Once the back-projection is performed on the remainder received signals from the other ranges and the other positions along the aperture, then accumulated, the focused SAR image is obtained. One particular pixel p_i of the focused SAR image spanning the Cartesian grid is constructed by:

$$\hat{f}(x_i, y_i; z = z_0) = \int_{x_a=-L/2}^{L/2} s(x_a, d_i(x_a))e^{jk_c d_i(x_a)}\mathrm{d}x_a \tag{5.11}$$

Spectral Estimation Methods may be applied on the focused SAR image to improve the spatial resolution. However, because the two point-like scatterers are in a near-field wide-band configuration, the 2D ambiguity function of each point scatterer spread on multiple rows and multiple columns (see Fig. 5.7a). Extracting the phase history of each point scatterer by the selection of one row or one column is not valid anymore as only partial information are selected.

To overcome this issue, a better solution, is to project the received signals over a polar grid that follows the 2D ambiguity function of point-like scatterers anywhere in the considered area from the radar system perspective. The polar coordinates is considered with non-uniform sampling of the range projected over a 2D plane and a non-uniform sampling of the angle taking into account the decrease of cross-range resolution at squint angles. Such sampling can be transformed to Cartesian coordinates that are dense near the array and sparse away from the array. Hence, the i^{th} pixel p_i covers a 2D spatial area of size δ_r the range resolution and δ_θ the angular resolution with spatial coordinates over the Cartesian coordinates ($x_i = r_i \cos\theta_i, y_i = r_i \sin\theta_i$), as shown in Fig. 5.7b. By doing so, the selection of one particular row or column gives full information about the target behavior. Because the 2D SAR image resolution is inherently limited by the frequency band used and the synthetic aperture dimensions, the polar grid is then critically sampled to match the SAR system resolution, reducing the size of the 2D SAR image to avoid long time calculation during the spectral estimation method process.

Figure 5.8a shows the projection of the range resolution δ_r over the 2D-plane. As it is the projection of the range resolution over the ground in SAR configuration, it is named as ground-range resolution. As regards a synthetic aperture that is located at a height $z_0 = H$ from the 2D plane, the ground range resolution (δ_{rg}) at the i^{th} pixel location is defined as:

$$\delta_{rg}(\phi_i) = \frac{\delta_r}{\cos\phi_i} \tag{5.12}$$

with ϕ_i being the elevation angle. In the same manner, Figure 5.8b shows the azimuth angular resolution. When the beam of the synthetic aperture is digitally steered at a broadside angle ($\theta_i = 0$), the angular resolution is defined as $\delta_\theta = \lambda_c/L$ with λ_c the carrier wavelength. When the beam of the synthetic aperture is digitally scanned, the length of the synthetic aperture seen from a θ_i angular point of view is reduced, given an aperture length of $L\cos\theta_i$. The azimuth angular resolution is then:

$$\delta_\theta(\theta_i) = \frac{\lambda_c}{L\cos\theta_i} \tag{5.13}$$

Considering the variation of the spatial resolution over the 2D-plane, the polar grid is critically sampled at the system resolution. Hence, each pixel has its own set of range and cross-range angular resolution. The i^{th} pixel covers a spatial area of size ($\delta_{rg}(\phi_i)$, $\delta_\theta(\theta_i)\, d_i(0)$) that corresponds to the area covered by the synthetic aperture beam at this particular location. As for the regular grid, the received raw data is then projected using focusing algorithms over the irregular sampled polar grid using (5.11), given the critically sampled 2D complex SAR matrix $\mathbf{Y} = f(x, y; z = z_0)$. Hence, the data is refocused so that the phase of the Radar ambiguity function is linear. This allows image formation via DFTs. The near-field and wide-band behaviors are compensated over the entire area of interest. Figure 5.9 shows the simulated results in the same near-field wide-band configuration used in Fig. 5.6 where the raw data is projected over a Cartesian and a polar grid. Thanks to the focusing technique, the projection over both the Cartesian and polar coordinates permits to have a linear phase variation, however, the 2D spectrums of reconstructed images after using a focusing technique show that the projection over a polar coordinate permits

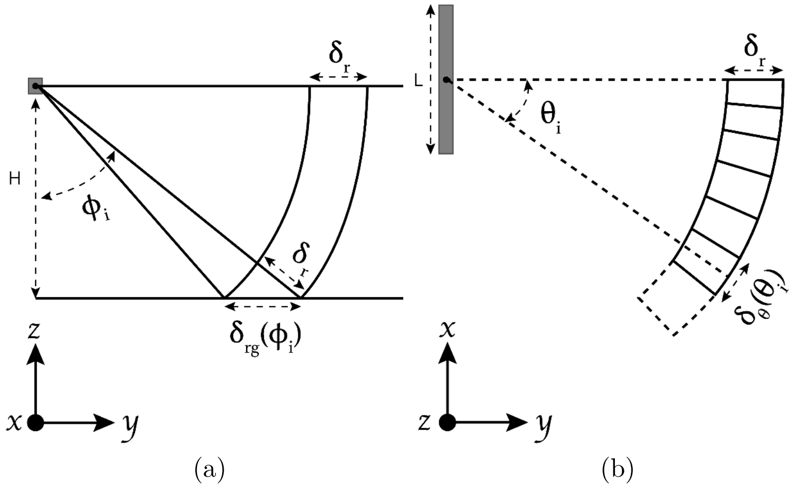

Figure 5.8: Cutting views of the Imaging geometry showing the variation of (a) the range resolution along the plane considered (b) the azimuth angular resolution along the range of observation angles.

to have a convenient spectrum to apply 2-D spectral estimation methods unlike the projection over a Cartesian grid. If large amount of data is to be processed, it may be of interest to apply spectrum analysis algorithms only on overlapping sub-images and then reconstruct the final results [20].

To be digitally processed, the continuous received signals $s(x_a, d)$ are sampled to give the 2-D data sequence $\mathbf{Y} \in \mathbb{C}^{N_a \times N_f}$ where N_f corresponds to the number of frequency components taken after the sampling process in the frequency (wavenumber) domain to be adapted to the analysis of the observed scene (avoiding any range ambiguity). The continuous aperture x_a is sampled in a group of N_a receiving elements with element spacing Δ_x. It gives $x_a(m) = \left(m - \frac{N_a+1}{2}\right) \Delta_x$ with $\{x_a(m)\}_{m=0}^{N_a-1}$. The range vector $\{d(n)\}_{n=0}^{N_f-1}$ is sampled at the range resolution with $d_{amb} = N_f\, \delta_r$, the ambiguous distance. Since the range vector d is a discrete vector, obtaining $d_i(x_a)$ from d for applying the back-projection algorithm in (5.11) requires an interpolation.

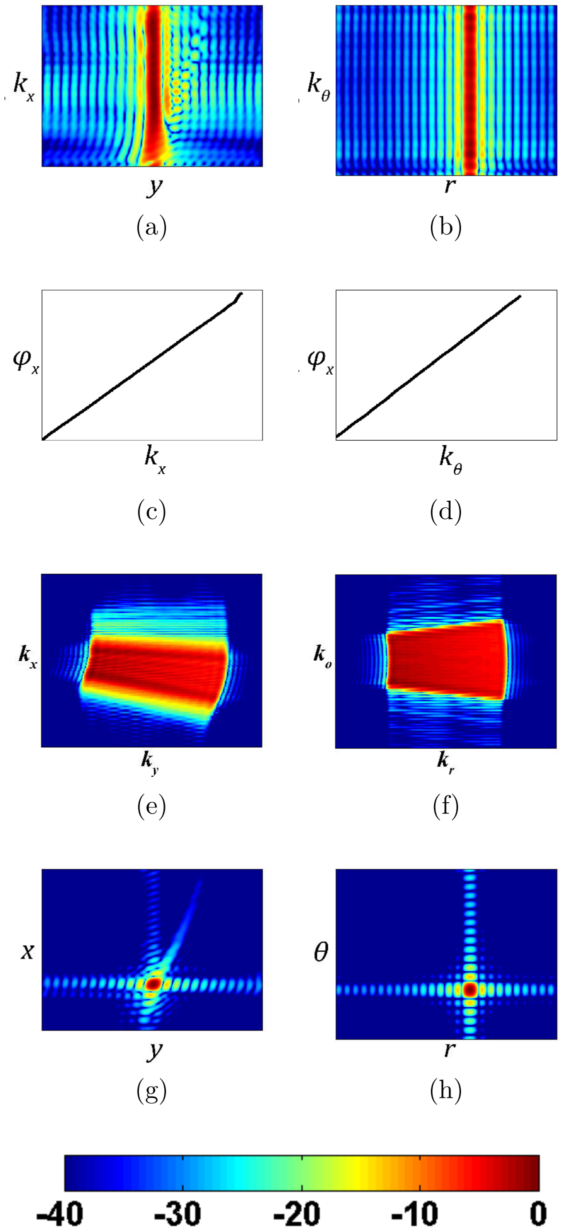

Figure 5.9: Simulation results of the raw data matrix **S** after applying the focusing technique in the near-field wide-band configuration. The raw data is projected over (a), (c), (e), (g) a Cartesian grid (see Fig. 5.7a) and over (b), (d), (f), (h) a polar grid (see Fig. 5.7b) after (a), (b) the range focusing, after (g), (h) The range and the cross-range focusing (Fourier SAR image). In (c) and (d) are shown the phase variation after the range focusing and (e), (f) shows the 2D spectrum of the reconstructed image.

5.3 Spectral analysis algorithms

Once the near-field and wide-band signal features have been accounted for, spectral estimation methods can be used to improve resolution and contrast with reduced speckle effects if the appropriate data model is used. In practice, the construction of an adequate data model based on a finite number of observations can not be perfectly achieved. The data model remains an estimated data model that attempts to match as far as possible the reality.

5.3.1 Signal Model

Spectral estimation methods may be used along both the range and the cross-range direction. Along the range direction, the spectral diversity is achieved from multiple frequency components in a finite frequency band. Once spectral estimation methods are applied, this gives improved range location estimates. Along the cross-range direction, the spectral diversity is achieved from a sampled aperture in the spatial domain. Applying spectral estimations methods on the spatial frequency domain gives improved Direction of Arrival (DoA) estimates. An established signal model of SAR data [20, 21] along the cross-range direction consists of N_s waves arriving from distinct directions θ_i, each corresponding to a specific scatterer. The complex amplitude of the i^{th} signal is s_i and an array of N_a elements is considered. The additive white Gaussian noise vector $n \sim \mathcal{N}_{\mathbb{C}}(0, \sigma_n^2)$ has zero mean and variance σ^2. The array output vector $\mathbf{y} \in \mathbb{C}^{N_a}$ is given by:

$$\mathbf{y} = \sum_{i=1}^{N_s} \mathbf{a}(\theta_i) s_i + \mathbf{n} = \mathbf{A}\mathbf{s} + \mathbf{n} \tag{5.14}$$

where

$$\mathbf{A} = [\mathbf{a}(\theta_1), \mathbf{a}(\theta_2), ..., \mathbf{a}(\theta_{N_s})] \in \mathbb{C}^{N_a \times N_s} \tag{5.15}$$

is the received signal steering matrix, which contains the steering vectors. It corresponds to the compensations applied on the synthetic array for a range of observation angles (DoAs). The signal vector, which represents the complex reflectivities of the scatterers, is given by:

$$\mathbf{s} = [s_1, s_2, ..., s_{N_s}]^T \in \mathbb{C}^{N_s} \tag{5.16}$$

In the narrow-band plane-wave case (far-field zone), the steering vector of the i^{th} signal using (5.6) is:

$$\mathbf{a}(\theta_i) = e^{-j\xi} \, [1, e^{-jk_c\Delta_x' \sin(\theta_i)}, ..., e^{-j(N_a-1)k_c\Delta_x' \sin(\theta_i)}]^T \tag{5.17}$$

where ξ is an arbitrary phase, and $\Delta_x' = \Delta_x/2$ represents the half of the array inter-element spacing and accounts for the radar definition of the round-trip wavenumber given earlier.

The data covariance matrix $\mathbf{R} \in \mathbb{C}^{N_a \times N_a}$ is expressed as:

$$\begin{aligned} \mathbf{R} &= \mathrm{E}\left\{\mathbf{y}\,\mathbf{y}^H\right\} \in \mathbb{C}^{N_a \times N_a} \\ &= \mathbf{A}\mathbf{R}_{\mathbf{ss}}\mathbf{A}^H + \sigma^2\mathbf{I} \end{aligned} \tag{5.18}$$

with $\mathrm{E}\{\cdot\}$ being the expectation operator, $\mathbf{R_{ss}}$ being the source covariance matrix, and $\sigma^2\mathbf{I}$ being the noise covariance matrix.
The covariance matrix may be decomposed onto its signal and noise subspaces such as [26]:

$$\mathbf{R} = \mathbf{U}\,\mathbf{\Lambda}\,\mathbf{U} = \mathbf{U_s}\,\mathbf{\Lambda_s}\,\mathbf{U_s}^H + \mathbf{U_n}\,\mathbf{\Lambda_n}\,\mathbf{U_n}^H \tag{5.19}$$

with $\Lambda = \mathrm{diag}(\lambda_1, ..., \lambda_{N_a})$ being the eigen-value matrix with $\lambda_i \geqslant \lambda_{i+1}$. Considering uncorrelated source and signal terms, $\Lambda_s = \mathrm{diag}(\lambda_1, ..., \lambda_{N_s})$ is the source eigen-value matrix and $\Lambda_n = \mathrm{diag}(\lambda_{N_s+1}, ..., \lambda_{N_a})$ is the noise eigen-value matrix. $\mathbf{U}$ is the eigen-vector matrix with $\mathbf{U}_s$ and $\mathbf{U}_n$, the corresponding signal-space and noise-space eigen-vector matrices.

The non-singularity of the covariance matrix estimate requires a pre-processing scheme, named spatial smoothing, which is, in practice, widely employed [27] to guarantee this property. It is based on a diversity of the ξ phase in (5.17) and consists in extracting the array covariance matrix as the average of a group of smaller overlapping sub-array covariance matrix. The number of sub-arrays is $K = N_a - N_u$ of length N_u. It corresponds to a spatial smoothing ratio $\eta = N_u/N_a$. Using $\mathbf{y} \in \mathbb{C}^{N_a}$, the estimated covariance matrix after spatial smoothing $\hat{\mathbf{R}} \in \mathbb{C}^{N_u \times N_u}$ is then determined as:

$$\hat{\mathbf{R}} = \frac{1}{K}\sum_{k=1}^{K} \mathbf{y}_k\,\mathbf{y}_k^H \tag{5.20}$$

with $\mathbf{y}_k = [y_k, ..., y_{k+N_u-1}]^T$. y_k being the received signal from the k^{th} element of $\mathbf{y}$. The objective is to estimate the DoAs (θ_i) and the reflectivities (s_i).

Various spectral analysis algorithms exist in the literature [6, 7, 9, 13, 28]. The capability of separation of two or more closely spaced scatterers is, in practice, mainly affected by the Signal-To-Noise ratio (SNR), the number of receiving elements (N_a), the kind of observed target responses (stochastic or deterministic/ correlated or uncorrelated ...) [29, 30]. In this section, two non-parametric and one parametric spectral analysis algorithms are summarized that are the conventional beamforming, the CAPON and the MUSIC methods. We do not wish to compare the performance of these algorithms, but rather to show that the proposed method may be applied to any existing spectral analysis approach. The results are then demonstrated using the three algorithms mentioned above.

5.3.2 Spectral Estimation Methods

All the methods considered belong to the filter bank category [7]. Given, $\mathbf{h}(\omega)$ a spatial filter and $\mathbf{Q}$ a square matrix, the methods follow the generic equation:

$$\hat{P}(\omega) = \Big(\mathbf{h}^H(\omega)\mathbf{Q}\mathbf{h}(\omega)\Big)^{\alpha} \tag{5.21}$$

The DoA estimation, on a finite range of observation angles, is applied with $\theta \in [\theta_{min}, \theta_{max}]$ with N_θ scanning angles. In the plane wave assumption, the phase shift generated by a backscattered plane-wave arriving at an angle θ from broadside between two receiving antennas is $\omega = k_c\Delta'_x \sin\theta$. $\mathbf{h}(\omega)$ is built from the steering matrix defined in (5.15). The methods are summarized in Tab. 5.2.

Table 5.2: Spectral estimation methods

Methods	**Spectrum estimation**
Beamforming [6]	$\mathbf{Q} = \hat{\mathbf{R}},\ \alpha = 1,\ \mathbf{h}(\omega) = \mathbf{a}(\omega)$ $\hat{P}_{bf}(\omega) = \mathbf{a}^H(\omega)\hat{\mathbf{R}}\mathbf{a}(\omega)$
CAPON [31]	$\mathbf{Q} = \hat{\mathbf{R}},\ \alpha = 1,\ \mathbf{h}(\omega) = \frac{\mathbf{a}(\omega)\hat{R}^{-1}}{\mathbf{a}(\omega)^H \hat{R}^{-1}\mathbf{a}(\omega)}$ $\hat{P}_{CAPON}(\omega) = \frac{1}{\mathbf{a}^H(\omega)\hat{\mathbf{R}}^{-1}\mathbf{a}(\omega)}$
MUSIC [26]	$\mathbf{Q} = \hat{\mathbf{U}}_\mathbf{n}\hat{\mathbf{U}}_\mathbf{n}^\mathbf{H},\ \alpha = -1,\ \mathbf{h}(\omega) = \mathbf{a}(\omega)$ $\hat{P}_{MUSIC}(\omega) = \frac{1}{\mathbf{a}^H(\omega)\hat{\mathbf{U}}_\mathbf{n}\hat{\mathbf{U}}_\mathbf{n}^\mathbf{H}\mathbf{a}(\omega)}$

The coordinates of the local maxima of $\hat{P}(\omega)$ are linked to the angular positions of the observed scatterers. As regards the Beamforming and CAPON algorithms, $\hat{P}(\omega_i)$ provides an estimate of $\mathrm{E}\left\{|s_i|^2\right\}$ whereas MUSIC do not provide amplitude information. $\mathrm{E}\left\{|s_i|^2\right\}$ may be estimated using a least-square approach [7]. The maximum outputs of the beamforming algorithm provide an estimate of the signal power s_i and the signal parameter estimate is given by the value of ω that achieves this maximum ($\omega_i = k_c \Delta'_x \sin(\theta_i)$). It produces coherent complex image that represents the output of banks of narrow-band filters where each filter output is tuned to a given DoA. The beamforming does not require any spatial smoothing pre-processing. Nevertheless, smoothing reveals useful to reduce speckle effects. CAPON uses selective adaptive filters around the current frequency (ω) and minimizes the total power subject to the constraint that the filter passes the frequency ω undistorted. It permits to improve the spatial resolution while maintaining high image contrast. MUSIC uses the sub-space decomposition (5.19) to indicate the presence of sinusoidal components in the studied signal. The main sinusoidal components are selected (model selection) by estimating the size of the noise sub-space. The Akaike Information Criterion [32] provides a means for model selection (to estimate N_s). This implies that $N_s < N_a$. Further, MUSIC only extracts the main components with the strongest responses. An extension of Table 5.2 for the 2-Dimensional case is shown in [33, 34].

5.3.3 Near-field wide-band configuration

In a near-field configuration with wide-band signals, it has been explained in Section 5.1.2 that the phase variation depends on the range and the DoA. This implies that the steering vectors have to be modified for each pair of locations θ and r. To overcome this important limitation, we propose here to apply the spectral analysis algorithms on the complex 2D focused SAR image where the near-field and wide-band effects have been compensated. A discrete 2-D SAR image is built from (5.11) as $[\mathbf{Y}]_{i,j} = \hat{f}(x_i, y_j; z = z_0)$ with $\mathbf{Y} \in \mathbb{C}^{N_n \times N_m}$. Then 1-D or 2-D spectral estimation techniques may be applied to improve the focusing over the ground-range (y), azimuth (x) or both domains.

The 1-D spatial smoothing in (5.20) is then applied on the DFT of one particular columns $y = C_i$ as shown in Fig.5.10a.

In the same manner as the 1-D spectral analysis case, it can be performed 2-D spectral estimation methods on the focused SAR image as in [20–23]. Unlike the approach proposed in [20], which consists in applying spectral estimation methods from a SAR image sampled in Cartesian coordinates, we propose to deal with SAR images projected in a polar format (r, θ) as depicted in Fig. 5.7. This permits to avoid limitations encounter by Cartesian sampling for the particular fan-beam configuration.

From the $N_n \times N_m$ matrix $\mathbf{Y}$, 2-D spectral estimation methods are applied. Given $\mathbf{Z}$ the 2D Fourier transform of the matrix $\mathbf{Y}$ and given a $(N_n\, N_m) \times 1$ vector as

$$\mathbf{z} \hat{=} \operatorname{vec}(\mathbf{Z}) \tag{5.22}$$

with vec(.) being the operation of stacking the columns of a matrix on top of each other, the covariance matrix is:

$$\mathbf{R} = \mathrm{E}\left\{\mathbf{z}\mathbf{z}^H\right\} \tag{5.23}$$

The spatial smoothing stated in (5.20) is also used for the 2D case (see Fig. 5.10b). The estimated covariance matrix is:

$$\hat{\mathbf{R}} = \frac{1}{KL} \sum_{k=1}^{K} \sum_{l=1}^{L} \mathbf{z}_{k,l}\, \mathbf{z}_{k,l}^H \tag{5.24}$$

with

$$\mathbf{z}_{k,l} = \operatorname{vec}\left(\begin{bmatrix} [\mathbf{Z}]_{k,l} & \cdots & [\mathbf{Z}]_{k,l+N_u-1} \\ \vdots & \ddots & \vdots \\ [\mathbf{Z}]_{k+N_u-1,l} & \cdots & [\mathbf{Z}]_{k+N_u-1,l+N_u-1} \end{bmatrix}\right). \tag{5.25}$$

Hence, $\mathbf{z}_{k,l}$ is a $(N_u \cdot N_u) \times 1$ vector.

The elements of the 2-D steering vector $\mathbf{a}_{\omega_1,\omega_2} = \mathbf{a}_{\omega_1} \otimes \mathbf{a}_{\omega_2}$ constitute the Kronecker product of the two 1-D steering vector associated with the exponential coefficients of the discrete Fourier transform applied on $\mathbf{Y}$ to obtain $\mathbf{Z}$ with $\omega_1 \,\&\, \omega_2 \in [0, 2\pi[$. The filter $\mathbf{h}(\omega)$ in the Table 5.2 is replaced by $\mathbf{a}_{\omega_1,\omega_2}$ and the estimated covariance matrix in (5.24) is used to apply 2D spectral estimation methods. The corresponding spectral estimation results may be represented using a re-sampling of the reflectivity maps $\hat{P}(\omega_1, \omega_2) \to \hat{P}(x, y)$ with $x = r\, \cos\theta$ and $y = r\, \sin\theta$.

Considering an aperture length $L = 0.1$ m and one point-like target located at an angle $\theta_i = 20°$ from broadside at a range $d_i(x_a = 0) = 1.5$ m from the radar, the steps for applying spectral analysis algorithms in a near-field wide-band configuration are outlined in Fig. 5.11 in the general 2D case and listed as follows:

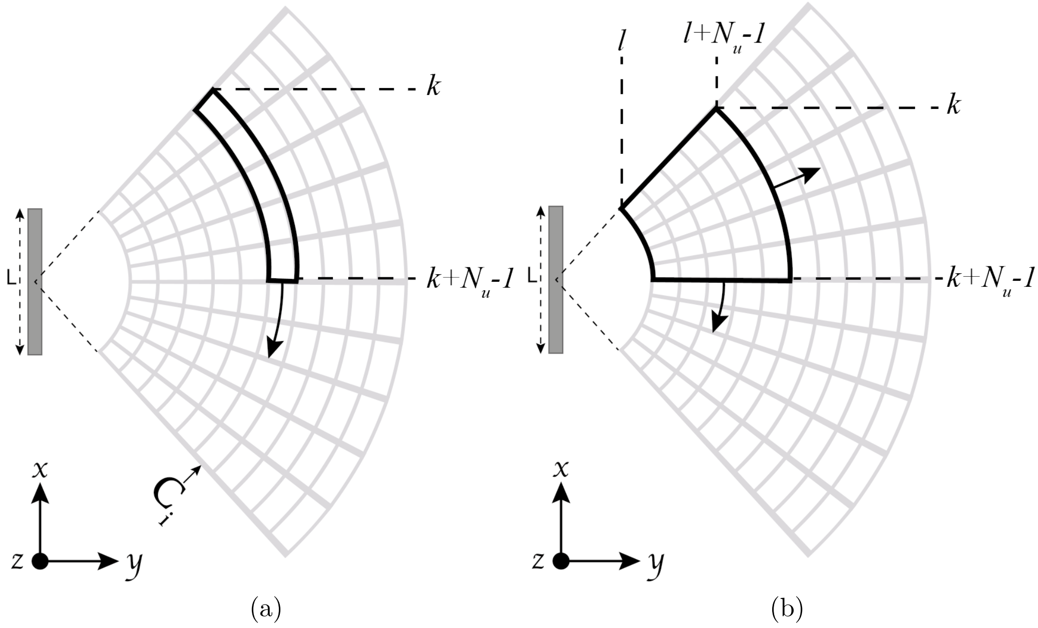

Figure 5.10: (a) 1D (b) 2D Spatial smoothing applied on the irregular grid.

- From simulation or measurement, the received signals are used to built the complex raw data matrix ($S(x_a, f)$).
- The complex raw data matrix is projected onto an over-sampled polar grid (complex 2D focused SAR image) by applying focusing techniques such as the back-projection algorithm ($\hat{f}(x,y; z = z_0)$).
- the complex 2D focused SAR image is transformed to the spectral domain using a 2D DFT.
- The useful spectrum is selected ($\mathbf{Z}$). Its limits are defined as the spectral region with a sufficiently high signal to noise ratio.
- 2D spatial smoothing is applied on the useful spectrum.
- 2D spectral estimation methods are applied on the spatially smoothed spectrum to give the final result ($\hat{P}(\omega_1, \omega_2)$).

The projection over a polar grid permits to have a symmetric and centred 2D spectrum unlike the projection over a Cartesian grid. Then it provides full capability to spectral estimation methods as shown in Fig. 5.12 in which the spectral estimation methods are applied on both projection methods to validate the principle. The final complex image results correspond to projections over a polar grid (x=r $\cos\theta, y = r$ $\sin\theta$). To have a physical interpretation of the final images, interpolations and denormalizations have to be applied to project the final results over a regular grid, which matches the Cartesian coordinates ($\hat{P}(x, y)$).

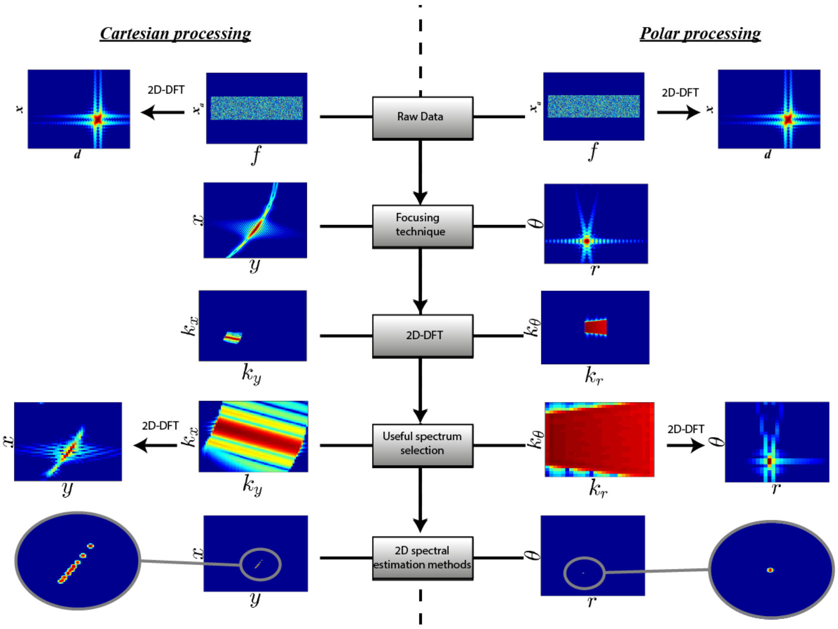

Figure 5.11: Flow chart of applying the spectral analysis algorithms in a near-field environment with wide-band signals.

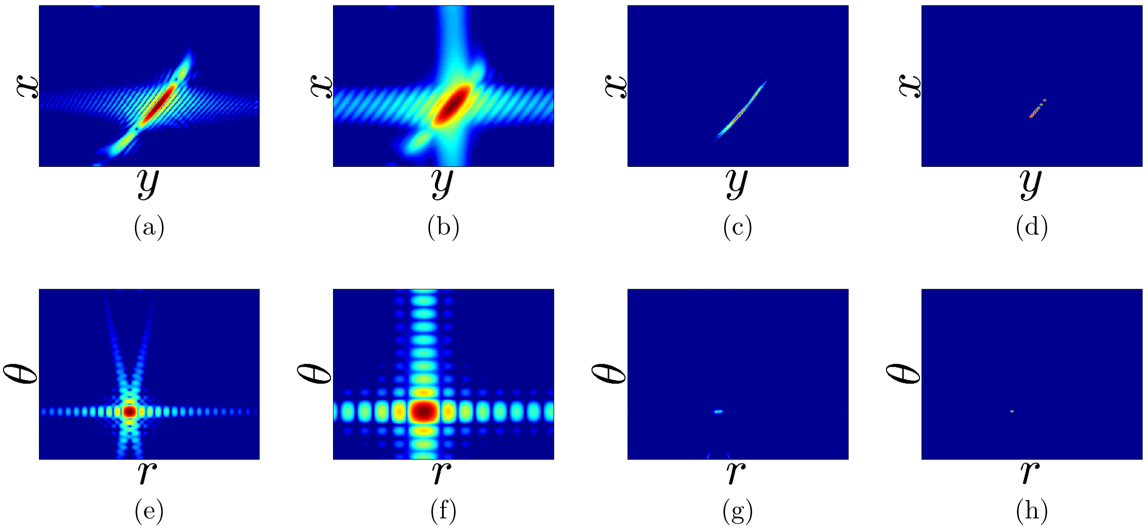

(a) (b) (c) (d)

(e) (f) (g) (h)

Figure 5.12: Simulated results of 2D spectral estimation methods using (a), (b), (c), (d) a Cartesian grid and (e), (f), (g), (h) a polar grid with (a), (e) the beamforming method, (b), (f) spatial smoothed beamforming, (c), (g) the CAPON method and (d), (h) the MUSIC method.

5.4 Simulations

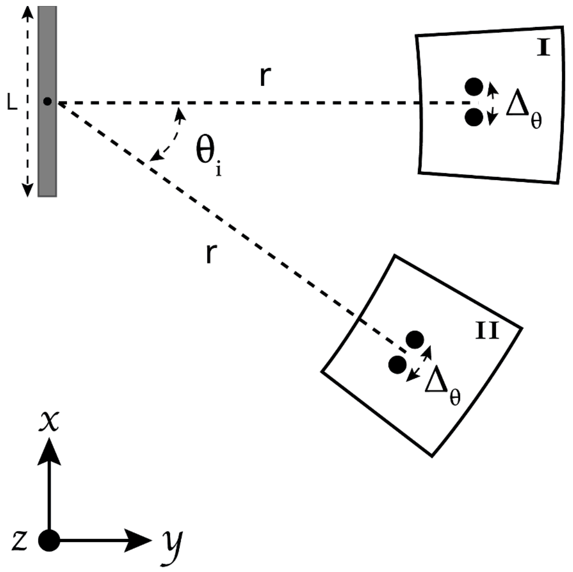

Figure 5.13: Imaging configurations with the two closely spaced point scatterers located in the broadside angle area I and the squint angle area II.

In this simulation, the study is focused at millimeter wave at a carrier frequency of 50 GHz using a frequency band of 20 GHz. The aperture length is 20 cm (100 elements) corresponding to a range resolution of $\delta_r = 0.75$ cm and an azimuth angular resolution of $\delta_\theta = 1.8°$ at broadside angle. Two closely spaced point scatterers ($\Delta_\theta = 1.5°$) are placed at a range r of 1 meter from the center of the aperture as shown in Fig. 5.13. Two target configurations are used. The targets are located at broadside angle ($\theta_i = 0°$) in Area I and at squint angle ($\theta_i = 45°$) in area II with a SNR= 20dB after range focusing.

In Fig. 5.14 is shown the three spectral estimation methods results in area I and II. For the CAPON and MUSIC methods, a spatial smoothing ratio η of 50% is applied and the methods are applied along the cross-range direction for one particular range, and sequentially applied to the other ranges. In the same way, in Fig. 5.15, the 2D spectral estimation methods are applied. The simulations demonstrate the capability of spectral estimation methods to separate two closely spaced targets that are not separable by means of classic beamforming methods. It also permits to show the capability of separation of closely targets even at squint angles with great accuracy when used with the irregular grid. Applying the beamforming method gives high side-lobes level that spreads over a wide spatial region. For the other methods, these artifacts are minimal in the 2D case. The resolution of MUSIC, when the area of interest is simulated using point-like targets, is greater than the resolution of CAPON.

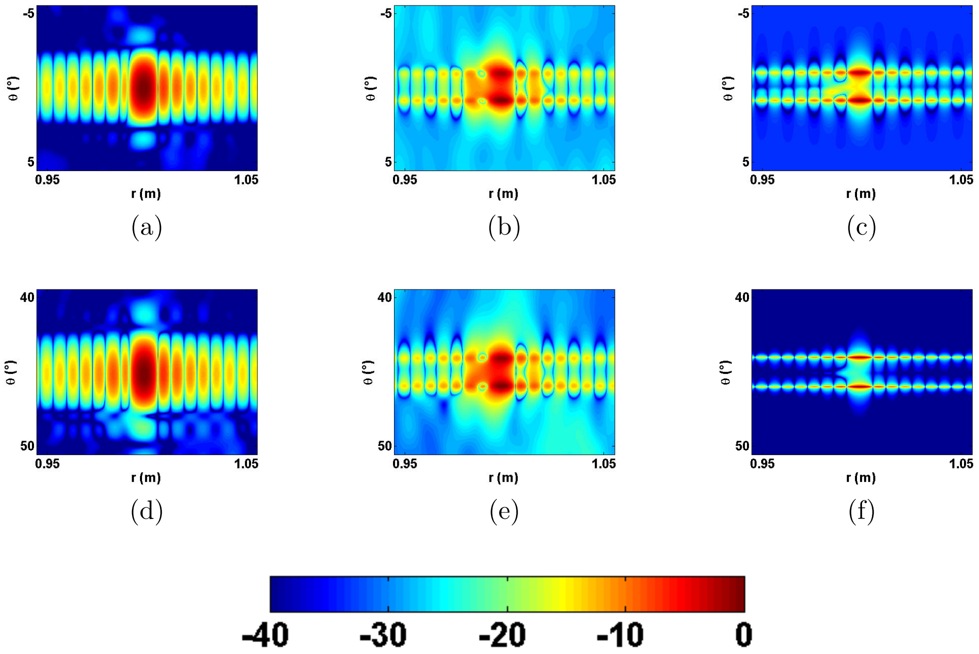

(a) (b) (c)

(d) (e) (f)

Figure 5.14: 1D spectral estimation methods applied along cross-range direction on the (a), (b), (c) broadside angle area I and (d), (e) (f) squint angle area II. (a), (d) show the beamforming method, while (b), (e) show the CAPON method and (c), (f) show the MUSIC pseudo-spectra method.

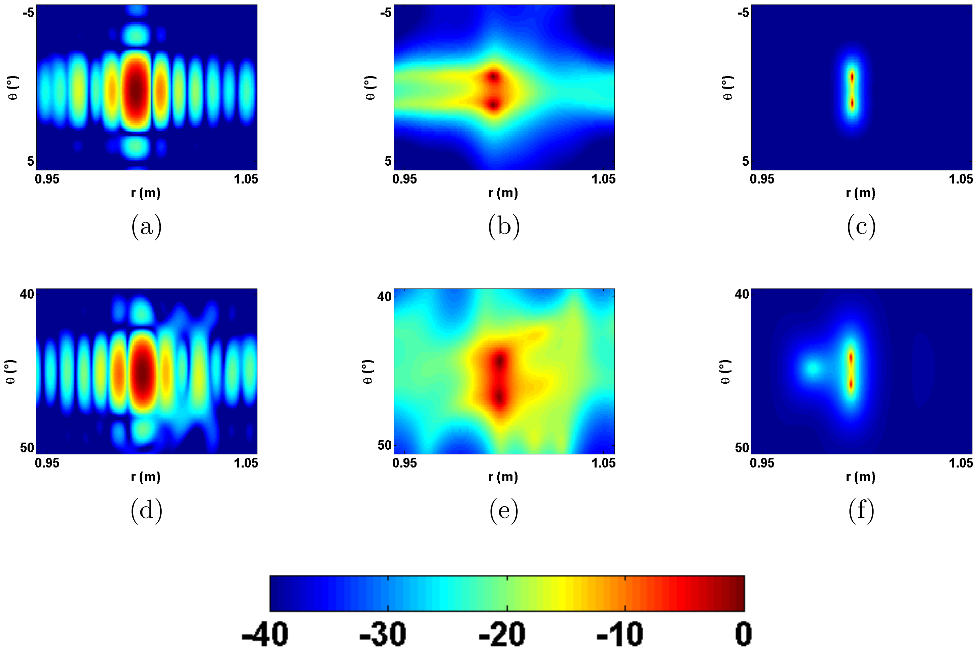

(a) (b) (c)

(d) (e) (f)

Figure 5.15: 2D spectral estimation methods applied on the (a), (b), (c) broadside angle area I and (d), (e) (f) squint angle area II. (a), (d) show the beamforming method, while (b), (e) show the CAPON method and (c), (f) show the MUSIC pseudo-spectra method.

5.5 Measurements

The measurements were performed in the IETR facility DIADEM (DIagnostic, Analysis and Dosimetry of EM fields). This facility dedicated to Electro-magnetic imaging is based on a 600 × 600 × 600 mm3 xyz scanner located in an anechoic chamber. The RF measurement system uses a classical architecture with a VNA and external VDI TxRef and Rx frequency extenders. In this configuration, the emission part is fixed to illuminate the scene to be imaged with an incident elevation angle of 30°. The 300 elements reception array is synthesized moving the RF reception module to 2 mm spaced discrete positions thanks to the scanner (see Fig. 5.16). The objects, to be imaged, are settled at 1m distance on a 1.5m height foam support. Thanks to this support whose relative electrical permittivity is close to one, the sources of diffraction are minimized and mainly limited to the backscattering of the anechoic chamber. A 20GHz bandwidth signal with a 50GHz central frequency has been used for all the tests. To speed up the acquisition of the 1001 frequency points obtained for each reception position, an IF Filter of 100 kHz was applied. It has to be noticed that even if the IF filter is broadband, the dynamic range provided by the VDI modules is high enough for the purposes of these tests. In such a configuration, a maximal range resolution of 7.5mm can be obtained, with an azimuth angular resolution of 0.57° corresponding to a 1cm cross-range resolution at 1m range distance. Moreover, the 7.5m ambiguous distance, longer than the anechoic chamber length, enables to compensate for the chamber backscattering in an efficient way. Considering the 30° elevation orientation of the emission part, the ground range resolution

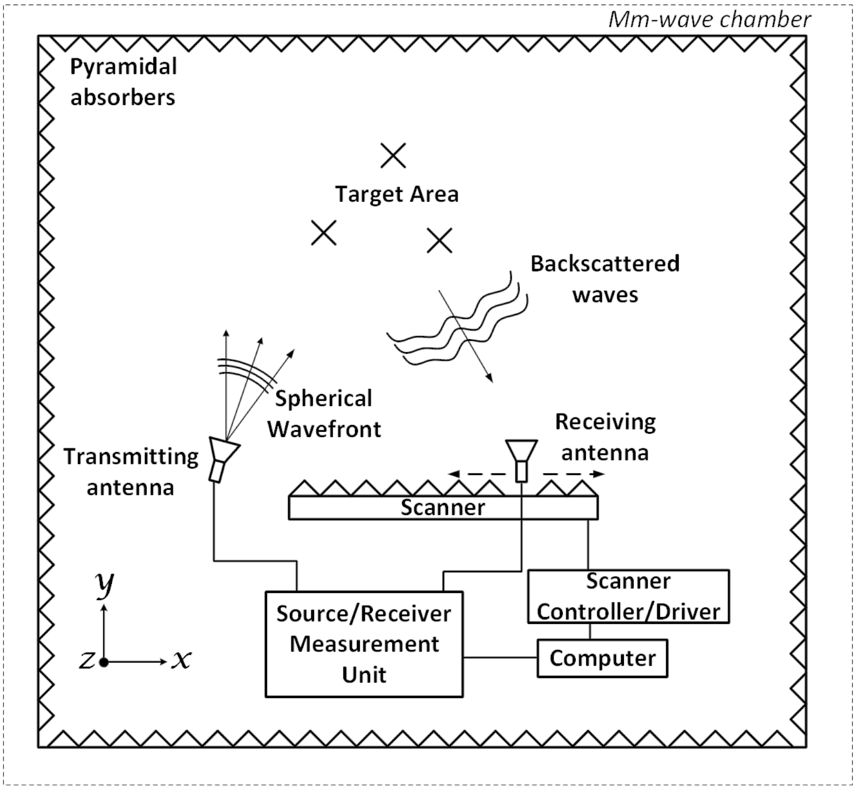

Figure 5.16: Measurement setup.

(a) (b) (c)

Figure 5.17: Picture of the three scene configurations with (a) 50 bolts of 5mm diameter configured to spell IETR,(b) a screw clamp, and (c) a knife hidden inside a thick book.

is limited to 8.7mm.

Three complex examples of targets that have been imaged are reported in Fig. 5.17: a canonical point scatterers scene made of dozen of 5mm diameter bolts positioned with a 10 mm spacing to write the word 'IETR'; a realistic scene with a screw clamp; a realistic scene with a 1mm blade stainless steel knife hidden inside a book. The estimation results of these three scenes applying the imaging techniques are reported in Fig. 5.18. The twelve images correspond to the results of four spectral estimation methods that are applied on the three complex targets. From top to bottom, the spectral estimation methods are: the beamforming, the spatially smoothed beamforming, CAPON and MUSIC. A spatial smoothing ratio $\eta = 50\%$ is used. Since the spatial smoothing pre-processing reduces the size of the covariance matrix, the spatial resolution of the spatially smoothed beamforming method is reduced by twice as compared to the beamforming method. Nonetheless, the spatial smoothing pre-processing becomes useful for CAPON and MUSIC algorithms. Further, since MUSIC does not provide an amplitude estimate, the amplitude is estimated using a least-square approach [7] and the Akaike Information Criterion [32] is used to provide a means for model selection. The bolt scene images show that the methods give good results as the word is readable, and the bolts can be discriminated from each other. The other test cases are more challenging as the point scatterers hypothesis is not fulfilled in such a straight way as the bolts scene, and considering the complexity of the surrounding of the target of interest. The results obtained with the beamforming method show that the screw clamp and the knife can be detected but the image contrast, including ripples effects, is not sufficient to apply an easy recognition of the target. The CAPON method gives better result, even if the contrast remains poor. The best result is obtained applying the MUSIC algorithm: the knife is well localized and the contrast is very high. However, it only extracts the main components with the strongest responses.

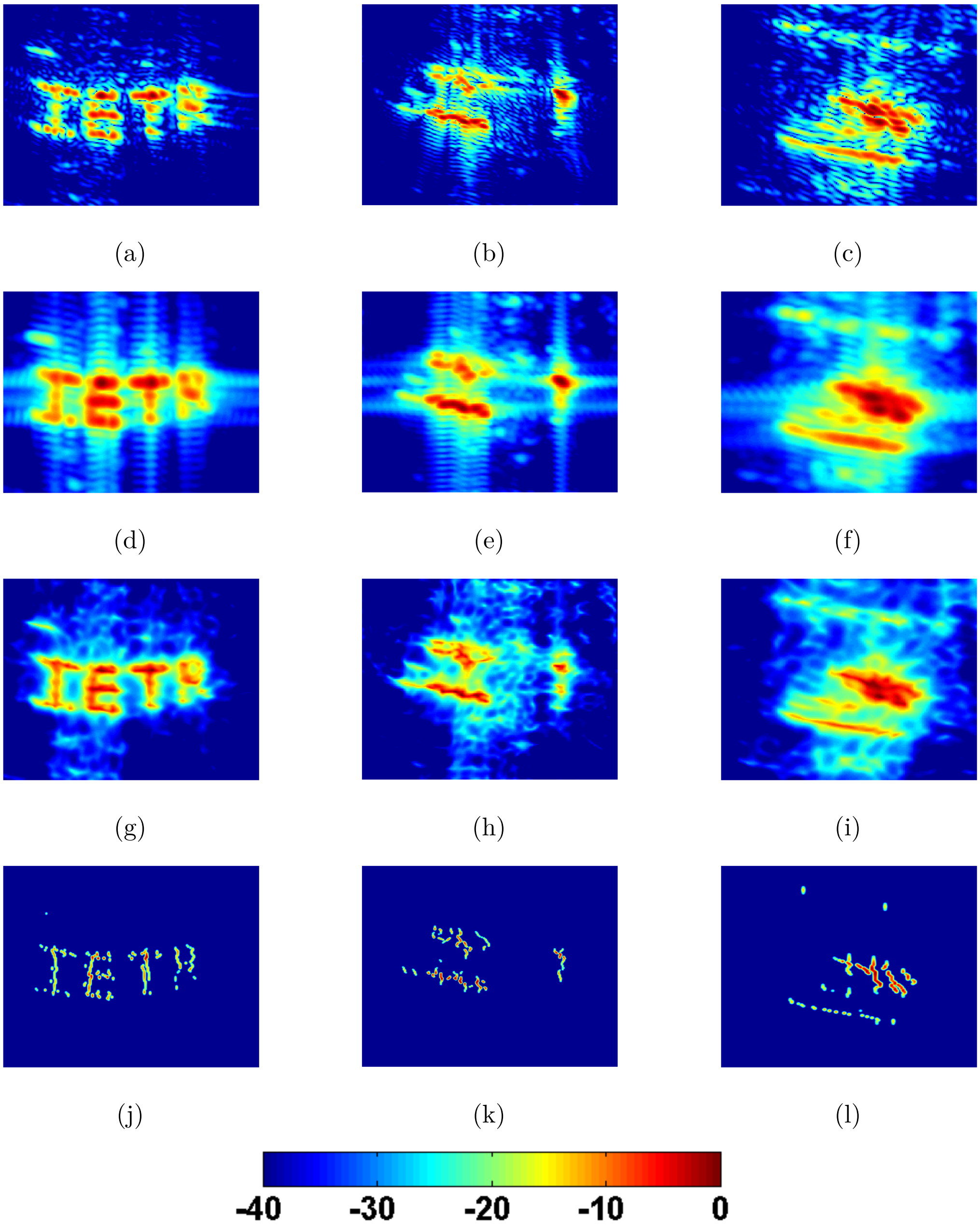

(a) (b) (c)

(d) (e) (f)

(g) (h) (i)

(j) (k) (l)

Figure 5.18: 2D spectral estimation methods applied on the (a), (d), (g), (j) bolts configured to spell IETR; (b), (e), (h), (k) the screw clamp and (c), (f), (i), (j) the knife hidden in a book. (a), (b), (c) show the beamforming method and (d), (e), (f) show the beamforming method after spatial smoothing, while (g), (h), (i) show the CAPON method and (j), (k), (l) show the MUSIC methods.

To show that the projection over a Cartesian grid is not the suitable solutions in fan-beam configurations and in near-field wide-band configurations to use spectral estimation methods, the methods are applied on the imaging results considering the MIMO configuration shown in Figs. 4.25 & 4.26, where the 4×1 passive compressive device is used. Two metallic trihedral corners with an edge length of 50 mm settled at about 1.4 m distance from the imaging system, on a foam support are used. The 2D spectral estimation methods are applied on the imaging result considering one, two, three or four output ports of the passive compressive device. The spectral estimation results for the four cases are shown in Fig. 5.19 when a Cartesian grid is used and in Fig. 5.20 when a polar grid is used. Considering the Cartesian case result, the phase history of the targets responses does not constitute the Kronecker product of the two 1-D steering vector associated with the exponential coefficients of the discrete Fourier transform unlike the polar grid case. Hence, the projection over a Cartesian grid does not provide full capability to spectral estimation methods and unlike the polar grid case, the methods does not achieve great spatial resolution. Furthermore, MUSIC methods is not capable to extract the two main components and each component is caracterized by a multitude of components that follows the point spread function of the MIMO system without improving the spatial resolution. Similarly, the same result is obtained for the CAPON method. However, thanks to the polar grid case, the phase history of the targets responses are equivalent to the the Kronecker product of the two 1-D steering vector associated with the exponential coefficients of the discrete Fourier transform. Then, this projection provides full capability to spectral estimation methods and both CAPON and MUSIC methods extract the two main components and achieve an improved spatial resolution.

Further, it is clear that the virtual array achieved by the MIMO configuration is enlarged by taking more and more output ports of the passive compressive device. Then, the spatial resolution is improved. This improvement provides more distinct information about the area of interest, hence, spectral estimation methods achieve better spatial resolution. The CAPON method result achieves better and better spatial resolution as the number of output ports used is increased. Considering the MUSIC method, using only one output port, only one target is detected but the target is discriminated by two points. Using only two or three output ports, the two targets are detected but the targets are discriminated by three points. Finally, using the four output ports, MUSIC method is able to discriminate the two targets with two points.

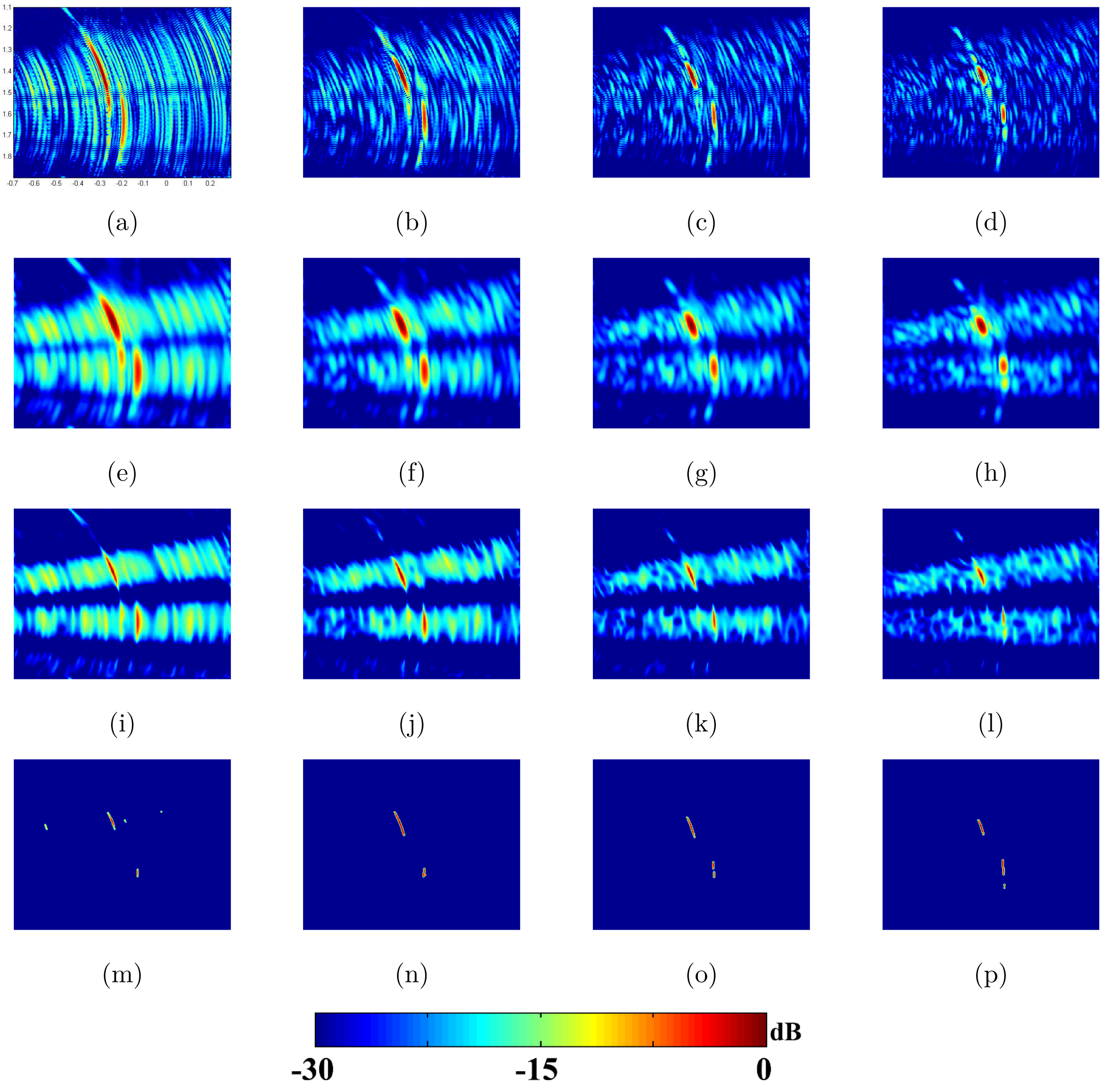

(a) (b) (c) (d)

(e) (f) (g) (h)

(i) (j) (k) (l)

(m) (n) (o) (p)

Figure 5.19: 2D spectral estimation methods applied on the imaging results (Cartesian grid) using the MIMO configuration with the passive compressive device considering (a), (e), (i), (m) one output, (b), (f), (j), (n) two outputs, (c), (g), (k), (o) three outputs and (d), (h), (l), (p) four outputs of the passive compressive device. (a), (b), (c), (d) show the beamforming method result and (e), (f), (g), (h) show the beamforming method result after spatial smoothing, while (i), (j), (k), (l) show the CAPON method result and (m), (n), (o), (p) show the MUSIC method result.

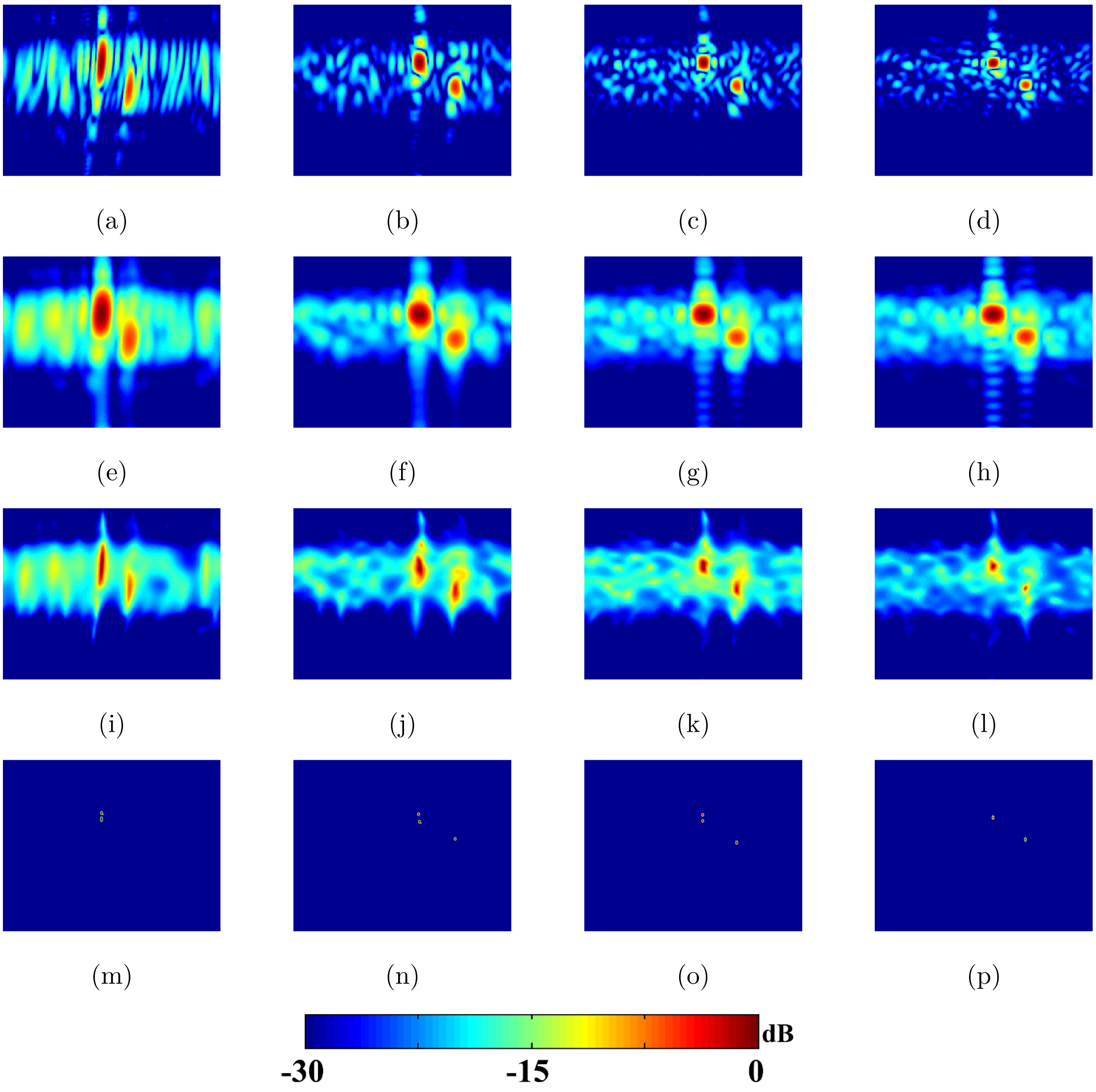

(a) (b) (c) (d)

(e) (f) (g) (h)

(i) (j) (k) (l)

(m) (n) (o) (p)

Figure 5.20: 2D spectral estimation methods applied on the imaging results (Polar grid) using the MIMO configuration with the passive compressive device considering (a), (e), (i), (m) one output, (b), (f), (j), (n) two outputs, (c), (g), (k), (o) three outputs and (d), (h), (l), (p) four outputs of the passive compressive device. (a), (b), (c), (d) show the beamforming method result and (e), (f), (g), (h) show the beamforming method result after spatial smoothing, while (i), (j), (k), (l) show the CAPON method result and (m), (n), (o), (p) show the MUSIC method result.

5.6 Summary

From a limited number of receiving antennas, it has been shown that it is possible to improve the spatial resolution of the system thanks to spectral estimation methods. Such methods are dedicated to specific data models made of assumptions that are the far-field and narrow-band assumptions. Radar Imaging systems working at millimeter-wave usually use wide-band signals and due to the high free-space losses, the configuration may be in near-field. Then the data model may be compromised and compensations are required to fit the data model and to give full capability to spectral estimation methods. It has been shown that the use of focusing techniques, such as the back-projection algorithm, allows such compensations and then spectral estimation methods are applied on the complex SAR images, generated by the focusing algorithms, to improve the spatial resolution. However, appropriate spectral estimation methods needs to be clearly defined depending on the expectation (i.e. to improve the final image quality or to improve the target localisation...). Further, it has been shown that the projection over a polar grid may be appropriate in a fan-beam configuration because it is a projection that respects the spherical wavefront propagation of the electromagnetic wave. The spectral estimation methods have been applied on the image results from the MIMO configuration used in the previous chapter to improve the spatial resolution of the system.

Bibliography

[1] Mehrdad Soumekh. *Synthetic aperture radar signal processing*, volume 7. New York: Wiley, 1999.

[2] L. M. H. Ulander, H. Hellsten, and G. Stenstrom. Synthetic-aperture radar processing using fast factorized back-projection. *IEEE Transactions on Aerospace and Electronic Systems*, 39(3):760–776, July 2003.

[3] Fabio Rocca. Synthetic aperture radar: A new application for wave equation techniques. *Stanford Exploration Project*, 56:167–189, 1987.

[4] C. Cafforio, C. Prati, and F. Rocca. Sar data focusing using seismic migration techniques. *IEEE Transactions on Aerospace and Electronic Systems*, 27(2):194–207, Mar 1991.

[5] AS Milman. Sar imaging by ω—κ migration. *International Journal of Remote Sensing*, 14(10):1965–1979, 1993.

[6] Steven M Kay and Stanley L Marple. Spectrum analysis—a modern perspective. *Proceedings of the IEEE*, 69(11):1380–1419, 1981.

[7] Petre Stoica, Randolph L Moses, et al. *Spectral analysis of signals*, volume 452. Pearson Prentice Hall Upper Saddle River, NJ, 2005.

[8] Arye Nehorai and Eytan Paldi. Vector-sensor array processing for electromagnetic source localization. *IEEE transactions on signal processing*, 42(2):376–398, 1994.

[9] Hamid Krim and Mats Viberg. Two decades of array signal processing research: the parametric approach. *IEEE signal processing magazine*, 13(4):67–94, 1996.

[10] M. R. Azimi-Sadjadi, A. Pezeshki, and N. Roseveare. Wideband doa estimation algorithms for multiple moving sources using unattended acoustic sensors. *IEEE Transactions on Aerospace and Electronic Systems*, 44(4):1585–1599, Oct 2008.

[11] J. C. Chen, R. E. Hudson, and Kung Yao. Maximum-likelihood source localization and unknown sensor location estimation for wideband signals in the near-field. *IEEE Transactions on Signal Processing*, 50(8):1843–1854, Aug 2002.

[12] T. L. Tung, K. Yao, D. Chen, R. E. Hudson, and C. W. Reed. Source localization and spatial filtering using wideband music and maximum power beamforming for multimedia applications. In *1999 IEEE Workshop on Signal Processing Systems. SiPS 99. Design and Implementation (Cat. No.99TH8461)*, pages 625–634, 1999.

[13] J. C. Chen, Kung Yao, and R. E. Hudson. Source localization and beamforming. *IEEE Signal Processing Magazine*, 19(2):30–39, Mar 2002.

[14] E. Grosicki, K. Abed-Meraim, and Yingbo Hua. A weighted linear prediction method for near-field source localization. *IEEE Transactions on Signal Processing*, 53(10):3651–3660, Oct 2005.

[15] Jeffrey Krolik and David Swingler. Focused wide-band array processing by spatial resampling. *IEEE Transactions on Acoustics, Speech, and Signal Processing*, 38(2):356–360, 1990.

[16] Kam W Lo. Adaptive array processing for wide-band active sonars. *IEEE Journal of Oceanic Engineering*, 29(3):837–846, 2004.

[17] Y-D Huang and Mourad Barkat. Near-field multiple source localization by passive sensor array. *IEEE Transactions on antennas and propagation*, 39(7):968–975, 1991.

[18] Joe C Chen, Ralph E Hudson, and Kung Yao. Maximum-likelihood source localization and unknown sensor location estimation for wideband signals in the near-field. *IEEE transactions on Signal Processing*, 50(8):1843–1854, 2002.

[19] Wanjun Zhi and Michael Yan-Wah Chia. Near-field source localization via symmetric subarrays. In *Acoustics, Speech and Signal Processing, 2007. ICASSP 2007. IEEE International Conference on*, volume 2, pages II–1121. IEEE, 2007.

[20] Stuart R DeGraaf. Sar imaging via modern 2-d spectral estimation methods. *IEEE Transactions on Image Processing*, 7(5):729–761, 1998.

[21] Jian Li and Petre Stoica. An adaptive filtering approach to spectral estimation and sar imaging. *IEEE Transactions on Signal Processing*, 44(6):1469–1484, 1996.

[22] Gerald R Benitz. High-definition vector imaging. *Lincoln Laboratory Journal*, 10(2):147–170, 1997.

[23] Müjdat Çetin and William Clement Karl. Feature-enhanced synthetic aperture radar image formation based on nonquadratic regularization. *IEEE Transactions on Image Processing*, 10(4):623–631, 2001.

[24] Charles VJ Jakowatz, Daniel E Wahl, Paul H Eichel, Dennis C Ghiglia, and Paul A Thompson. *Spotlight-Mode Synthetic Aperture Radar: A Signal Processing Approach: A Signal Processing Approach*. Springer Science & Business Media, 2012.

[25] Kiyo Tomiyasu. Conceptual performance of a satellite borne, wide swath synthetic aperture radar. *IEEE Transactions on Geoscience and Remote Sensing*, (2):108–116, 1981.

[26] Ralph Schmidt. Multiple emitter location and signal parameter estimation. *IEEE transactions on antennas and propagation*, 34(3):276–280, 1986.

[27] Tie-Jun Shan, Mati Wax, and Thomas Kailath. On spatial smoothing for direction-of-arrival estimation of coherent signals. *IEEE Transactions on Acoustics, Speech, and Signal Processing*, 33(4):806–811, 1985.

[28] Abigael Taylor, Philippe Forster, Franck Daout, Hélène M Oriot, and Laurent Savy. A generalization of the fixed point estimate for packet-scaled complex covariance matrix estimation. *IEEE Transactions on Signal Processing*, 65(20):5393–5405, 2017.

[29] Yue Huang, Laurent Ferro-Famil, and Andreas Reigber. Under-foliage object imaging using sar tomography and polarimetric spectral estimators. *IEEE transactions on geoscience and remote sensing*, 50(6):2213–2225, 2012.

[30] Stefan Sauer, Laurent Ferro-Famil, Andreas Reigber, and Eric Pottier. Three-dimensional imaging and scattering mechanism estimation over urban scenes using dual-baseline polarimetric insar observations at l-band. *IEEE Transactions on Geoscience and Remote Sensing*, 49(11):4616–4629, 2011.

[31] Jack Capon. High-resolution frequency-wavenumber spectrum analysis. *Proceedings of the IEEE*, 57(8):1408–1418, 1969.

[32] H. Akaike. A new look at the statistical model identification. *IEEE Transactions on Automatic Control*, 19(6):716–723, Dec 1974.

[33] James H McClellan. Multidimensional spectral estimation. *Proceedings of the IEEE*, 70(9):1029–1039, 1982.

[34] Andreas Jakobsson, S Lawrence Marple, and Petre Stoica. Computationally efficient two-dimensional capon spectrum analysis. *IEEE Transactions on Signal Processing*, 48(9):2651–2661, 2000.

Conclusion and prospects

Conclusion

The objective of this PhD project was to investigate solutions to image concealed objects through the use of active imaging radars. To achieve sufficient range and cross-range resolution (several centimeters), it has been decided to work at millimeter wave range to have a wide available frequency band (several Gigahertz) and a reasonable radiating aperture size to be embedded on portable system which can be deployed in many areas (buldings, streets..).

First of all, in the two first chapters, different imaging systems are presented. Direct imaging techniques using Real Aperture Radar (RAR) thanks to antennas with mechanically, electronically and frequency beam-scanning capability have been listed. Lastly, indirect imaging systems are presented using Synthetic Aperture Radar (SAR) configurations and the associated SAR algorithms. From this state of art it has been decided to study two different solutions to image scene composes of multiple targets :

- Direct imaging technique using a high directive antenna to improve the cross-range resolution thanks to the use of a narrow beam width (several degrees) radiation pattern.
- Indirect imaging techniques (SAR, SIMO, MIMO configurations) using one or several transmitters and receivers antennas, and by applying a synthetic aperture signal processing and high resolution algorithms.

In the third chapter (direct Imaging technique), a special focus on Fresnel lens antenna, as the focusing antenna, has been chosen. Particular attention has been devoted to maintain a high efficiency over a wide frequency band-width. This guarantees a high gain antenna (38 dBi) with a compact size for long-range applications (about 25 m) and a 59% of total efficiency. This antenna has been used in a Real Aperture Radar configuration to image an outdoor scene by mechanically rotating the antenna. Two papers in international journals and one international conference have been published concerning this work. Even if very interesting results have been obtained, the main drawback of this solution is that it is not suitable for real-time applications (motion of targets).

Then, Synthetic Aperture Radar configuration and algorithms have been theoretically studied and applied on measured data. The main goal was to find solutions to reduce the number of RF chains required while maintaining unchanged the spatial resolution. In parallel, spectral estimation methods have been investigated to improve the spatial resolution. It has been required to find solutions to use spectral estimation methods in near-field and wide-band configurations. Therefore, the study investigated SAR configuration in the chapter four. Measurements have been done at millimeter-wave to image small objects such as a knife concealed inside a book. The measurements proved the reliability to work at millimeter-wave for imaging small objects. However, to reach great spatial resolution, it is required an important number of RF chains to be used for real-time applications. Then, the study continues on finding solutions to reduce the number of chains while maintaining unchanged the spatial resolution. The study focuses on MIMO configurations and especially on Passive Compressive Device which allows to decrease the number of RF chains in a passive manner with great capability. Such passive compressive device has been designed and realized at millimeter wave (V band). In emission configuration, this device allows to obtain 4 decorrelated transmitting signals from only one transmitter. The cross-correlation level between the four outputs remains lower than -15dB which is a good compromise as compared to the size of the device. An enlarged size may improve this cross-correlation level. This device has been associated with a virtual receiving array (performed by a scanner setup) to be used in a MIMO configuration to image corner reflectors. Such measurements allow to prove the concept. In a more realistic system, the scanner setup should be replaced by a real active switching antenna array as explained in the last section of this chapter.

Finally in the chapter five, it has been investigated spectral estimation methods to be used to improve the spatial resolution for a limited number of chains. It has been proposed solution to use spectral estimation methods even in near-field and wide-band configurations. This permits to improve the capability of discrimination and detection of targets and to improve the image quality removing the speckle effects. These algorithms have been applied on real measured data of complex objects located in a near field (1 meter between radar and scene) and wide band configuration (20 GHz). This work has been published in an international journal (PIERS Journal).

Prospects

Concerning Direct Imaging techniques and the use of very directive antennas, many prospects can be considered:

- The manufactured Fresnel lens antenna could be illuminated by multiple sources that would be switched. . Each source would illuminate the Fresnel lens to focus the beam in different direction. This would benefit for multi-beam configuration, over a narrow field of view. This electronically scanning system allows to image moving targets in almost real time. In the same idea, it would be interesting to illuminate the lens with multiple sources coming from a passive compressive device allowing to obtain a real time multibeam antenna without any active component.

- To improve the spatial resolution while maintaining the radiating aperture size unchanged, it would benefit to increase the working frequency up to sub millimeter wave range. Such lens is under study at 300GHz but we have to verify before the accuracy of the manufacturing process (pressed foam) at such frequency.

Concerning the Indirect Imaging techniques and the use of the passive compressive device, new studies can be also considered:

- For the passive compressive device, only a 4 × 1 PCD has been realized with output ports performing a linear array. It would be interesting to increase the number of output ports, and to arrange them as a 2D (fully-populated or sparse) array to be used for 3D imaging.
- Various passive compressive device can be used together either as a transmitter or a receiver. Because it is possible to use only a limited transmitted power at millimeter-wave.
- Solutions need to be found to improve the efficiency of the passive compressive device.
- Like for direct imaging techniques, it would benefit to increase the working frequency to improve the cross-correlation level while maintaining the device size unchanged.
- The output ports of the passive compressive device could be arranged to have different electromagnetic wave polarization to be used in a polarimetric MIMO imaging radar configuration.

Scientific production

Journal papers

- Jouade, A., Ferro-Famil, L., Meric, S., Lafond, O. and Le Coq, L., "High Resolution Radar Focusing using Spectral Estimation Methods in Wide-band and Near-field Configurations: Application to Millimeter-wave Near-range Imaging.",Progress In Electromagnetics Research.
- A. Jouade, M. Himdi and O. Lafond, "Fresnel Lens at Millimeter-wave: Enhancement of Efficiency and Radiation Frequency Bandwidth," in IEEE Transactions on Antennas and Propagation, vol. PP, no. 99, pp. 1-1.
- Jouade, A., Bor, J., Himdi, M. and Lafond, O. (2016) 'Millimeter-Wave Fresnel Zone Plate Lens with new technological process', International Journal of Microwave and Wireless Technologies, , pp. 1–6. doi: 10.1017/S1759078716000854.

Patent

- A. Jouade, M. Himdi, O. Lafond and X. Castel, "LENTILLE POUR SYSTEME ANTENNAIRE", FR17/56992
- P. Le Bars, M. Achir, and A. Jouade, "RADAR SYSTEM AND METHOD FOR OPTIMIZING RADAR DETECTION OF TARGETS ", GB 1708062.3
- F. Thoumy, M. Achir, A. Caillerie, and A. Jouade, "METHOD AND APPARATUS FOR RECEIVING A CONTINUOUS RADAR WAVE ", GB1615207.6
- A. Caillerie, A. Jouade and F. Thoumy, "METHOD AND APPARATUS FOR TRANSMITTING A CONTINUOUS RADAR WAVE", GB2545678

Conferences

- Jouade, A., Bor, J., Lafond, O. and Himdi, M. (2016, April). Millimeter-wave fresnel zone plate lens based on foam gradient index technological process. In Antennas and Propagation (EuCAP), 2016 10th European Conference on (pp. 1-4). IEEE.

Appendix A

Emitted waveform

A.1 Matched filter

In a Radar imaging system, the detection of transmitted signals over a channel corrupted by noise is performed by the receiver and the main goal is to minimize the effects of the noise (due to electronic noises, jamming ...) to enhance, distinguish and extract the desired signal knowing that the receiver has the knowledge of the transmitted waveform.

Let us consider an emitted signal $s_e(\tau)$ which is a periodic function of period $T_p = 1/PRF$ with the variable PRF being the Pulse Repetition Frequency. This signal is obtained by the elementary signal $u(\tau)$ with a duration limited from $-\tau_p/2$ to $\tau_p/2$. The elementary signal $u(\tau)$ may be a pulsed or continuous waveform. In the case of continuous waveform the period T_p is equal to τ_p and both waveforms will be further investigated in this report.

The emitted signal is then given by:

$$s_e(\tau) = \sum_k u(\tau - kT_p)$$

This signal will be up-converted around the carrier frequency f_c which corresponds to an angular frequency given by $\omega_c = 2\pi f_c$ before being sent to the emitting antenna. The up-converted emitted signal is given by:

$$s_{e_{RF}}(\tau) = s_e(\tau)e^{j\omega_c\tau}$$

Assuming that the received signals arriving to the receiver are weighted (s_i) and delayed (τ_i) replicas of the up-converted emitted signal backscattered by N_s targets plus an additive white noise of zero mean and power spectral density of N_n which is:

$$s_{r_{RF}}(\tau) = \sum_{i=1}^{N_s} s_i s_{e_{RF}}(\tau - \tau_i) = \sum_{i=1}^{N_s} s_i s_e(\tau - \tau_i)e^{j\omega_c(\tau-\tau_i)} + n(\tau)$$

The signal is down-converted to be sampled and saved which yields the following:

$$s_r(\tau) = s_{r_{RF}}(\tau)e^{-j\omega_c\tau} = \sum_{i=1}^{N_s} s_i s_e(\tau - \tau_i)e^{-j\omega_c\tau_i} + n(\tau)$$

$$s_r(\tau) = s_e(\tau) * [\sum_{i=1}^{N_s} s_i e^{-j\omega_c \tau_i} \delta(\tau - \tau_i)] + n(\tau) = s_e(\tau) * e(\tau) + n(\tau)$$

in which the operator * represents a convolution product such as:

$$x(\tau) * y(\tau) = \int_{-\infty}^{+\infty} x(t) y(t - \tau) dt$$

The received signal can be divided into two different signals, the useful signal $s_{r_u}(\tau)$ and the noise signal $n(\tau)$ such as:

$$s_r(\tau) = s_{r_u}(\tau) + n(\tau)$$

where the Signal to Noise Ratio is defined such as:

$$SNR(\tau) = \frac{|s_{r_u}(T)|^2}{E(|n(\tau)|^2)}$$

with $|s_{r_u}(T)|^2$ is the instantaneous power of the output signal at sampling instant T and $E(|n(\tau)|^2)$ is the average power of the output noise.

On this signal a filter is applied to detect $s_{r_u}(\tau)$ in an optimal manner. To achieve this, let us filter the received signal to minimize the effects of the noise in some statistical sense. Let us call the linear filter $g_r(\tau)$ which leads to the focusing received signal given by:

$$s_{rf}(\tau) = g_r(\tau) * s_r(\tau) = s_e(\tau) * e(\tau) * g_r(\tau) + n(\tau) * g_r(\tau) = s_{r_{uf}}(\tau) + n_f(\tau)$$

with $n_f(\tau)$ the filtered noise component and $s_{r_uf}(\tau)$ the filtered useful signal.

$$h(\tau) = s_e(\tau) * g_r(\tau)$$

is called the impulse response of the process chain when $e(\tau) = \delta(\tau)$ without taking into account the noise. The goal is to maximise $s_{r_{uf}}(\tau)$ with respect to $n_f(\tau)$ or to maximise the Signal to Noise Ratio (SNR) given by:

$$SNR(\tau) = \frac{|s_{r_{uf}}(\tau)|^2}{E(|n_f(\tau)|^2)}$$

The fourier transform decomposes a function of time $x(\tau)$ into the frequencies $X(f)$ that make it up and given by:

$$X(f) = FT(x(\tau)) = \int_{-\infty}^{+\infty} x(\tau) e^{-j\omega\tau} d\tau$$

$$X(\tau) = FT^{-1}(X(f)) = \int_{-\infty}^{+\infty} X(f) e^{j\omega\tau} df$$

The filtered useful signal power can be redefined as the magnitude squared of the inverse Fourier transform of $S_{r_uf}(f) = S_{r_u}(f) G_r(f) = FT(s_{r_u}(\tau) * g_r(\tau))$ and

$S_{r_u}(f) = S_e(f)E(f)$ with $E(f)$ the fourier transform of a summation of dirac function which is equal to one ($E(f) = 1$).

$$|s_{r_uf}(\tau)|^2 = |\int_{-\infty}^{+\infty} S_e(f)G_r(f)e^{j\omega\tau}df|^2$$

The average power of the output noise is defined thanks to the Perseval's identity such as:

$$P_{nf} = \int_{-\infty}^{+\infty} N_n|G_r(f)|^2df = N_n\int_{-\infty}^{+\infty} |G_r(\tau)|^2d\tau$$

which lead to a rewritten signal to noise ratio and given by:

$$SNR(\tau) = \frac{|\int_{-\infty}^{+\infty} S_e(f)G_r(f)e^{j\omega\tau}df|^2}{N_n\int_{-\infty}^{+\infty} |G_r(\tau)|^2d\tau}$$

We need to solve $G_r(f)$ that yields the largest possible signal to noise ratio. By means of Schwarz's inequality, if we have two complex functions, $x(\tau)$ and $y(\tau)$ such that:

$$\int_{-\infty}^{+\infty} |x(\tau)|^2d\tau < \infty$$

and

$$\int_{-\infty}^{+\infty} |y(\tau)|^2d\tau < \infty$$

then:

$$|\int_{-\infty}^{+\infty} x(\tau)y(\tau)d\tau|^2 \leq (\int_{-\infty}^{+\infty} |x(\tau)|^2d\tau) \cdot (\int_{-\infty}^{+\infty} |y(\tau)|^2d\tau)$$

This becomes an equality when $x(\tau) = k \cdot y^*(\tau)$ then we obtain:

$$|\int_{-\infty}^{+\infty} S_e(f)G_r(f)e^{j\omega\tau}df|^2 \leq \int_{-\infty}^{+\infty} |S_e(f)|^2df \cdot \int_{-\infty}^{+\infty} |G_r(f)|^2df$$

which lead to reword the equation of SNR:

$$SNR(\tau) \leq \frac{\int_{-\infty}^{+\infty} |S_e(f)|^2df \cdot \int_{-\infty}^{+\infty} |G_r(f)|^2df}{N_n\int_{-\infty}^{+\infty} |G_r(\tau)|^2d\tau} = \frac{\int_{-\infty}^{+\infty} |S_e(f)|^2df}{N_n}$$

We are able to define the optimum filter which maximizes the signal to noise ratio and is given by:

$$G_{r_{opt}}(f) = K \cdot S_e^*(f)e^{-j\omega T}$$

By applying the inverse Fourier Transform, this give the optimal filter or the so called adapted filter:

$$g_{r_{opt}}(\tau) = K \cdot \int_{-\infty}^{+\infty} S_e^*(f)e^{-j\omega T}e^{-j\omega\tau}df = K \cdot S_e(T - \tau)$$

Then we obtain the focusing received signal in the time domain:

$$s_{rf}(\tau) = g_r(\tau) * s_r(\tau) = h(\tau) * [\sum_{i=1}^{N_s} s_i exp(-j\omega_c \tau_i)\delta(\tau - \tau_i)])$$

and in the frequency domain:

$$S_{rf}(f) = H(f) \cdot [\sum_{i=1}^{N_s} s_i exp(-j\omega_c \tau_i)]$$

with the impulse response of the processing chain given by:

$$h(\tau) = \int_{-\infty}^{+\infty} s_e(t) s_e(t - \tau) dt$$

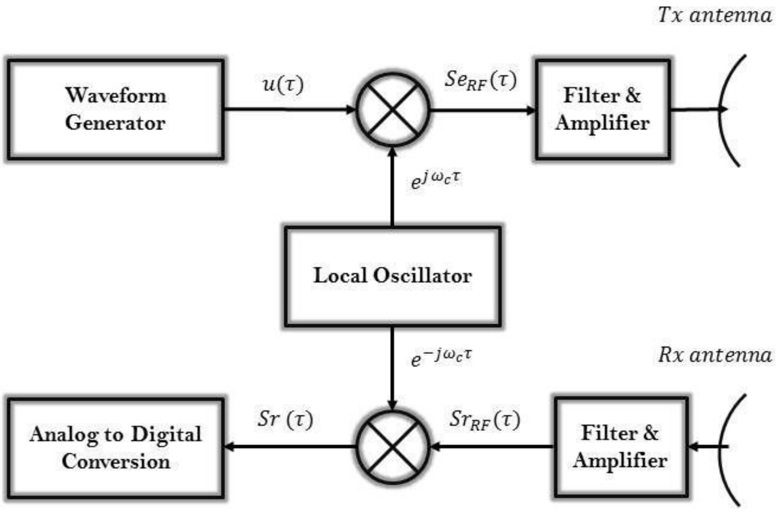

Figure A.1: Synoptic of a pulsed RADAR

A.2 Pulsed linear frequency modulated waveform: Chirp waveform

Also called Chirp waveform, this signal is a linear frequency modulated pulse of frequency bandwidth B_f and duration τ_p. During this time, the instantaneous frequency is linearly increased from the minimum frequency f_{min} at $\tau = -\tau_p/2$ until f_{max} at $\tau = \tau_p/2$.

The synoptic of such a RADAR is given by the following synoptic:

Its instantaneous frequency is given by:

$$f_{inst}(\tau) = \begin{cases} \alpha\tau \text{ when } \frac{-\tau_p}{2} + k \cdot T_p \leq \tau \leq \frac{\tau_p}{2} + k \\ \hfill 0 \text{ otherwise} \end{cases}$$

with $\alpha = \frac{B_f}{\tau_p}$ and k a real number.

considering only the first period for $k = 0$, the chirp waveform can be defined as:

$$u_c(\tau) = e^{j\theta(\tau)} rect(\frac{\tau}{\tau_p})$$

with:

$$\theta(\tau) = \int_{-\tau_p/2}^{\tau_p/2} \omega(\tau) d\tau = \int_{-\tau_p/2}^{\tau_p/2} 2\pi f_{inst}(\tau) d\tau = 2\pi \frac{\alpha}{2} \tau^2$$

$$u_c(\tau) = e^{j2\pi\frac{\alpha}{2}\tau^2} rect(\frac{\tau}{\tau_p})$$

As it has been proved previously, the focusing received signal is given by:

$$s_{rf}(\tau) = h(\tau) * [\sum_{i=1}^{N_s} s_i e^{-j\omega_c\tau_i}\delta(\tau - \tau_i)])$$

with:

$$h(\tau) = \int_{-\infty}^{+\infty} s_e(t)s_e(t-\tau)dt = \int_{-\infty}^{+\infty} u_c(t)u_c(t-\tau)dt$$

then:

$$h(\tau) = \int_{-\infty}^{+\infty} e^{j2\pi\frac{\alpha}{2}t^2} rect(\frac{t}{\tau_p}) e^{j2\pi\frac{\alpha}{2}(t-\tau)^2} rect(\frac{t-\tau}{\tau_p})dt$$

$$h(\tau) = e^{j\pi\alpha\tau^2} \int_{-\infty}^{+\infty} e^{j2\pi\alpha\tau t} rect(\frac{t}{\tau_p}) rect(\frac{t-\tau}{\tau_p})dt$$

Let us define two sub-functions from the previous one. We consider $A(\tau) = e^{j\pi\alpha\tau^2}$ and $f(t,\tau) = e^{j2\pi\alpha\tau t}$ which gives:

$$h(\tau) = A(\tau) \int_{-\infty}^{+\infty} f(t,\tau) rect(\frac{t}{\tau_p}) rect(\frac{t-\tau}{\tau_p})dt$$

with:

$$rect(\frac{t}{\tau_p}) = \begin{cases} 1 \text{ if } |t| \leq \frac{\tau_p}{2} \\ 0 \text{ otherwise} \end{cases}$$

and

$$rect(\frac{t-\tau}{\tau_p}) = \begin{cases} 1 \text{ if } \frac{-\tau_p}{2} + \tau < t < \frac{\tau_p}{2} + \tau \\ 0 \text{ otherwise} \end{cases}$$

if the function $h(\tau)$ doesn't respect the two conditions then:

$$h(\tau) = 0 \begin{cases} t < \frac{-\tau_p}{2} \longrightarrow t < \frac{\tau_p}{2} + \tau < \frac{-\tau_p}{2} \text{ when } \tau < -\tau_p \\ t > \frac{\tau_p}{2} \longrightarrow t < \frac{-\tau_p}{2} + \tau > \frac{\tau_p}{2} \text{ when } \tau > \tau_p \end{cases}$$

When $0 < \tau < \tau_p \longrightarrow \frac{-\tau_p}{2} + \tau < t < \frac{+\tau_p}{2}$ and when $-\tau_p < \tau < 0 \longrightarrow \frac{-\tau_p}{2} < t < \frac{\tau_p}{2} + \tau$ which gives:

$$h(\tau) = \begin{cases} 0 \text{ when } \tau > \tau_p \text{ and } \tau < -\tau_p \\ h_1(\tau) = A(\tau)\int_{\frac{-\tau_p}{2}+\tau}^{\frac{+\tau_p}{2}} f(t,\tau)dt \text{ when } 0 < \tau < \tau_p \\ h_2(\tau) = A(\tau)\int_{\frac{-\tau_p}{2}}^{\frac{\tau_p}{2}+\tau} f(t,\tau)dt \text{ when } -\tau_p < \tau < 0 \end{cases}$$

$$h_1(\tau) = A(\tau)\int_{\frac{-\tau_p}{2}+\tau}^{\frac{+\tau_p}{2}} f(t,\tau)dt = A(\tau)\int_{\frac{-\tau_p}{2}+\tau}^{\frac{+\tau_p}{2}} e^{j2\pi\alpha\tau t}dt$$

$$h_1(\tau) = \frac{A}{j2\pi\alpha\tau}[e^{j2\pi\alpha\tau t}]_{\frac{-\tau_p}{2}+\tau}^{\frac{+\tau_p}{2}} = \frac{A}{j2\pi\alpha\tau}[e^{j2\pi\alpha\tau\frac{+\tau_p}{2}} - e^{j2\pi\alpha\tau(\frac{-\tau_p}{2}+\tau)}]$$

$$h_1(\tau) = \frac{A}{\pi\alpha\tau}e^{j2\pi\alpha\frac{\tau^2}{2}}sin(\pi\alpha\tau(\tau_p-\tau)) = (\tau_p-\tau)sinc(\alpha\tau((\tau_p-\tau)))$$

The same development is performed for $h_2(\tau)$ which gives:

$$h_2(\tau) = (\tau_p+\tau)sinc(\alpha\tau((\tau_p+\tau)))$$

We define the triangular function $tri(\tau)$such as:

$$tri(\tau)\begin{cases} 1-2|t| \text{ when } |t| < \frac{1}{2} \\ \\ \qquad 0 \text{ otherwise} \end{cases}$$

then the exact equation of the impulse response using a chirp waveform is given by:

$$h(\tau) = \tau_p tri(\frac{\tau}{2\tau_p})sinc(\alpha\tau\tau_p tri(\frac{\tau}{2\tau_p}))$$

furthermore, we have $\alpha = \frac{B_f}{\tau_p}$:

$$h(\tau) = \tau_p tri(\frac{\tau}{2\tau_p})sinc(B_f tri(\frac{\tau}{2\tau_p})\tau)$$

An approximation can be made if the width of the main lobe of the sinc function $(\frac{2}{B_f})$ is low as compared to the duration of the triangular fonction of width $2\tau_p$.

$$\frac{2}{B_f} << 2\tau_p \longrightarrow B_f\tau_p >> 1$$

We can consider that the approximation is valid when $B_f\tau_p > 200$

A.3 Increasing linear frequency modulated continuous waveform: L-FMCW

The signal is a continuous carrier modulated by a periodic function. In this report, we will concentrate only on the linear FMCW. This waveform disposes of a frequency bandwidth B_f and duration T_p. During this time, the instantaneous frequency is linearly increased by a waveform generator (DDS, VCO...) from the minimum frequency f_{min} at $\tau = -T_p/2$ until f_{max} at $\tau = T_p/2$.

The synoptic of a FMCW RADAR is given in the following figure.

Its instantaneous frequency is given by:

$$f_{inst}(\tau) = \alpha\tau$$

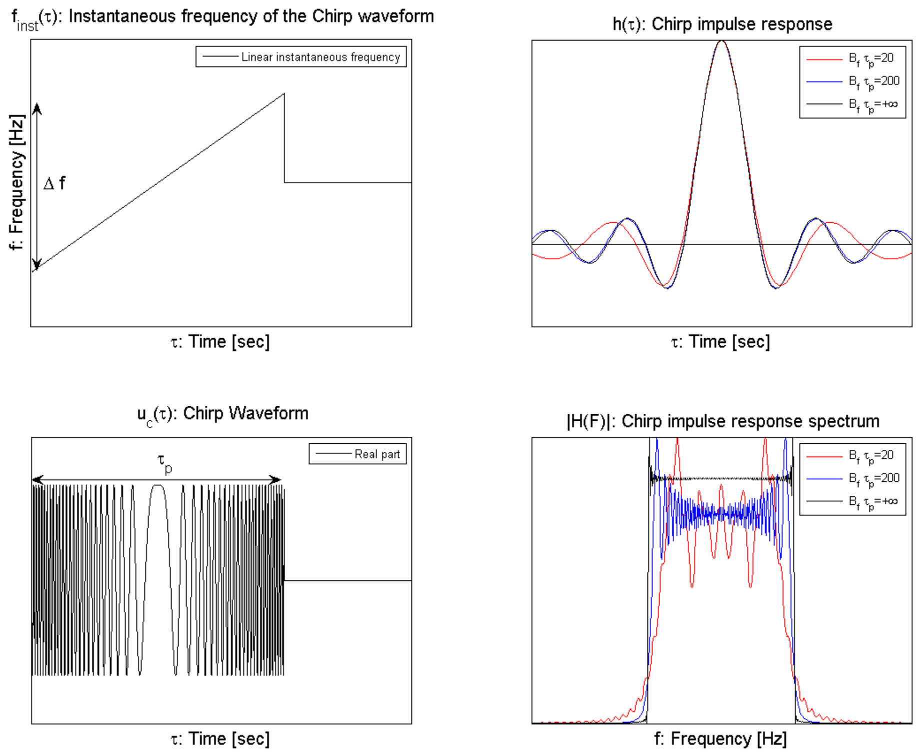

Figure A.2: Chirp Waveform and the associated impulse response

when $\frac{-T_p}{2} + k \cdot T_p \leq \tau \leq \frac{T_p}{2} + k \cdot T_p$

with $\alpha = \frac{B_f}{\tau_p}$ and k a real even number.

considering only the first period for $k = 0$, the L-FMCW waveform can be defined as:

$$u_{FMCW}(\tau) = cos(\theta(\tau))rect(\frac{\tau}{T_p})$$

with:

$$\theta(\tau) = \int_{\tau=-\infty}^{\tau=+\infty} \omega(\tau)d\tau = \int_0^{\tau} 2\pi f_{inst}(\tau)d\tau = \pi\alpha\tau^2$$

$$u_{FMCW}(\tau) = cos(\pi\alpha\tau^2)rect(\frac{\tau}{T_p})$$

The principle is to modulate the received signal with the transmitting one to down-convert the signal in baseband and to generate at the output of the mixer, directly the focused received signal.

The up-converted emitted signal at the carrier frequencyf_c is given by:

$$s_{e_{RF}}(\tau) = u_{FMCW}(\tau)cos(2\pi f_c\tau) = cos(2\pi[f_c\tau + \frac{\alpha}{2}\tau^2])cos(2\pi[f_c\tau - \frac{\alpha}{2}\tau^2])rect(\frac{\tau}{T_p})$$

The second cosinus is the up-converted signal coming from the baseband signal in the negative frequency domain and is usually directly filtered out after the mixer:

$$s_{e_{RF}}(\tau) = cos(2\pi[f_c\tau + \frac{\alpha}{2}\tau^2])rect(\frac{\tau}{T_p})$$

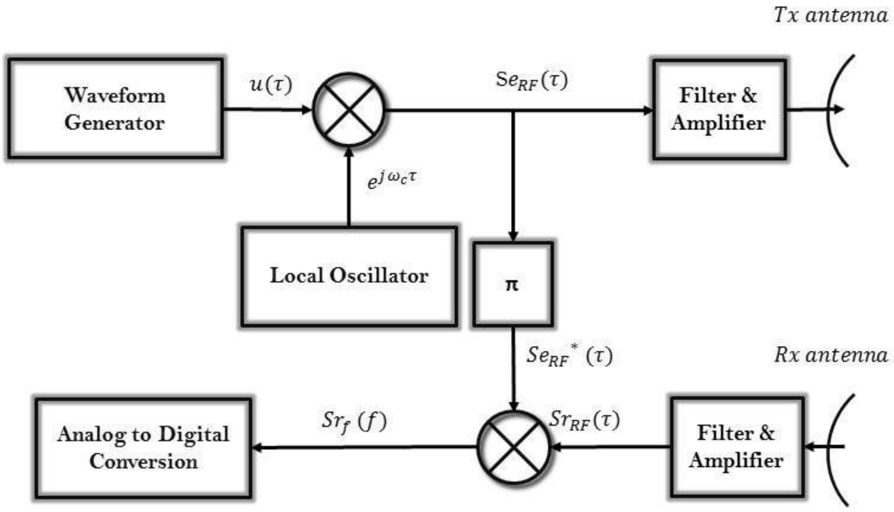

Figure A.3: Synoptic FMCW RADAR

Assuming return signals arriving to the receiver are weighted and delayed replicas of the up-converted emitted signal backscattered by N_s targets, the received signal gives:

$$s_{r_{RF}}(\tau) = \sum_{i=1}^{N_s} s_i S_{e_{RF}}(\tau-\tau_i) = \sum_{i=1}^{N_s} s_i cos(2\pi[f_c(\tau-\tau_i(\tau))+\frac{\alpha}{2}(\tau-\tau_i(\tau))^2])rect(\frac{\tau-\tau_i(\tau)}{T_p})$$

In the following part, only one target is taken into account and the weighted coefficient is omitted. The delay linked to the target location and velocity is given by:

$$\tau_0(\tau) = \frac{2(R_0+V_0\tau)}{c}$$

with: c: The celerity
R_0: The distance Radar-Target
V_0: The radial velocity of the target

This signal is mixed with the emitting signal in order to give a beat signal whose frequency is directly related to the delays τ_i.

$$s_b(\tau) = s_{e_{RF}}(\tau)s_{r_{RF}}(\tau)$$

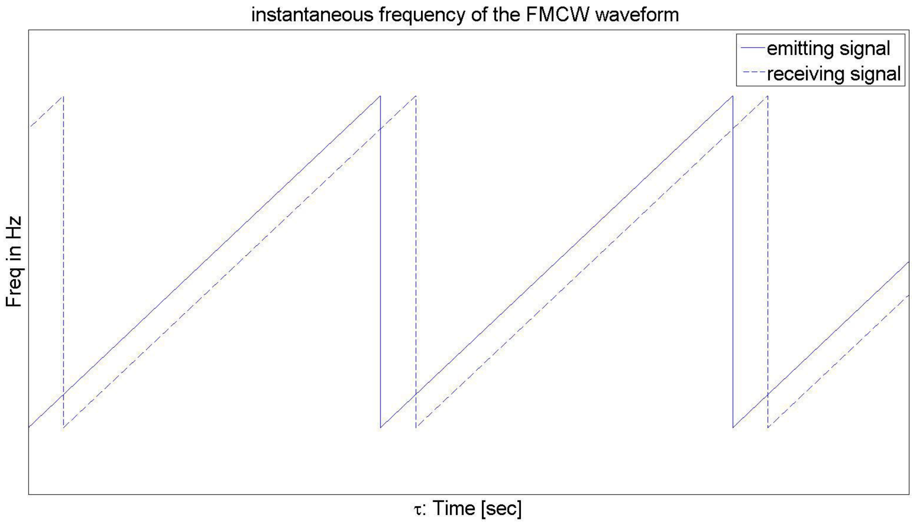

Figure A.4: Instantaneous frequency

$$s_b(\tau) = cos(2\pi[f_c\tau + \frac{\alpha}{2}\tau^2])cos(2\pi[f_c(\tau - \tau_0(\tau)) + \frac{\alpha}{2}(\tau - \tau_0(\tau))^2])rect(\frac{\tau - \tau_0(\tau)}{T_p})rect(\frac{\tau}{T_p})$$

$$s_b(\tau) = \begin{cases} cos(2\pi[2f_c(\tau) - f_c\tau_0(\tau) + \frac{\alpha}{2}(\tau - \tau_0(\tau))^2 + \frac{\alpha}{2}\tau^2])rect(\frac{\tau - \tau_0(\tau)}{T_p})rect(\frac{\tau}{T_p}) \\ +cos(2\pi[f_c\tau_0(\tau) + \alpha\tau_0(\tau)\tau - \frac{\alpha}{2}\tau_0^2(\tau)])rect(\frac{\tau - \tau_0(\tau)}{T_p})rect(\frac{\tau}{T_p}) \end{cases}$$

The first cosinus which is around $2f_c$ is filtered out keeping only the second term downconverted at baseband frequency. Furthermore,

$$rect(\frac{\tau - \tau_0(\tau)}{T_p})rect(\frac{\tau}{T_p}) = rect(\frac{\tau - \frac{\tau_0(\tau)}{2}}{T_p - \tau_0})$$

By using the formula of the delay τ_0 linked to the range and velocity of the target we may rewrite the equation such as:

$$s_b(\tau) = cos(2\pi[f_c(\frac{2(R_0 + V_0\tau)}{c}) + \alpha(\frac{2(R_0 + V_0\tau)}{c})\tau - \frac{\alpha}{2}(\frac{2(R_0 + V_0\tau)}{c})^2(\tau)])rect(\frac{\tau - \frac{\tau_0(\tau)}{2}}{T_p - \tau_0})$$

The last part inside the cosinus phase is called the residual video phase and is omitted because it can be compensated.

$$s_b(\tau) = cos(2\pi[f_c(\frac{2(R_0 + V_0\tau)}{c}) + \alpha(\frac{2(R_0 + V_0\tau)}{c})\tau])rect(\frac{\tau - \frac{\tau_0(\tau)}{2}}{T_p - \tau_0})$$

$$s_b(\tau) = cos(2\pi[\frac{2R_0f_c}{c} + \frac{2V_0f_c}{c}\tau + \frac{2\alpha R_0}{c}\tau + \frac{2\alpha V_0}{c}\tau^2])rect(\frac{\tau - \frac{\tau_0(\tau)}{2}}{T_p - \tau_0})$$

The instantaneous frequency of such a signal is:

$$f_{b_{inst}}(\tau) = 2\pi[\frac{2\alpha R_0}{c} + \frac{2V_0 f_c}{c} + \frac{4\alpha V_0 \tau}{c}]$$

The first term is the beat frequency directly linked to the range of the target, the second term is the doppler frequency generated by the velocity of the target and the last term is a parasite term which must be as low as possible. Defining:

$$\Theta(\tau) = 2\pi[\frac{2R_0 f_c}{c} + \frac{2V_0 f_c}{c}\tau + \frac{2\alpha R_0}{c}\tau + \frac{2\alpha V_0}{c}\tau^2]$$

The beat frequency signal possesses a time Fourier transform (TFT) defined as:

$$S_b(\omega) = \int_{\tau=-\infty}^{\tau=+\infty} s_b(\tau) e^{-i\omega\tau} d\tau$$

$$S_b(\omega) = \int_{\tau=-\infty}^{\tau=+\infty} \frac{e^{+i\Theta(\tau)} + e^{-i\Theta(\tau)}}{2} e^{-i\omega\tau} rect(\frac{\tau - \frac{\tau_0(\tau)}{2}}{T_p - \tau_0}) d\tau$$

$$S_b(\omega) = (\int_{\tau=-\infty}^{\tau=+\infty} \frac{e^{+i\Theta(\tau)} e^{-i\omega\tau}}{2} rect(\frac{\tau - \frac{\tau_0(\tau)}{2}}{T_p - \tau_0}) d\tau + \int_{\tau=-\infty}^{\tau=+\infty} \frac{e^{-i\Theta(\tau)} e^{-i\omega\tau}}{2}) rect(\frac{\tau - \frac{\tau_0(\tau)}{2}}{T_p - \tau_0}) d\tau$$

The second sum represents the negative frequency of the real received signal. We will only define the positive frequency spectrum component of the signal because the physical signal is real-valued ad hence its spectrum should be even (symmetric about $\omega = 0$).

$$S_b(\omega) = (\int_{\tau=-\infty}^{\tau=+\infty} \frac{e^{+i\Theta(\tau) - i\omega\tau}}{2} rect(\frac{\tau - \frac{\tau_0(\tau)}{2}}{T_p - \tau_0}) d\tau$$

$$+i\Theta(\tau) - i2\pi f\tau = -i2\pi[(f - (\frac{2V_0 f_c}{c} + \frac{2\alpha R_0}{c} + \frac{2\alpha V_0}{c}\tau))\tau - \frac{2R_0 f_c}{c}]$$

$$S_b(\omega) = \frac{e^{i2\pi\frac{2R_0 f_c}{c}}}{2} \int_{\tau=-\infty}^{\tau=+\infty} e^{-i2\pi[(f - (\frac{2V_0 f_c}{c} + \frac{2\alpha R_0}{c} + \frac{2\alpha V_0}{c}\tau))\tau]} rect(\frac{\tau - \frac{\tau_0(\tau)}{2}}{T_p - \tau_0}) d\tau$$

Defining the beat frequency f_{b_0} directly related to the target range and velocity such as:

$$f_{b_0}(\tau) = \frac{2\alpha R_0}{c} + \frac{2V_0 f_c}{c} + \frac{2\alpha V_0}{c}\tau$$

$$S_b(\omega) = \frac{e^{i2\pi\frac{2R_0 f_c}{c}}}{2} \int_{\tau=-\infty}^{\tau=+\infty} e^{-i2\pi[(f - f_{b_0}(\tau))\tau]} rect(\frac{\tau}{T_p - \tau_0}) \delta(\tau - \frac{\tau_0}{2}) d\tau$$

$$S_b(\omega) = (T_p - \tau_0)\pi\delta(2\pi(f - f_{b_0}(\tau))) \cdot sinc((Tp - \tau_0)f) \cdot e^{i2\pi\frac{2R_0 f_c}{c}} \cdot e^{-i2\pi f\frac{\tau_0}{2}}$$

$$S_b(\omega) = (T_p - \tau_0)\pi \cdot sinc[(Tp - \tau_0)(f - f_{b_0}(\tau))] \cdot e^{i2\pi\frac{2R_0 f_c}{c}} \cdot e^{-i2\pi f\frac{\tau_0}{2}}$$

If $T_p >> \tau_0$ then

$$\pi sinc[(Tp-\tau_0)(f-f_{b_0}(\tau))] \cdot e^{-i2\pi f\frac{\tau_0}{2}} \approx \pi sinc[(Tp-\tau_0)(f-f_{b_0}(\tau))]$$

Omitting the different amplitudes constant,

$$\boxed{S_b(\omega) = sinc[(Tp-\tau_0)(f-f_{b_0}(\tau))]}$$

A.4 Stepped frequency continuous waveform: SFCW

the stepped frequency continuous waveform is generated by a group of monochromatic signals of discrete frequency f_n transmitted with a fixed frequency increment df. The waveform can be written such as:

$$u_{SFCW}(\tau) = \sum_{n=1}^{N_f} e^{j2\pi f_n \tau}$$

with $f_n = -\frac{B_f}{2} + (n-1)df$ and $df = \frac{B_f}{N_f - 1}$ The focusing received signal using the equivalent of the matched filter for infinite time support is given by:

$$s_{rf}(\tau) = \sum_{n=1}^{N_f} \frac{1}{T_p} \int_{-T_p/2}^{T_p/2} s_r(t) u^*_{SFCW}(t-\tau) dt$$

$$s_{rf}(\tau) = \sum_{n=1}^{N_f} \frac{1}{T_p} \int_{-T_p/2}^{T_p/2} \sum_{i=1}^{N_s} s_i e^{-j\omega_c \tau_i} e^{j2\pi f_n (t-t_i)} e^{-j2\pi f_n (t-\tau)} dt$$

$$s_{rf}(\tau) = \sum_{n=1}^{N_f} \frac{1}{T_p} \int_{-T_p/2}^{T_p/2} \sum_{i=1}^{N_s} s_i e^{-j\omega_c \tau_i} e^{j2\pi f_n (t-t_i-(t-\tau))} dt$$

$$s_{rf}(\tau) = \sum_{n=1}^{N_f} \frac{1}{T_p} \sum_{i=1}^{N_s} s_i e^{-j\omega_c \tau_i} e^{j2\pi f_n (\tau-t_i)} \int_{-T_p/2}^{T_p/2} 1 dt$$

The term $e^{-j\omega_c \tau_i}$ will be suppressed by means of a low pass filter.

$$s_{rf}(\tau) = \sum_{n=1}^{N_f} e^{j2\pi f_n \tau} \sum_{i=1}^{N_s} s_i e^{-j2\pi f_n \tau_i}$$

This shows that the impulse response is equal to the waveform of the continuous signal such as:

$$h(\tau) = \sum_{n=1}^{N_f} e^{j2\pi f_n \tau} = \sum_{n=1}^{N_f} e^{j2\pi(-\frac{B_f}{2}+(n-1)df)\tau} = e^{-j2\pi\frac{B_f}{2}\tau} \sum_{n=1}^{N_f} e^{j2\pi(n-1)df\tau}$$

$$h(\tau) = e^{-j2\pi\frac{B_f}{2}\tau} \cdot \frac{e^{j2\pi N_f df \tau} - 1}{e^{j2\pi df \tau} - 1} == e^{-j2\pi\frac{B_f}{2}\tau} \cdot \frac{e^{j\pi N_f df \tau}}{e^{j2\pi df \tau}} \cdot \frac{2j}{2j} \frac{e^{j\pi N_f df \tau} - e^{-j\pi N_f df \tau}}{e^{j\pi df \tau} - e^{-j\pi df \tau}}$$

$df = \frac{B_f}{N_f - 1} \longrightarrow B_f = df(Nf - 1)$

$$h(\tau) = e^{-j\pi\tau(df(N_f-1)-N_f df+df)}\frac{sin(\pi N_f df\tau)}{sin(\pi df\tau)} = \frac{sin(\pi N_f df\tau)}{sin(\pi df\tau)}$$

We can define the maximum value of the sinc function thanks to:

$$\lim_{x\to 0}\frac{sin(N_f x)}{sin(x)} \approx N_f$$

if we consider that $B_f = df(N_f - 1) \approx df N_f$ then

$$h(\tau) \approx \frac{sin(\pi B_f\tau)}{sin(\pi df\tau)} \longrightarrow h(\tau) \approx N_f sinc(B_f\tau)$$

when $\tau << \frac{1}{df}$. The choice of df will define the periodicity of $h(\tau)$ and hence the ambiguous time (related to the range) such as:

$$T_{amb} = \frac{1}{df}$$

Appendix B

Résumé étendu en français

Le développement de nouvelles technologies d'imagerie nous permet aujourd'hui de voir l'invisible. Selon la bande de fréquence spectrale choisie (Rayons X, Infra rouge, RF, ..), la capacité d'imager les objets diffère du fait que chaque bande de fréquences interagit différemment avec la matière (émission, absorption, réflexion, ..). Nos travaux se sont orientés vers des systèmes actifs en bande millimétrique permettant d'obtenir un compromis acceptable entre résolution, détection d'objets enfouis et taille du système.

Une introduction générale précisant le contexte de l'étude et l'organisation du manuscrit est faite dans le chapitre 1. Durant cette thèse, l'objectif principal était l'étude, la conception, la réalisation et la mesure de modules antennaires en bande millimétrique, ainsi que la mise en œuvre d'algorithmes de traitement de signal et de haute résolution rentrant dans la conception d'un radar imageur.

Dans le second chapitre, un état de l'art des différents systèmes est effectué. Les techniques directes et indirectes sont étudiées afin dans ressortir les avantages et inconvénients. Concernant les techniques directes, plus communément appelées «radar à ouverture réelle», elles permettent, grâce à des antennes directives, de générer des images radar par le biais d'un dépointage du lobe principal de l'antenne qui peut se faire de façon mécanique, électronique ou fréquentiel. Grâce à cet état de l'art, les techniques directes sont étudiées dans le troisième chapitre, et plus précisément, la lentille de Fresnel a été choisie comme dispositif focalisant afin de générer un diagramme directif. La difficulté majeure de cette lentille réside dans sa réalisation et son optimisation car elle est au choix coûteuse, difficile à réaliser et peut avoir une mauvaise efficacité suivant la technique et le procédé de fabrication utilisé.
L'efficacité de compensation de phase est théoriquement déterminée (voir Fig. B.1a) pour démontrer qu'une compensation régulière (smooth) permet une efficacité optimale sans dépendre de la fréquence considérée ce qui n'est pas le cas pour une compensation régulière en apliquant un modulo 2π (smooth $[2\pi]$). De la même manière, l'efficacité d'illumination est théoriquement déterminée (voir Fig. B.1b) afin de permettre l'optimisation optimale de la source primaire qui illumine la lentille. Les compensations régulière et régulière modulo $[2\pi]$ sont théoriquement déterminées afin de définir les permittivités nécessaire pour les deux compensations (voir Fig. B.1c). A partir d'un nouveau procédé technologique permettant le contrôle de la permittivité diélectrique d'un matériau composite, il est possible, avec plus de facil-

ité, de réaliser une lentille inhomogène permettant de compenser la phase de l'onde sphérique émise par une source primaire afin d'obtenir une onde plane en sortie de la lentille et donc un gain optimum. Les deux lentilles ont été réalisées (voir Fig. B.1d) et mesurée dans la bande 75-110 GHz (voir Fig. B.1e) démontrant la viabilité du procédé technologique à très hautes fréquences. En effet, cela a permis d'atteindre une efficacité totale de 59% (voir Fig. B.1f) avec un gain de 38.9 dBi. De plus, grâce à la compensation régulière de la phase, une augmentation de l'efficacité totale de 60% et de la bande de fréquence de 72% respectivement a été obtenue et ce comparativement à des solutions de compensations non régulières issues de l'état de l'art.

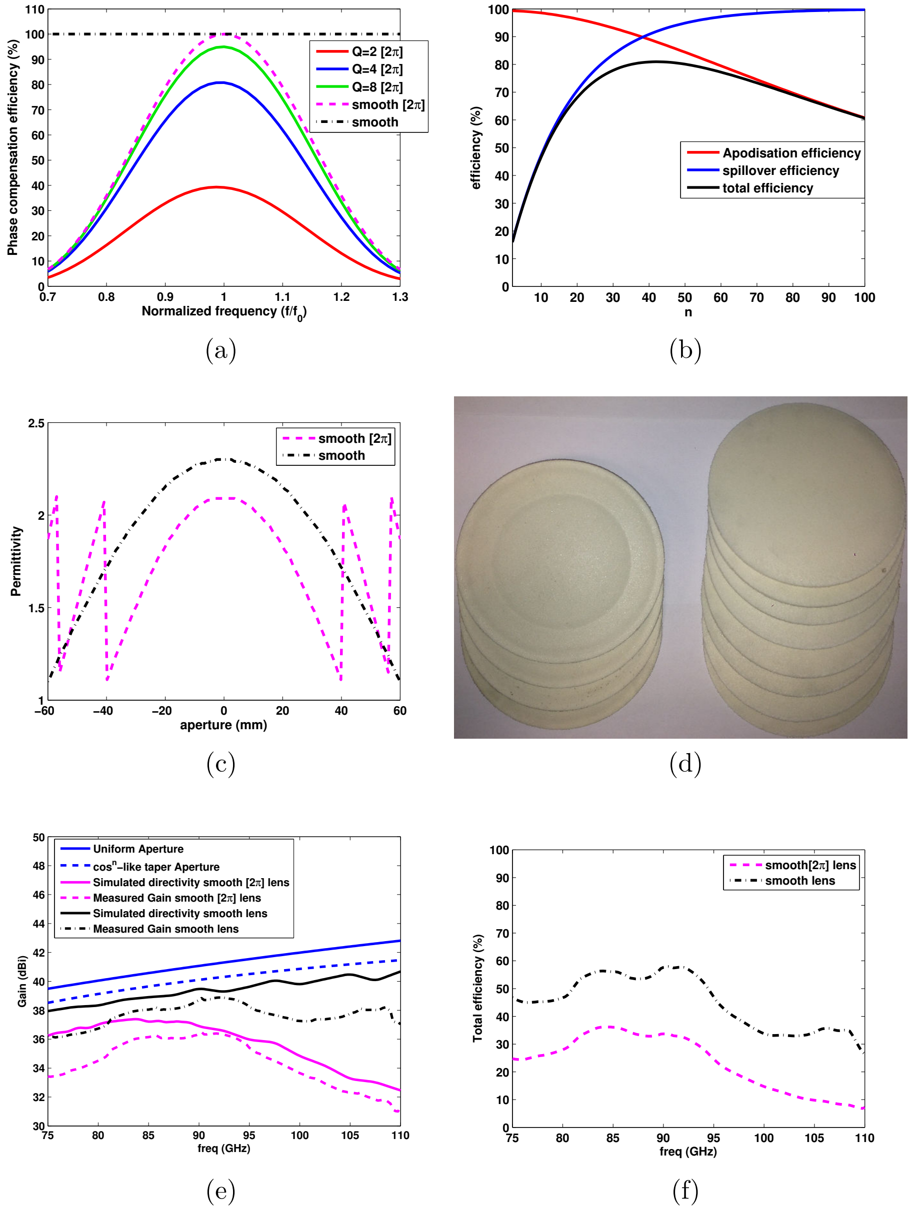

(a) (b)

(c) (d)

(e) (f)

Figure B.1: (a) efficacité de compensation de phase, (b) efficacité d'illumination de la lentille, (c) variation de permittivités nécessaire des lentilles, (d) les lentilles réalisées et (e), (f) résultats de mesures du système antennaire.

Cette antenne a été utilisée pour imager une scène en environnement extérieur en tournant mécaniquement l'antenne sur 360° par pas de 1°. Cette mesure (voir Fig. B.2) a permis de montrer que l'imagerie radar en utilisant une technique directe peut être simple à mettre en œuvre et est peu coûteuse (1 émetteur / 1 récepteur). Néanmoins, pour des applications temps réel, les techniques directes ne sont pas adaptées du fait du temps d'acquisition trop élevé notamment quand le balayage du faisceau d'antenne se fait mécaniquement.

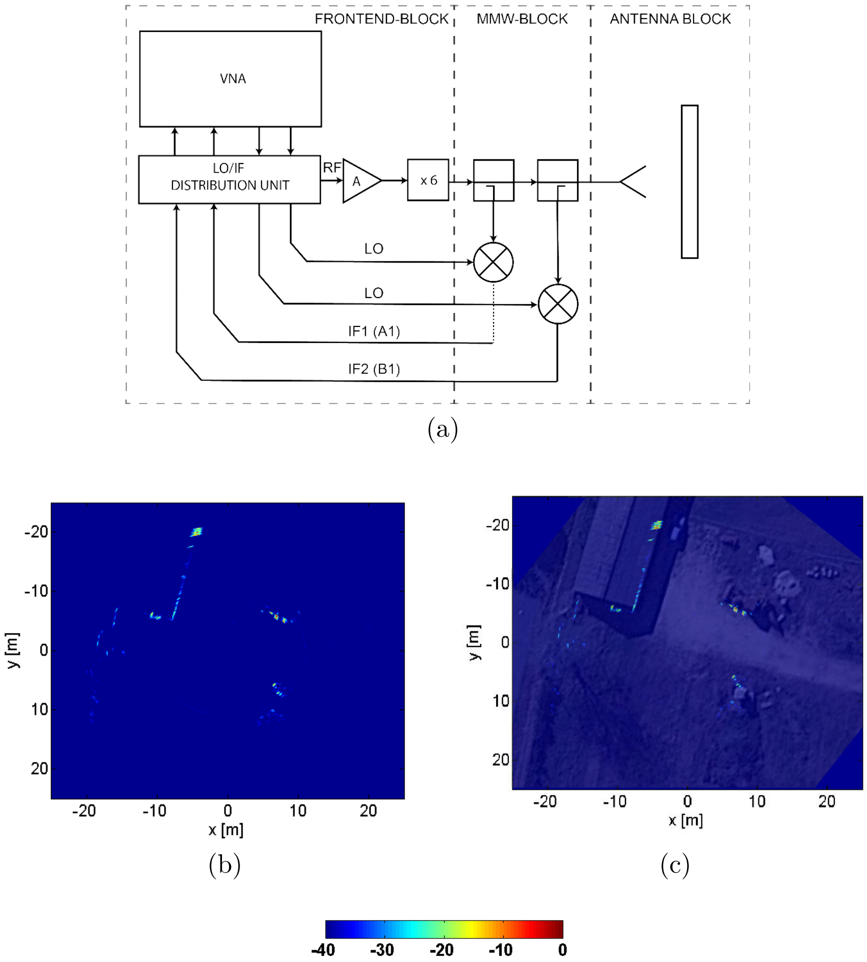

(a)

(b)

(c)

Figure B.2: Résultats des mesures radar avec (a) le système radar utilisé et (b), l'image radar et (c) l'image radar superposée avec une image de la scène pris grâce à google map.

Dans le quatrième chapitre sont donc étudiées et mises en œuvre des techniques indirectes. Elles permettent, à partir de l'acquisition simultanée de signaux sur plusieurs chaînes (émission et/ou réception), de réaliser une image radar grâce au principe de l'ouverture synthétique. La théorie est tout d'abord explicitée et des mesures en bande millimétriques sont effectuées (voir Fig. B.3) pour montrer le grand intérêt de cette technique. Néanmoins, du fait du grand nombre de chaînes RF nécessaire afin d'obtenir une résolution suffisante, elle est extrêmement coûteuse.

Il a alors été étudié le principe de systèmes MIMO (Multiple-Input-Multiple-Output) qui permet de réduire le nombre de chaînes nécessaire sans affecter la résolution du système. En outre, il est étudié et mis en œuvre un dispositif passif (boîte chaotique voir Fig. B.4a) qui permet de compresser de nombreux signaux

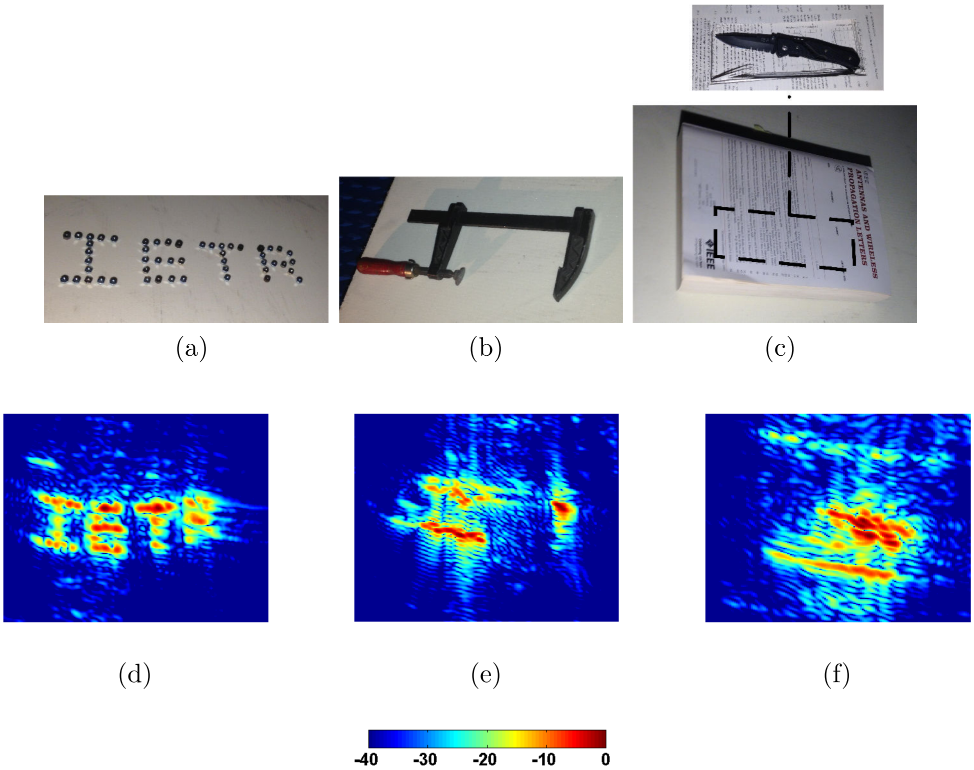

Figure B.3: Résultats de mesures pour trois différentes scènes.

en un nombre réduit qui seront décompressés par la suite en traitement du signal (post-traitement). Le dispositif est basé sur la variation des modes en fonction de la fréquence au sein d'une grande cavité. Ce dispositif a été conçu, réalisé et mesuré de 50 à 66 GHz afin de compresser quatre voies en une seule voie. Durant la décompression des signaux, la corrélation croisée entre les signaux n'excède pas les -15 dB, valeur obtenue grâce à une large bande fréquentielle (16 GHz). Ce dispositif a été utilisé à l'émission dans une configuration MIMO (voir Fig. B.4b) pour montrer que cela permet de réduire par quatre le nombre de chaînes, et de manière complètement passive. Côté réception, il a été utilisé un scanner pour synthétiser le réseau de récepteurs. Le résultat de mesures (voir Fig. B.4d) est comparé avec un cas SIMO avec quatre fois plus de récepteur (voir Fig. B.4c). Cependant, dans l'objectif de réaliser un système antennaire complet réaliste, un réseau actif de huit patchs contrôlés par switchs a été étudié (en cours de réalisation). En commutant entre les 8 antennes de réception, il est alors possible de synthétiser un grand réseau virtuel avec une antenne à l'émission et 41 antennes à la réception, en utilisant seulement une chaine à l'émission et une chaîne à la réception et ceci pour générer des images radar en quasi-temps réel.

Dans le dernier chapitre, toujours dans l'objectif d'améliorer la résolution angulaire du système en utilisant un nombre limité de capteurs, il est étudié des méthodes d'estimation spectrales. Ces algorithmes ont été développés avec des postulats de départ, à savoir un fonctionnement en bande étroite et pour des distances radar-cibles importantes par rapport à la taille de l'antenne (champ lointain). Or, afin d'obtenir une résolution en distance performante (qq cm), il est nécessaire d'acquérir les sig-

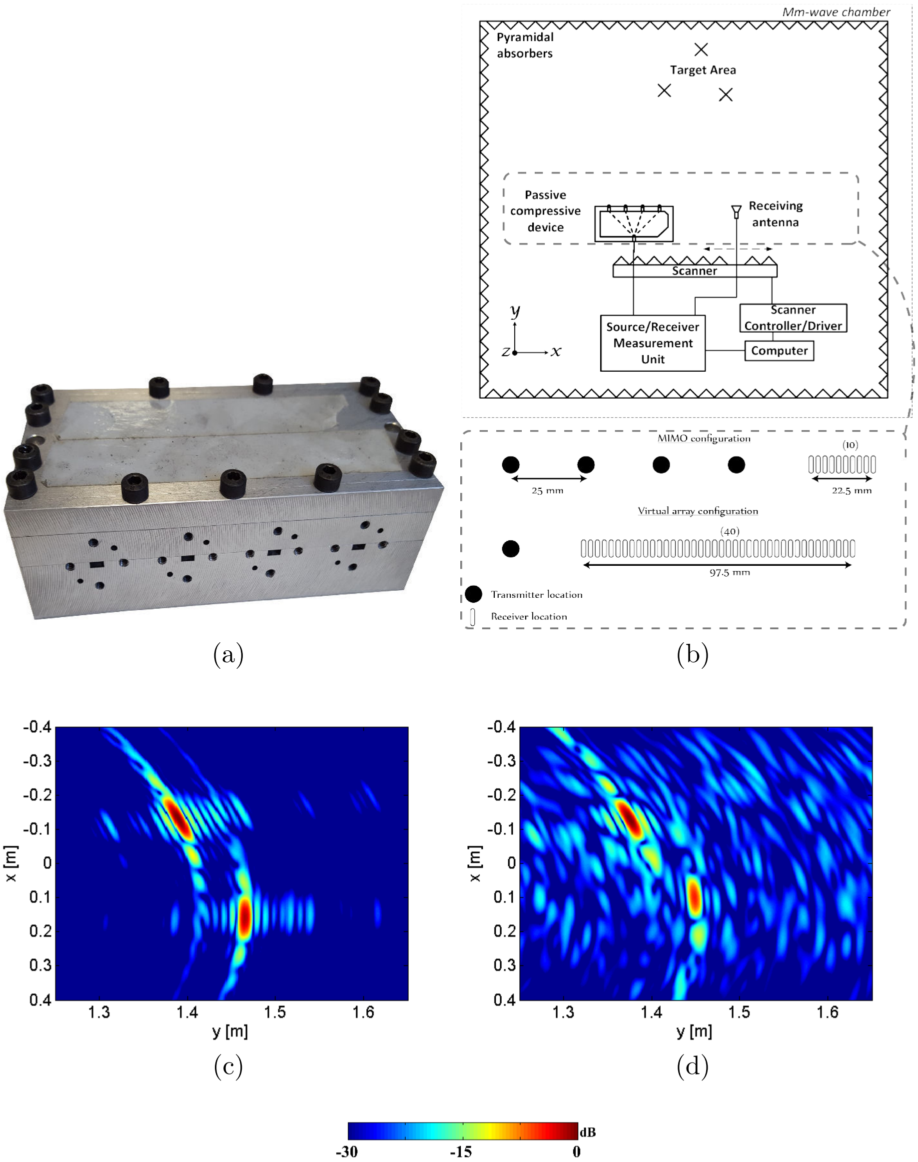

(a) (b)

(c) (d)

Figure B.4: Dispositif compressif passif.

naux sur une large bande (plusieurs GHz) d'où le choix d'un fonctionnement autour d'une porteuse en bande millimétrique. Ces fréquences élevées induisent naturellement des pertes en espace libre prohibitives ce qui limite la portée du radar et donc la condition en champ lointain n'est plus obligatoirement vérifiée. Par conséquent, les postulats de départ pour les méthodes d'estimation spectrale ne sont plus respectés. Il a donc été étudié plusieurs techniques pour compenser les signaux reçus avant de pouvoir appliquer les méthodes d'estimation spectrale.

L'une des techniques est de focaliser les signaux reçus pour générer une image complexe. Grâce à la focalisation, les compensations sont effectuées et les méthodes d'estimation spectrales sont appliquées sur l'image complexe afin d'améliorer la résolution du système (voir Fig. B.5). Les méthodes sont donc appliquées sur des images radar réalisées à l'institut sur des cibles réelles tel qu'un couteau caché dans

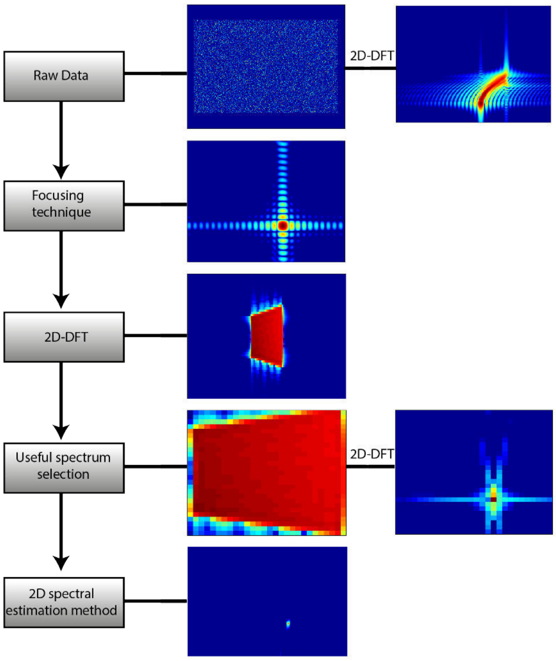

Figure B.5: Flow chart of applying the spectral analysis algorithms in a near-field environment with wide-band signals.

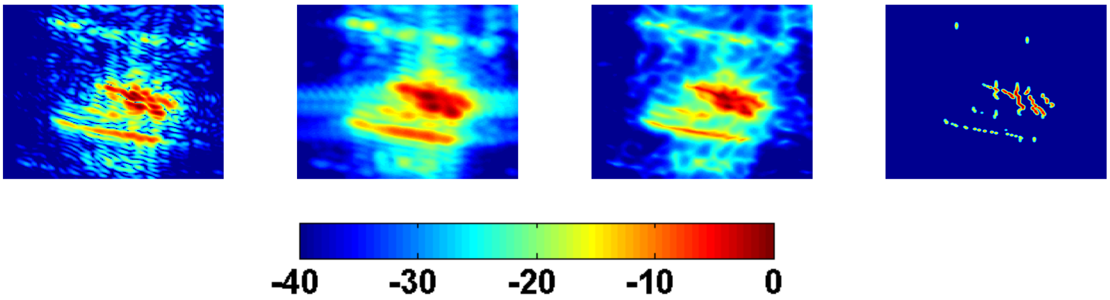

Figure B.6: Resultats des méthodes d'estimation spectrales (Beamforming, Beamofrming avec "spatial smoothing", CAPON et MUSIC) 2D appliqué sur une scène avec un couteau caché dans un livre.2D spectral estimation methods applied on the knife hidden in a book.

un livre (voir Fig. B.6).

Ce manuscrit de thèse se termine par une conclusion et des perspectives concernant l'ensemble du travail effectué. L'ensemble de ce travail de thèse a été valorisé par quatre dépôts de brevets, un article dans une revue internationale, quatre articles soumis dans des revues internationales avec comité de lecture ainsi qu'une publication dans un congrès international.

Résumé

Les travaux présentés dans cette thèse sont une contribution à l'étude des systèmes d'imagerie active en bande millimétrique et plus spécifiquement sur les parties antennaires et le traitement de signal. Ces travaux ont été menés dans le cadre d'une collaboration entre différents départements au sein de l'IETR. Une première étude a porté sur les antennes focalisantes et plus spécifiquement sur la lentille de Fresnel avec un procédé de fabrication de matériau à gradient d'indice qui a permis d'améliorer l'efficacité (59%) et la largeur bande de fréquence (75-110 GHz). Cette antenne a été utilisée sur un système rotatif pour imager une scène réelle exterieure. L'étude s'est ensuite focalisée sur la conception d'une configuration Multiple-Input Multiple-Output ou MIMO (« entrées multiples, sorties multiples ») grâce notamment à l'utilisation d'un dispositif compressif passif 4×1 permettant de réduire, par compression, le nombre de chaînes RF. Ces chaînes sont décompressées par post-traitement. Le dispositif, placé à l'émission, a été associé avec un scanner qui permet de synthétiser un réseau d'antennes à la réception. Cette configuration a permis de générer virtuellement un réseau de plus grande taille, permettant d'améliorer la résolution azimutale du système tout en limitant le nombre de chaînes RF. Cette configuration est utilisée pour imager une scène en chambre anéchoique afin de valider le concept. Pour améliorer encore plus la résolution du système avec un nombre limité de chaînes RF, l'étude d'algorithmes de haute-résolution, ou méthodes d'estimation spectrales, sont utilisés dans des configurations à large bande de fréquences pour imager des cibles en champs proche. L'association de la configuration MIMO, du dispositif compressif passif et des méthodes d'estimation spectrales permet d'améliorer la résolution du système tout en limitant le nombre de chaînes RF nécessaire.

Mots clés : Lentilles de Fresnel, ondes millimétriques, configuration MIMO, dispositif compressif passif, algorithmes de haute-résolution, large bande, champ proche.

Abstract

The broad topic of the presented Ph.D. thesis consists in the contribution to the study of Radar imaging systems at millimeter-wave and more specifically to the antennas and signal processing. These works have been carried out during a partnership between different departments of the IETR. A first study on focusing antennas, particularly on Fresnel lens antennas, thanks to a technological process to manufacture inhomogeneous materials, has allowed to improve the efficiency and the frequency bandwidth. The antenna has been mounted on a rotary system to image a real outdoor scene. Then, the study has been focused on the realization of a Multiple-Input Multiple-Output (MIMO) configuration notably using a 4×1 passive compressive device allowing to reduce, by compression, the number of radiofrequency (RF) chains. The chains are decompressed by post-processing. The device, used at the transmitting part, is associated with a scanner that synthetizes a receiving array of antennas. This configuration allows to generate a large virtual array, to improve the azimutal resolution of the system while maintaining acceptable the number of RF chains. This configuration has been used to image a scene in an anechoid chamber to validate the concept. To further improve the spatial resolution of the system for a given number of RF chains, the study of high resolution algorithms, or spectral estimation methods, are used to image scenes in near field and wide-band configurations. The combination of MIMO configurations, the passive compressive device and the spectral estimation methods have allowed to drastically improve the spatial resolution of the radar imaging system while limiting the number of RF chains.

Keywords: Fresnel lens, millimeter-waves, MIMO configuration, passive compressive device, high-resolution techniques, wide-band, near-field.